TUM School of Engineering and Design

# The finite cell method for the biomechanical simulation of vertebral bone

Mohamed Hassan Abdelaziz Elhaddad, M.Sc.(hons)

Vollständiger Abdruck der von der TUM School of Engineering and Design der Technischen Universität München zur Erlangung des akademischen Grades eines

Doktors der Ingenieurwissenschaften

genehmigten Dissertation.

| | | |
|---|---|---|
| Vorsitzender: | | Priv.-Doz. Dr.-Ing. habil. Stefan Kollmannsberger |
| Prüfer der Dissertation: | 1. | Prof. Dr. rer. nat. Ernst Rank |
| | 2. | Prof. Dr.-Ing. habil. Martin Ruess<br>Hochschule Düsseldorf |

Die Dissertation wurde am 11.05.2022 bei der Technischen Universität München eingereicht und durch die TUM School of Engineering and Design am 31.10.2022 angenommen.

# Zusammenfassung

In den letzten Jahren hat die Verwendung bildbasierter Finite-Elemente-Analysen (FEA) zur Bewertung des Bruchrisikos in menschlichen Knochen an Bedeutung gewonnen. Bei der herkömmlichen Finite Element Analyse muss die Geometrie durch ein geeignetes Netz diskretisiert werden. Bei komplexen dreidimensionalen Geometrien kann die Generierung eines für die Analyse geeigneten Netzes eine schwierige und zeitaufwändige Aufgabe sein. In dieser Arbeit wird die Anwendbarkeit der Finite-Cell-Methode (FCM) für die Simulation der Wirbelknochenmechanik untersucht. Die FCM kombiniert die Immersed-Boundary-Idee mit den Vorteilen Finiter Elemente hoher Ordnung, wodurch sie in der Lage ist, Probleme mit komplexen Geometrien ohne den Aufwand der Netzgenerierung genau zu lösen.

Es wird eine neue Validierungsstudie für die FCM-Analyse vorgestellt, in der Modelle von vier menschlichen Wirbelkörpern untersucht werden, die auf Mikro-CT-Bilddaten basieren. Die numerischen Vorhersagen der Verschiebungsfelder werden mit der in Kompressionsversuchen gemessenen Verformung verglichen. Die Analyse der Ergebnisse zeigt eine sehr gute Übereinstimmung zwischen den experimentellen Daten und den FCM-Vorhersagen, was das Potenzial der FCM als Simulationswerkzeug für mikro-CT-basierte Analysen unterstreicht.

Für Gebiete mit mehreren Materialien verschlechtert sich das Konvergenzverhalten der FCM. In dieser Arbeit wird eine Behandlung von Materialgrenzflächenproblemen im Rahmen der FCM vorgeschlagen. Es wird gezeigt, dass die Verwendung eines Domänenzerlegungsansatzes in Verbindung mit einem *hp*-Verfeinerungsschema zu einer deutlichen Verbesserung der Konvergenzraten führt. Eine Anwendung des vorgeschlagenen Schemas für die Simulation eines hochaufgelösenten Wirbel-Schrauben-Modells wird vorgestellt. Darüber hinaus wird ein numerisches Verfahren für die Einbeziehung von Kräften aus Muskel-Skelett-Modellen in die FCM vorgeschlagen. Ein numerisches Beispiel, das ein Wirbelsäulensegment betrachtet, demonstriert die Möglichkeiten des vorgeschlagenen Ansatzes.

# Abstract

In recent years, the use of image-based finite element analysis (FEA) to assess the risk of fracture in human bones has been gaining importance. In conventional FEA, the geometry needs to be discretized by a suitable mesh. For complex three-dimensional geometries, the generation of an analysis-suitable mesh can be a difficult and time-consuming task. This thesis investigates the applicability of the finite cell method (FCM) to the simulation of vertebral bone mechanics. The FCM combines the immersed-boundary idea with the benefits of high-order finite elements, which enables it to accurately solve problems involving complex geometry without the burden of mesh generation.

A new validation study for FCM analysis of vertebral bodies is presented, where models of four human samples that are based on micro-CT imaging data are examined. The numerical predictions of the displacement fields are compared to the deformation measured in compression experiments. Analysis of the results shows very good agreement between the experimental data and the FCM predictions, which underlines the potential of the FCM as a simulation tool for micro-CT-based analysis.

For domains with multiple materials, the convergence behavior of the FCM deteriorates. In this work, a treatment for material interface problems in the framework of the FCM is proposed. It is shown that the use of a domain decomposition approach in conjunction with an *hp*-refinement scheme leads to a significant improvement of the convergence rates. An application of the proposed scheme for the simulation of a high-resolution vertebra–screw model is presented. Additionally, a numerical technique for the inclusion of loads stemming from musculoskeletal models in the FCM is proposed. A numerical example which considers a spinal segment demonstrates the capability of the proposed approach.

# Acknowledgments

The work presented in this dissertation was carried out during my time as a doctoral candidate at the Chair for Computation in Engineering. I am grateful to everyone who has supported me along the way.
First, I would like to thank my advisor Prof. Ernst Rank for his continuous trust, support and guidance since my time as a student assistant at the Chair and throughout all the years. I am also grateful for the opportunities he offered me for both scientific and personal development.
I also thank Prof. Martin Ruess for his valuable guidance, and I am grateful for his contribution to the success of this work. I really enjoyed my research visit to him at TU Delft. I also thank Martin for reviewing this dissertation.
I thank Dr. Stefan Kollmannsberger for his valuable input to this work and continuous support throughout the years. I am also grateful for the friendly working environment he provides as a leader of the Simulation in Applied Mechanics group in which I always enjoyed working. I also thank Stefan for chairing my examination.
This work was financially supported by the German Research Foundation (DFG) under Grant RA 624/26-1 and the European Research Council under Grant ERC-2014-StG 637164, which I gratefully acknowledge. In the scope of this collaboration project, I had the pleasure of working together with members of the Departments of Neuroradiology, Sports Orthopaedics, Biomedical Physics, Sport Equipment and Sport Materials of the TUM. I gratefully acknowledge the efforts of Prof. Jan S. Kirschke , Prof. Franz Pfeiffer, Alexander Valentinitsch, Tanja Lerchl, Amirhossein Bayat, Peter Föhr and Klaus Achterhold and their work on experiments, image acquisition, image processing and musculoskeletal modeling.
I thank my colleagues at the Chair for Computation in Engineering. Being part of this group and working alongside everyone was a great pleasure. In particular, I express my thanks to Philipp Kopp, Nina Korshunova, John Jomo, Ali Özcan, Lisa Hug, Davide D'Angella, Alexander Paolini, Benjamin Wassermann, Ralf-Peter Mundani, Jérôme Frisch, Christoph Ertl, Nevena Perovic, Bobby Ginting and Jing Rao. My special thanks go to Nils Zander and Tino Bog, who guided me since I first started as their student assistant.
I am also thankful to Hagen Wille and Prof. Zohar Yosibash for all of our discussions on bone mechanics from which I always learned more.
I also thank Lukas Rinderer, Oguz Oztoprak and Sindhu Nagaraja. I really enjoyed working with them as a supervisor, learned a lot from them, and acknowledge their contributions to the success of this work.
I was very lucky to share an office during this journey with my friend and colleague László Kudela. I enjoyed all the discussions and activities we shared, both at university and elsewhere. I also thank Hanne Cornils for her invaluable help with all administrative matters.
Finally, I am very grateful to my family and friends for their unconditional love and support. Above all, I thank my girlfriend Lara for her help, encouragement and loving understanding.

# Contents

# Chapter 1

# Introduction

## 1.1 Motivation

Osteoporosis compromises bone strength, increasing the risk of fractures with severe health consequences. Vertebral fractures are a major clinical problem that is associated with with increased mortality. As osteoporosis is an age-related disease, the ongoing demographic shift toward a more elderly population means that the number of individuals with vertebral fractures will continue to increase [127].

Reliable patient-specific estimates of vertebral strength should improve diagnosis and management of osteoporosis. Therefore, the development of a biomechanical simulation method for the prognosis of insufficiency fractures is of major interest. This method needs to be able to provide accurate predictions of the mechanical response of the patient's bones to estimate the risk of fracture. The mechanical response of the vertebra is determined by its geometry and the bone mass density [51]. Hence, a patient-specific approach is necessary for an individualized treatment, which takes the variable geometry and material properties into consideration. Additionally, due to variations in the spine's geometry, e.g. in patients with spinal deformities such as scoliosis, the considered loads which act on the vertebrae also need to be estimated differently for each patient. Hence, a reliable simulation tool for patient-specific biomechanical analysis needs to be robust in dealing with different geometries and boundary conditions. Furthermore, biomechanical simulations could be used to gain a better understanding of bone–implant interaction. Hence, they could be a useful instrument in designing better implants, and to aid surgeons in their decision-making and planning of operations.

The finite element method (FEM) is ubiquitous in engineering practice as a simulation tool for structural mechanics [111, 16]. In recent years, the use of finite element analysis for the prediction of the mechanical behavior of bones has been gaining importance [210]. Subject-specific FE models based on quantitative computed tomography (QCT) images have been used to predict in vitro vertebral strength, with better accuracy in comparison to conventional prediction methods solely based on analysis of the bone mineral density [47, 51]. Research in the application of FE analysis to the simulation of vertebral bone mechanics has also addressed the anisotropy of bone's material properties [187], and the simulation of large deformations and failure [110, 42].

However, there are some challenges in conventional FE analysis that hinder its applicability as an automated simulation tool for subject-specific biomechanical analysis. FE analysis requires the discretization of the geometry by a suitable mesh. In continuum-level voxel-based FEM, the segmented CT images can be directly converted into grids of hexahedral finite elements [47]. This approach can be highly automated, and allows for a direct mapping of the material parameters to the finite elements. However, its resolution is limited by the low resolution of clinical CT scans, resulting in a very coarse geometric description. The Cartesian voxel grid-based meshes have jagged boundaries with re-entrant corners which induce artificial singularities and limit the numerical accuracy. Higher fidelity approximations with higher numerical accuracy can be obtained for *the same scans* by considering a linear, or higher-order, approximation of the geometry, as demonstrated in [253, 193]. Unfortunately, the task of three-dimensional mesh generation can be a complex and time-consuming one that is hard to automate [46]. Moreover, the standard $h$-version of the FEM relies on low-order basis functions, making it numerically less efficient than higher-order approaches [237], which have been also demonstrated to be very well suited for continuum-level biomechanical analysis [270].

On the microstructural level, the micro-voxel based finite element method ($\mu$-FEM) has been used to provide better understanding of the influence of the trabecular microstructure on the bone's mechanical behavior [246], and to simulate bone–implant interaction [261]. Whereas $\mu$-FEM models of bone can be used to perform highly accurate numerical simulations, they can be numerically very expensive due to the one-to-one mapping of micro-voxels and hexahedral finite elements, which limits their applicability to the analysis of whole vertebral bodies. High resolution $\mu$-FEM models typically have several tens to hundreds of millions of degrees of freedom, which require high performance/supercomputing resources [9, 2, 3].

Fictitious domain, or immersed boundary methods have emerged as an alternative to the boundary conforming FEM. These methods are attractive because they avoid complex mesh generation, and allow the use of solvers that take advantage of structured meshes. One example of this class of methods is the finite cell method (FCM), which was introduced in [190], combining the fictitious domain concept with high-order basis functions. The main idea is to extend the originally complex geometry by a fictitious domain to a much simpler shape, which can be easily meshed using a Cartesian grid. The use of high-order basis functions, which smoothly extend into the fictitious domain, allows the FCM to achieve exponential rates of convergence for smooth problems. The FCM has been investigated and successfully applied in various problems, including three-dimensional solid mechanics [70], shell mechanics [199],linear thermoelasticity [278], geometrical nonlinearities [219], contact mechanics [23, 24], implicit and explicit elastodynamics [67, 76, 121, 86]. In the field of biomechanics, continuum-level FCM models of the human femur have been validated in an in vitro study, showing high correlation between the numerical predictions and the experiments [209]. The FCM has also been used for the microstructural analysis of trabecular bone [249]. In particular, the flexibility of the FCM in dealing with complex geometry, and in handling different types of geometric description make it very promising as an automatic simulation kernel.

For problems with smooth solutions, the FCM achieves exponential convergence for uniform $p$-refinement, which has been demonstrated in numerous numerical investiga-

tions [190, 70, 30, 219, 278]. However, for non-smooth problems the convergence behavior of the FCM significantly deteriorates. In problems with material interfaces, the displacement field is piecewise smooth, exhibiting a kink ($C^0$-continuity) at the material interface. In the FCM, the edges and faces of the Cartesian mesh do not exactly match the material interfaces. Within a finite cell, the smooth polynomial basis functions are unable to represent the discontinuity across the material interface, which causes an oscillatory solution and reduces the convergence rate. Moreover, singularities and high solution gradients require local refinement of the mesh to limit the approximation error, which does not fit with the Cartesian grid nature of the FCM mesh. These problems need to be adequately treated in order to unlock the FCM's potential as a simulation tool for biomechanics.

## 1.2 Objectives

In the scope of this work, we address these challenges as we investigate the applicability the FCM for the numerical simulation of the mechanics of vertebral bone. The FCM will be used for image-based structural analysis, with the geometry and material properties of the vertebral bone originating from CT scans.
We present a new validation study of micro-CT-based FCM analysis of whole vertebral bodies. To validate the numerical method, the predictions of the simulations are compared to the results of mechanical experiments.
Concerning the application of FCM to non-smooth problems, we investigate the combination of the FCM with a domain decomposition technique to resolve the weak discontinuity at material interfaces, and a local mesh refinement scheme. We verify the proposed approach using a series of numerical benchmarks, and apply it for the simulation of a vertebra–implant system.
In a patient-specific biomechanical simulation framework, realistic boundary conditions could be provided by multibody simulations of musculoskeletal models. In these simulations, biomechanical joints are idealized as points. Accordingly, the resulting loads are given as concentrated forces and moments. In this work, we tackle another challenge facing the FCM, as we propose a numerical approach for the consideration of concentrated loads in patient-specific FCM vertebra models.
We hypothesize that, owing to its inherent flexibility in dealing with geometry, the FCM has great potential as a simulation tool for biomechanical analysis. As an immersed boundary method, the FCM can be used for simulations of complex geometry without mesh generation. The use of high-order basis function, together with the weak enforcement of interface conditions, and the multi-level *hp*-refinement scheme ensures high accuracy, even for non-smooth problems.

## 1.3 Outline

This thesis is organized as follows: In **Chapter 2** we present a literature review of finite element analysis of vertebral bone. We start by summarizing the relevant background information on the anatomy of the spine and the biomechanics of vertebral bone. Then, we

present a survey of the different types of FEM models used in literature for the simulation of biomechanics of the vertebra.
In **Chapter 3**, we present the finite cell methods and its application in the simulation of bone mechanics. Starting with a summary of the theory of linear elasticity and the respective governing equations, we present the fundamentals of the finite element method, and the extension to its $p$-version. We then present the concept of the finite cell method as an extension of the $p$-version of the FEM with an embedded domain approach. We give special attention to image-based finite cell analysis. Finally, we review previous efforts in the application of the FCM for bone mechanics, its verification and validation.
In **Chapter 4**, we present a validation study for micro-CT-based FCM models of human vertebral bodies. The study makes use of digital volume correlation techniques to quantify the displacements occurring due to compression of vertebral bodies during a compression experiment. The measured displacements are used to define the boundary conditions for the FCM models, and to validate the predictions of the FCM models.
In **Chapter 5**, we propose a numerical technique for the efficient simulation of embedded material interface problems using the FCM in conjunction with a coupling method and a local refinement scheme. We present a series of numerical benchmarks of material interface problems—in two and three dimensions—to verify the proposed method.
In **Chapter 6**, we present two applications of the FCM for solving problems including material interfaces in bone mechanics. The first application presents a numerical technique for the inclusion of loads stemming from musculoskeletal models into patient-specific FCM models. The second application shows the potential of the FCM with multi-level $hp$-refinement for the simulation of vertebrae with pedicle screws, and demonstrates that the proposed method can be used to solve material interface problems involving very complex geometry.
Finally, in **Chapter 7**, we present a summary of the scientific conclusions of the work presented in this dissertation and discuss possibilities for further development in future work.

# Chapter 2

# Finite element analysis of vertebral bone: a literature review

In this chapter, we discuss previous efforts in the application of conventional finite element analysis for the simulation of vertebral bone. We start by summarizing the basic anatomy, structure and function of the human spine. Following that, we discuss the structural mechanics of the vertebra, the loads which are considered in biomechanical simulations and the mechanical properties of vertebral bone. Finally, we present a literature review of conventional finite element simulations of vertebral biomechanics, pointing out the different scales of biomechanical models, and the various numerical modeling and discretization techniques.

## 2.1 Anatomy of the spine

In the following, we present a brief introduction to the anatomy of the human spine. For further in-depth information, the interested reader is referred to [170, 25].

### 2.1.1 Spinal column

The vertebral column serves to support the human body in the upright posture, while allowing for movement and locomotion. Additionally, it surrounds and protects the spinal cord which is housed within the vertebral canal [170].
The adult spine is composed of 24 separate bony vertebrae, together with five fused vertebrae which form the sacrum and four fused vertebrae which form the coccyx (the tailbone). The spine can be divided into three main regions as shown in Figure 2.1: the *cervical* (neck), *thoracic* (chest), and *lumbar* (trunk) spine. In this work, we focus on the lower thoracic and lumbar regions.
Adjacent vertebra are separated by intervertebral discs, with the exception of the first and second cervical vertebrae. At the rear (posterior), spinal muscles attach to the bony processes of the vertebrae. Ligaments extend along the vertebral column at the front and at the back. They are made of fibrous connective tissue which joins the vertebrae to restrict movement and prevent damage to the vertebral column [170].

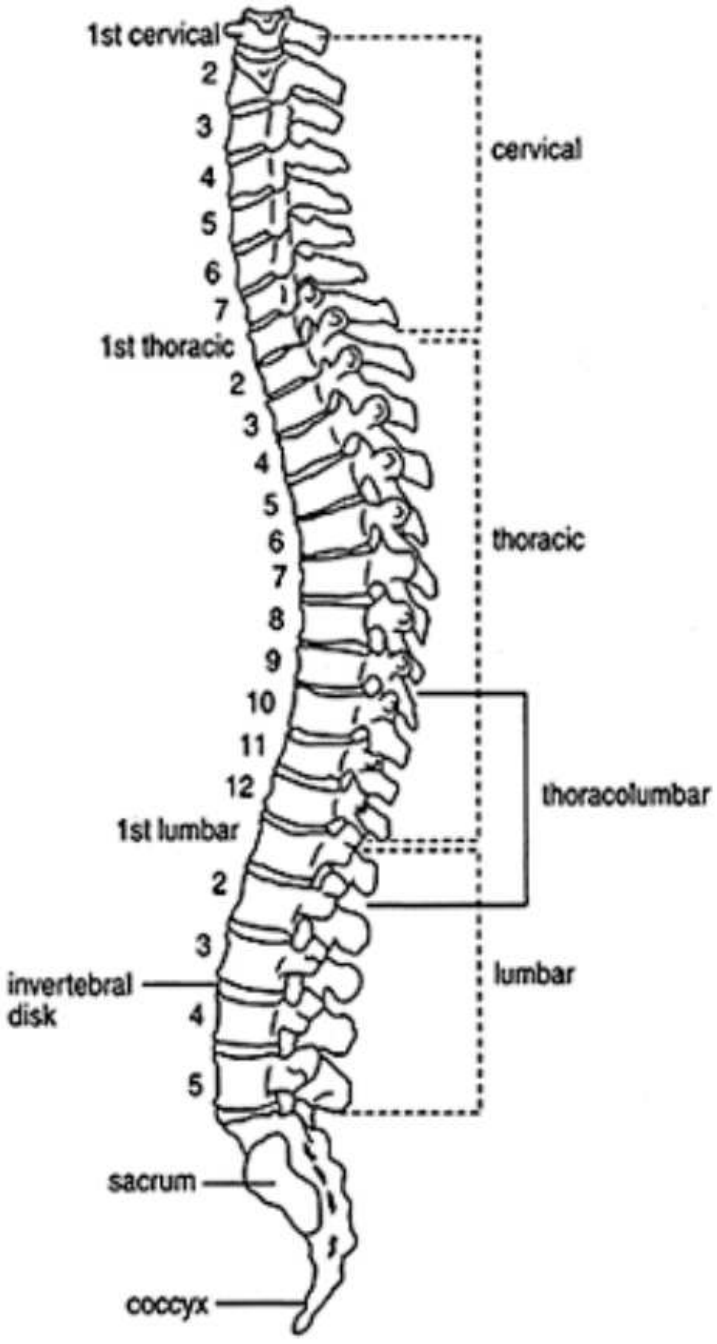


Figure 2.1: Anatomy of the spinal column, reproduced from [25].

In the sagittal plane (viewed from the side), the vertebral column has an S-shaped curved shape, with *lordotic* curves in the cervical and lumbar regions (convex forward), and a *kyphotic* curve in the thoracic spine (concave forward). These curves give it increased flexibility and better shock-absorbing capacity, while maintaining adequate stiffness and stability at the intervertebral joint level. When viewed from the back, a normal spine is vertically straight. If the spine shows an abnormal lateral curvature, this indicates a condition named scoliosis [25].

### 2.1.2 Vertebrae

The vertebrae are the building blocks of the vertebral column. Figure 2.2 depicts the anatomy of a lumbar vertebra. The vertebra can be divided into three functional components: the vertebral body, the pedicles and the posterior elements.

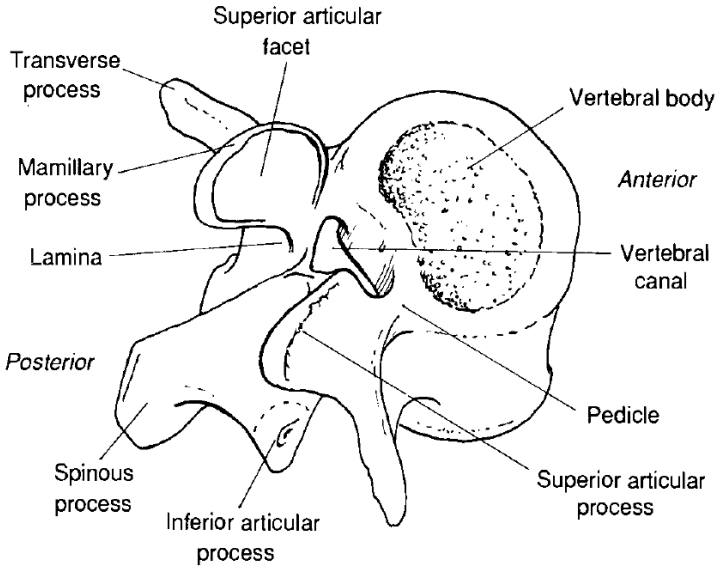


Figure 2.2: Anatomy of a typical lumbar vertebra, reproduced from [170].

The vertebral body mainly serves the function of weight bearing and is roughly cylindrical in shape. It is composed of a trabecular core surrounded by a cortical bone shell. The microstructure of trabecular (also called cancellous) bone consists of a network of rods or plates called *trabeculae*, whereas cortical (or compact) bone is a highly dense bone. The superior and inferior endplates of the vertebral body are composed of a thin layer of cortical bone, and are dedicated to supporting loads transferred from the adjoining intervertebral discs.
The two pedicles connect the vertebral body and the posterior elements which project from the vertebral arch. The vertebral body and the vertebral arch form the vertebral canal, which houses the spinal cord. The posterior elements of the vertebra are the laminae and the processes. They form a very irregular mass of bone, with various protruding bars of bone. The articular processes of neighboring vertebrae can interlock to resist forward sliding and twisting of the vertebral bodies. The spinous and transverse processes provide areas for muscle attachments, and act as levers to magnify the action of the attached

muscles. The laminae serve to transmit the forces from the spinous and inferior articular processes, providing stability in the horizontal plane [25]. However, the posterior elements have little contribution to vertebral strength in axial compression [108].

While all vertebrae share this general structure, specific characteristics of individual vertebrae vary along the vertebral column. The cervical vertebrae are the smallest and lightest. The thoracic vertebrae are larger in comparison, and contain facets at which the ribs connect to the vertebral column. The lumbar vertebrae are the largest, as they need to support more weight [170].

### 2.1.3 Intervertebral discs

The intervertebral discs lie between the vertebrae and form the major joints of the vertebral column. Their principal functions are to transmit loads between the vertebral bodies, and to allow and restrain motion at the interbody joints. Discs are bounded anteriorly and posteriorly by ligaments [170].

The two main components of the disc are the annulus fibrosus and the nucleus pulposus, as depicted in Figure 2.3. The annulus fibrosus is a composite structure consisting of concentric lamellae of collagen fibers with alternating orientations, which are embedded in a proteoglycan gel matrix. The annulus fibrosus encloses the nucleus pulposus, which is a highly viscous gelatinous mass. The discs are separated from the adjoining vertebral bodies by thin cartilaginous plates [170].

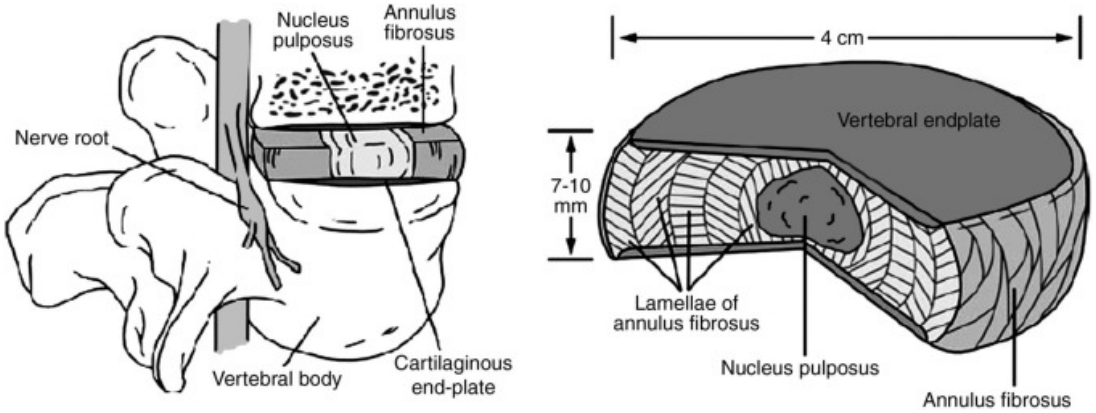


Figure 2.3: Anatomy of the intervertebral disc, reproduced from [197].

## 2.2 Biomechanics of the vertebra

In this section, we discuss the structural mechanics of the vertebra and the mechanical properties of vertebral bone. More details on the rich subject of vertebral biomechanics are found in [180, 48, 130, 224].

### 2.2.1 Structure of vertebral bone

Bone is a complex material with a multi-scale hierarchical structure. This structure makes it efficient in load bearing, as it results in a high strength to weight ratio [48]. As mentioned in the previous section, the vertebral body is composed of a cortical shell which is reinforced by a trabecular core. This structure has the advantage of being lightweight, due to the porous trabecular core, while having high compressive strength. In compression, the vertical trabeculae reinforce the cortical shell to carry the load, while the horizontal trabeculae maintain stability by creating transverse tension (lateral support) [25].

#### Microstructure of cortical bone

At the microscale, cortical bone is very dense, with a porosity of approximately 6%. The thickness of the vertebral shell is in the range a few hundred $\mu$m. Blood vessels in the cortical bone are surrounded by *osteons*, which are composed of concentric rings of calcified matrix called lamellae. Osteons can be several millimeters long and they run parallel to the long axis of the bone [224].

#### Microstructure of trabecular bone

Trabecular bone is usually found in bones that are loaded in compression. It has a foam-like microstructure, with an interconnecting network of microscopic lamellae, called *trabeculae*. They are surrounded by bone marrow which has little mechanical role except perhaps in high-energy impact. Trabeculae range from 50 to 300 $\mu$m in thickness, and their spacing is in the order of 1 mm. The orientation of the trabecular network depends on the loading direction in the bone, with a principal direction along which mechanical stiffness and strength are greatest, leading to an anisotropic behavior. In the vertebral body, the principal orientation is along the inferior–superior axis [224].

### 2.2.2 Vertebral loading

The vertebra is mainly loaded through the adjacent intervertebral discs. Additionally, spinal muscles attach to the vertebral processes and act to stabilize the spinal column. The effect of muscle forces can significantly influence the results of biomechanical analysis of the spine [259]. The spine is loaded with a combination of compression, bending and torsion. Flexion, extension and lateral bending movements result in compressive and tensile stresses in the intervertebral disc as illustrated in Figure 2.4, whereas axial rotation subjects the disc to shear stresses [258].
The compressive load is transferred between the vertebral endplates through the nucleus pulposus and the annulus fibrosis. In a non-degenerated disc, hydrostatic pressure builds up within the nucleus and acts on the endplates and the annular ring. In an aging spine, the disc degenerates and the nucleus loses its water content and is not capable of building up sufficient pressure. As a result, the endplates are subjected to less pressure at the center, and the load distribution shifts towards the posterior endplate and vertebral arch [168].

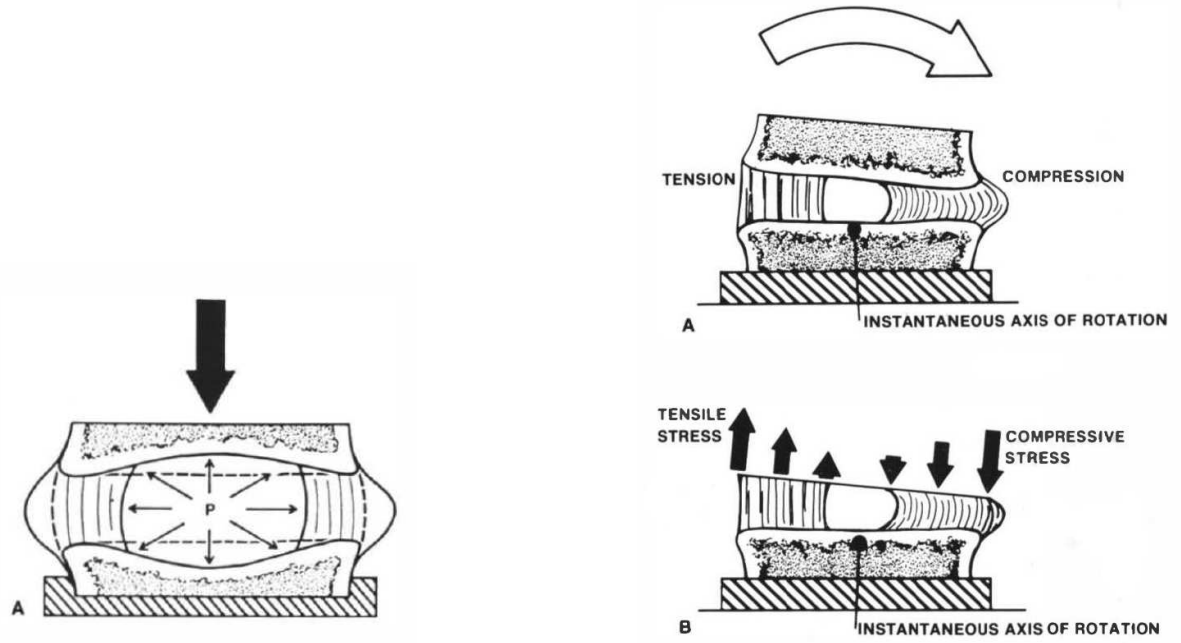


(a) Axial compression (b) Bending

Figure 2.4: Stresses in the intervertebral disc, reproduced from [258]

### 2.2.3 Mechanical properties of vertebral bone

An accurate description of the material properties is essential for reliable modeling of the mechanical behavior of bone. The material properties of vertebral bone can be characterized at different length scales. Here, we distinguish between the *tissue*- and *continuum*-level properties. Tissue-level mechanical properties describe the mechanical behavior of the constituent material independently of microscopic porosity, whereas the coarser continuum-level mechanics describe the overall mechanical response of the bone structure.

Several studies which have investigated the tissue-level material properties of cortical and trabecular bone suggest that the mechanical properties of the two types of bone are highly similar on the tissue level. The values for the Young's modulus estimated for the longitudinal direction using acoustic and nano-indentation experiments range between 16 and 22 GPa [132, 245, 202, 204].

On the continuum-level, the mechanical behavior of trabecular bone exhibits an initial linear elastic regime, followed by a nonlinear yield region where failure initiates. The final post-yield phase occurs when the trabeculae reach their ultimate stress in compression (ductile failure), or abruptly ends due to fracture in tension (brittle failure). Generally, trabecular bone is weaker in tension than in compression. However, this asymmetry is rather small for the spine and can be neglected [130]. The stress–strain response of vertebral trabecular bone samples shows that the yield point is reached at strains less than 1.0% both in tension and compression, and reach the ultimate strains in compression at less than 2.0%. Under tensile loading, trabecular bone fractures at a strain of approximately

1.5% [140].

Vertebral bone is anisotropic in both stiffness and strength. Mean values of Young's modulus and strength along the inferior–superior axis have been reported to be around 3 times higher than in the transverse directions [130]. While this anisotropy is considered mild in comparison with fiber-reinforced composites, its biomechanical influence on whole bone strength could be significant, especially for complex off-axis load scenarios.

An important characteristic of trabecular bone is its heterogeneity which leads to wide variations in its apparent (continuum-level) mechanical properties. In the vertebra, this mainly results from local variations in the bone volume fraction and the microstructural architecture. This results in large variations in the Young's modulus (from 50 MPa to over 700 MPa) and the bone strength (from about 0.5 MPa to 5 MPa) [130].

The stiffness of trabecular bone depends primarily on the bone volume fraction or its apparent density, which is defined as the product of the bone volume fraction and tissue density (approximately constant around 2.0 g/cm$^3$). However, an exact form of this $E$–$\rho$ relationship has not been unequivocally determined [102]. Other variables significantly influence this relationship including the anatomical site of the bone specimen [173], the loading direction, and testing method [224]. Similarly, bone strength also depends on the density, as there is a strong linear correlation between the stress at which trabecular bone fails and the corresponding Young's modulus [130]. For trabecular vertebral bone, Kopperdahl et al. [141] reported density–mechanical property regressions that are based on mechanical testing of 45 vertebral bodies. These relationships are commonly used in QCT-based biomechanical models of the human spine.

## 2.3 Biomechanical finite element analysis of vertebral bone

The finite element method (FEM) represents the current state-of-the-art in biomechanical simulations of bone [210]. Since the 1980s, there have been numerous efforts in the application of the FEM to the simulation of bone mechanics [112]. Substantial research has been devoted to the development of material models, medical image processing techniques, and the development of novel finite element technologies. Detailed reviews of the application of FE analysis in bone research are found in [120, 210]. The fundamentals of the theory of linear elasticity and the FEM are presented in Section 3.2 and Section 3.3, respectively. In the following, we present an overview of previous efforts in the application FEM for the biomechanical analysis of vertebral bone.

Subject-specific numerical models of bone need to capture the relevant geometric details and corresponding material properties of the actual structure. To this end, geometric descriptions that are reconstructed from medical images are used. FE modeling approaches of bone can be grouped into two major categories, based on the length scale in which the geometry and the biomechanics are considered: continuum-level, and microstructural FE models. Both approaches are based on three-dimensional reconstructions of the geometry that can be obtained non-destructively using computed tomography (CT) or magnetic resonance imaging (MRI) [156, 153].

### 2.3.1 Continuum-level FE analysis

Continuum-level FE models consider the heterogeneous material properties of the trabecular bone but do not include the microstructural details [210]. Most commonly, they are based on quantitative CT (QCT) scans which have a resolution of about 1 mm.
Computed tomography is a non-invasive medical imaging technique used to obtain detailed internal three-dimensional images of the body. A CT scanner uses a rotating X-ray source and special digital X-ray detectors, which are located directly opposite the X-ray source. A three-dimensional image is obtained as a series of cross-sectional two-dimensional images, where the X-ray attenuation value of the tissue at each point in the slice is computed. A voxel is a volume element corresponding to a pixel in a two-dimensional slice. CT image calibration can be used to convert the attenuation values to equivalent density [103].
To reconstruct the geometry of the vertebra from a CT scan, a segmentation is carried out. This is the process of detecting and identifying separate structures in the image, and labeling the voxels accordingly. Depending on the size and resolution of the scan, it can be a tedious and time-consuming task that requires considerable manual effort. Hence, a lot of research effort has been dedicated for the development of automatic segmentation algorithms for the vertebra [221].
The intervertebral discs transmit forces between the spinal segments, and including their influence is important for realistic modeling of the boundary conditions. Ligaments and muscles attached to the bone also exert forces which could be significant to the outcome of the biomechanical analysis. One possibility is to extend the model to also include finite element models of the ligaments and the discs, which consider the geometric and material nonlinearities [255]. Alternatively, musculoskeletal models of the spine can be used to model the dynamic behavior and define the boundary conditions to the FE analysis of the bone, as discussed in Section 6.1 in detail.

#### Voxel-FEM

In the voxel-based finite element method (voxel-FEM), the finite element meshes are automatically generated from the segmented CT images, where each voxel in the three-dimensional image is converted to an 8-noded hexahedral (brick) finite element. To model the heterogeneity of the bone, $E$–$\rho$ relationships are used to assign a separate Young's modulus for each elements corresponding to the voxel's density value. This simple approach was originally introduced by Keyak et al. [134] to carry out CT image-based FE analysis of the femur. Voxel-FEM analysis holds the advantage of being fully automated, requiring no manual modeling effort, while providing numerical predictions with good accuracy. However, the voxel-based description of the surface geometry gives jagged surfaces with re-entrant corners, which lead to a lower accuracy in comparison to modeling approaches that consider a smooth description of the geometry, as shown in a comparative study of femur models [253].
Voxel-FEM models of vertebral bodies were presented by Crawford et al. [47] in a study which validated FEM predictions of vertebral strength. In that study, the authors considered 13 human vertebral bodies which were scanned with QCT (0.674 mm voxel size), which does not resolve the trabecular microstructure (see Figure 2.5). The $E$–$\rho$ relationship developed by Kopperdahl et al. [141] was used to assign the transverse isotropic

material properties. The vertebral strength determined in experiments was positively correlated with the FE measures of strength ($R^2 = 0.86$), which demonstrated the better performance of voxel-FEM models in predicting vertebral compressive strength in comparison to the existing state of the art, which was solely based on analysis of the bone density.

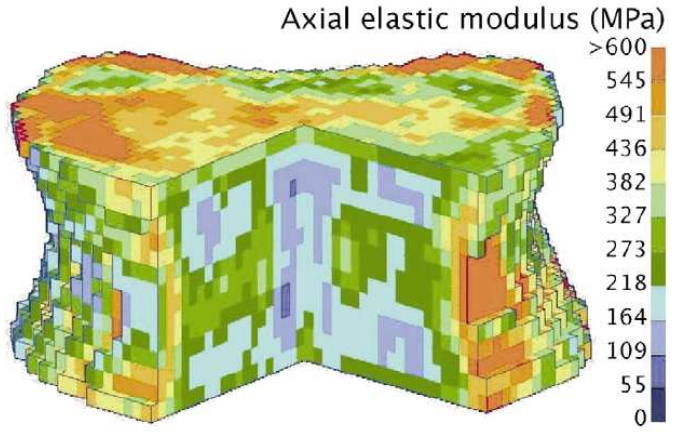


Figure 2.5: The distribution of axial elastic moduli in a voxel-based finite element model of a vertebral body. The finite element dimensions are $1 \times 1 \times 1.5$ mm$^3$. Reproduced from [47]

Voxel-FEM models of vertebral bodies have been extensively used to study the mechanics of vertebral bone, and to assess vertebral strength as influenced by osteoporosis [131, 40, 139, 4]. A more accurate prediction of the mechanical response, especially for cases with off-axial loading, can be obtained using more complex material models which account for the bone's anisotropy. In [34], a fabric-based model [286] was used in voxel-FEM analysis to predict damage accumulation in vertebral bodies under combined loads. Nonlinear continuum-level voxel-FEM models were also developed to study vertebral fractures and damage [52, 38].

### *h*-FEM

A more sophisticated FEM modeling approach considers the smooth surface geometry of the bone. To that end, a boundary-representation (B-rep) surface model is reconstructed from the segmented CT images. This be achieved for example using the marching cubes algorithm. An unstructured mesh of the B-rep model can then be generated using standard meshing algorithms. Hexahedral and tetrahedral elements are commonly used for *h*-FEM simulations of bone mechanics [253]. For biomechanical analysis of the femur, it has been shown that quadratic tetrahedral elements (with 10 nodes) achieve higher accuracy and computational efficiency in comparison to linear four-noded tetrahedra [193].
For density-based models, the material properties are defined voxel-wise. In finite element analysis, the material properties are evaluated during numerical integration at specified points within the element. Unlike voxel-FEM which uses a one-to-one mapping between voxels and finite elements, *h*-FEM models with unstructured meshes require a specialized strategy for material mapping. Whereas earlier modeling approaches employed an average

element density [280], it was demonstrated that a voxel-wise interpolation of the "Young's modulus continuum field" provides significantly more accurate predictions [239].
For biomechanical simulations of the vertebra, the use of unstructured $h$-FEM meshes allows for a more detailed modeling approach. Structural shell elements can be more readily used to model the cortical shell, which are coupled to the tetrahedral finite elements used to model the trabecular core [37]. They also allow for more flexibility in the definition of the boundary conditions [155], and modeling contact at the vertebral endplates. Figure 2.6 shows a detailed $h$-FEM model of a vertebral segment [42] which illustrates these points. Continuum-level $h$-FEM models were also used in conjunction with anisotropic

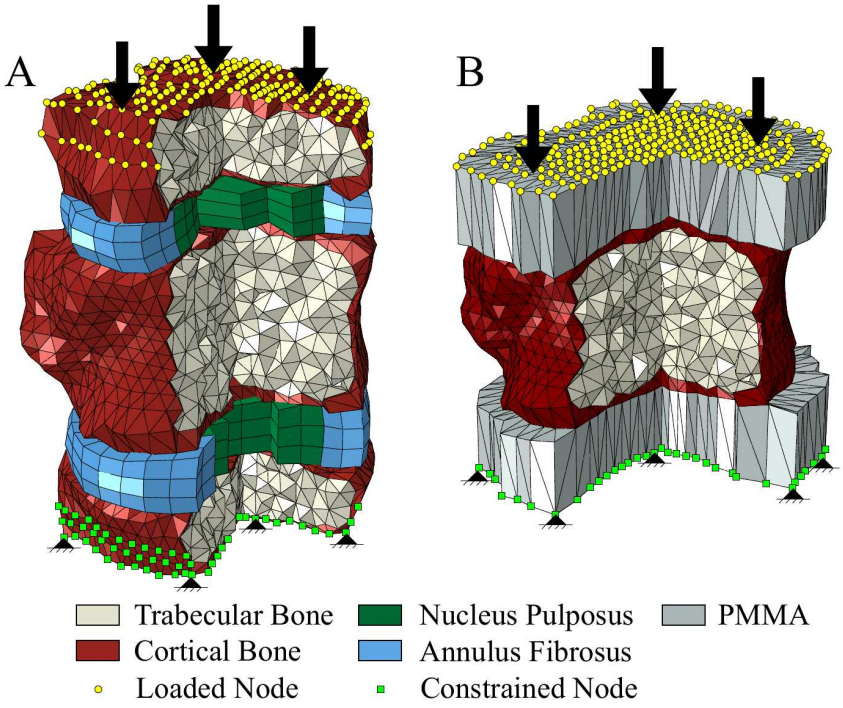


Figure 2.6: $h$-FEM vertebral models A) Mesh for a whole spine segment, including intervertebral discs. B) Mesh with PMMA embedding of center vertebra endplates. Reproduced from [42].

material models to study the damage mechanisms and fracture risk in vertebral bodies [37, 39, 20]. Nonlinear models accounting for large strain compression and damage were also developed and used in $h$-FEM models to accurately predict experimental failure patterns in vertebral bodies [110, 109, 42]

### $p$-FEM

An alternative simulation approach for the biomechanical analysis of bone is given by the $p$-version of the finite element method ($p$-FEM). In this approach, high-order polynomials are used as basis functions to approximate the solution. This results in a more favorable convergence behavior, which allows for more accurate and efficient simulations in comparison to the standard $h$-FEM. However, the $p$-FEM requires special attention for the

geometric modeling and mesh generation [237]. To ensure accurate numerical predictions, the smooth geometry needs to be accurately described by high-order elements which can represent the curvature. For image-based bone simulations, this requires additional processing of the segmented CT scans to identify the boundaries of the bone, and apply boundary smoothing to create solid models of the bone, which are finally subdivided into finite elements with curved boundaries. This geometry reconstruction and meshing pipeline is illustrated in Figure 2.7.

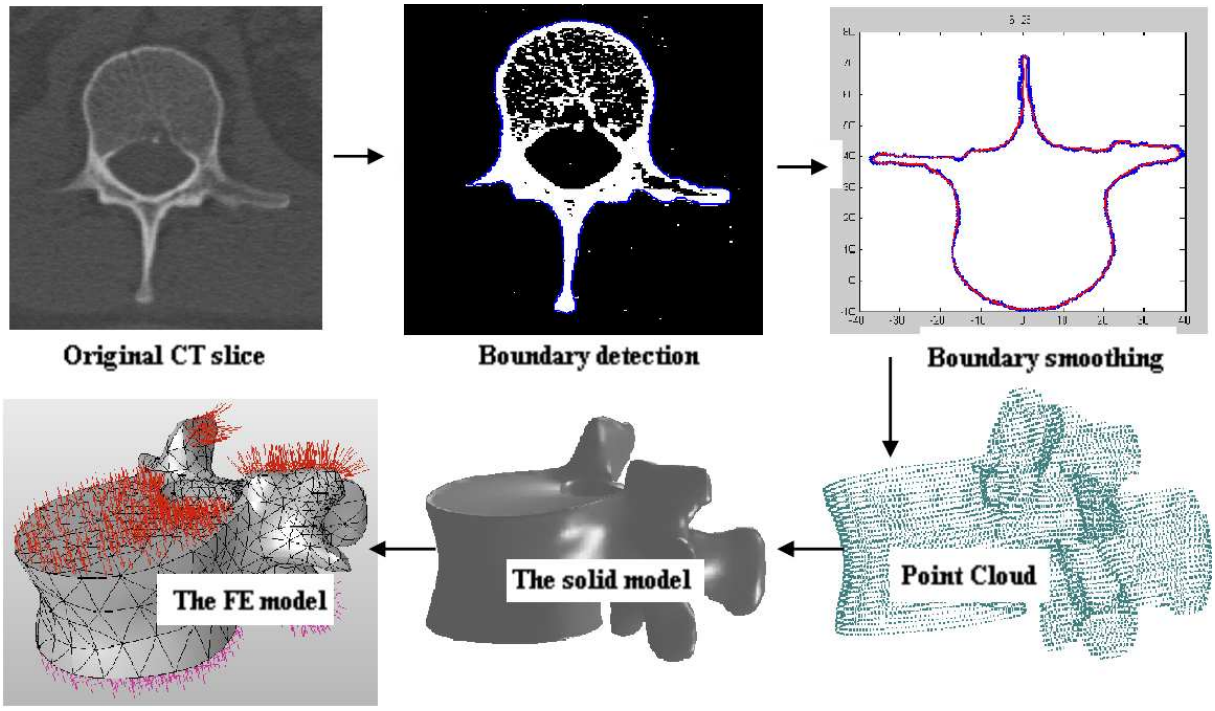


Figure 2.7: Continuum-level $p$-FEM vertebra modeling pipeline, reproduced from [192].

In the field of bone mechanics, the $p$-FEM was first applied for the biomechanical analysis of the human tibia, showing realistic predictions of stresses and displacements under static loading [175]. Several validation studies were presented for subject-specific $p$-FEM analysis of the femur, showing very good agreement between the $p$-FEM predictions and the experiments [273, 244]. Both isotropic material models based on $E$–$\rho$ relationships, and anisotropic models based on micromechanical approaches were shown to be applicable [272]. Similarly, $p$-FEM models of the humerus were validated through comparison to experiments. In direct comparison to standard $h$-FEM models generated using Abaqus, $p$-FEM models were shown to be more numerically efficient [49]. Further applications for the simulation of hip prosthesis were also presented in [271, 129]. For $p$-FEM simulations of the vertebra, preliminary work presented in [192] reported realistic results that are close to experimentally and numerically reported values in the literature.

### 2.3.2 Microstructural FE analysis

Microstructural finite element models are based on high-resolution images that resolve the details of the trabecular microstructure. Such images can be obtained using micro-CT

scanners, which resolve the trabecular microstructure of bone samples at a resolution in the order of 10–50 $\mu$m. High-resolution peripheral QCT (HR-pQCT) scanners have also seen technological advancements in recent years, which enable scanning of the extremities of the musculoskeletal system with a resolution of 55 $\mu$m [159]. Currently, such resolutions are not possible in vivo for the human vertebra, which hinders the possibility of clinical assessment of bone strength using microstructural FE models. However, such models have been essential in gaining a better understanding of bone micromechanics and the different contributions of the vertebra's structural components, as well as bone–implant and bone–cement interactions.

### $h$-FEM

On a microstructural level, carrying out FE analysis based on boundary-fitted meshes can be very challenging. The foam-like trabecular microstructure has a complex three-dimensional geometry, which makes the generation of analysis-suitable finite element meshes very difficult [162]. To that end, the high-resolution CT images first need to be segmented to identify the trabecular structure. Then, it is often necessary to exclude regions of bone that are disconnected from the main structure, as they would lead to singular stiffness matrices. Based on the segmentation mask, a surface model of the bone can be reconstructed e.g. using the marching cubes algorithm. Finally, the surface representation can be then used to generate the FE mesh with linear or quadratic tetrahedral elements with element sizes in the range of 20–80 $\mu$m.
Due to this level of complexity, boundary-fitted microstructural FE models are often limited to analysis of small specimens of trabecular bone. However, they can be used to simulate very complex stress states with high local accuracy. Applications include the modeling of trabecular bone damage and fracture [95], and the micromechanical damage modeling in bone–cement interfaces [115, 282].

### $\mu$-FEM

An alternative approach that does not require the generation of boundary-fitted meshes is the micro-voxel finite element method ($\mu$-FEM), which is considered the current gold standard for simulation of the micromechanics of bone [106, 247, 246]. Similar to continuum-level voxel-FEM described in the previous section, it relies on the conversion of each voxel to a hexahedral finite element, but with voxel size in the range of 20-80 $\mu$m. However, on the microstructural-level trabecular bone is considered homogeneous and isotropic, and hence each element is assigned the same tissue Young's modulus. This assumption is sufficient for predicting the apparent elastic properties of trabecular bone specimens, as reported in several studies [247, 148, 251, 266]. It has also been shown that $\mu$-FEM models and continuum-level $h$-FEM models that were enhanced by an anisotropic density-fabric-based material model and subject-specific cortical shell modeling provided equivalent structural predictions [187, 186].
Due to the high resolution necessary to accurately represent the complex geometry of the trabecular microstructure using a voxel grid, $\mu$-FEM models result in systems with a very large number of unknowns, making them computationally expensive. Hence, they were limited to studying small samples of bone. High-resolution models of whole vertebral

bodies have hundreds of millions of degrees of freedom, which required supercomputing resources [3, 2, 9]. Figure 2.8 shows the $\mu$-FEM model of a vertebral body modeled at 30 $\mu$m resolution, which was presented in [2]. The complexity of the trabecular microstructure and the large size of the model are obvious.

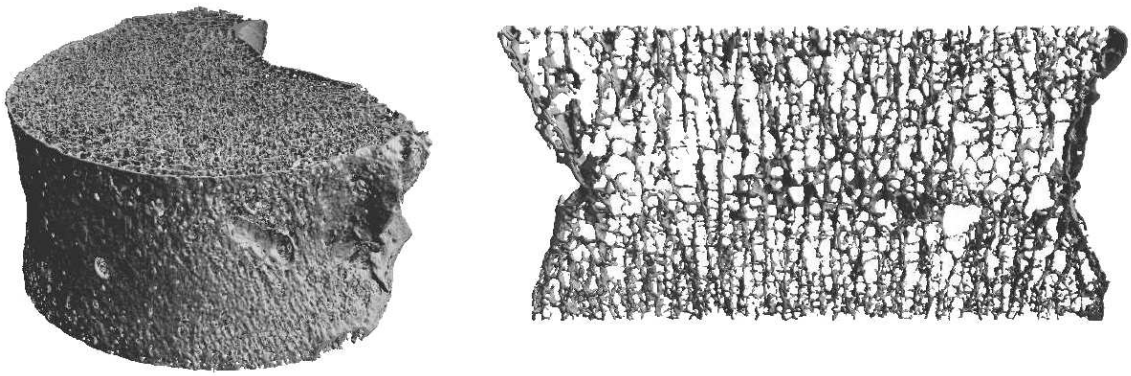

Figure 2.8: $\mu$-FEM model of vertebral body modeled at 30 $\mu$m resolution, reproduced from [2].

With high-performance computing resources becoming more available, and with advances in algorithms for the solution of very large linear systems, $\mu$-FEM analysis of larger bone specimens is becoming more feasible [45]. It has been an important tool in understanding the mechanics of the vertebra, e.g. how the cortical shell contributes to vertebral body stiffness [17]. Convergence studies of the linear elastic models of the $\mu$-FEM verified the numerical predictions of the displacements and the strains [33]. Models of vertebral bodies have also been validated through comparison to mechanical experiments [45], which we discuss in detail in Chapter 4.
The $\mu$-FEM has also been extensively used to study bone–implant mechanics and pedicle-screw fixation [262, 242, 35], where the high spatial resolution is necessary for accurate modeling. Nonlinear $\mu$-FEM models have also been applied to accurately predict failure of trabecular bone [178, 250] and model its behavior post-yield [251]. Fields [79] presented an application of nonlinear $\mu$-FEM analysis of the vertebra to study failure mechanisms, and the different contributions of the trabecular bone, the cortical shells and the endplates.

# Chapter 3

# The finite cell method for biomechanical analysis of bone

In this chapter, we present a review of the finite cell method (FCM) for the simulation of bone mechanics. Starting with the necessary theoretical background, we present a brief summary of the theory of linear elasticity which is used to model the mechanical behavior of bones. Following that, we present the fundamentals of the finite element method (FEM), and discuss the standard $h$- and high-order $p$-versions. We explain the concept of the FCM as an immersed boundary method that is based on the $p$-version of the FEM and discuss its special aspects. Finally, we review previous work in literature where the FCM was applied for the simulation of bone mechanics.

## 3.1 Introduction

For problems that involve complex geometries in engineering practice, subdividing the domain into boundary-conforming finite elements remains a challenging task that can constitute a severe bottleneck in the simulation process [46]. This is especially relevant for problems in biomechanics, where only an implicit description of the geometry originating from tomography scans is available.
In the $p$-version of the finite element method, the use of high-order basis functions leads to a more desirable convergence behavior, allowing for more efficient simulations in comparison to the classical $h$-FEM. However, mesh generation of complex geometry presents even more challenges for the $p$-version of the FEM. In comparison to low order FEM meshes, meshes used for $p$-FEM analysis are typically composed of fewer but larger elements. To ensure an accurate numerical solution, the geometric mapping in the $p$-version needs to represent the curved element boundaries with sufficient accuracy. For cases involving complex geometry, creating a suitable mesh for the $p$-version with accurately curved elements can be prohibitively difficult. A mesh generator for thin structures which can accurately represent the curved boundaries was presented in [233]. However, general curved meshing of bulky volumetric structures is more challenging [234]. For $p$-FEM applications in bone mechanics, an additional step of reconstructing a smooth surface representation from the tomography images is necessary. A mesh based on the curved boundary-representation

model can be subsequently generated [272], describing the geometry by curved hexahedral and tetrahedral elements.

Immersed boundary methods, also known as fictitious or embedded domain methods, have emerged as an alternative to the classical boundary-conforming FEM to avoid complex mesh generation. Notable examples of this class of methods include Cut-FEM [98], extended and generalized FEM [82] and weighted extended B-spline approximation [105]. These methods circumvent the challenging task of mesh generation by extending the domain of interest beyond the boundaries of the object's physical domain to a bounding box with a simple shape which can be trivially meshed. The finite cell method (FCM), which was introduced in [190], combines the fictitious domain idea with the $p$-version of the FEM. The use of high-order basis functions, which smoothly extend into the fictitious domain, allows the FCM to achieve exponential rates of convergence for smooth problems. The FCM has been investigated and successfully applied in various problems, including three-dimensional solid mechanics [70], linear thermoelasticity [278], geometrically nonlinear problems [219], contact mechanics [23, 24], implicit and explicit elastodynamics [67, 76, 121, 86] and topology optimization [69, 90].

A remarkable feature of the FCM is its ability to handle different types of geometric representations. In the FCM, the geometric representation is only needed during the numerical integration of the weak form. Therefore, the implicit geometric representation only needs to be able to determine whether a given point lies inside or outside the exact geometry: the so-called point membership test (or inside-outside test) [190]. The FCM can hence be used with virtually any type of geometric representation: constructive solid geometry (CSG) [256, 200], boundary representation (B-Rep) provided by CAD models [76], voxel representations [70], and point clouds [142]. Furthermore, a methodology for handling flawed models using the FCM has been presented in [257], allowing direct computations on CAD models containing geometric and topological flaws. This flexibility and robustness of the FCM in dealing with geometric models makes it an ideal choice for an automated simulation pipeline based on medical images. Moreover, using the FCM allows for an easy combination of different geometric types of descriptions, such as using voxel models for biological tissues and CAD models for implants, as demonstrated in this work in Section 6.2.

## 3.2 Theory of linear elasticity

The field of continuum mechanics deals with the mechanical behavior of solid bodies. Here, the solid bodies are regarded as continuous masses rather than sets of discrete particles. Under certain assumptions regarding the kinematics and constitutive relationship, a linear elastic behavior is deduced. This section provides a brief summary of the fundamental concepts of continuum mechanics and the theory of linear elasticity, which are required to describe the subsequent finite element formulations. Comprehensive details on the subject can be found in [157, 26, 227]. The notation used in this thesis closely follows the work of Bonet and Wood [26].

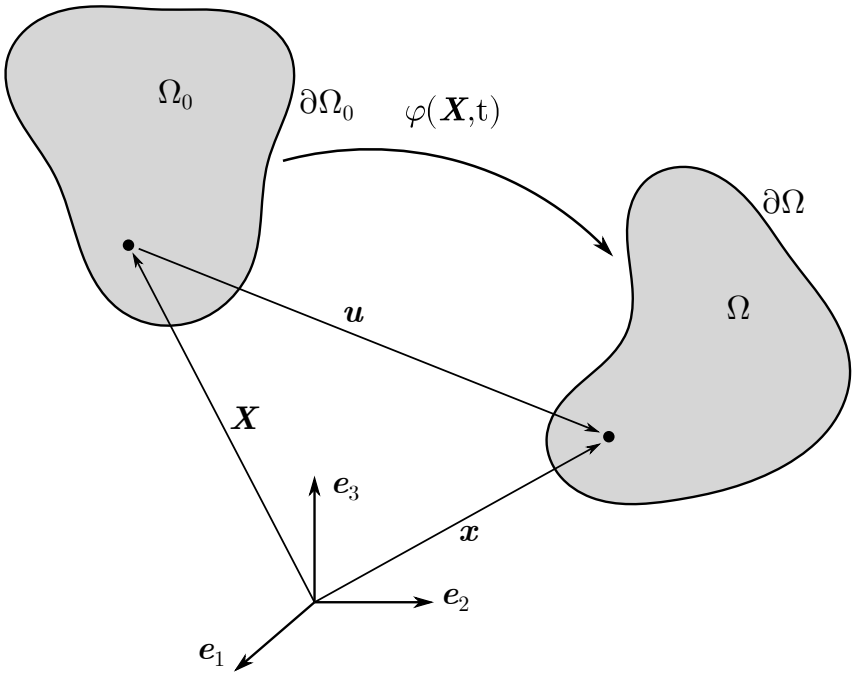


Figure 3.1: Reference and current configurations

### 3.2.1 Kinematics

Kinematics describe the motion and deformation of the solid body in space without considering the forces that cause this transformation. In the initial configuration, a material point can be defined by its position $\boldsymbol{X}$ within the domain $\Omega_0 \subset \mathbb{R}^3$. The boundary of the domain in the reference configuration is denoted by $\partial\Omega_0$. The position of the material point in the current configuration at time $t$ is given by $\boldsymbol{x} \in \Omega$. A continuous and one-to-one mapping function $\varphi$ describes the transformation from the reference to the current configuration

$$\boldsymbol{x} = \varphi(\boldsymbol{X}, t), \tag{3.1}$$

as illustrated in Figure 3.1.
Two traditional viewpoints are considered to describe the motion. The first one is the Lagrangian (material) description, where the motion of the material material is described with respect to its position in the reference configuration $\boldsymbol{X}$; that is, the observer is fixed to the material point. The second viewpoint is the Eulerian (spatial) description, which is usually used in fluid mechanics, considers the current configuration as the observer's position is fixed in space. In this work, we follow the Lagrangian description.
The position vectors $\boldsymbol{X}$ and $\boldsymbol{x}$ are defined using a Cartesian basis

$$\boldsymbol{X} = X_i \boldsymbol{e}_i \tag{3.2a}$$
$$\boldsymbol{x} = x_i \boldsymbol{e}_i. \tag{3.2b}$$

The displacement field $\boldsymbol{u}$ is introduced as the difference between the two vectors

$$\boldsymbol{u} = \boldsymbol{u}(t) = \boldsymbol{x} - \boldsymbol{X} = [u, v, w]^\top. \tag{3.3}$$

The deformation can be characterized using the deformation gradient tensor $\boldsymbol{F}$. The linear mapping between infinitesimal line elements in the initial configuration $\mathrm{d}\boldsymbol{X}$ and in the current configuration $\mathrm{d}\boldsymbol{x}$ is carried out by

$$\mathrm{d}\boldsymbol{x} = \boldsymbol{F} \cdot \mathrm{d}\boldsymbol{X}. \tag{3.4}$$

The deformation gradient tensor is given by

$$\boldsymbol{F} = \frac{\partial \boldsymbol{x}}{\partial \boldsymbol{X}} = \frac{\partial \left(\boldsymbol{X} + \boldsymbol{u}\right)}{\partial \boldsymbol{X}} = \boldsymbol{I} + \frac{\partial \boldsymbol{u}}{\partial \boldsymbol{X}} = \boldsymbol{I} + \nabla_{\boldsymbol{X}} \boldsymbol{u}, \tag{3.5}$$

where $\nabla_{\boldsymbol{X}}$ denotes the gradient with respect to the initial configuration, and $\boldsymbol{I}$ is the second-order identity tensor.
The unsymmetric deformation tensor $\boldsymbol{F}$ describes the total transformation including any rigid body rotations. Hence, strain measures are introduced to characterize the local deformation excluding rigid body motions. The Green-Lagrange strain tensor $\boldsymbol{E}$ characterizes this deformation in terms of the change of length of a line element, and is given by

$$\boldsymbol{E} = \frac{1}{2}\left(\boldsymbol{F}^{\top}\boldsymbol{F} - \boldsymbol{I}\right) = \frac{1}{2}\left(\nabla_{\boldsymbol{X}} \boldsymbol{u} + \nabla_{\boldsymbol{X}} \boldsymbol{u}^{\top} + \nabla_{\boldsymbol{X}} \boldsymbol{u}^{\top} \nabla_{\boldsymbol{X}} \boldsymbol{u}\right). \tag{3.6}$$

Unlike $\boldsymbol{F}$, the Green-Lagrange strain tensor $\boldsymbol{E}$ is symmetric and vanishes for pure rigid body transformations. For small deformations, i.e. $\|\nabla_{\boldsymbol{X}} \boldsymbol{u}\| \ll 1$, the high-order terms in (3.6) can be neglected. Linearization of $\boldsymbol{E}$ leads to the symmetric infinitesimal strain tensor $\boldsymbol{\varepsilon}$

$$\boldsymbol{\varepsilon} = \frac{1}{2}\left(\nabla_{\boldsymbol{X}} \boldsymbol{u} + \nabla_{\boldsymbol{X}} \boldsymbol{u}^{\top}\right) \approx \boldsymbol{E}. \tag{3.7}$$

In this work, we follow the assumption of small deformations to study the mechanical behavior of bones and metal implants. This is considered sufficient for studying the apparent properties of bone under small loads, but would not be a valid for studying bone damage and failure, where large deformations need to be taken into account, as shown e.g. in [110, 42].

### 3.2.2 Stress

Stress is a physical quantity which describes the internal interactions between neighboring material particles within a continuum due to deformation. Considering the force $\mathrm{d}\boldsymbol{f}$ acting on a surface element $\mathrm{d}a$ of the deformable body in its current configuration. The surface traction $\boldsymbol{t}$ is defined as the force per unit area

$$\boldsymbol{t} = \frac{\mathrm{d}\boldsymbol{f}}{\mathrm{d}a}. \tag{3.8}$$

Cauchy's stress theorem relates the traction vector to the outward pointing unit normal vector on $\mathrm{d}a$, denoted by $\boldsymbol{n}$, through the Cauchy stress tensor $\boldsymbol{\sigma}$

$$\boldsymbol{t} = \boldsymbol{\sigma} \cdot \boldsymbol{n}. \tag{3.9}$$

The tensor consists of nine components that define the stress state at a point due to the deformation:

$$\boldsymbol{\sigma} = \begin{bmatrix} \sigma_{xx} & \tau_{xy} & \tau_{xz} \\ \tau_{yx} & \sigma_{yy} & \tau_{yz} \\ \tau_{zx} & \tau_{zy} & \sigma_{zz} \end{bmatrix} \tag{3.10}$$

Figure 3.2 depicts the sign convention for the Cauchy stress tensor. The tensor is symmetric, $\boldsymbol{\sigma} = \boldsymbol{\sigma}^\top$, which can be shown to be the result of the conservation of angular momentum [26].

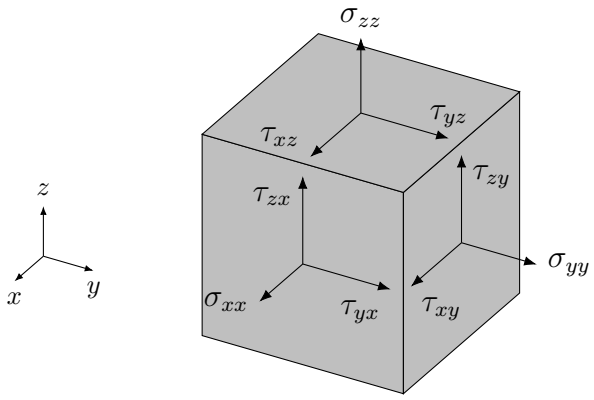


Figure 3.2: Sign convention of stress tensor components

### 3.2.3 Equilibrium equation

The linear momentum of the deformable body $\Omega$ is defined as

$$\boldsymbol{\mathcal{L}} = \int_\Omega \rho \dot{\boldsymbol{x}} \, \mathrm{d}\Omega. \tag{3.11}$$

The conservation of linear momentum, as stated by Newton's second law of motion, postulates that the rate of change of $\boldsymbol{\mathcal{L}}$ in time is equal to the sum of all forces applied to the body

$$\frac{\partial}{\partial t} \int_\Omega \rho \dot{\boldsymbol{x}} \, \mathrm{d}\Omega = \int_\Omega \boldsymbol{b} \, \mathrm{d}\Omega + \int_{\partial\Omega} \boldsymbol{t} \, \mathrm{d}\Gamma, \tag{3.12}$$

where $\boldsymbol{b}$ and $\boldsymbol{t}$ are the body force and the surface traction acting on the body. Using Cauchy's stress theorem (3.9), and applying the divergence theorem and the law of conservation of mass gives Cauchy's first equation of motion

$$\nabla \cdot \boldsymbol{\sigma} + \boldsymbol{b} = \rho \ddot{\boldsymbol{u}} \qquad \forall \boldsymbol{x} \in \Omega. \tag{3.13}$$

For quasistatic problems, the inertia forces are much smaller than the internal forces and can therefore be neglected

$$\nabla \cdot \boldsymbol{\sigma} + \boldsymbol{b} = 0 \qquad \forall \boldsymbol{x} \in \Omega. \tag{3.14}$$

### 3.2.4 Constitutive relationship

In continuum mechanics, constitutive models connect the kinematic variables (strains) to the stresses, which makes it possible to compute all the unknowns of the boundary-value problem [107]. These models describe the material's behavior in response to deformation. A material is called *elastic* if its stress state depends only on the current deformation state; i.e. it is independent of the deformation history. Elastic deformation is completely reversible, meaning that the material returns to its undeformed state after unloading—in contrast to plastic deformation which is permanent. In case of small elastic deformations, a linear constitutive relationship is given by the generalized Hooke's law:

$$\boldsymbol{\sigma} = \mathbb{C} : \boldsymbol{\varepsilon}. \tag{3.15}$$

Here, the linear elastic material tensor $\mathbb{C}$ is a fourth order tensor relating the Cauchy stresses to the infinitesimal strain tensor. If the material behavior is also assumed to be isotropic, i.e. independent of the material's orientation with respect to the load, $\mathbb{C}$ is given as

$$\mathbb{C} = \lambda\, \boldsymbol{I} \otimes \boldsymbol{I} + 2\mu\, \mathbb{I}^{sym}, \tag{3.16}$$

where $\mathbb{I}^{sym}$ denotes the fourth order symmetric identity tensor. The Lamé constants $\lambda$ and $\mu$ can be defined in terms of the Young's modulus $E$ and the Poisson ratio $\nu$

$$\mu = \frac{E}{2(1+\nu)} \quad \text{and} \quad \lambda = \frac{E\nu}{(1+\nu)(1-2\nu)}. \tag{3.17}$$

In this work, we apply isotropic linear elastic material models for bone tissue and metal implants. As discussed in Section 2.3, these assumptions are justified for simple load cases.

### 3.2.5 Boundary-value problem

A boundary-value problem for (3.14) involves imposing boundary conditions on the displacement function $\mathbf{u}$ on the boundary $\partial\Omega$. Here, we consider two types of boundary conditions: Dirichlet (or essential) boundary conditions which specify the values of the primary variable $\mathbf{u}$, and Neumann (or natural) boundary conditions which specify the values of the derivative. To incorporate both types of conditions, we assume that the boundary admits the decomposition into two distinct parts $\partial\Omega = \Gamma_D \cup \Gamma_N$, with $\Gamma_D \cap \Gamma_N = \emptyset$, as illustrated in Figure 3.3.
The boundary-value problem is stated in its strong form as:
Given $\boldsymbol{b} : \Omega \to \mathbb{R}^3$, $\hat{\boldsymbol{t}} : \Gamma_N \to \mathbb{R}^3$, $\hat{\boldsymbol{u}} : \Gamma_D \to \mathbb{R}^3$, find $\boldsymbol{u} : \Omega \to \mathbb{R}^3$ such that:

$$\nabla \cdot \boldsymbol{\sigma} + \boldsymbol{b} = \boldsymbol{0} \qquad \forall \boldsymbol{x} \in \Omega, \tag{3.18a}$$

$$\boldsymbol{u} = \hat{\boldsymbol{u}} \qquad \forall \boldsymbol{x} \in \Gamma_D, \tag{3.18b}$$

$$\boldsymbol{\sigma} \cdot \boldsymbol{n} = \hat{\boldsymbol{t}} \qquad \forall \boldsymbol{x} \in \Gamma_N, \tag{3.18c}$$

where $\hat{\boldsymbol{u}}$ is the prescribed value for the displacement on the Dirichlet boundary and $\hat{\boldsymbol{t}}$ is the prescribed value for the traction on the Neumann boundary.

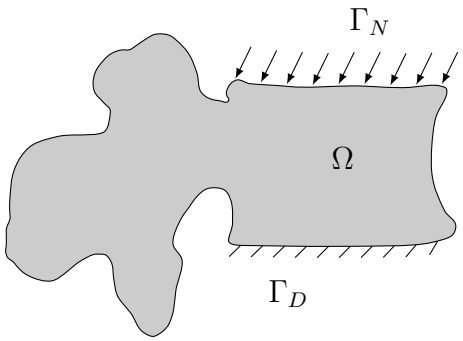


Figure 3.3: Boundary-value problem on $\Omega$

## 3.3 The finite element method

Finding closed-form solutions to the strong form of the boundary-value problem (3.18) defined by the partial differential equations and boundary conditions is only possible in a few cases—when the geometry and boundary conditions are very simple. For problems of practical relevance, numerical approaches are commonly used to estimate the solution. Such approaches include the finite difference method [241], boundary element methods [28, 128] and the finite element method (FEM), which is most commonly applied for engineering problems in solid mechanics [16, 111].
In the FEM, a weak form of the boundary-value problem is considered, and the solution is approximated using piecewise-continuous (multivariate) polynomials. The domain of interest is partitioned into a set of elements, which are used to define the basis functions. In comparison to other numerical schemes, the FEM holds an advantage in its ability to deal with complex geometry and boundary conditions. An important aspect is the possibility for local mesh refinement to accurately describe solution features. Moreover, the FEM formulation leads to a computationally efficient analysis due to the sparsity of the resulting systems of equations. In this section, we briefly present the fundamentals of the FEM and its $p$-version. More detailed discussion can be found e.g. in the textbooks by Hughes [111], Bathe [16], Zienkiewicz et al. [285] and Szabó and Babuška [237].

### 3.3.1 Weak form

To define the weak form of the problem, we first need to characterize two classes of functions. The first is composed of *trial* functions $\boldsymbol{u}$, which are required, by definition, to satisfy the Dirichlet boundary conditions (3.18b) on $\Gamma_D$. Furthermore, the derivatives of the trial functions are required to be square-integrable over $\Omega$. We denote the trial function space by $\mathcal{S}$

$$\mathcal{S} = \{\boldsymbol{u} \in \left[H^1(\Omega)\right]^3 \mid \boldsymbol{u} = \hat{\boldsymbol{u}} \quad \forall \boldsymbol{x} \in \Gamma_D\}, \tag{3.19}$$

where $H^1(\Omega)$ is the Sobolev space of first order [201].

Similarly, we define the second class of functions $\boldsymbol{v}$, which are called the *test* or *weighting* functions, to be the homogeneous counterpart of $\mathcal{S}$

$$\mathcal{V} = \{\boldsymbol{v} \in \left[H^1(\Omega)\right]^3 \mid \boldsymbol{v} = \boldsymbol{0} \quad \forall \boldsymbol{x} \in \Gamma_D\}. \tag{3.20}$$

The weak form is obtained by multiplying the equilibrium equation (3.14) by a test function $\boldsymbol{v} \in \mathcal{V}(\Omega)$ and integrating over $\Omega$

$$\int_\Omega (\nabla \cdot \boldsymbol{\sigma}) \cdot \boldsymbol{v} \, \mathrm{d}\Omega + \int_\Omega \boldsymbol{b} \cdot \boldsymbol{v} \, \mathrm{d}\Omega = 0. \tag{3.21}$$

Using the product rule of differentiation:

$$\nabla \cdot (\boldsymbol{\sigma} \cdot \boldsymbol{v}) = (\nabla \cdot \boldsymbol{\sigma}) \cdot \boldsymbol{v} + \boldsymbol{\sigma} : \nabla \boldsymbol{v}, \tag{3.22}$$

we can rewrite the equation (3.21) as

$$\int_\Omega \boldsymbol{\sigma} : \nabla \boldsymbol{v} \, \mathrm{d}\Omega = \int_\Omega \boldsymbol{b} \cdot \boldsymbol{v} \, \mathrm{d}\Omega + \int_\Omega \nabla \cdot (\boldsymbol{\sigma} \cdot \boldsymbol{v}) \, \mathrm{d}\Omega. \tag{3.23}$$

Making use of the symmetry property of the Cauchy stress tensor, we can define the integral on the left-hand side in terms of the infinitesimal strain tensor instead of the gradient

$$\boldsymbol{\sigma} : \nabla \boldsymbol{v} = \boldsymbol{\sigma} : \boldsymbol{\varepsilon}(\boldsymbol{v}). \tag{3.24}$$

Applying the divergence theorem gives

$$\int_\Omega \nabla \cdot (\boldsymbol{\sigma} \cdot \boldsymbol{v}) \, \mathrm{d}\Omega = \int_{\partial\Omega} \boldsymbol{\sigma} \cdot \boldsymbol{n} \cdot \boldsymbol{v} \, \mathrm{d}\Gamma = \underbrace{\int_{\Gamma_D} \boldsymbol{\sigma} \cdot \boldsymbol{n} \cdot \boldsymbol{v} \, \mathrm{d}\Gamma}_{=0} + \int_{\Gamma_N} \boldsymbol{\sigma} \cdot \boldsymbol{n} \cdot \boldsymbol{v} \, \mathrm{d}\Gamma. \tag{3.25}$$

Note that the integral over $\Gamma_D$ vanishes due to the definition of the test functions (3.20). Finally, the weak formulation of the boundary value problem reads:
Given $\boldsymbol{b} : \Omega \to \mathbb{R}^3$, $\hat{\boldsymbol{t}} : \Gamma_N \to \mathbb{R}^3$, $\hat{\boldsymbol{u}} : \Gamma_D \to \mathbb{R}^3$, find $\boldsymbol{u} \in \mathcal{S}(\Omega)$ such that:

$$\mathcal{B}(\boldsymbol{u}, \boldsymbol{v}) = \mathcal{F}(\boldsymbol{v}) \qquad \forall \boldsymbol{v} \in \mathcal{V}(\Omega) \tag{3.26a}$$

with

$$\mathcal{B}(\boldsymbol{u}, \boldsymbol{v}) = \int_\Omega \boldsymbol{\varepsilon}(\boldsymbol{u}) : \mathbb{C} : \boldsymbol{\varepsilon}(\boldsymbol{v}) \, \mathrm{d}\Omega \tag{3.26b}$$

and

$$\mathcal{F}(\boldsymbol{v}) = \int_\Omega \boldsymbol{b} \cdot \boldsymbol{v} \, \mathrm{d}\Omega + \int_{\Gamma_N} \hat{\boldsymbol{t}} \cdot \boldsymbol{v} \, \mathrm{d}\Gamma \tag{3.26c}$$

The Lax–Milgram Lemma [29] states that if $\mathcal{B}$ is a continuous and coercive bilinear form, and $\mathcal{F}$ is a continuous linear form, then the variational problem has a unique solution. These conditions are fulfilled if the elasticity tensor $\mathbb{C}$ is bounded away from zero and infinity. It can be shown that these properties also carry over to the discrete form of the variational problem [41].

### 3.3.2 Galerkin's approximation method

The Galerkin method is used to obtain approximate solutions to boundary-value problems based upon weak formulations. The first step in the solution approach is to construct finite-dimensional approximations of the function spaces $\mathcal{S}$ and $\mathcal{V}$, denoted by $\mathcal{S}^h$ and $\mathcal{V}^h$, which are defined such that

$$\mathcal{S}^h \subset \mathcal{S} \tag{3.27}$$

$$\text{and} \quad \mathcal{V}^h \subset \mathcal{V}. \tag{3.28}$$

Next, we address the mismatch between $\mathcal{S}^h$ and $\mathcal{V}^h$ in the case of inhomogeneous Dirichlet boundary conditions, i.e. if $\hat{\boldsymbol{u}} \neq \boldsymbol{0}$. Following the derivation presented in [111], for each function $\boldsymbol{u}_0^h \in \mathcal{V}$, we construct a function $\boldsymbol{u}^h \in \mathcal{S}$ by

$$\boldsymbol{u}^h = \boldsymbol{u}_0^h + \hat{\boldsymbol{u}}^h, \tag{3.29}$$

where $\hat{\boldsymbol{u}}^h$ is a given function satisfying the prescribed Dirichlet boundary condition. Hence, the (Bubnov)–Galerkin form of the boundary-value problem reads:
Given $\boldsymbol{b}$, $\hat{\boldsymbol{t}}$, $\hat{\boldsymbol{u}}$ as before, find $\boldsymbol{u}^h = \boldsymbol{u}_0^h + \hat{\boldsymbol{u}}^h$, where $\boldsymbol{u}_0^h \in \mathcal{V}^h$ such that:

$$\begin{aligned} \mathcal{B}(\boldsymbol{u}_0^h, \boldsymbol{v}^h) &= \mathcal{F}(\boldsymbol{v}^h) - \mathcal{B}(\hat{\boldsymbol{u}}^h, \boldsymbol{v}^h) \\ &= \hat{\mathcal{F}}(\boldsymbol{v}^h) \qquad\qquad \forall \boldsymbol{v}^h \in \mathcal{V}^h \end{aligned} \tag{3.30}$$

In the Bubnov–Galerkin approach, the same space is used to construct both the trial and test functions. The finite-dimensional subspace $\mathcal{V}^h$ can be spanned by a finite number of basis functions. Since the trial and test functions are vector-valued functions, we introduce the basis function matrix

$$\boldsymbol{N} = \begin{bmatrix} \boldsymbol{N}_u & \boldsymbol{0} & \boldsymbol{0} \\ \boldsymbol{0} & \boldsymbol{N}_v & \boldsymbol{0} \\ \boldsymbol{0} & \boldsymbol{0} & \boldsymbol{N}_w \end{bmatrix} = \begin{bmatrix} N_1 & \dots & N_n & 0 & \dots & 0 & 0 & \dots & 0 \\ 0 & \dots & 0 & N_1 & \dots & N_n & 0 & \dots & 0 \\ 0 & \dots & 0 & 0 & \dots & 0 & N_1 & \dots & N_n \end{bmatrix}. \tag{3.31}$$

For simplicity, we use the same basis functions $\{N_1, N_2, ..., N_n\}$ for all vector components $u$, $v$ and $w$ of the trial and test functions. In general, a different basis could be used for each vector component. The trial and test functions are constructed as a linear combination of the basis functions $\boldsymbol{N}_i$ and the coefficient vectors

$$\boldsymbol{u}_0^h = \sum_{i=1}^{N} \boldsymbol{N}_i d_i, \tag{3.32a}$$

$$\boldsymbol{v}^h = \sum_{i=1}^{N} \boldsymbol{N}_i c_i, \tag{3.32b}$$

where $N = 3n$ is the total number of unconstrained degrees of freedom.
Substituting the approximations (3.32) into the Galerkin form of the boundary-value problem (3.30)

$$\mathcal{B}\left(\sum_{i=1}^{N} \boldsymbol{N}_i c_i, \sum_{j=1}^{N} \boldsymbol{N}_j d_j\right) = \hat{\mathcal{F}}\left(\sum_{i=1}^{N} \boldsymbol{N}_i c_i\right) \tag{3.33}$$

Using the (bi)-linearity properties of $\mathcal{B}$ and $\mathcal{F}$, (3.33) becomes

$$\sum_{i=1}^{N} c_i \mathcal{G}_i = 0 \tag{3.34}$$

where

$$\mathcal{G}_i = \sum_{j=1}^{N} \mathcal{B}\left(\boldsymbol{N}_i, \boldsymbol{N}_j\right) d_j - \hat{\mathcal{F}}\left(\boldsymbol{N}_i\right). \tag{3.35}$$

As the Galerkin equation (3.30) holds for all $\boldsymbol{v}^h$, the coefficients $c_i \neq 0$. As a result, it follows that each $\mathcal{G}_i = 0$ for $i = 1, \ldots, N$

$$\sum_{j=1}^{N} \mathcal{B}\left(\boldsymbol{N}_i, \boldsymbol{N}_j\right) d_j = \hat{\mathcal{F}}\left(\boldsymbol{N}_i\right). \tag{3.36}$$

In this form, all terms are known except for $d_j$. This constitutes a system of $N$ equations with $N$ unknowns, which expresses the matrix form of the boundary-value problem

$$\boldsymbol{K}\boldsymbol{d} = \boldsymbol{f} \tag{3.37}$$

with

$$K_{ij} = \mathcal{B}(\boldsymbol{N}_i, \boldsymbol{N}_j), \tag{3.38}$$

$$f_i = \hat{\mathcal{F}}(\boldsymbol{N}_i) \tag{3.39}$$

where $\boldsymbol{K}$ is the stiffness matrix, $\boldsymbol{f}$ the load vector, and $\boldsymbol{d}$ the displacement vector. Solving this system of equations provides the approximate solution to the boundary-value problem.

### 3.3.3 Voigt notation

For a more concise formulation with simpler structure, we use the Voigt notation in the following. This notation exploits symmetry to transform the second-order stress and strain tensors to vectors, and the fourth-order elasticity tensor to a square matrix [111, 26].
In this notation, the Cauchy stress tensor (3.10), which is symmetric, is expressed as a vector of its six unique components

$$\bar{\boldsymbol{\sigma}} = \left[\sigma_{xx}, \sigma_{yy}, \sigma_{zz}, \tau_{xy}, \tau_{yz}, \tau_{zx}\right]^{\top} \tag{3.40}$$

Similarly, the infinitesimal strain tensor is transformed to a vector

$$\bar{\boldsymbol{\varepsilon}} = \boldsymbol{L}\,\boldsymbol{u} = \left[\varepsilon_{xx}, \varepsilon_{yy}, \varepsilon_{zz}, \gamma_{xy}, \gamma_{yz}, \gamma_{zx}\right]^{\top}, \tag{3.41}$$

where $\boldsymbol{L}$ denotes the differential operator matrix:

$$\boldsymbol{L} = \begin{bmatrix} \dfrac{\partial}{\partial x} & 0 & 0 \\ 0 & \dfrac{\partial}{\partial y} & 0 \\ 0 & 0 & \dfrac{\partial}{\partial z} \\ \dfrac{\partial}{\partial y} & \dfrac{\partial}{\partial x} & 0 \\ 0 & \dfrac{\partial}{\partial z} & \dfrac{\partial}{\partial y} \\ \dfrac{\partial}{\partial z} & 0 & \dfrac{\partial}{\partial x} \end{bmatrix}. \tag{3.42}$$

Note that a factor of $\frac{1}{2}$ was eliminated from the shear components $\gamma_{xy}$,$\gamma_{yz}$ and $\gamma_{zx}$.
The constitutive equation (3.15) in Voigt notation reads:

$$\bar{\boldsymbol{\sigma}} = \boldsymbol{C} \cdot \bar{\boldsymbol{\varepsilon}}, \tag{3.43}$$

where $\boldsymbol{C}$ is the elasticity matrix relating the stress and strain vectors. In the case of linear isotropic elasticity, it is given by

$$\boldsymbol{C} = \frac{E}{(1+\nu)(1-2\nu)} \begin{bmatrix} 1-\nu & \nu & \nu & 0 & 0 & 0 \\ \nu & 1-\nu & \nu & 0 & 0 & 0 \\ \nu & \nu & 1-\nu & 0 & 0 & 0 \\ 0 & 0 & 0 & \dfrac{1-2\nu}{2} & 0 & 0 \\ 0 & 0 & 0 & 0 & \dfrac{1-2\nu}{2} & 0 \\ 0 & 0 & 0 & 0 & 0 & \dfrac{1-2\nu}{2} \end{bmatrix}. \tag{3.44}$$

The bilinear form $\mathcal{B}$ can be rewritten as

$$\mathcal{B}(\boldsymbol{u}, \boldsymbol{v}) = \int_\Omega \bar{\boldsymbol{\varepsilon}}(\boldsymbol{u}) \cdot \boldsymbol{C} \cdot \bar{\boldsymbol{\varepsilon}}(\boldsymbol{v}) \, \mathrm{d}\Omega = \int_\Omega [\boldsymbol{L}\,\boldsymbol{u}]^\top \cdot \boldsymbol{C} \cdot [\boldsymbol{L}\,\boldsymbol{v}] \, \mathrm{d}\Omega. \tag{3.45}$$

### 3.3.4 Linear finite element approximation

In the FEM, the basis functions $N_i$ of the space $\mathcal{V}^h$ are defined in an element-wise manner. To that end, the domain $\Omega$ is partitioned into $n_{\text{el}}$ non-overlapping subdomains, which we refer to as *finite element domains* $\Omega^e$, or simply *elements*, with $e = 1, \ldots, n_{\text{el}}$. We call the collection of finite elements a *mesh*. Typical element shapes for two-dimensional meshes are quadrilaterals and triangles. Figure 3.4 depicts a quadrilateral finite element mesh. For three-dimensional problems, common element types are hexahedra (bricks), tetrahedra, as well as triangular prisms (pentahedra).
For elasticity, the basic convergence requirements are that the shape functions be [111]

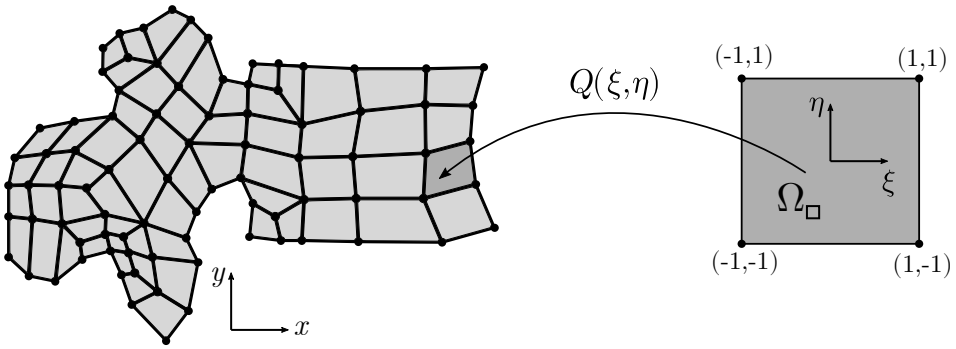


Figure 3.4: A two-dimensional quadrilateral mesh and mapping from a reference element

1. smooth (i.e. at least $C^1$) within the element domain $\Omega^e$
2. $C^0$-continuous across the element boundaries $\Gamma^e$
3. complete (can exactly represent all rigid motions).

Piecewise linear basis functions (and their generalizations in higher dimensions) defined on the finite element domains satisfy these requirements. The linear basis functions are associated to the *nodes*, which are defined at the vertices (corners) of the finite element domains.

For the three-dimensional case, we consider the standard trilinear hexahedral element, which has eight nodes that are connected by twelve edges. The local coordinates $\boldsymbol{\xi}$ are defined in the standard integration domain $\Omega_\square = [-1,1]^3$. The nodal shape functions are defined in the local coordinate space as

$$N_i = \frac{1}{8}\left(1+\xi_i\xi\right)\left(1+\eta_i\eta\right)\left(1+\zeta_i\zeta\right), \qquad i = 1,\ldots,8 \tag{3.46}$$

where $\boldsymbol{\xi}_i = (\xi_i, \eta_i, \zeta_i)$ denotes the local coordinates $(\pm1, \pm1, \pm1)$ of node $i$.

The function $Q$ defines the mapping between the local coordinates $\boldsymbol{\xi}$ of the standard element and the corresponding global coordinates $\boldsymbol{x}$, as illustrated in Figure 3.4. For the trilinear hexahedral element, this is given by

$$\boldsymbol{x} = Q(\boldsymbol{\xi}) = \sum_{i=1}^{8} N_i(\boldsymbol{\xi})\,\boldsymbol{x}_i, \tag{3.47}$$

where $\boldsymbol{x}_i$ are the global coordinates $(x_i, y_i, z_i)$ of node $i$. The Jacobian matrix for this mapping reads

$$\boldsymbol{J} = \frac{\partial \boldsymbol{x}}{\partial \boldsymbol{\xi}} = \begin{bmatrix} \dfrac{\partial x}{\partial \xi} & \dfrac{\partial y}{\partial \xi} & \dfrac{\partial z}{\partial \xi} \\ \dfrac{\partial x}{\partial \eta} & \dfrac{\partial y}{\partial \eta} & \dfrac{\partial z}{\partial \eta} \\ \dfrac{\partial x}{\partial \zeta} & \dfrac{\partial y}{\partial \zeta} & \dfrac{\partial z}{\partial \zeta} \end{bmatrix} = \sum_{i=1}^{8} \boldsymbol{x}_i \otimes \frac{\partial N_i(\boldsymbol{\xi})}{\partial \boldsymbol{\xi}}. \tag{3.48}$$

Following the isoparametric concept, the *same* functions used to describe the geometry are used to construct $\mathcal{V}^h$ and approximate the trial and test functions [111]. To this

end, the shape function matrix $\boldsymbol{N}$ defined in (3.31) is assembled from the element shape functions $N_i$. Substituting the finite element approximation into the weak form (in Voigt notation) (3.45) yields the matrix form of the boundary-value problem.
Since the shape functions are defined element-wise, the weak form integrals are also evaluated for each element, and assembled to a global system of equations:

$$\boldsymbol{K} = \bigwedge_{e=1}^{n_{\mathrm{el}}} \boldsymbol{K}^e \tag{3.49}$$

$$\boldsymbol{f} = \bigwedge_{e=1}^{n_{\mathrm{el}}} \boldsymbol{f}^e, \tag{3.50}$$

where $\bigwedge$ is the assembly operator, and $\boldsymbol{K}^e$ and $\boldsymbol{f}^e$ respectively denote the element stiffness matrix and force vector, which are given by

$$\boldsymbol{K}^e = \int_{\Omega^e} \boldsymbol{B}^\top \boldsymbol{C} \boldsymbol{B} \,\mathrm{d}\Omega \tag{3.51}$$

$$\boldsymbol{f}^e = \int_{\Omega^e} \boldsymbol{N}^\top \boldsymbol{b} \,\mathrm{d}\Omega + \int_{\Gamma_N^e} \boldsymbol{N}^\top \hat{\boldsymbol{t}} \,\mathrm{d}\Gamma_N^e. \tag{3.52}$$

Here, $\boldsymbol{B}$ denotes the strain-displacement matrix

$$\boldsymbol{B} = \boldsymbol{L}\,\boldsymbol{N} = \begin{bmatrix} \boldsymbol{B}^1 & \boldsymbol{B}^2 & \dots & \boldsymbol{B}^n \end{bmatrix}, \tag{3.53}$$

where each block is given by

$$\boldsymbol{B}^i = \begin{bmatrix} \dfrac{\partial N_i}{\partial x} & 0 & 0 \\ 0 & \dfrac{\partial N_i}{\partial y} & 0 \\ 0 & 0 & \dfrac{\partial N_i}{\partial z} \\ \dfrac{\partial N_i}{\partial y} & \dfrac{\partial N_i}{\partial x} & 0 \\ 0 & \dfrac{\partial N_i}{\partial z} & \dfrac{\partial N_i}{\partial y} \\ \dfrac{\partial N_i}{\partial z} & 0 & \dfrac{\partial N_i}{\partial x} \end{bmatrix}. \tag{3.54}$$

In order to compute the derivatives of the shape functions with respect to $\boldsymbol{x}$, the chain rule is applied:

$$\begin{bmatrix} \dfrac{\partial N_i}{\partial x} \\ \dfrac{\partial N_i}{\partial y} \\ \dfrac{\partial N_i}{\partial z} \end{bmatrix} = \begin{bmatrix} \dfrac{\partial \xi}{\partial x} & \dfrac{\partial \eta}{\partial x} & \dfrac{\partial \zeta}{\partial x} \\ \dfrac{\partial \xi}{\partial y} & \dfrac{\partial \eta}{\partial y} & \dfrac{\partial \zeta}{\partial y} \\ \dfrac{\partial \xi}{\partial z} & \dfrac{\partial \eta}{\partial z} & \dfrac{\partial \zeta}{\partial z} \end{bmatrix} \begin{bmatrix} \dfrac{\partial N_i}{\partial \xi} \\ \dfrac{\partial N_i}{\partial \eta} \\ \dfrac{\partial N_i}{\partial \zeta} \end{bmatrix} = \boldsymbol{J}^{-1} \begin{bmatrix} \dfrac{\partial N_i}{\partial \xi} \\ \dfrac{\partial N_i}{\partial \eta} \\ \dfrac{\partial N_i}{\partial \zeta} \end{bmatrix}. \tag{3.55}$$

### 3.3.5 The $p$-version of the FEM

In the FEM, higher numerical accuracy is attained by increasing the number of degrees of freedom. In the standard $h$-version of the FEM this is achieved by spatially refining the mesh, thereby decreasing the element size $h$. In the $p$-version, degrees of freedom are added by increasing the polynomial order $p$ of the basis functions without changing the mesh.
The standard shape functions for finite elements are given by the Lagrange polynomials [111], shown for a one-dimensional case in Figure 3.5a. For each polynomial degree $p$, a separate set of shape functions is defined. In order to improve the approximation by increasing $p$, the basis functions need to be replaced.

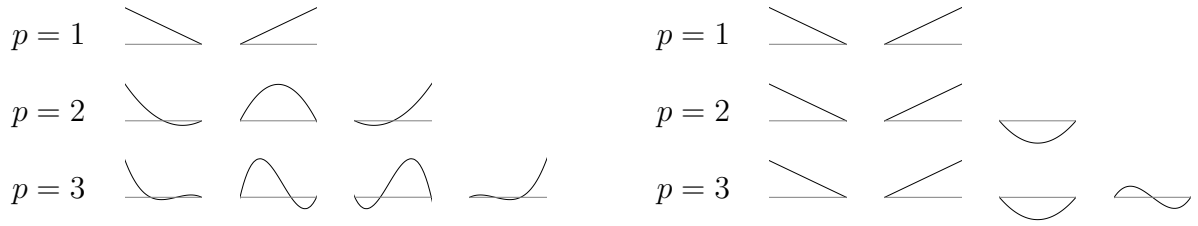


(a) Lagrange basis (b) Hierarchic basis

Figure 3.5: One dimensional high-order shape functions

The hierarchic basis functions based on the integrated Legendre polynomials are given by [237]

$$N_1 = \frac{1}{2}(1-\xi) \tag{3.56a}$$

$$N_2 = \frac{1}{2}(1+\xi) \tag{3.56b}$$

$$N_i = \phi_{i-1}(\xi), \quad i = 3, ..., p+1 \tag{3.56c}$$

with

$$\phi_j(\xi) = \sqrt{\frac{2j-1}{2}} \int_{-1}^{\xi} L_{j-1}(x)\mathrm{d}x = \frac{1}{\sqrt{4j-2}}(L_j(\xi) - L_{j-2}(\xi)), \quad j = 2, 3, ... \tag{3.57}$$

where $L_j(\xi)$ are the Legendre polynomials, which are defined by:

$$L_n(x) = \frac{1}{2^n n!}\frac{\mathrm{d}^n}{\mathrm{d}x^n}(x^2-1)^n, \quad x \in (-1,1), \quad n = 0, 1, 2, ... \tag{3.58}$$

or using the recursion formula:

$$L_n(x) = \frac{1}{n}[(2n-1)xL_{n-1}(x) - (n-1)L_{n-2}(x)], \quad x \in (-1,1), \quad n = 2, 3, 4, ... \tag{3.59}$$

with

$$L_0(x) = 1, \tag{3.60}$$

$$L_1(x) = x. \tag{3.61}$$

In contrast to the standard Lagrange basis, the integrated Legendre polynomials constitute a *hierarchic* basis, which can be seen in Figure 3.5b. This means that the set of basis functions for a certain polynomial order $p$ contains all the functions for the lower orders. This allows for a $p$-refinement where the mesh is kept fixed, and for local adaptation of the polynomial degree. Moreover, using the integrated Legendre polynomials as basis functions leads to well-conditioned linear systems of equations, as their derivatives are orthogonal by definition.
For higher dimensions (2D and 3D), basis functions are constructed by taking the tensor product of the one-dimensional basis functions [237].

$$N_{i,j}^{2D}(\xi,\eta) = N_i^{1D}(\xi)\, N_j^{1D}(\eta) \tag{3.62}$$

$$N_{i,j,k}^{3D}(\xi,\eta,\zeta) = N_i^{1D}(\xi)\, N_j^{1D}(\eta)\, N_k^{1D}(\zeta). \tag{3.63}$$

Figure 3.6 illustrates the high-order basis functions for a quadrilateral element.

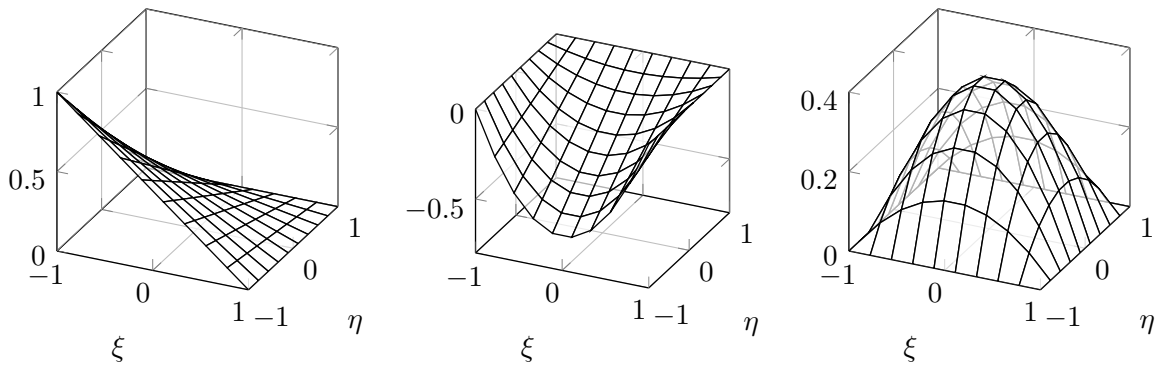


(a) Nodal mode (b) Quadratic edge mode (c) Quadratic internal mode

Figure 3.6: Two dimensional $p$-version shape functions

Considering the three-dimensional case, the tensor product structure gives the high-order shape functions for hexahedral elements. Each of the resulting shape functions can be directly associated to a topological component (node, edge, face, interior) of the underlying element. Furthermore, the tensor product space can be reduced, without sacrificing completeness, by excluding some of the face and interior modes. The four types of modes are defined as follows:

- **Nodal modes:** the trilinear shape functions

$$N_{1,1,1}^{N_i}(\xi,\eta,\zeta) = \frac{1}{8}\,(1-\xi_i\,\xi)\,(1-\eta_i\,\eta)\,(1-\zeta_i\,\zeta) \qquad i = 1,\ldots,8 \tag{3.64}$$

  are the standard shape functions for the isoparametric hexahedral (brick) element (3.46).
- **Edge modes:** there are $(p_r - 1)$ functions per edge, where $p_r$ is the polynomial order in the direction of the edge, $r \in \{\xi,\eta,\zeta\}$. If we consider, for example, edge E1 (see Figure 3.7), the corresponding edge modes are given by

$$N_{i,1,1}^{E_1}(\xi,\eta,\zeta) = \frac{1}{4}\,(1-\eta)\,(1-\zeta)\,\phi_i(\xi) \qquad i = 2,\ldots,p_\xi \tag{3.65}$$

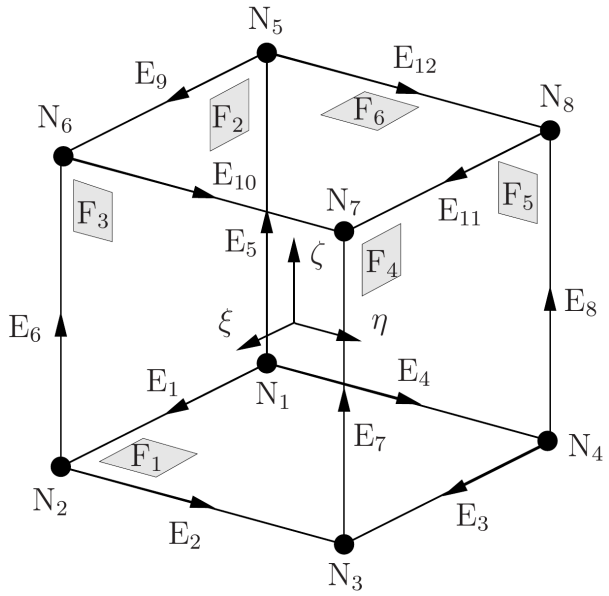


Figure 3.7: Standard high-order hexahedral element, reproduced from [68].

- **Face modes:** are the product of two high-order polynomials along the two local directions of a face, and a linear blending term in the third orthogonal direction. Hence, they vanish at all nodes and edges. For face F1, the corresponding modes are defined as

$$N_{i,j,1}^{F_1}(\xi,\eta,\zeta) = \frac{1}{2}(1-\zeta)\,\phi_i(\xi)\,\phi_j(\eta) \tag{3.66}$$

The total number of face modes differ between the tensor product and trunk spaces

| **tensor space** | **trunk space** |
|---|---|
| $i = 2,\ldots,p_\xi$ | $i = 2,\ldots,p_\xi - 2$ |
| $j = 2,\ldots,p_\eta$ | $j = 2,\ldots,p_\eta - 2$ |
| | $i + j = 4,\ldots,\max\{p_\xi, p_\eta\}$ |

- **Internal modes:** are the product of three high-order shape functions, They are purely local to the element, and vanish on all nodes, edges and faces.

$$N_{i,j,k}^{int}(\xi,\eta) = \phi_i(\xi)\,\phi_j(\eta)\,\phi_k(\zeta) \tag{3.67}$$

The trunk space also includes fewer internal modes than the tensor product space with the same polynomial degrees.

| **tensor space** | **trunk space** |
|---|---|
| $i = 2,\ldots,p_\xi$ | $i = 2,\ldots,p_\xi - 4$ |
| $j = 2,\ldots,p_\eta$ | $j = 2,\ldots,p_\eta - 4$ |
| $k = 2,\ldots,p_\zeta$ | $k = 2,\ldots,p_\zeta - 4$ |
| | $i + j + k = 6,\ldots,\max\{p_\xi, p_\eta, p_\zeta\}$ |

The $p$-version of the FEM exhibits a more favorable convergence behavior compared to low-order approximations [237]. For problems with smooth solutions, the $p$-FEM achieves exponential convergence in the energy norm under $p$-refinement. Hence, it is able to attain numerical solutions with much higher accuracy compared to uniform $h$-refinement in low-order FEM which can only have algebraic convergence. This exponential convergence rate can even be obtained for non-smooth problems, if the $p$-version is combined with an adequate local mesh refinement. Moreover, high-order finite elements are more immune to locking behavior, and are more robust against mesh distortion.

Despite these desirable convergence properties, the $p$-version of the FEM does not yet enjoy widespread use in industry. Some challenges are presented by the application of the $p$-version to larger classes of problems, e.g. nonlinear problems found in elastoplasticity or contact mechanics. It has, however, been shown that the $p$-version can be successfully used in these problems, and even outperform the standard $h$-version [181, 101]. A major obstacle remaining for the $p$-version is the handling of complex geometrical models, which are abundant in practical engineering problems. To fully utilize the high-order approximations, isoparametric $p$-finite elements need to use a high-order approximation of the geometry. To that end, it is possible to use the blending function method [88], where the function $Q$ has additional terms accounting for the curved edges and faces. Unfortunately, this could be prohibitively difficult for cases with complex geometry, which hinders the applicability of the $p$-version of the FEM in practice.

## 3.4 Immersed boundary approach

Immersed boundary methods are an alternative to conventional finite elements that enables simulations involving complex (or evolving) geometry without boundary-conforming mesh generation. The main idea of these methods is to augment the physical domain of interest $\Omega_{\text{phy}}$ with a fictitious domain $\Omega_{\text{fict}}$ to form a simple-shaped domain $\hat{\Omega} = \Omega_{\text{phy}} \cup \Omega_{\text{fict}}$. The boundary-value problem is extended such that it is defined over $\hat{\Omega}$ which can be trivially meshed. This approach is illustrated in Figure 3.8.

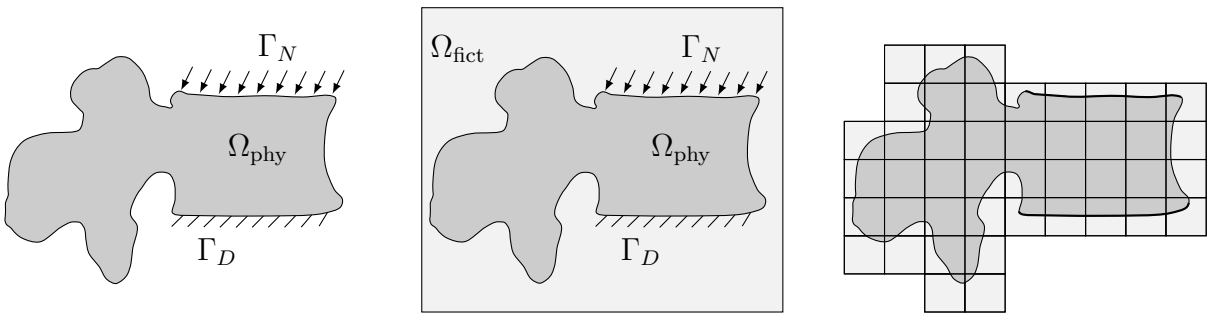


Figure 3.8: Main concept of the FCM following [190]

In order to recover the original boundary-value problem (3.26), the influence of the fictitious domain on the weak form is penalized. To that end, we define an indicator function

$\alpha$ as

$$\alpha(\boldsymbol{x}) = \begin{cases} 1 & \forall \boldsymbol{x} \in \Omega_{\text{phy}} \\ \epsilon \ll 1 & \forall \boldsymbol{x} \in \Omega_{\text{fict}}. \end{cases} \tag{3.68}$$

Using this indicator function, we can rewrite the bilinear form as

$$\begin{aligned} \mathcal{B}(\boldsymbol{u}, \boldsymbol{v}) &= \int_{\Omega_{\text{phy}}} \bar{\boldsymbol{\varepsilon}}(\boldsymbol{u}) \cdot \boldsymbol{C} \cdot \bar{\boldsymbol{\varepsilon}}(\boldsymbol{v}) \, \mathrm{d}\Omega + \int_{\Omega_{\text{fict}}} \bar{\boldsymbol{\varepsilon}}(\boldsymbol{u}) \cdot \epsilon \, \boldsymbol{C} \cdot \bar{\boldsymbol{\varepsilon}}(\boldsymbol{v}) \, \mathrm{d}\Omega \\ &= \int_{\hat{\Omega}} \bar{\boldsymbol{\varepsilon}}(\boldsymbol{u}) \cdot \alpha \, \boldsymbol{C} \cdot \bar{\boldsymbol{\varepsilon}}(\boldsymbol{v}) \, \mathrm{d}\Omega. \end{aligned} \tag{3.69}$$

An intuitive interpretation of this penalization is the application of a void material with negligible stiffness in the fictitious domain. The scaling factor for the material parameters $\epsilon$ is chosen as small as possible—clearly for $\epsilon = 0$ the original problem is recovered—yet large enough to prevent extreme ill-conditioning of the resulting stiffness matrix. Typical values for $\epsilon$ range between $10^{-4}$ and $10^{-15}$. The linear form $\mathcal{F}(\boldsymbol{v})$ is extended by zero in the fictitious domain $\Omega_{\text{fict}}$.

The FCM combines the immersed boundary approach with high-order finite element discretization. The extended domain, which has a simple shape, is subdivided into a uniform Cartesian grid of high-order finite elements, which we will call finite cells. In finite cells that are cut by the boundary of the physical domain, the FCM solution smoothly extends into the fictitious domain. Similar to high-order FE analysis, the finite cell mesh consists of relatively large finite cells. To achieve a higher numerical accuracy, the polynomial degree of the basis functions is increased for a fixed mesh ($p$-refinement). For problems with smooth solutions, the FCM achieves exponential rates of convergence for $p$-refinement on uniform Cartesian meshes [190, 70, 219].

For image-based simulations, discretization using Cartesian FCM grids has several advantages. The grids can be chosen to be axis-aligned with the voxel grids, and the finite cell sizes can be chosen as an exact multiple of the voxel dimensions, such that each finite cell is 'composed' of a set of voxels. This allows for a more efficient and accurate numerical integration, as described in the next section. However, the use of uniform Cartesian grids is not suitable for non-smooth problems with locally high gradients or singularities, as such problems require local mesh refinement [215]. Alternative versions of the FCM make use of unstructured tetrahedral or polygonal meshes where local refinement is possible. Another possibility explored in this work is the application of the *hp*-version of the FEM to refine the FCM meshes, which is presented in Section 5.3.

Considering the choice of high-order basis functions, several possibilities exist. Typical choices are the integrated Legendre polynomials described in the previous section, as well as B-Splines used in isogeometric analysis [219]. For applications in high frequency dynamics, another possibility is the use of Lagrange interpolation polynomials based on the Gauss-Lobatto quadrature points [67, 121, 86]. These functions hold the advantage that suitable mass lumping schemes are available, making it possible to fully exploit the advantages of explicit time-integration schemes.

The combination of the immersed boundary approach and high-order basis functions requires special attention for the numerical integration of the weak form, enforcement of

the boundary conditions and solution of the linear system. We discuss these aspects in the remaining part of this chapter.

## 3.5 Numerical integration

In general, the integrals of the weak form (3.51) cannot be analytically evaluated. In the FEM, the Gauss-Legendre quadrature is usually applied for their numerical evaluation. In a one-dimensional setting, the integral of a function $f$ is approximated by the quadrature rule

$$\int_{-1}^{1} f(\xi)\ \mathrm{d}\xi \approx \sum_{i=1}^{n} f(\xi_i) w_i, \tag{3.70}$$

where $\xi_i$ denote the quadrature points at which $f$ is evaluated, and $w_i$ are the corresponding weights [237]. Using $n$ integration points, the quadrature rule can be used to integrate a polynomial of order up to $2n-1$ exactly. For smooth functions, Gauss-Legendre quadrature can converge exponentially. However, for functions with singularities, the convergence is slower. The Gauss-Legendre quadrature rule can be also used for integrals over surfaces or volumes

$$\int_{-1}^{1}\int_{-1}^{1} f(\xi,\eta)\ \mathrm{d}\xi\mathrm{d}\eta \approx \sum_{j=1}^{m}\sum_{i=1}^{n} f(\xi_i,\eta_j)\, w_i w_j \tag{3.71}$$

$$\int_{-1}^{1}\int_{-1}^{1}\int_{-1}^{1} f(\xi,\eta,\zeta)\ \mathrm{d}\xi\mathrm{d}\eta\mathrm{d}\zeta \approx \sum_{k=1}^{l}\sum_{j=1}^{m}\sum_{i=1}^{n} f(\xi_i,\eta_j,\zeta_k)\, w_i w_j w_k = \sum_{i=1}^{N} f(\boldsymbol{\xi}_i)\, W_i. \tag{3.72}$$

For the three-dimensional integral, we combine the triple summation to a single sum over $N = n \times m \times l$, whereas $W_i$ denotes the combined weights of the quadrature points. To evaluate an integrand over $\Omega$, a change of variables is carried out

$$\int_{\Omega} f(\boldsymbol{x})\, \mathrm{d}\Omega \approx \sum_{i=1}^{N} f(\boldsymbol{x}(\boldsymbol{\xi}_i))\, W_i\ \det \boldsymbol{J}(\boldsymbol{\xi}_i), \tag{3.73}$$

where the Jacobian matrix $\boldsymbol{J}$ (3.48) accounts for the mapping.
Standard Gauss-Legendre quadrature can be used for accurate and efficient integration of smooth functions. However, in the FCM, the integrals of cells that are cut by the boundary of the physical domain are discontinuous due to the penalization of the material parameters (3.69). Hence, standard Gauss-Legendre quadrature cannot be directly applied to evaluate the integrals [190]. The challenge of integrating discontinuous functions is faced by immersed boundary approaches, as well as partition of unity methods, the generalized (G-FEM) and extended (XFEM) finite element methods [83].
Several approaches have been developed for accurate evaluation of the discontinuous domain integrals in the FCM. A straightforward possibility is to use a fine grid of integration

sub-cells to partition each finite cell, with the Gauss-Legendre quadrature applied for each sub-cell [190, 268]

$$\int_{\Omega} f(\boldsymbol{x})\,\mathrm{d}\Omega \approx \sum_{j=1}^{M}\sum_{i=1}^{N} f(\boldsymbol{x}(\boldsymbol{\xi}_i))\,W_i\,\det\boldsymbol{J}(\boldsymbol{\xi}_i)\det\tilde{\boldsymbol{J}}_j, \tag{3.74}$$

where $\tilde{\boldsymbol{J}}_j$ considers the mapping between the integration sub-cells and the finite cell. This approach is very well suited for image-based FCM models, where the material parameters are also defined on a voxel grid. Defining the integration sub-cell grid to correspond to the voxel grid enables direct FCM simulation using the image data with minimal pre-processing. An example of such an integration grid is illustrated in Figure 3.9.

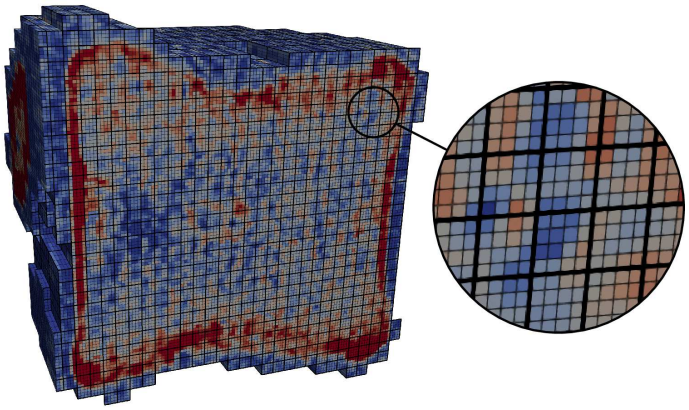

Figure 3.9: FCM mesh of a vertebral body showing the underlying voxel-grid

Another advantage of this integration approach for the voxel-based FCM is the possibility of pre-computation. Here, the integration points and their mapping Jacobian are identical among all finite cells—only differing in the material properties which are defined voxel-wise. Hence, a pre-computation of the stiffness matrix on a voxel-level is possible, which can be used to drastically reduce the computational effort of the voxel-based FCM as presented by Yang et al. [268] and Groen et al. [90].

An alternative scheme for composed integration applies recursive sub-division of the finite cells cut by the boundary, leading to a spacetree of integration sub-cells [219]. The spacetree approach is robust and easy to implement. It is generally well suited for models of complex CAD geometry which have a homogeneous material distribution, e.g. medical implant. More sophisticated integration schemes have been developed to efficiently evaluate the discontinuous domain integrals for the FCM. These schemes include the blended partitioning using the smart-octree [143, 144], moment-fitting [123], adaptively weighted quadratures [1, 240], and quadratic re-parametrization for the tetrahedral finite cell method [235] and a special technique where the volume integrals are transformed to surface integrals [65]

## 3.6 Enforcement of boundary conditions

In the FCM, the boundary does not coincide with the edges and faces of the discretization mesh. Hence, the boundary conditions cannot be enforced in the classical manner followed in conventional FEM. In the following, alternative techniques for imposing boundary conditions in the FCM are discussed.

### 3.6.1 Neumann boundary conditions

Similar to conventional FEM, homogeneous Neumann boundary conditions are automatically satisfied in the FCM. For heterogeneous Neumann boundary conditions, the boundary integral over the Neumann boundary $\Gamma_N$ needs to be evaluated. However, as $\Gamma_N$ is not resolved by the boundaries of the finite cells (edges in 2D, faces in 3D), the integral cannot be numerically evaluated over the element's boundaries as usually done in conventional FEM. Hence, an additional surface mesh for the boundary is introduced, which is only used to evaluate the traction integrals. Here, we emphasize that this surface mesh is not used to define additional basis functions, and doesn't introduce additional degrees of freedom. Figure 3.10 illustrates a surface mesh within a finite cell. For FCM analysis in 3D, a suitable surface mesh can be provided, for example, by surface tessellation of CAD models. Alternatively, for implicit geometry descriptions, the marching cubes algorithm can be used to automatically generate surface descriptions that can be used to evaluate the surface integrals, as demonstrated in [24, 22]. Considering geometric models stemming from medical images, this approach can be conveniently used together with the segmented models, as demonstrated in the next chapter.

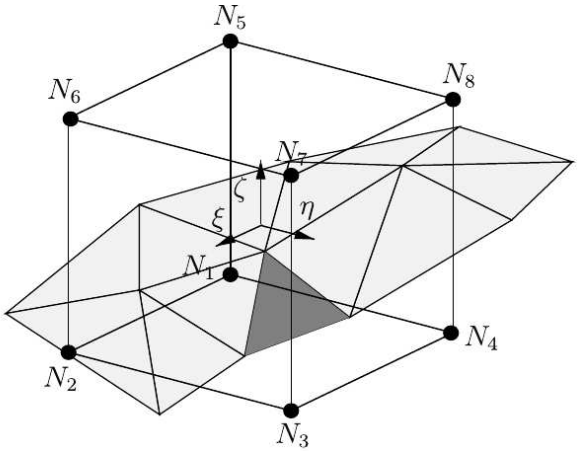


Figure 3.10: Surface mesh for evaluation of boundary integrals, reproduced from [70].

Later in this work (in Section 6.1.3), we present a numerical approach for the weak imposition of concentrated (point) forces and moments for the FCM.

### 3.6.2 Dirichlet boundary conditions

The imposition of Dirichlet conditions in the FCM presents an additional challenge. In conventional FEM, Dirichlet conditions are enforced by manipulating the corresponding

entries of the stiffness matrix and the load vector [77]. To that end, the degrees of freedom are classified as either unknown or prescribed. The system of linear equations can be then reduced to solve for the unknown degrees of freedom taking the contribution from the prescribed values into account. Clearly, this approach is not applicable for immersed boundary discretizations where the Dirichlet boundary $\Gamma_D$ is not directly resolved by the mesh. There are, however, several possibilities to weakly impose Dirichlet boundary conditions in immersed boundary methods—including the use of Lagrange multipliers [11, 99, 85] the penalty method [12, 284] and Nitsche's method [78, 97, 18, 278, 209].

### The penalty method

To weakly enforce the Dirichlet boundary conditions using the penalty method, the weak form (3.69) and (3.26c) is modified:

$$\hat{\mathcal{B}}(\boldsymbol{u}, \boldsymbol{v}) = \mathcal{B}(\boldsymbol{u}, \boldsymbol{v}) + \beta \int_{\Gamma_D} \boldsymbol{v} \cdot \boldsymbol{u} \, \mathrm{d}\Gamma \tag{3.75a}$$

$$\hat{\mathcal{F}}(\boldsymbol{v}) = \mathcal{F}(\boldsymbol{v}) + \beta \int_{\Gamma_D} \boldsymbol{v} \cdot \hat{\boldsymbol{u}} \, \mathrm{d}\Gamma, \tag{3.75b}$$

where $\beta$ is a scalar penalty parameter. This modification adds the weighted residual

$$\mathcal{W}_p = \beta \int_{\Gamma_D} \boldsymbol{v} \cdot (\boldsymbol{u} - \hat{\boldsymbol{u}}) \, \mathrm{d}\Gamma$$

to the weak form of the equilibrium equation. If $\beta$ is chosen to be large compared to the entries of the stiffness matrix, $\boldsymbol{u} - \hat{\boldsymbol{u}} = \boldsymbol{0}$ will be approximately satisfied on $\Gamma_D$. This method can be mechanically interpreted as a distributed spring with very high stiffness $\beta$ which acts along the Dirichlet boundary to enforce the prescribed displacements. Similar to the Neumann case, a separate surface mesh is needed for the numerical integration of the penalty terms over $\Gamma_D$.
The penalty method is popular since it is easy to implement and involves a single scalar parameter. However, the accuracy of the method depends on the chosen value of the penalty parameter $\beta$, which is influenced by the material parameters, the size of the finite cells as well as the polynomial degree of the shape functions. The penalty method is also inconsistent, as it slightly modifies the original problem. The exact solution is hence only attainable using an infinite penalty parameter. Nevertheless, this approach delivers sufficiently accurate solutions without severe conditioning problems, making it suitable for several engineering applications of the FCM [218, 219]. In this work, we follow this approach.

### Nitsche's method

An alternative approach, which is commonly applied in immersed boundary methods, is the weak enforcement of essential boundary conditions using Nitsche's method [179].

Here, the weak form is modified as follows:

$$\tilde{\mathcal{B}}(\boldsymbol{u},\boldsymbol{v}) = \mathcal{B}(\boldsymbol{u},\boldsymbol{v}) - \int_{\Gamma_D} (\boldsymbol{\sigma}(\boldsymbol{u})\cdot\boldsymbol{n})\cdot\boldsymbol{v}\,\mathrm{d}\Gamma - \int_{\Gamma_D} (\boldsymbol{\sigma}(\boldsymbol{v})\cdot\boldsymbol{n})\cdot\boldsymbol{u}\,\mathrm{d}\Gamma + \lambda\int_{\Gamma_D}\boldsymbol{v}\cdot\boldsymbol{u}\,\mathrm{d}\Gamma \tag{3.76a}$$

$$\tilde{\mathcal{F}}(\boldsymbol{v}) = \mathcal{F}(\boldsymbol{v}) - \int_{\Gamma_D} (\boldsymbol{\sigma}(\boldsymbol{v})\cdot\boldsymbol{n})\cdot\hat{\boldsymbol{u}}\,\mathrm{d}\Gamma + \lambda\int_{\Gamma_D}\boldsymbol{v}\cdot\hat{\boldsymbol{u}}\,\mathrm{d}\Gamma. \tag{3.76b}$$

The first additional boundary integral in (3.76a) stems from applying the divergence theorem–see (3.25). In the case of immersed boundary discretizations, it is not guaranteed to vanish on $\Gamma_D$ as the test functions $\boldsymbol{v}$ are not restricted to be zero at the (immersed) Dirichlet boundary. The second additional term in (3.76a) and the first additional term in (3.76b) are introduced to retain the symmetry of the resulting stiffness matrix. The remaining terms are similar to the penalty terms introduced in (3.75a) and (3.75b), with $\lambda$ being a scalar stabilization parameter. These terms are introduced to retain coercivity of the bilinear form after subtracting the other terms.
This approach has also been applied to weakly enforce Dirichlet boundary conditions in the FCM [278, 207]. Unlike the penalty method, it is variationally consistent. However, finding the optimal value for the stabilization parameter $\lambda$ in each finite cell that is cut by $\Gamma_D$ is challenging. Moreover, as the stabilization parameter additionally depends on the shape and size of the cut cell, it is generally not bounded, which motivates the introduction of additional stabilization, e.g. using ghost penalty [56]. Alternative parameter-free approaches were also investigated for the weak imposition of Dirichlet boundary conditions in the FCM [138, 217].

## 3.7 Solution of system of linear equations

After applying the boundary conditions and constraints, the remaining step is to solve the system of equations (3.37). For systems of linear equations, solution procedures can be classified as direct and iterative solvers. Direct solvers based on Gaussian elimination, such as LU, QR and Cholesky factorization, can be used to solve systems of linear equations with high precision. For sparse linear systems, such as those arising in finite element analysis, the numerical effort for the solution using direct methods strongly depends on the fill ratio and the bandwidth. Hence, renumbering the equations to minimize the bandwidth can reduce the total computational cost. However, direct solvers can be very expensive to use for very large systems, as they have a complexity of $\mathcal{O}(N^3)$. Moreover, they have high memory requirements to store the factorized matrices, which are generally not sparse. This imposes a hard limit on the maximum problem size that can be solved.
Regarding iterative solvers, the most commonly used methods in structural FE analysis are based on the conjugate gradient method. The time complexity for the conjugate gradient method is determined by the condition number and the number of non-zeros of the stiffness matrix. For FE analysis, it is well-known that the condition number increases with the number of unknowns, the dimensionality of the problem, and the polynomial degree $p$ of the shape functions [285, 73]. The condition number is also influenced by the

boundary conditions and the material distribution within the element. For large well-conditioned linear systems, iterative methods can be more computationally efficient than direct methods. Moreover, they generally require considerably less storage in comparison to direct methods, as they do not need to store the factorized matrices. Nevertheless, direct methods could prove more feasible for small linear problems with multiple right-hand sides, e.g. in linear elastodynamics [16], where the factorized matrix can be reused for the forward/backward substitution at each time-step.

In the FCM, penalization of the stiffness within the fictitious domain (3.69) leads to ill-conditioning of the system of linear equations. The analysis carried out by de Prenter et al. [58] reveals that the ill-conditioning stems either from basis functions being small on finite cells with small volume fractions, or from basis functions being quasi-linearly dependent on such cells. Furthermore, it was shown that the condition number is inversely proportional to the smallest cut cell volume fraction, and that the inverse proportionality scales with the power of $2p$, explaining why the problem is more severe for high-order FCM discretizations. This limits the applicability of iterative linear solvers for the FCM and renders the use of direct solvers necessary. Owing to the high accuracy achievable by the employed high-order basis functions, and its flexibility in dealing with complex geometry, FCM discretizations lead to smaller linear systems compared to conventional FEM (for a given accuracy) which can be solved using direct methods. Nevertheless, the high memory requirements of direct solvers prevents the use of the FCM to model larger problems. To overcome this limitation, there have been several efforts dedicated to the development of preconditioners tailored for the FCM.

Preconditioners improve the conditioning of the system of linear equations which in turn improves the performance of iterative solvers. Considering the linear system $\boldsymbol{K}\boldsymbol{d} = \boldsymbol{f}$ (3.37), the non-singular preconditioning matrix $\boldsymbol{S}$ is sought such that $\boldsymbol{S}\boldsymbol{K}$ has a smaller condition number than $\boldsymbol{K}$. The symmetrically preconditioned system is then solved instead:

$$\boldsymbol{S}\boldsymbol{K}\boldsymbol{S}^{\top}\tilde{\boldsymbol{d}} = \boldsymbol{S}\boldsymbol{f} \tag{3.77}$$

$$\boldsymbol{d} = \boldsymbol{S}^{\top}\tilde{\boldsymbol{d}}. \tag{3.78}$$

De Prenter *et al.* [58] also developed an effective algebraic preconditioner for the FCM, named the Symmetric Incomplete Permuted Inverse Cholesky (SIPIC), which applies diagonal scaling to the applied basis followed by local Gram–Schmidt orthonormalization. The diagonal scaling treats ill-conditioning due to small basis functions on finite cells with small volume fractions, whereas the orthonormalization addresses the quasi-linear dependence of the basis functions. Numerical investigation of the performance of SIPIC shows that it considerably improves the conditioning of FCM systems, which enables the use of iterative solvers for larger systems, and is more robust than other competitive preconditioning schemes, e.g. incomplete Cholesky preconditioning.

In further work, an Additive-Schwarz type preconditioner for the FCM was presented [117], which enables the iterative solution of large-scale multi-level *hp*-refined finite-cell systems in an efficient and parallel-scalable manner. The general idea of Additive-Schwarz preconditioning schemes is to approximate the inverse matrix, $\boldsymbol{K}^{-1}$, through the

inversion and summation of sub-matrices of $\boldsymbol{K}$:

$$\boldsymbol{S} = \sum_{I \in \mathcal{I}} \boldsymbol{R}_I^\top \boldsymbol{K}_I^{-1} \boldsymbol{R}_I. \tag{3.79}$$

Here, $I$ denotes a block (a set of indices) of basis functions in the set of blocks $\mathcal{I}$, and multiplying with $\boldsymbol{R}_I$,the restriction matrix, restricts $\boldsymbol{K}$ to the indices in $I$. The choice of which blocks of basis functions $\mathcal{I}$ to locally invert determines the effectiveness of the preconditioner. For the FCM, choosing $\mathcal{I}$ to include basis functions with small contributions, and those functions which could become quasi-linearly dependent treats the underlying cause for ill-conditioning. Selecting blocks of basis functions for finite cells whose volume fraction is below a set threshold leads to a robust and effective preconditioner. Further research proposes the use of multigrid methods for more efficient preconditioners for the FCM [57, 118].
Another technique that is commonly applied in the $p$-version of the FEM to improve the efficiency of the solution procedure is known as static condensation [237]. This technique makes use of the hierarchical structure of the stiffness matrix to reduce the size of the global system of equations. Nodal, edge and face modes are considered as external modes, since they contribute to more than one element. In contrast, internal (bubble) modes only contribute to a single element, and do not introduce coupling between neighboring elements. Therefore, it is possible to condense the stiffness contributions of the internal modes on the element level, and thereby reduce the size of the system to be solved.
To that end, the system of linear equations (3.37) can be expressed as:

$$\begin{bmatrix} \boldsymbol{K}_{ee} & \boldsymbol{K}_{ei} \\ \boldsymbol{K}_{ei}^\top & \boldsymbol{K}_{ii} \end{bmatrix} \begin{bmatrix} \boldsymbol{d}_e \\ \boldsymbol{d}_i \end{bmatrix} = \begin{bmatrix} \boldsymbol{f}_e \\ \boldsymbol{f}_i \end{bmatrix}, \tag{3.80}$$

where $\boldsymbol{K}_{ii}$ represents the stiffness contributions from the internal modes, $\boldsymbol{K}_{ee}$ represents the contributions from the external modes, and $\boldsymbol{K}_{ei}$ represents the coupling between the internal and external modes. Solving (3.80) for the internal unknowns $\boldsymbol{d}_i$ results in

$$\boldsymbol{d}_i = \boldsymbol{K}_{ii}^{-1} \left( \boldsymbol{f}_i - \boldsymbol{K}_{ei}^\top \boldsymbol{d}_e \right). \tag{3.81}$$

Substituting the result into the first equation of (3.80) gives the reduced system

$$\left( \boldsymbol{K}_{ee} - \boldsymbol{K}_{ei} \boldsymbol{K}_{ii}^{-1} \boldsymbol{K}_{ei}^\top \right) \boldsymbol{d}_e = \boldsymbol{f}_e - \boldsymbol{K}_{ei} \boldsymbol{K}_{ii}^{-1} \boldsymbol{f}_i \tag{3.82}$$

$$\boldsymbol{K}^* \boldsymbol{d}_e = \boldsymbol{f}^*. \tag{3.83}$$

Here, $\boldsymbol{K}^*$ and $\boldsymbol{f}^*$ are the condensed stiffness matrix and the corresponding load vector. As the internal modes account for a major part of the linear system, especially for high-order discretizations, the condensed system has a much smaller size. It is important to note that the inversion of $\boldsymbol{K}_{ii}$ in (3.82) can be performed on element-level, i.e. prior to the assembly of the global system of equations—which is much cheaper than inverting the assembled block corresponding to the internal modes. After solving the condensed system, the internal degrees of freedom can be recovered by solving (3.81). Static condensation has also been applied to improve the efficiency of direct solvers for applications of the FCM in topology optimization [90].

## 3.8 Previous work and validation

The FCM has been previously utilized for the simulation of bone mechanics, and the numerical predictions of the FCM models for subject-specific continuum-scale models of femur were validated. The first work addressing this topic was presented by Ruess et al. [209]. Therein, the authors presented a verification study of the FCM for analysis of inhomogeneous isotropic materials, demonstrating that the FCM retains the favorable convergence properties of $p$-FEM models with the same geometric description. The authors also present a validation study of a subject-specific continuum-level FCM model of a human femur. A mechanical experiment had been carried out to measure the deformation due to a force applied to the femoral head. There, the displacements were measured at predefined points on the surface of the bone and the strains were measured using strain gauges. The subject-specific FCM model was based on QCT scans of the fresh-frozen femur. Analysis of the computed results showed a very good overall correlation between the experiments and the simulation ($R^2 > 0.97$). Moreover, the numerical results were of similar accuracy to the predictions of a conforming $p$-FEM simulation—which had been previously presented in [273]—despite the fact that the QCT-based FCM model does not consider a smooth surface description, which requires a large modeling effort to generate, and is necessary for boundary-conforming $p$-FEM analysis. The $p$-FEM and FCM models and the results of the validation study are shown here in Figure 3.11. Further work by Schillinger [214] demonstrated that, for the same femur model, the B-Spline version of the FCM obtains results of similar accuracy to the $p$-version of the FCM.

In related work, Yang et al. [268] presented an efficient numerical integration technique for the voxel-based FCM, which exploits the similarity of the finite cells within a uniformly discretized domain which we described earlier (see Section 3.5). Using the pre-computation scheme, real-time updates to the patient-specific bone simulation were made possible, which enabled applications for interactive implant planning in orthopedics through computational steering [267].

Another application of the FCM for bone mechanics was presented by Wille et al. [260] in an investigation of the uncertainties in bone material properties and loads. To that end, the authors utilized the FCM as a "black box" solver to perform personalized analyses and compute the deformations given the geometry, loads and material properties. As the stochastic analysis using polynomial chaos expansion—and more so the verification with a Monte Carlo simulation—required a large number of simulation runs (more than 10,000 simulations) with different stochastic parameters, the high computational efficiency of the voxel-based FCM with pre-computation made it very-well suited for this application.

Whereas these efforts considered continuum-level bone models based on QCT scans, Verhoosel et al. [249] presented a microstructural modeling approach for the FCM. This approach considers micro-CT based models of trabecular bone, reconstructs a smooth geometry of the microstructure using a B-Spline approximation, then applies goal-oriented local refinement to compute the apparent elastic properties of bone samples.

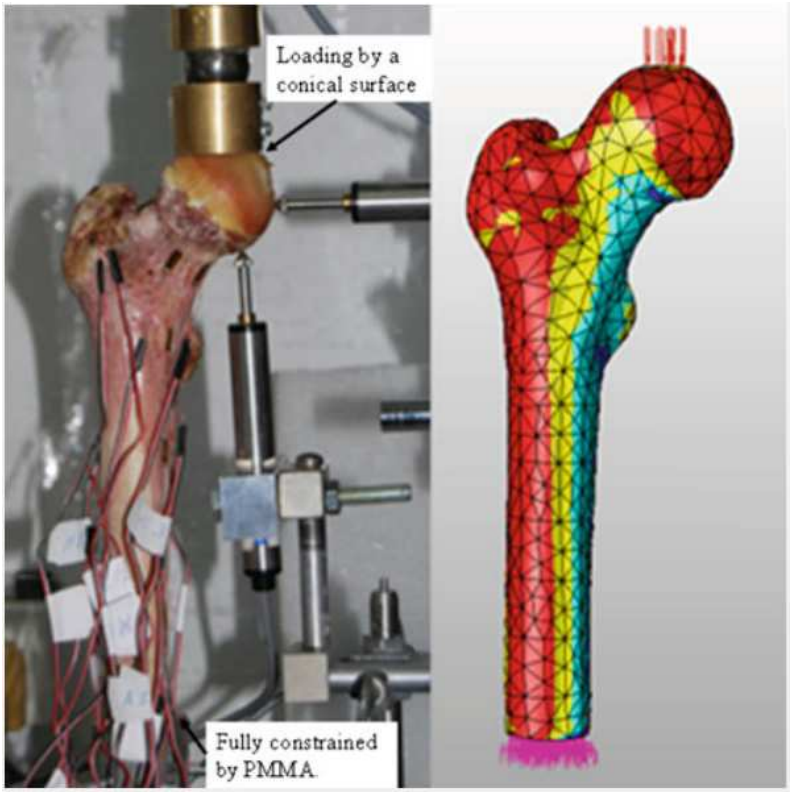


(a) Experimental setup and $p$-FEM model

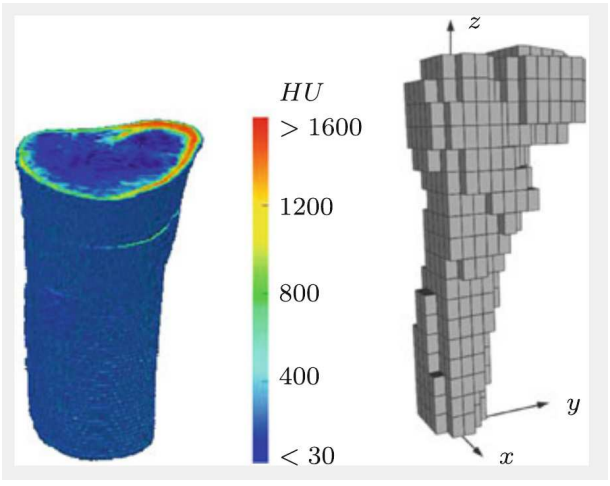


(b) FCM model

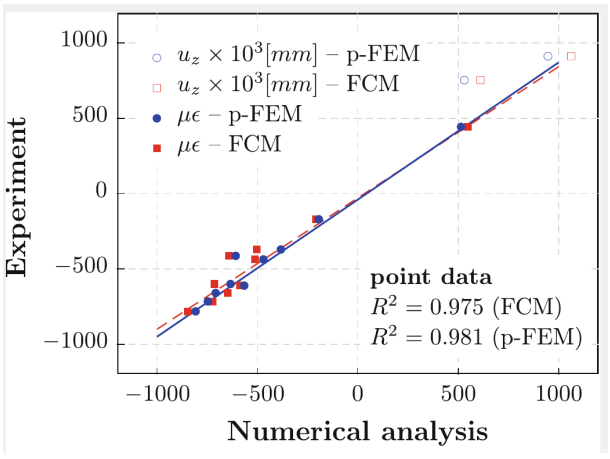


(c) Validation results

Figure 3.11: Femur-model validation study, adapted from [209]

# Chapter 4

# Micro-CT-based finite-cell analysis of vertebral bodies: a validation study

In this chapter, we present a new validation study of the finite cell method (FCM) for bone mechanics. We study FCM models of four human vertebral bodies that are based on micro-CT imaging data, and compare the numerical predictions of the displacement fields to the deformation measured in compression experiments. We employ digital volume correlation (DVC) to estimate the local displacement fields of the compression experiments. The DVC data is interpolated on the boundary and used to define the displacement boundary conditions for the FCM models, whereas the interior DVC displacements are compared to the numerical predictions of the FCM models. Analysis of the results shows very good agreement between the DVC data and the FCM predictions for all components of the displacements of all examined specimens ($0.73 < R^2 < 0.97$, slope of the regression line = 0.91–1.14). The results illustrate the potential of the FCM as a simulation tool for micro-CT based analysis, as an attractive alternative to the well-established $\mu$-FEM.
The work presented in this chapter was carried out as part of a collaboration project. The contributions and efforts of Alexander Valentinitsch[1], Peter Föhr[2], Klaus Achterhold[3], Franz Pfeiffer[3], Jan S. Kirschke[1] and Martin Ruess[4] are gratefully acknowledged. Part of this work was presented in [74].

## 4.1 Introduction

Bone has complex hierarchical structure [48]. Numerical studies of bone mechanics at a micro-scale provide a better understanding of the biomechanical behavior of trabecular bone. To that end, the discrete micro-architecture of trabecular bone needs to be resolved by the mechanical analysis. This is especially important in studying the mechanical interaction of bone and implants, as the discrete nature of the trabecular bone affects the local distribution of peri-implant strains [261, 263].

[1]Department of Neuroradiology, Technical Univeristy of Munich
[2]Department of Sports Orthopaedics, Technical Univeristy of Munich
[3]Chair of Biomedical Physics, Technical Univeristy of Munich
[4]Faculty of Mechanical and Process Engineering, Düsseldorf University of Applied Sciences

The current state of the art for numerical analysis of cancellous bone is the micro-CT-based finite element method ($\mu$-FEM)[106, 247, 246]. This relies on the conversion of micro-computed tomography (micro-CT) images into 3D finite element meshes. Thereby, specimen-specific numerical models are generated, where the geometry and material properties are based on high-resolution imaging data.

Validation of numerical methods in biomechanics is of crucial importance to their utility and clinical relevance [5]. Typically, the numerical predictions are compared to the data of a validation experiment (gold standard). The validation of micro-scale numerical analysis of trabecular bones presents significant challenges. Unavoidable imperfections in the setup of the validation experiment lead to false assumptions of the boundary conditions given to the numerical model and diverging results [31]. Moreover, only apparent quantities of the trabecular bone (such as strength and stiffness) can be directly measured in the validation experiments, whereas local quantities (such as displacements and strains) can only be directly measured at the surface of the bone using conventional techniques such as optical sensors and strain gauges [89].

There have been several efforts towards the verification and validation of $\mu$-FEM for the biomechanical analysis of trabecular bone. A verification study of large scale $\mu$-FEM models of trabecular bone tissue shows the convergence of local displacements and strains for linear analysis [33]. Validation studies of $\mu$-FEM mainly deal with apparent measures (strength and stiffness) [191, 36, 266], as the measurement of local quantities within the trabecular microstructure is not trivial.

An increasingly popular technique for use in validation of biomechanical models is digital volume correlation (DVC) [189, 188]. Here, two volumetric images (micro-CT scans) of the unloaded specimen and the specimen under load are processed to estimate displacement and strain maps. It has been demonstrated that DVC can be reliably used to estimate local displacement fields for trabecular bone if sufficient resolution is used [50]. A validation study of $\mu$-FEM analysis of trabecular bone by Zauel et al. [281] shows high correlation ($R^2 = 0.97$) between the DVC data for the displacements and $\mu$-FEM prediction, albeit only for the component in the loading direction. Further work by Chen et al. [32] shows that the replication of boundary conditions by the interpolation of the DVC data at the boundary of the specimens yields excellent agreement of the $\mu$-FEM predictions and the interior DVC data, for all components of the displacement field ($R^2 = 0.99$, slope = 0.98 – 1.07). Further investigation of $\mu$-FEM models of porcine vertebrae by Costa et al. [45] shows results of similar accuracy for models of porcine vertebral bodies. Another study investigating $\mu$-FEM models of mouse tibia using the same approach of interpolating DVC measurements to provide the boundary conditions found correlation between the predicted displacements and experimental measurements with higher but still reasonable errors ($0.69 < R^2 < 0.90$, slope = 0.50–0.97) [183]. The use of DVC to replicate the displacement boundary conditions has also been applied for the validation of the displacements predicted by continuum-level FE models of the scapula based on quantitative CT (QCT) images [146], and for the validation of the strains of continuum-level models of the humeral head [145] and the scapula [147]. In other work, DVC procedures have also been used to study the mechanics of whole bones [113], bone-implant models [14], cement-augmented bones [283] and to assess micro-damage progression in vertebral bodies [243].

There are, however, some difficulties with the $\mu$-FEM that limit its applicability for the analysis of whole vertebral bodies. Due to the one-to-one mapping of micro-voxels and hexahedral finite elements, high resolution $\mu$-FEM models typically have several tens to hundreds of millions of degrees of freedom, which require high performance/supercomputing resources [9, 2, 3].

Moreover, studies involving $\mu$-FEM models of vertebral bodies often exclude the endplates to simplify the application of the boundary conditions. However, including the endplates can improve the accuracy of the numerical models, as they have been shown to contribute to the vertebral strength [167]. Further, failure of vertebrae loaded via healthy intervertebral discs is often initiated in the endplates [166], and they can also be utilized to incorporate more complex boundary conditions through coupling to models of the intervertebral disc [42].

The finite cell method (FCM), as described Chapter 3, is an alternative to conventional finite element methods. Due to the application of higher-order shape functions and specialized integration techniques, the FCM can use much coarser meshes without compromising the accurate resolution of complex boundary shapes or local material features. Similar to the $\mu$-FEM, it relies on trivial mesh generation, whereas material properties are assigned voxel-wise. Thereby, the FCM can be used to resolve the trabecular structure without complex mesh generation procedures. Moreover, within the framework of the FCM, essential boundary conditions can be imposed on surfaces of complex geometry in a flexible manner using weak imposition methods [207]. Furthermore, it has been demonstrated that using a pre-integration technique yields higher computational efficiency for the FCM in comparison to conventional low-order voxel-FEM [268, 90].

In this work, we present a new validation study for the FCM. Here, we consider micro-CT-based FCM ($\mu$-FCM) models of four human vertebral bodies. The validation experiments use DVC to estimate the displacement fields within the vertebral bodies under axial compression. We follow an approach, similar to the one presented by Costa et al. [45], to interpolate the DVC data at the boundary. We validate the $\mu$-FCM models by demonstrating a high correlation between the DVC estimations and the numerical predictions of the displacement fields.

The $\mu$-FCM models in our study consider the whole height of the vertebral bodies (including the intact endplates)—in contrast to the $\mu$-FEM models presented by Costa et al. which only cover the middle 50% of the total height of each vertebral body. We use a penalty method to weakly impose the interpolated DVC displacements at the automatically reconstructed surfaces of the endplates and the cortical shells. As an embedded domain approach, the $\mu$-FCM models require virtually no modelling effort. Furthermore, the method requires significantly less degrees of freedom to achieve the same numerical accuracy—compared to conventional low order FEM—owing to the higher-order shape functions. We propose the $\mu$-FCM as an attractive alternative to the well-established $\mu$-FEM, that can be used to perform micro-CT based analysis of whole bone specimens with high accuracy for a moderate computational effort—without the need for high-performance computing resources.

## 4.2 Materials and methods

Micro-CT scans of four human vertebral body specimens were obtained first while applying a small preload, and later while applying additional axial compression. A digital volume correlation (DVC) procedure was applied on the two sets of micro-CT scans to estimate the displacement fields caused by the axial compression loading. $\mu$-FCM models based on the preloaded scans were used to numerically predict the displacements. Trilinear interpolation of the DVC displacement fields at the endplates and the cortical shells of the vertebral bodies was used to define the displacement boundary conditions for the $\mu$-FCM models. Finally, the internal DVC displacement fields were compared to the numerical predictions for validation. The workflow of our study is depicted in Figure 4.1.

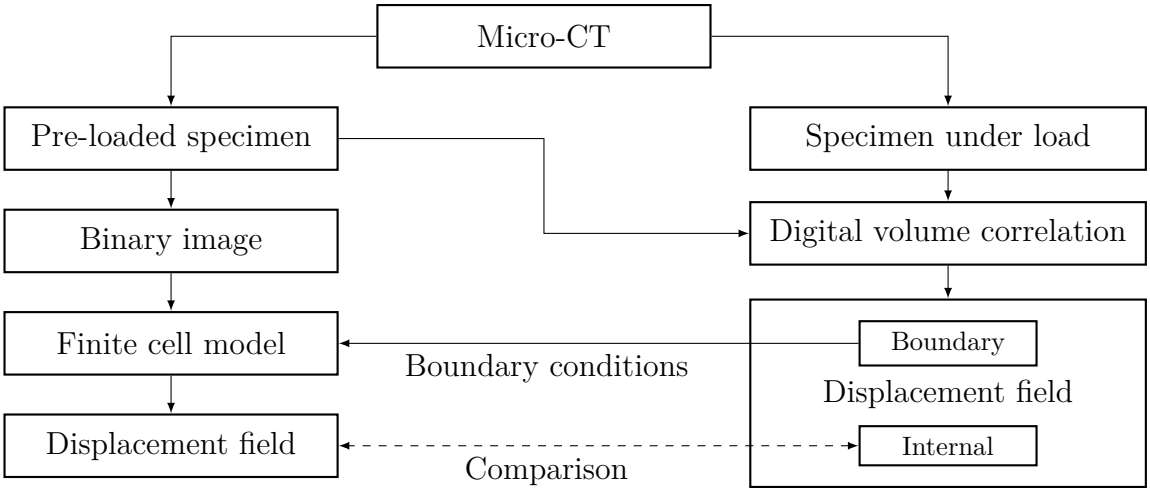


Figure 4.1: Workflow of the validation study, following [32, 45]

### 4.2.1 Compression experiment and image acquisition

A validation experiment was carried out to measure the deformation of specimens of human vertebral bodies under axial compression.* Four human vertebral bodies were used for the experiment — one lumbar and three thoracic vertebral bodies from four different donors. Details about the specimens, height and bone volume fraction (BV/TV), are listed in Table 4.1. Two additional vertebral bodies were initially scanned, but were later excluded from our study as they had pre-existing fractures.
The vertebral bodies used for the validation experiment are fresh frozen specimens. They had been first prepared by removing the intervertebral discs and the surrounding soft tissue. The transverse and spinous processes were also removed, as our study only considers the deformation within the vertebral bodies. Next, the vertebral bodies were embedded at their end-plates in a layer of dental cement and additionally embedded in polymethyl

*The experiments were designed and carried out at the Department of Sports Orthopaedics, TUM, by Peter Föhr and Alexander Valentinitsch. Their efforts are gratefully acknowledged.

Table 4.1: Specimen data

| # | Segment no. | Height[mm] | Voxel size [$\mu$m] | BV/TV [%] |
|---|---|---|---|---|
| 1 | L3 | 25.2 | 65 | 20.0 |
| 2 | T12 | 24.6 | 65 | 26.0 |
| 3 | T12 | 23.1 | 65 | 25.9 |
| 4 | T12 | 23.9 | 60 | 21.6 |

methacrylate (PMMA). This embedding provides a homogeneous surface on which to apply the compression load.
A specially designed *in situ* compression jig was used to apply axial pressure, which is shown in Figure 4.2a. The compression jig is designed to fit within the micro-CT scanner (Figure 4.2b), and is used to apply a uniform pressure throughout the duration of the scan (approximately 3 hours).

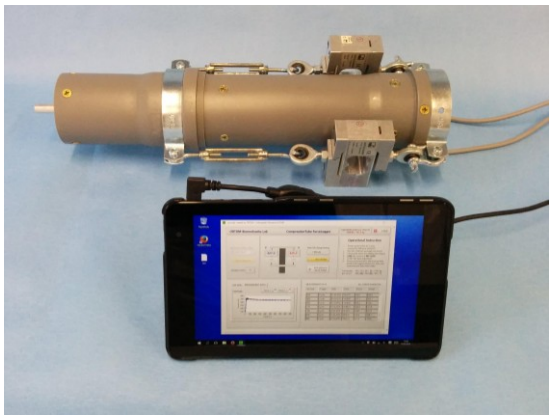

(a) Compression device[1]

(b) Phoenix/GE v|tome|x s240 micro-CT scanner at the Munich School of BioEngineering[2]

Figure 4.2: Experimental setup

The compression jig including the bone specimens were scanned using a micro-CT scanner. For each specimen, two scans were made: the first scan applying a small compression load to avoid moving artifacts during the scan, which we refer to in the following as the "preloaded scan". The second scan was made with the specimen under an additional axial compression load of 180 kg—the "loaded scan". To compensate for the initial relaxation after applying the load, the applied load was re-adjusted every 5 minutes over the first 20 minutes until a steady value of 180 kg was obtained.
The tomography was performed with a Phoenix/GE v|tome|x s240 micro-CT scanner.[†] For the tomographic reconstruction with filtered back projection (FBP), the proprietary datos|x reconstruction software was used. The v|tome|x s240 scanner is equipped with an

[1]Image taken by Peter Föhr
[2]Image taken by Klaus Achterhold
[†]Image acquisition was carried out at the Munich School of BioEngineering, by Klaus Achterhold. His efforts are gratefully acknowledged.

XS 240D direct tube. For all measurements, the peak voltage of the tube was 200 kVp and the current 200 $\mu$A. The spot size of the X-ray tube is automatically adjusted with the power to prevent damage of the anode. The voltage and current values were chosen to optimize the polychromatic tube spectrum with respect to the transmission through the bone and compression jig and an acceptable spot size compared to the effective reconstructed voxel sizes of 60 $\mu$m and 65 $\mu$m (compare Table 4.1). A rule of thumb estimate of the spot size gives about 40 $\mu$m for the given power of 40 W. An additional filter of 1.8 mm of copper was used to absorb low energy parts of the polychromatic X-ray spectrum and prevent beam hardening artifacts in the reconstruction.
A total of 1601 projections of 6 seconds duration followed by a 1 second skipped projection were collected for 360° rotation of the samples with an amorphous silicon DXR 250 RT detector (GE) equipped with a caesium iodide (CsI) scintillator. The skipped projection ensures decay of the scintillator afterglow for the next sample orientation angle. The temperature stabilized detector has a pixel pitch of 200 $\mu$m, 1000 $\times$ 1000 pixel and 14 bit depth. With the geometric magnification of 3.33 and 3.08 the above mentioned voxel sizes of 60 and 65 $\mu$m were obtained respectively.

### 4.2.2 Digital volume correlation[‡]

Next, a digital volume correlation (DVC) procedure was carried out between the preloaded and loaded scans to estimate the displacement fields resulting from the compression load. To this end, the software package `elastix` [136, 223] was used in the current work.
The DVC procedure consists of a rigid, followed by an elastic registration. Image registration is applying a transformation to a source image to match it to a target image. It is often formulated as an optimization problem, seeking the transformation which minimizes a cost function representing the difference between the source and target images [137].
For the rigid registration, the images are only transformed through translation and rotation. This was carried out to align the preloaded (source) and loaded scans (target). The reference planes for the rigid registration were chosen at the mid-height of the vertebral bodies, as demonstrated in Figure 4.3.

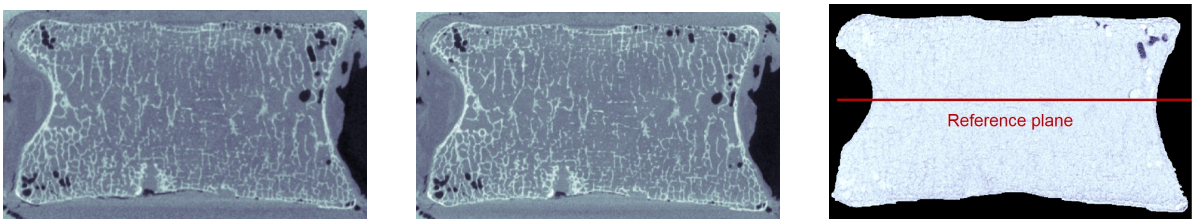


(a) Unloaded scan: $A$ (b) Loaded scan: $B$ (c) Difference image: $B - A$

Figure 4.3: Rigid registration

Here, we point out the air bubbles which are visible within the trabecular structure in the images. As some of the air bubbles moved between the scans, special attention was necessary to eliminate their influence on the registration. Hence, a separate segmentation

[‡]Image processing was carried out at the Department of Neuroradiology, TUM, by Alexander Valentinitsch. His efforts are gratefully acknowledged.

mask for the air bubbles was created to exclude them from the process. To physically eliminate the air bubbles, the samples would need to be submerged in a saline solution, and the compression jig would need to be made watertight. However, this was not carried out in this work to avoid the risk of leakage and damage to the scanner.
Next, the elastic registration procedure was carried out to estimate the displacement field. In the current work, this is achieved by applying affine transformations (translation, rotation, scaling and shearing) to the images. The transformations were carried out on patches of the images of size $60 \times 60 \times 60$ voxels, which are overlapping by 30 voxels in each direction. A numerical solution to the optimization problem provides the affine transformations for the elastic registration. The relatively large patch size is necessary to ensure that there are enough physical features to be identified in the transformed patch. Finally, the resulting affine transformations were utilized to estimate the displacement field within the overlapping sub-patches. The results were stored as regular grids with nodes at the centers of the sub-patches, which we refer to in the following as the "DVC grids". An example of the displacement field approximated from the elastic registration is shown in Figure 4.4.

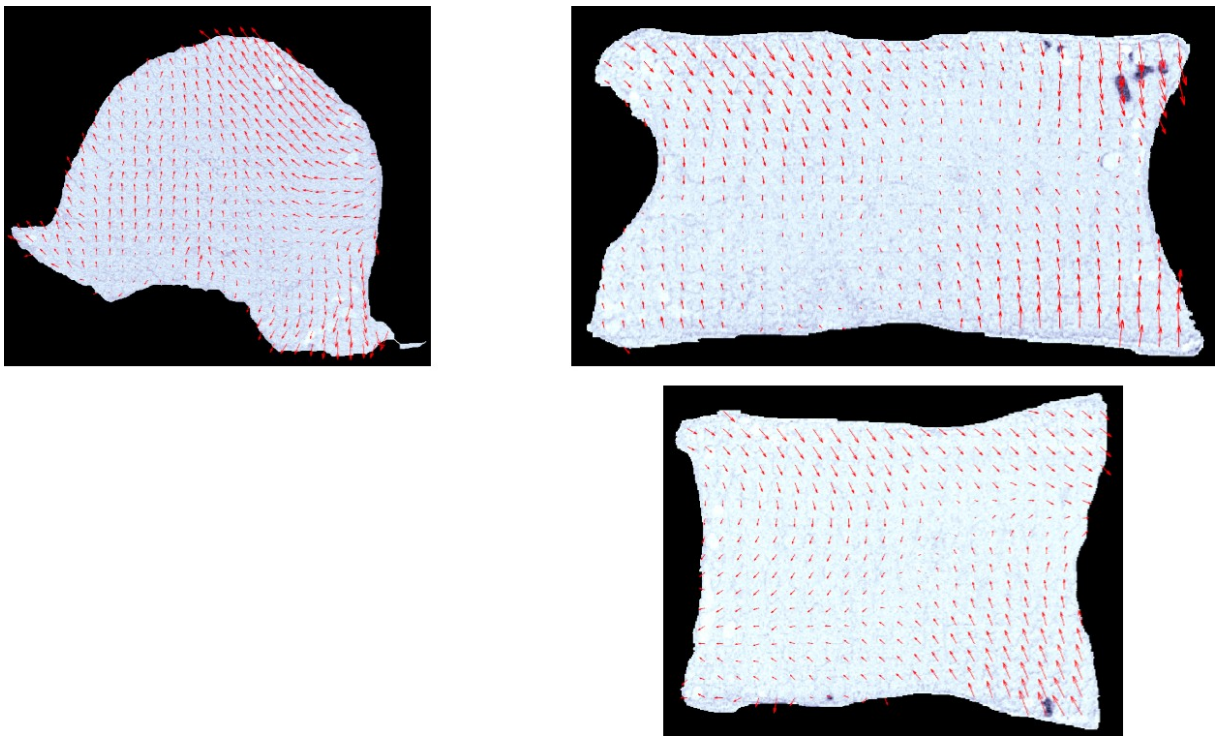

Figure 4.4: Digital volume correlation: displacement field

### 4.2.3 Micro-CT-based finite cell models

For the numerical analysis, we employ the FCM, as described in Chapter 3. Unlike previous validation studies of the FCM which considered continuum-level numerical models [209], the work presented here considers microstructural models . To this end, the

geometric model and the material properties for the numerical models are based on the micro-CT scans of the preloaded specimens.

### Pre-processing—Segmentation

The first step in setting up the numerical models is to perform a segmentation of the micro-CT scans. Here, the segmentation only needs to consider the outer boundary of the vertebral bodies, without distinction between the trabeculae and the marrow within the bone's structure. An example of such a segmentation is shown in Figure 4.5. The segmentation is used in conjunction with the CT image to identify the physical domain inside the region of interest—the so-called point membership test. The segmentation is also used to generate a surface tessellation for the enforcement of the boundary conditions. In the current study, the segmentation was carried out using a partially automated approach. First, a specimen-specific threshold was manually identified to delineate the cortical and trabecular bone regions. The automated algorithm used a connectivity filter followed by morphological closing (dilation followed by erosion) operation to extract a filled cortical shell. Noise was reduced by applying a median filter. The segmentations were then manually revised using `ITK-SNAP` [274] to ensure an accurate representation of the boundaries. For the current work, the quality of the segmentation is of greater importance, as they are used to identify the physical domain, and later utilized to generate surface meshes which are used to apply the boundary conditions.

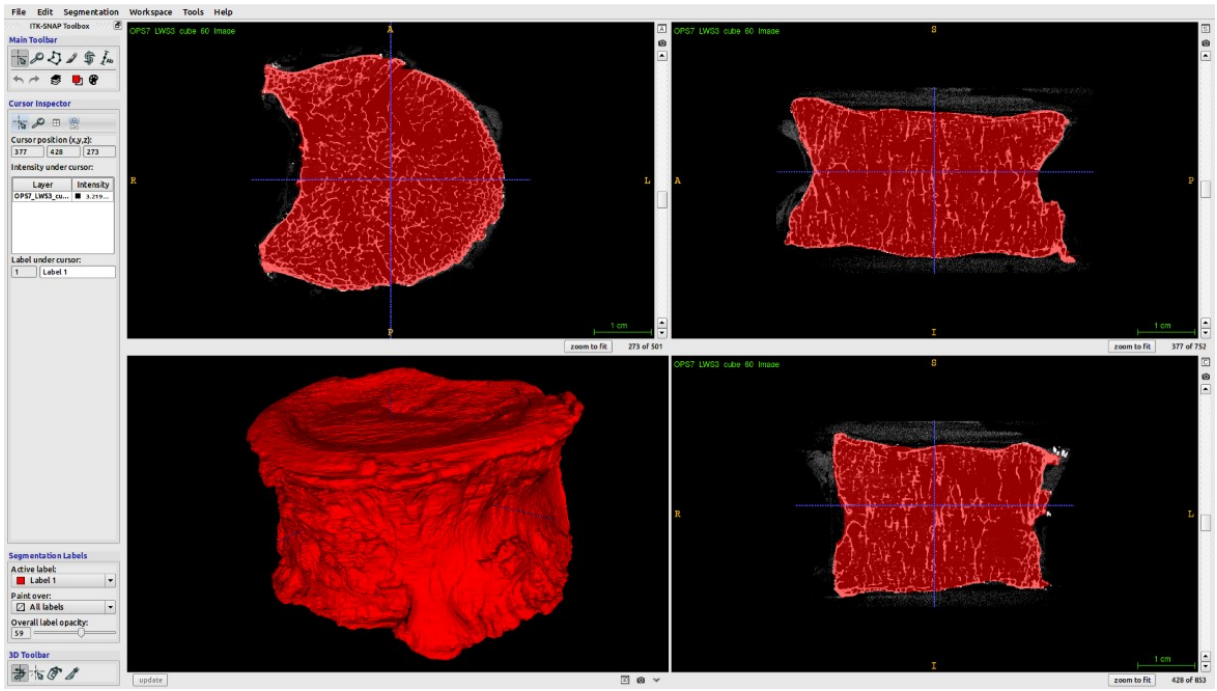


Figure 4.5: Segmentation in `ITK-SNAP`

### $\mu$-FCM discretization

The micro-CT scans of the pre-loaded vertebra together with the matching segmentations were used to generate the $\mu$-FCM models using our in-house finite-cell framework `AdhoC++`. The bounding box of the region of interest in each scan was discretized using a regular grid of finite cells. The dimensions of the finite cells were chosen as an integer number of voxels in each spatial direction. In this study, we used $14 \times 14 \times 14$ voxels per finite cell. A polynomial order $p = 3$ with the trunk space was chosen [71]. All finite cells that were completely inside the fictitious domain were excluded from the models. This excluded mostly cells that were outside the vertebral body yet within the bounding box of the defined region of interest, or in some cases cells that were within larger "voids" inside the trabecular structure. Excluding these cells reduces the size of the numerical model, and improves the condition number of the system's stiffness matrix. The resulting $\mu$-FCM models had between 50 and 56 thousand finite cells, and approximately 1.1 to 1.3 million degrees of freedom. An example of the resulting models is presented in Figure 4.6.

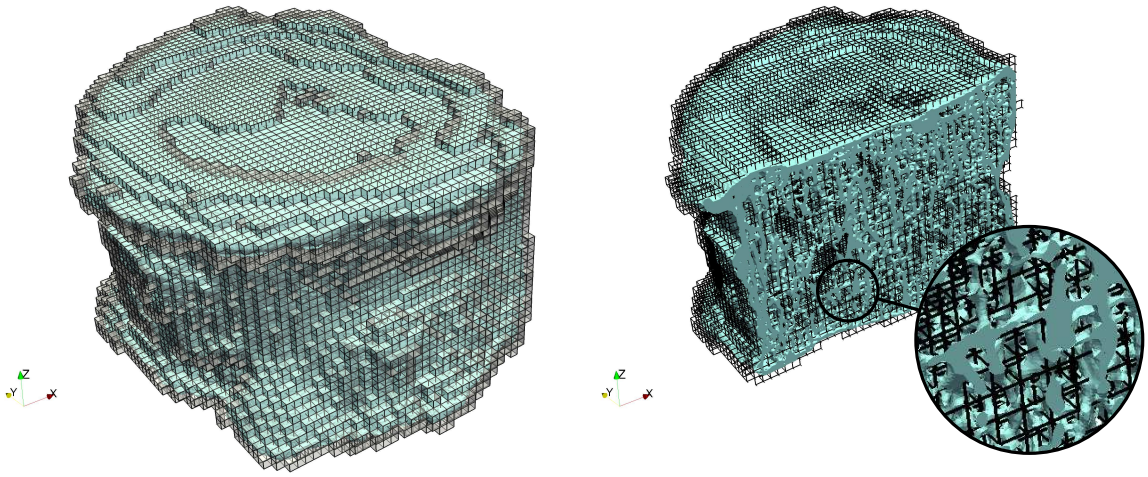

(a) $\mu$-FCM mesh (b) Section view

Figure 4.6: FCM discretization of specimen #1

Here, we elaborate on the suitability of the chosen parametrization of the $\mu$-FCM meshes. The finite cell sizes ($910\mu$m for specimens #1-3 and $840\mu$m for specimen #4) were chosen such that they resolve the trabecular structure, defined by a length parameter equal to the sum of the trabecular thickness (Tb.Th) and trabecular spacing (Tb.Sp). In other words, the meshes are fine enough such that a single finite cell does not contain several trabeculae. This can be observed in the detailed view of the mesh for specimen #1, shown in Figure 4.6b. With a moderately low polynomial degree, a parametrization with several trabeculae per finite cell would induce nonphysical coupling between the separate trabeculae, as shown e.g. by Coradello et al. [44] in the context of shell analysis using the FCM. This would significantly overestimate the stiffness of the trabecular structure. Another example of such artificial stiffness induced in finite cell models by the mismatch

between the polynomial order and the spatial resolution of the material description was observed in the context of topology optimization [90]. This is avoided here through an appropriate choice of the finite cell size.

Unlike common practice in $\mu$-FEM analysis of trabecular specimens, we made no special considerations to ensure that the trabecular structures were well-connected or exclude non-connected regions to avoid singular stiffness matrices. This was not necessary for our study, since the $\mu$-FCM models enclosed the whole vertebral bodies.

For the numerical integration we utilized grids of sub-cells which match the voxel grids of the $\mu$-CT images. Here, the resolution of the $\mu$-CT scans allows to geometrically resolve the trabecular structure. Hence, the material properties were assigned voxel-wise. A threshold value for each scan was selected manually by inspection of the images and the intensity histograms. Voxels with intensity above the threshold were assigned material properties of the bone tissue with Young's modulus $E = 17$ GPa and $\nu = 0.3$ [245]. Note that we do not use different material parameters for the cortical shell. The higher (macroscopic) stiffness in this part results from the higher local density, i.e. the larger number of filled voxel per unit volume compared to the spongy trabecular region. Voxels that were outside of the segmentation, or with an intensity below the threshold were assigned a fictitious material, with $E_{\text{fict}} = 1 \times 10^{-7}$ GPa and $\nu_{\text{fict}} = 0.3$.

Since all elements of the $\mu$-FCM mesh are of identical shape and size, differing only in the material parameters of linear elasticity defined for each voxel, it is possible to significantly improve the computational performance by means of a pre-integration [268].

### Boundary conditions

In the current work, the boundary conditions are defined to replicate the experimental displacements (estimated using DVC) on the boundary in a similar approach to the work of Costa et al. [45], where we use a trilinear interpolation of the DVC data on the boundary. In contrast to Costa et al., we apply the displacement boundary condition on the whole physical boundary of the vertebral bodies. The Dirichlet boundary conditions were enforced weakly using the penalty method.

The surface meshes used to define the boundary and evaluate the penalty terms were created using the marching cubes (MC) algorithm [154]. To this end, our implementation of MC in `AdhoC++` was used to generate the isosurfaces of the domains defined by the segmentations. An example of the generated surface meshes is presented in Figure 4.7. As the voxel grids of the CT-images were aligned with the $\mu$-FCM grids, the resulting triangles of the reconstructed surfaces did not have additional intersections with the faces of the finite cells—meaning that each triangle lied completely within a single cell, as shown in the detail view in Figure 4.7b. This allows for an accurate evaluation of the surface integrals that can be easily parallelized to improve computational performance.

For the weak enforcement of the boundary conditions, the choice of the penalty value, $\beta_D$, is influenced by the parameters of the finite cell discretization (element size and polynomial degree), as well as the material parameters. In this work, the penalty parameter was chosen empirically as $\beta_D = 1 \times 10^9$.

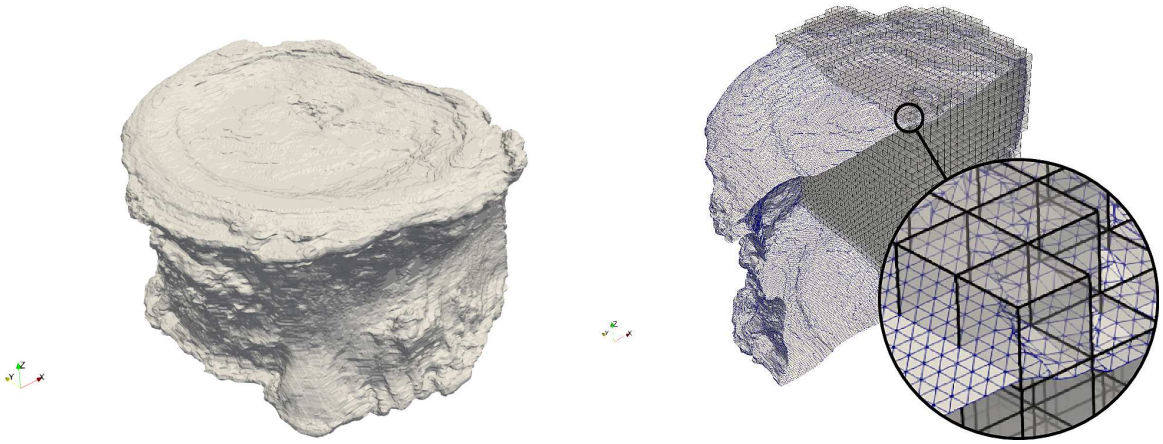

(a) Surface mesh (b) Detail view

Figure 4.7: Surface mesh of specimen #1

### 4.2.4 Comparison and statistics

To validate the $\mu$-FCM models, we compare the numerical approximations of the interior displacement fields to the DVC data from the experiment. The comparison is carried out pointwise at selected nodes of the DVC grid.

We performed a linear regression analysis to assess the correlation between the displacement fields. For each component (in the $x$-, $y$- and $z$-directions), the slope, intercept and coefficient of determination $R^2$ were reported for each specimen. Additionally, we recorded the absolute root mean square error (RMSE), and the relative RMSE, which was normalized w.r.t the absolute maximum value from the DVC measurements for each field component and each specimen.

We carried out the comparison at the nodes of the DVC grid that lie within the physical structure of the $\mu$-FCM models. To identify these nodes, we filtered the nodes where the average value of the image intensity (bone density) in their close proximity is above a certain threshold. Similar to the approach presented by Costa et al. [45], we excluded the nodes of the DVC grid that are too close to the boundary, as the displacement fields described by these nodes were used to define the boundary conditions of the $\mu$-FCM models. In our study, we interpolated the DVC data at the geometric boundaries to impose the Dirichlet boundary conditions. Hence, we needed to filter out the nodes that lie in the proximity of the boundaries from the comparison to remove their influence on the linear regression analysis. In this work, this filtering was carried out by utilizing a scaling (affine transformation) of the geometries of the vertebrae. Nodes that were outside of the 80% scaled geometries of the domains defined by the segmentations were excluded from the comparison.

To mitigate the influence of outliers on the results of the regression analysis, we excluded points with Cook's distance [43] higher than five times its mean value for each component of the displacement field of each specimen. This filtering process finally left 734, 919, 663 and 754 comparison nodes of the DVC grids of the four specimens.

## 4.3 Results

The simulations based on the $\mu$-FCM models were performed using our in-house software framework `AdhoC++`. To solve the resulting systems of linear equations we applied the parallel direct solver `Intel® Pardiso` which is provided as part of the Intel Math Kernel Library [114]. All simulations were run on two eight-core Intel® Xeon® E5-2690 @ 2.9 GHz CPUs, and a maximum memory of 192 GB. Run-time for the largest model was approximately 40 minutes.
Surface triangulations of the trabecular microstructure were reconstructed for sagittal sections making use of the `IsoVolume` filter in the visualization package `ParaView` [10]. The DVC results were interpolated, and projected onto the recovered surface of the segmentation. The numerically approximated displacement fields are shown in Figure 4.8.
At the boundaries of the vertebral bodies, it can be clearly seen by inspection of the contour plots that the displacements of the $\mu$-FCM models closely match the interpolated values of the DVC measurements. This indicates the effectiveness of the proposed approach for the enforcement of the boundary conditions. Within the interior regions , it can be observed that the predicted displacement fields of the $\mu$-FCM models exhibit very similar patterns to the interpolated DVC data. The absolute values of the displacements are largest for the $z$-component, which corresponds to the axial direction, where the compression was applied. The displacement fields have smaller components in the transverse directions—mostly sub-voxel magnitude. The results of the linear regression analysis are presented in Table 4.2, and the scatter diagrams comparing the predicted displacements and the DVC data are shown in Figure 4.9.

Table 4.2: Results of linear regression analysis

| **Spec. #** | **Component** | **Number of points (%)** | **Slope** | **Intercept [$\mu$m]** | $R^2$ | **RMSE [$\mu$m]** | **RMSE %** |
|---|---|---|---|---|---|---|---|
| 1 | $u_x$ | 714 (97.3%) | 0.99 | -1.44 | 0.93 | 7.07 | 7.54 |
| | $u_y$ | 710 (96.7%) | 0.97 | -5.61 | 0.91 | 10.2 | 4.63 |
| | $u_z$ | 703 (95.7%) | 0.99 | -3.02 | 0.97 | 16.4 | 3.79 |
| 2 | $u_x$ | 900 (97.9%) | 1.07 | -0.01 | 0.93 | 3.06 | 5.16 |
| | $u_y$ | 900 (97.9%) | 1.09 | 1.02 | 0.96 | 3.48 | 7.37 |
| | $u_z$ | 889 (96.7%) | 1.14 | -0.61 | 0.96 | 4.17 | 4.65 |
| 3 | $u_x$ | 641 (96.7%) | 0.91 | -2.22 | 0.86 | 2.32 | 8.59 |
| | $u_y$ | 658 (99.2%) | 1.09 | 1.03 | 0.93 | 3.24 | 9.72 |
| | $u_z$ | 638 (96.2%) | 1.14 | -1.83 | 0.96 | 3.37 | 5.49 |
| 4 | $u_x$ | 714 (94.7%) | 1.00 | 0.04 | 0.86 | 3.19 | 8.81 |
| | $u_y$ | 734 (97.3%) | 1.13 | 0.19 | 0.73 | 4.92 | 13.7 |
| | $u_z$ | 725 (96.2%) | 1.13 | -1.78 | 0.94 | 4.42 | 4.26 |

The filtering according to the Cook's distance criterion eliminated 0.8% - 5.3% of the DVC grid nodes. Excluding the outliers, the regression analysis shows that all components of

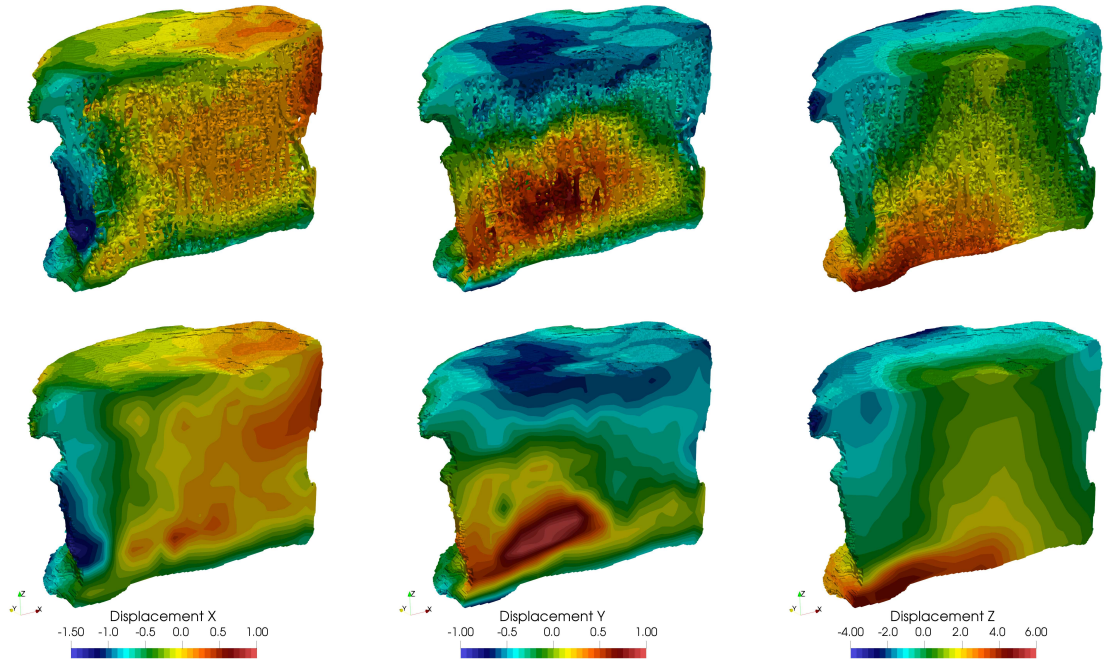


(a) Specimen 1

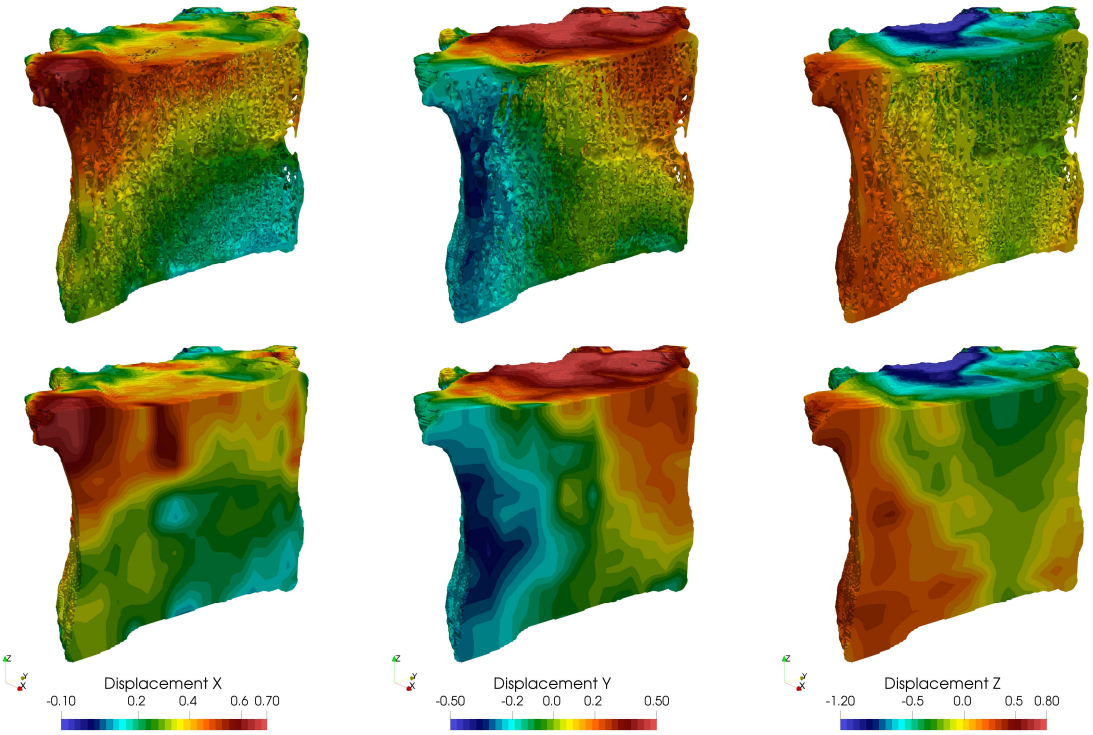


(b) Specimen 2

Figure 4.8: Comparison of numerical approximation of displacements using $\mu$-FCM (top row) and the DVC data (bottom row), units are voxel-size.

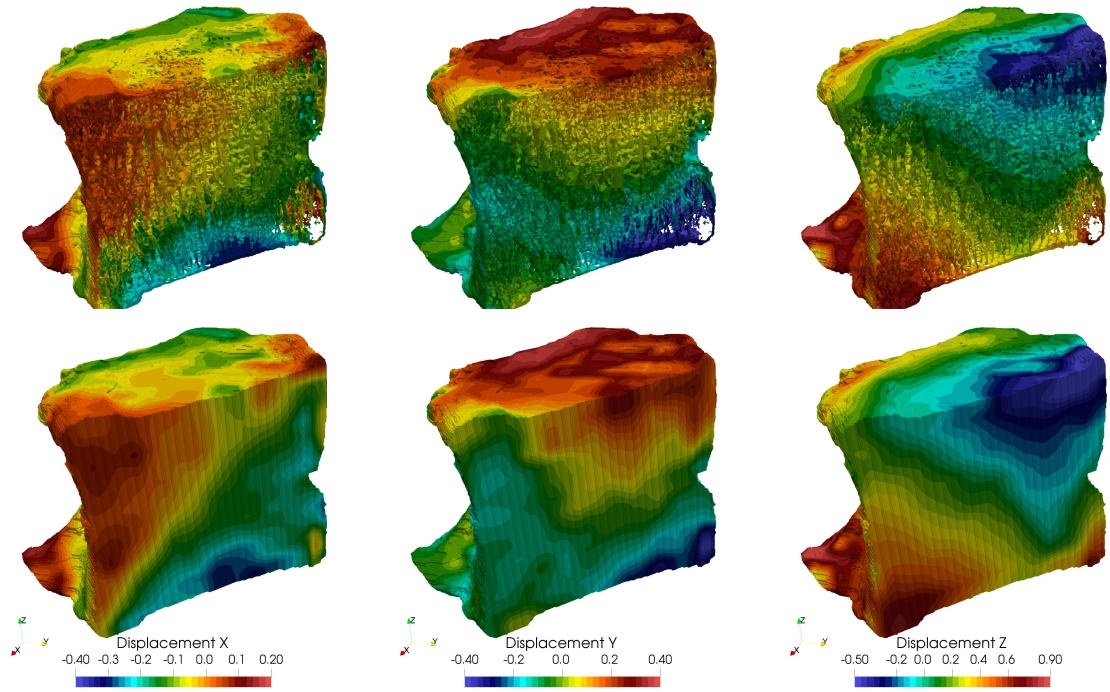


(c) Specimen 3

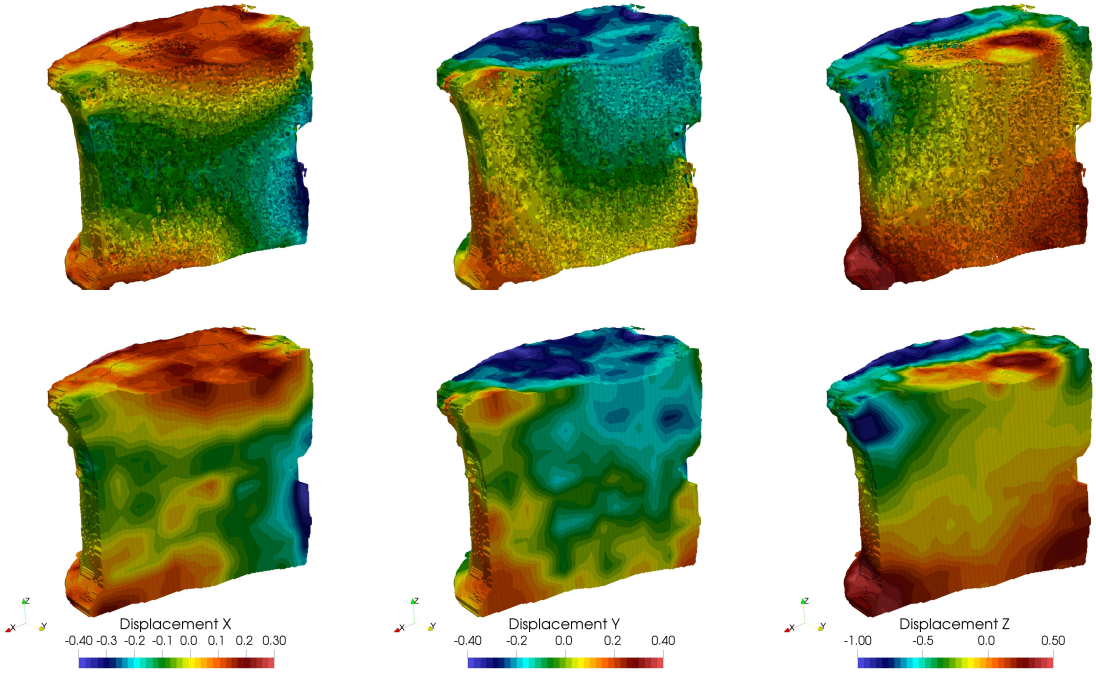


(d) Specimen 4

Figure 4.8: Comparison of numerical approximation of displacements using $\mu$-FCM (top row) and the DVC data (bottom row), units are voxel-size – (continued)

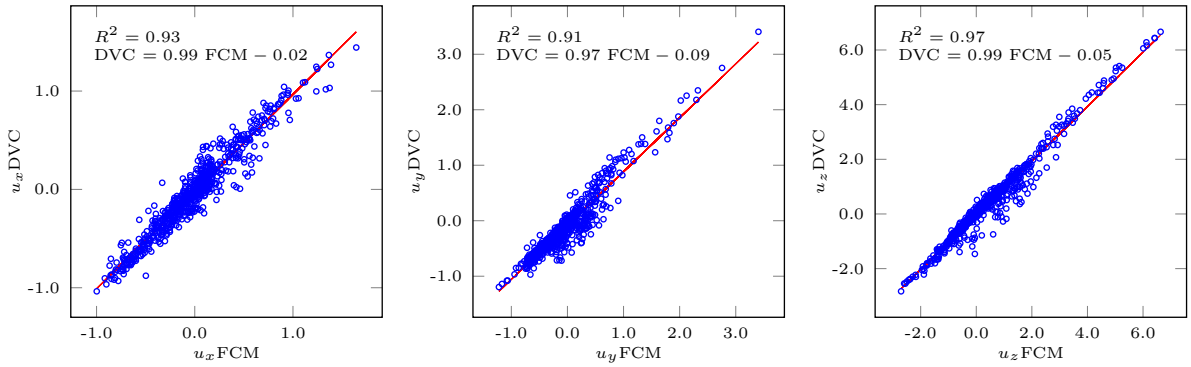


(a) Specimen 1

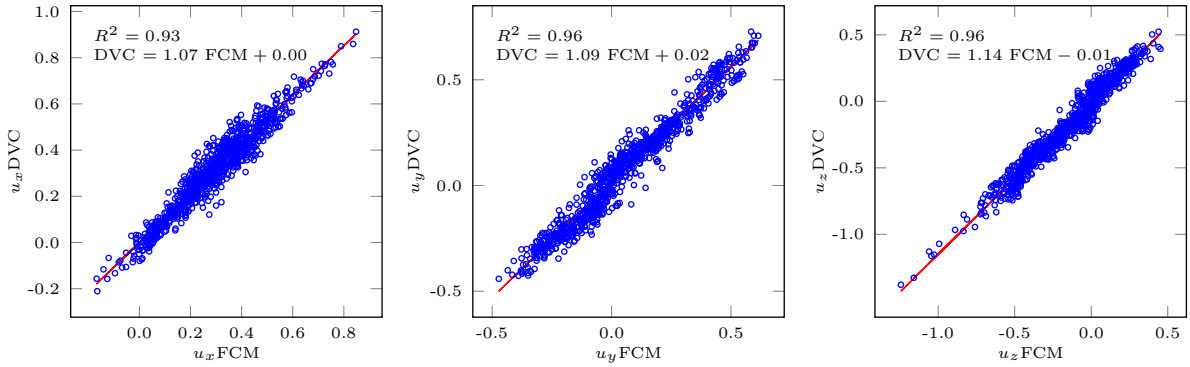


(b) Specimen 2

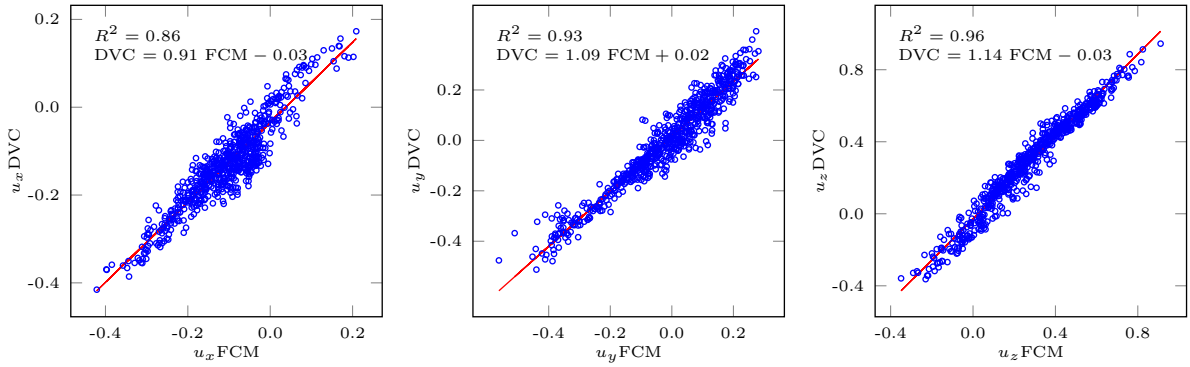


(c) Specimen 3

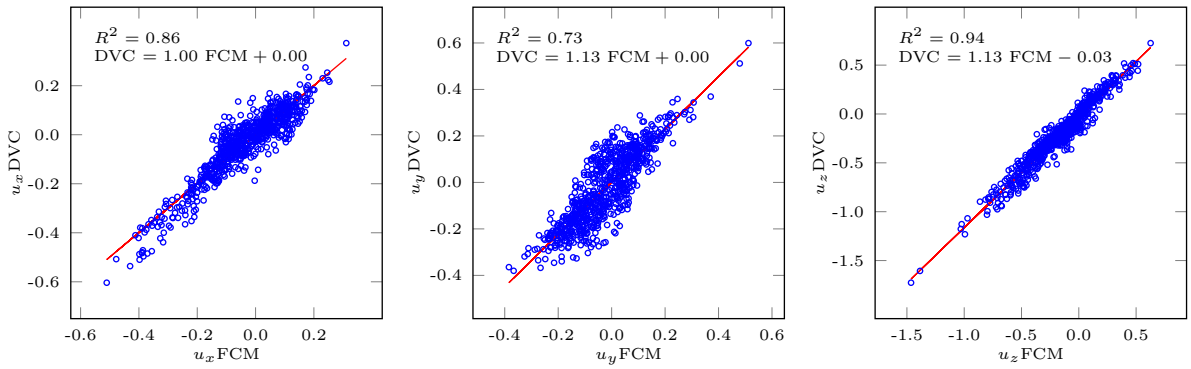


(d) Specimen 4

Figure 4.9: Linear regression analysis for displacement fields, units are voxel-size

the displacement fields predicted by the $\mu$-FCM models were highly correlated and in very good agreement with the values estimated by DVC for all specimens, with coefficients of determination $0.73 < R^2 < 0.97$. The slopes of the linear regression ranged between 0.91 and 1.14. Most analyses (except for specimen #1) had a slope slightly above 1.0. The absolute values for the intercepts are small relative to the displacements (maximum 5.61 $\mu$m).
It is observed that the relative root mean square error (RMSE) in the $z$-component (axial) of the displacement ($3.79 - 5.49\%$) is lower than the relative RMSE for the transverse ($x$- and $y$-components) for all of the tested specimens. The reported values for the relative RMSE are below 10% for all displacement components of specimens #1–3. However, for the $y$-component of specimen #4 a relative RMSE of 13.7% is reported. For this specific case, it can be seen that the absolute values of the displacements are the lowest among all displacement components of all of the tested specimens. Yet the error is an order of magnitude smaller than the resolution of the micro-CT scan.

## 4.4 Discussion

The results of the validation study show a very good agreement between the displacement fields predicted by the $\mu$-FCM models and the experimental DVC measurements. The combination of the penalty method for the weak imposition of essential boundary conditions with the trilinear interpolation of the DVC measurements has been shown to be a simple yet effective approach for replicating the experimental boundary conditions for the $\mu$-FCM analyses.
A high correlation was observed in the regression analyses of all displacement field components of all four specimens. For the majority of the linear regression analyses, a slope with value slightly larger than 1.0 was reported. This suggests that the $\mu$-FCM models overestimate the stiffness of the trabecular structure to some extent. Further refinement of the $\mu$-FCM models by using a higher polynomial order ($p$-refinement) or decreasing the finite cell size ($h$-refinement) would improve the accuracy of the numerical approximation of the displacements.
The relative RMSE reported by the linear regression analysis for all components of the displacement field was below 10% for all of the examined specimens, with the exception of the $y$-component for specimen #4, which had relative RMSE of 13.7%. It can also be observed in Figure 4.8d that the estimated DVC displacement field for the $y$-component (middle column) exhibits some nonphysical oscillations. This component of specimen #4 also has the weakest correlation ($R^2 = 0.73$) between the numerical predictions and the DVC data for all of the examined specimens. For this specific case, it was observed that the absolute values of the displacements are the lowest from all components of all tested specimens. Hence, it is more difficult for the DVC algorithm to estimate the displacement field, where the displacements are a small fraction of the voxel size (the resolution of the micro-CT images). Similar observations were reported by Oliviero et al. [183] for a validation study of micro-CT based $\mu$-FEM models of mouse tibia using DVC. Larger displacements would be easier to detect, but require higher compression loads, which increases the risk of fracturing the specimens during the validation experiment.

By contrast, the relative RMSE reported for the $z$-components, which corresponds to the axial loading direction, were lower than the transverse directions for all four specimens. The axial components of the displacement fields had the highest absolute values, and hence, are more easily identified by the DVC algorithm.

In comparison, the results of the $\mu$-FEM validation study reported in the work of Costa et al. [45] show even better agreement between the DVC measurements and the numerical predictions of the $\mu$-FEM models, with $0.89 < R^2 < 0.99$ and maximum relative RMSE of 5.20%. Here, we highlight some differences between the two studies that we believe explain this better accordance. Firstly, Costa et al. used micro-CT images with higher resolution (38.6–39 $\mu$m compared to our images with 60–65 $\mu$m). Secondly, their study used specimens of porcine vertebrae, which have higher strength. Hence, they were able to apply higher compression loads on the vertebral bodies (up to 308 kg). The resulting displacements in the axial direction were as high as 420 $\mu$m, approximately 11 times the voxel size. In comparison, in our study we were limited to 180 kg compression load to avoid fractures in the human specimens, and the largest displacements in the axial direction were around 360 $\mu$m, or 6 times the voxel resolution. Therefore, in our study the displacement fields due to the compression load were more difficult to detect by the DVC algorithm. Additionally Costa et al. excluded the vertebral endplates, omitting the regions with the most complex loading conditions. Compared to our approach, this results in more uniform, but less physiological loading patterns, making their results less transferable to in-vivo conditions. Moreover, Costa et al. used very high resolution $\mu$-FEM models with up to 962 million degrees of freedom which deliver extremely accurate results, whereas our $\mu$-FCM models were limited to a moderate polynomial degree $p = 3$, giving accurate models with a moderate computational cost—the $\mu$-FCM models had approximately 1.3 million degrees of freedom, and required significantly less computational resources.

There are, however, a few limitations of our study. Firstly, the sample size of the vertebral specimens which we examined is small ($n = 4$). The detailed analysis required for the validation study makes a large sample size not feasible. Considering the solution of the numerical models, the main limitation was imposed by the use of a direct solver for the linear systems of equations. Direct solvers have large memory requirements, which limited our models to a moderately low polynomial order. In the study, we only used a linear elastic, isotropic material model for the bone material. However, this was effective in showing the applicability of the FCM for micro-CT-based analysis. More involved material models are also applicable in the framework of the FCM.

The current validation study only examined the predictions of the displacement field. Validation of the strains is more challenging, firstly from the experimental side, as the registration algorithms require coarser grids to have enough physical features to identify the displacements, which in turn limits their applicability for the pointwise validation of strain fields. A qualitative comparison presented by Costa et al. [45] shows that strains predicted by high resolution $\mu$-FEM models exhibit similar patterns to the DVC estimations, albeit with much higher spatial resolution. Quantitative validation of numerically predicted strain fields using QCT-based continuum-level FE models and DVC measurements also show lower accordance in comparison to the validation of the displacements [145, 147, 146]. Secondly, to provide numerically accurate predictions of the strain fields on a microstructural level, the $\mu$-FCM models need to be further refined.

To study the effect of further refinement on the accuracy of the predictions—by either increasing the polynomial order ($p$-refinement) or reducing the size of the finite cells ($h$-refinement)—the use of an iterative solver is necessary. To this end, an Additive-Schwarz type pre-conditioner has been shown to be an effective approach for $\mu$-FCM analysis, which can enable the solution of larger systems with moderate memory requirements [117]. For a more accurate estimation of the displacement field resulting from the compression load using DVC, a B-Spline registration can be employed, which is able to describe the deformation with higher accuracy than the affine registration used in this work [206].
To summarize, in this work, we have presented a new validation study for the micro-CT based finite cell method ($\mu$-FCM). We have shown that the $\mu$-FCM provides accurate predictions of the displacements when the boundary conditions of the experiment are replicated from the DVC measurements. Our results corroborate the findings of Chen et al. [32] and Costa et al. [45] despite using different finite element approaches. In conclusion, the results presented in this study illustrate the potential of the $\mu$-FCM as an attractive alternative simulation approach that provides accurate results for a moderate computational effort, and flexibility in dealing with complex geometry.

# Chapter 5

# The finite cell method for material interface problems *

In this chapter, a numerical discretization technique for solving three-dimensional material interface problems involving complex geometry without conforming mesh generation is presented. The finite cell method (FCM) is used for the numerical approximation of the solution without a boundary-conforming mesh. Weak discontinuities at material interfaces are resolved by using separate FCM meshes for each material sub-domain, and weakly enforcing the interface conditions between the different meshes. Additionally, a recently developed hierarchical *hp*-refinement scheme is employed to locally refine the FCM meshes in order to resolve singularities and local solution features at the interfaces. Thereby, higher convergence rates are achievable for non-smooth problems. A series of numerical experiments with two- and three-dimensional benchmark problems is presented, showing that the proposed *hp*-refinement scheme in conjunction with the weak enforcement of the interface conditions leads to a significant improvement of the convergence rates, even in the presence of singularities.

## 5.1 Introduction

In engineering problems, an accurate resolution of domains with discontinuous material properties is often required to ensure a reliable design. Possible applications include the simulation of multi-phase materials, composite structures and biomechanical problems, where different tissues—often in combination with implants—are considered.
Problems of linear elasticity show a reduced regularity at the material interfaces, where the displacement field is in general only $C^0$-continuous. This fits perfectly to the classical finite element method (FEM) using a $C^0$-continuous approximation space [111, 16], as long as the material interface is matched exactly by edges (2D) or faces (3D) of the finite element mesh. However, this requires that the mesh generator is able to follow the material interfaces exactly, which can be cumbersome in cases of complex geometry. Moreover, high curvatures and kinks along the interfaces induce high solution gradients

*The following chapter is based on [75]. The main scientific research as well as the textual elaboration of the publication was performed by the author of this work.

and singularities. This requires local mesh refinement for an accurate solution, which makes the task of mesh generation even more challenging.
To avoid complex mesh generation, embedded or fictitious domain methods have emerged as an alternative to the boundary-conforming FEM. The finite cell method (FCM) is an example of this class of method that combines the immersed boundary approach with high-order basis functions. Thereby, the FCM can be used for mechanical simulations involving very complex geometry without generating a boundary conforming mesh, as explained in Chapter 3. For problems with smooth solutions, the FCM achieves exponential convergence thanks to the underlying high-order approximation.
Unfortunately, the standard FCM loses some of its attractive approximation properties for domains with multiple materials [218, 122]. There are two main challenges facing the FCM for embedded interface problems:

(1) The approximate solution within a finite cell is a polynomial ($C^\infty$-continuous) whereas the exact solution is only $C^0$-continuous. The inability of the smooth polynomials to represent the discontinuity across the material interface yields an oscillatory solution and a reduction of the convergence rate.
(2) The use of a uniform Cartesian grid is not suitable for problems with locally high gradients or singularities, which are expected for material interfaces with complex geometry, as such problems require local mesh refinement.

To handle the first challenge, the numerical approximation needs to be able to reproduce a $C^0$-continuous solution. Several finite element approaches emerged that are suitable to handle weak discontinuities *without* generating an interface-conforming mesh. Two major approaches are the partition of unity enrichment and the weak coupling of non-matching discretizations.
Partition of unity methods (PUM) [169], such as the generalized and extended finite element methods (GFEM, XFEM) [236, 82] enhance the numerical solution by enriching the basis with specially constructed functions to approximate the weakly discontinuous solutions [171, 81]. Recent developments in XFEM and GFEM for material interface problems include the use of adaptive mesh refinement in conjunction with the level-set method [149, 150], and the interface-enriched GFEM [230, 231, 229, 212, 213]. The local enrichment approach was combined with the FCM as presented by Joulaian and Düster for two-dimensional problems [122]. This combination leads to a significant improvement in the convergence rates of the FCM. However, the efficient and robust application of PUM enrichments to complex three-dimensional geometries remains a challenge.
The weak coupling approach allows for non-matching discretizations of the sub-domains, and it enforces the interface conditions in a weak sense. To that end, it is possible to apply the penalty method, Lagrange multipliers or Nitsche's method [179]. Nitsche's method is commonly used to weakly enforce interface conditions, as presented by Hansbo and Hansbo [96], and further developed by Dolbow and Harari [63, 7, 6, 116, 217]. The weak coupling approach has also been applied in the context of the FCM, using Nitsche's method [208, 235], or based on a parameter-free coupling method [138]. There, it has been shown that a weak enforcement of the interface conditions enables the FCM to recovers its favorable convergence properties for piecewise smooth problems.
To address the second challenge, the finite cell mesh needs to be locally refined. Alternative versions of the FCM make use of unstructured meshes, and apply a local mesh

refinement to resolve local solution features [248, 64, 66]. However, these mesh-based refinement approaches sacrifice the uniform grid structure of the FCM, which is particularly useful for image-based geometries that are common in biomechanical applications.

An attractive alternative is the application of the *hp*-version of the FEM for the non-uniform refinement of the underlying FCM meshes. The classical *hp*-FEM [91–93] is a powerful method which uses a combination of *h*- and *p*-refinement to efficiently approximate non-smooth solutions. The main idea is to sub-divide the elements close to the singularities in a recursive manner, in order to achieve a geometrical progression of element size. The resulting mesh has low order elements of small size close to the singularities, and high order elements of larger size further away from the singularities to approximate the smooth solution. While numerically efficient, *hp*-FEM for two- and three-dimensional problems requires to constrain the hanging nodes, which demands for a sophisticated discretization kernel [232, 60].

A simpler variant, which we employ in this work, is the recently introduced multi-level *hp*-version of the FEM [277, 275]. Instead of the classical refine-by-replacement concept, where an element is replaced by a set of smaller elements, the multi-level *hp*-FEM superposes the refined element with a hierarchy of overlay meshes. Using a simple formulation, in which homogeneous Dirichlet boundary conditions are enforced on the overlay meshes, the multi-level *hp*-FEM avoids the need to constrain hanging nodes. Thereby, it offers a simpler implementation for arbitrary hanging nodes, making it readily applicable to three-dimensional problems [276]. The multi-level *hp*-FEM has also been applied to cohesive fracture modeling [279], and to phase-field fracture modeling [176], demonstrating its efficiency for propagating phenomena.

In this chapter, we apply the FCM in conjunction a weak enforcement of interface conditions and the multi-level *hp*-refinement scheme to solve material interface problems. This combination of these numerical techniques enables us to handle complex three-dimensional geometries, without the need for mesh generation. We demonstrate that the multi-level *hp*-scheme is very well-suited for the resolution of geometry induced stress concentrations, and presents a natural compliment to the FCM's strategy to avoid mesh generation.

This chapter is organized as follows: Section 5.2 offers a brief review of the finite cell method for embedded interface problems. In Section 5.3, we outline the multi-level *hp*-refinement scheme, and elaborate on the refinement strategy applied for material interface problems. In Section 5.4, we present a series of numerical experiments of embedded interface problems with geometry-induced stress concentrations. The results demonstrate the improved approximation accuracy of coupled FCM with multi-level *hp*-refinement. The chapter closes with a concluding outlook in Section 5.5.

## 5.2 Embedded interface problems in the FCM

In this section, we present a brief review of the finite cell method for material interface problems, outlining the main concept of the method—including a coupling formulation that allows to weakly impose the interface conditions among sub-domains.

### 5.2.1 Model problem

We consider an open and bounded $d$-dimensional domain, denoted as the physical domain $\Omega_{\text{phy}} \subset \mathbb{R}^d, d \in \{2, 3\}$, with the boundary $\partial\Omega_{\text{phy}} = \Gamma_D \cup \Gamma_N$, and $\Gamma_D \cap \Gamma_N = \emptyset$ [208]. The physical domain $\Omega_{\text{phy}}$ is subdivided into $n$ disjoint, open, and bounded subsets $\Omega^{(k)}$

$$\Omega_{\text{phy}} = \bigcup_{k=1}^{n} \Omega^{(k)}, \quad \Omega^{(i)} \cap \Omega^{(j)} = \emptyset \text{ for } i \neq j. \tag{5.1}$$

The sub-domains $\Omega^{(k)}$ are separated by internal boundaries $\Gamma_{ij}$, denoting the material interfaces between $\Omega^{(i)}$ and $\Omega^{(j)}$. The model is governed by the partial differential equations of linear elastostatics, given in the strong form of the boundary value problem by:

$$\nabla \cdot \boldsymbol{\sigma}^{(i)} + \boldsymbol{b}^{(i)} = \boldsymbol{0} \qquad \forall \boldsymbol{x} \in \Omega^{(i)}, \quad i = 1, \dots, n \tag{5.2a}$$

$$\boldsymbol{\sigma}^{(i)} = \mathbb{C}^{(i)} : \boldsymbol{\varepsilon}(\boldsymbol{u}^{(i)}) \qquad \forall \boldsymbol{x} \in \Omega^{(i)}, \quad i = 1, \dots, n \tag{5.2b}$$

$$\boldsymbol{\varepsilon}(\boldsymbol{u}^{(i)}) = \frac{1}{2}\left(\nabla \boldsymbol{u}^{(i)} + \nabla \boldsymbol{u}^{(i)^\top}\right) \qquad \forall \boldsymbol{x} \in \Omega^{(i)}, \quad i = 1, \dots, n, \tag{5.2c}$$

where $\boldsymbol{\sigma}^{(i)}$ is the stress tensor, $\boldsymbol{b}^{(i)}$ is the body load, $\mathbb{C}^{(i)}$ is the elastic material tensor, $\boldsymbol{\varepsilon}$ is the strain tensor, and $\boldsymbol{u}^{(i)}$ is the displacement vector of the sub-domain $\Omega^{(i)}$. The system is subject to the boundary conditions:

$$\boldsymbol{u}^{(i)} = \hat{\boldsymbol{u}}^{(i)} \qquad \forall \boldsymbol{x} \in \Gamma_D^{(i)}, \quad i = 1, \dots, n \tag{5.3a}$$

$$\boldsymbol{\sigma}^{(i)} \cdot \boldsymbol{n}^{(i)} = \hat{\boldsymbol{t}}^{(i)} \qquad \forall \boldsymbol{x} \in \Gamma_N^{(i)}, \quad i = 1, \dots, n, \tag{5.3b}$$

where $\hat{\boldsymbol{u}}^{(i)}$ are the prescribed displacements on the Dirichlet boundary, $\hat{\boldsymbol{t}}^{(i)}$ are the prescribed tractions on the Neumann boundary, and $\boldsymbol{n}^{(i)}$ denotes the outward facing normal vector on the sub-domain's boundary $\partial\Omega^{(i)}$ (see Figure 5.1), and

$$\Gamma_D^{(i)} = \Gamma_D \cap \partial\Omega^{(i)} \tag{5.4a}$$

$$\Gamma_N^{(i)} = \Gamma_N \cap \partial\Omega^{(i)}. \tag{5.4b}$$

Additionally, the following interface conditions apply along $\Gamma_{ij}$:

$$\boldsymbol{u}^{(i)} = \boldsymbol{u}^{(j)} \qquad \forall \boldsymbol{x} \in \Gamma_{ij}, \tag{5.5a}$$

$$\boldsymbol{\sigma}^{(i)} \cdot \boldsymbol{n}^{(i)} = -\boldsymbol{\sigma}^{(j)} \cdot \boldsymbol{n}^{(j)} \qquad \forall \boldsymbol{x} \in \Gamma_{ij}. \tag{5.5b}$$

The first interface condition ensures the kinematic compatibility between the sub-domains, whereas the second condition prescribes the equilibrium of normal traction across the interfaces.

### 5.2.2 Weak enforcement of interface conditions

For material interface problems, the standard FCM—where a single mesh is used to discretize the entire extended domain—requires additional means to maintain its attractive approximation properties. The solution exhibits a weak discontinuity across the interface

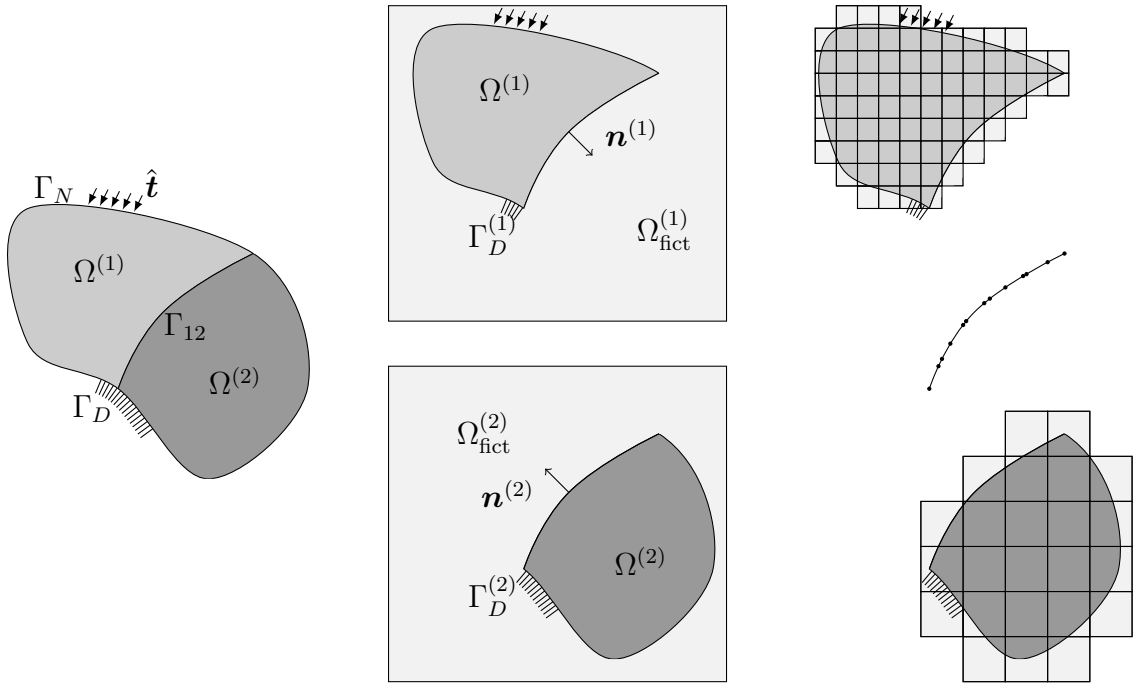


Figure 5.1: Coupling of non-matching FCM meshes, following [208].

(a kink in the displacement field), and this discontinuity cannot be well represented by the high-order polynomial basis functions used in the FCM. This leads to an oscillatory solution in the cells cut by the material interface, and the convergence is reduced to a slow algebraic rate.
To overcome this challenge, we use a separate FCM mesh for each extended sub-domain:

$$\hat{\Omega}^{(i)} = \Omega^{(i)} \cup \Omega^{(i)}_{\text{fict}}, \tag{5.6}$$

and couple the FCM meshes to weakly impose the interface conditions, as presented in [208]. Figure 5.1 illustrates this approach for two sub-domains. The use of a separate set of basis functions for each sub-domain allows the discretization to approximate the strain fields with different gradients on each sub-domain. Additionally, the coupling of the FCM meshes recovers the weak discontinuity (jump in the strain field). Thereby, the FCM is able to recover its exponential convergence rates for piecewise-smooth problems [208, 138]. Moreover, this makes it possible to use discretizations with different resolutions in each sub-domain, which allows for a higher numerical efficiency. However, this multiple-mesh approach requires an additional discretization of the material interfaces $\Gamma_{ij}$ for the integration of the coupling terms along the interfaces. Fortunately, the discretization of the interface for integration is considerably less demanding than FEM mesh-generation for multiple sub-domains.
Several methods can be applied for the weak coupling of the non-matching discretizations. A commonly used approach, which has also been applied in the context of the FCM, is the application of Nitsche's method [208]. It is variationally consistent, but requires the estimation of additional stabilization parameters. In the present work, we use a pure

penalty approach for the coupling of FCM meshes, and for the weak enforcement of Dirichlet boundary conditions. The penalty method is inconsistent, and the accuracy depends on the choice of the penalty parameters. However, it is easy to implement—and it delivers sufficiently accurate solutions (for engineering purposes), as demonstrated by the numerical experiments presented in Section 5.4.
Finally, the weak form of the coupled FCM problem reads:

Find $\boldsymbol{u}^{(i)} \in \mathcal{S}(\hat{\Omega}^{(i)}), \quad i = 1, \dots, n$ such that:

$$\hat{\mathcal{B}}(\boldsymbol{u}, \boldsymbol{v}) = \hat{\mathcal{F}}(\boldsymbol{v}) \qquad \forall \boldsymbol{v}^{(i)} \in \mathcal{V}(\hat{\Omega}^{(i)}) \tag{5.7}$$

with:

$$\begin{aligned}
\hat{\mathcal{B}}(\boldsymbol{u}, \boldsymbol{v}) &= \sum_i \int_{\hat{\Omega}^{(i)}} \boldsymbol{\varepsilon}(\boldsymbol{v}^{(i)}) : \alpha^{(i)}(\boldsymbol{x})\ \mathbb{C}^{(i)} : \boldsymbol{\varepsilon}(\boldsymbol{u}^{(i)})\, \mathrm{d}\Omega \\
&\quad + \sum_{\substack{ij \\ i<j}} \beta_{ij} \int_{\Gamma_{ij}} [\![\boldsymbol{v}]\!]_{ij} \cdot [\![\boldsymbol{u}]\!]_{ij}\, \mathrm{d}\Gamma + \sum_i \beta_D^{(i)} \int_{\Gamma_D^{(i)}} \boldsymbol{v}^{(i)} \cdot \boldsymbol{u}^{(i)}\, \mathrm{d}\Gamma \qquad (5.8a) \\
\hat{\mathcal{F}}(\boldsymbol{v}) &= \sum_i \int_{\hat{\Omega}^{(i)}} \boldsymbol{v}^{(i)} \cdot \alpha^{(i)}\ \boldsymbol{b}^{(i)}(\boldsymbol{x})\, \mathrm{d}\Omega + \sum_i \int_{\Gamma_N^{(i)}} \boldsymbol{v}^{(i)} \cdot \hat{\boldsymbol{t}}^{(i)}\, \mathrm{d}\Gamma \\
&\quad + \sum_i \beta_D^{(i)} \int_{\Gamma_D^{(i)}} \boldsymbol{v}^{(i)} \cdot \hat{\boldsymbol{u}}^{(i)}\, \mathrm{d}\Gamma \qquad (5.8b)
\end{aligned}$$

where $\boldsymbol{v}^{(i)}$ are the test functions in the space of admissible functions $\mathcal{V}(\hat{\Omega}^{(i)})$, and

$$\alpha^{(i)}(\boldsymbol{x}) = \begin{cases} 1 & \forall \boldsymbol{x} \in \Omega^{(i)} \\ \epsilon^{(i)} \ll 1 & \forall \boldsymbol{x} \in \Omega^{(i)}_{\text{fict}}. \end{cases} \tag{5.9}$$

The two penalty parameters, $\beta_{ij}$ and $\beta_D$ control the weak enforcement of the kinematic compatibility condition across $\Gamma_{ij}$ and of the Dirichlet boundary condition, respectively. Here, $[\![\boldsymbol{u}]\!]_{ij}$ denotes the jump operator

$$[\![\boldsymbol{u}]\!]_{ij} = \boldsymbol{u}^{(i)} - \boldsymbol{u}^{(j)}. \tag{5.10}$$

The choice of the penalty parameters influences the accuracy of the numerical solution. Values that are too small lead to a large error in the imposed conditions (observed in the levelling-off of the convergence curves), whereas values that are too large yield an ill-conditioned system of equations [12, 254, 8]. In the numerical examples that follow in this paper, the penalty parameters are chosen heuristically, starting with an initial value of $E \cdot 10^3$, where $E$ is the Young's modulus of the stiffest material. In case the resulting error in the imposed condition is too large, the penalty value is increased stepwise by one order of magnitude.

## 5.3 Multi-level *hp*-refinement

For problems with local solution characteristics such as stress concentration and singularities, *hp*-refinement is a powerful method of discretization, as it is more efficient than uniform *h*- or *p*-refinement [91–93]. Smaller elements with low polynomial degree close to the singularities are able to capture the local solution and confine the discretization error, whereas large elements with high polynomial degree are best suited to describe the smooth solution further away from singularities.
However, the Cartesian grid nature of the FCM discretization does not easily incorporate local mesh refinement without having to introduce hanging nodes. In this work, we apply the multi-level *hp*-refinement scheme to locally refine FCM grids, without the difficulties of constraining hanging nodes. Thereby, the method is able to achieve higher convergence rates, while retaining the advantages of using Cartesian finite cell grids. This section provides a brief review of the multi-level *hp*-FEM and elaborates on the refinement strategy used for material-interface problems.

### 5.3.1 Basic refinement concept

The principal idea of the multi-level *hp*-FEM is to enhance the local approximation of the solution through a local superposition of coarse base elements in the refinement zones with finer overlay elements. The final approximation $\boldsymbol{u}$ is the sum of the base mesh solution $\boldsymbol{u}_b$ and the fine-scale overlay solution $\boldsymbol{u}_o$. This *refine-by-superposition* approach is related to the pioneering work of Mote [174]. This concept was applied in the context of *hp*-domain decomposition, to overlay coarse *p*-FEM meshes with fine linear *h*-elements [198], and in the hierarchic *hp-d*-scheme, which adds several layers of *linear* overlay meshes [215].
The multi-level *hp*-scheme generalizes the hierarchic overlay idea of the *hp-d* scheme by introducing high-order overlay meshes. Here, the support of the high-order basis functions is chosen on the finer overlay meshes—instead of the base discretization, as illustrated in Figure 5.2. This corresponds to an *h*-refinement of the high-order basis functions, as the size of their support is reduced. This limited support—combined with an adequate geometric grading—has the desirable effect of confining the (global) pollution error in the smallest elements around the singularities. This is not the case for the linear overlay approach presented in [198] and the hierarchic *hp-d* linear overlays [215], as the error propagates in the large base elements of the base mesh [277]. Consequently, the multi-level *hp*-FEM leads to superior convergence rates for problems with singularities and sharp features. Numerical experiments demonstrate that the multi-level *hp*-FEM converges exponentially, for problems including vertex and edge singularities in two and three dimensions [277, 276, 279].
The multi-level *hp*-FEM avoids the implementational burden of constraining hanging nodes. A simple implementation is possible, wherein two requirements are satisfied to ensure convergence: *compatibility* of the discretization, and *linear independence* of the basis functions. The overlay meshes, generated by recursive sub-divisions of the base mesh, are geometrically incompatible. To guarantee compatibility of the discretization, homogeneous Dirichlet boundary conditions are prescribed on the boundary of each layer of overlay meshes. This maintains a $C^0$-continuous approximation by construction. To

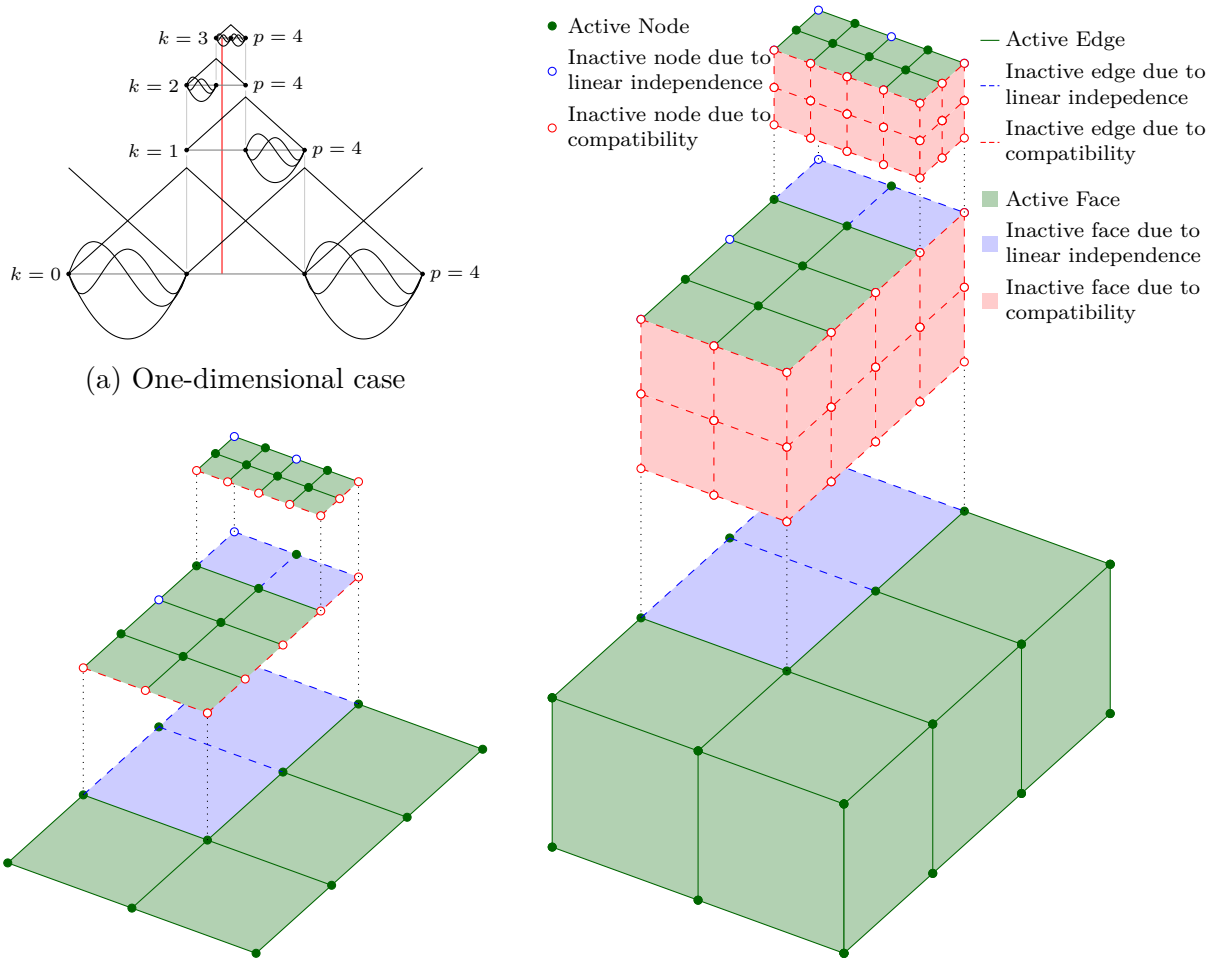


(a) One-dimensional case

(b) Two-dimensional case

(c) Three-dimensional case

Figure 5.2: Conceptual idea of the multi-level *hp*-method [276].

ensure linear independence of the basis functions, the high-order shape functions on overlay elements are excluded from their respective parent elements, as demonstrated in Figure 5.2. The fulfillment of these requirements leads to a simple yet powerful discretization technique, that exploits the benefits of the *hp*-FEM without the burden of constraining hanging nodes. Additionally, using a suitable data structure in an object-oriented framework allows for a dynamic update of the overlay meshes without introducing a noticeable computational cost [276]. For an in-depth discussion of the multi-level *hp*-FEM for two- and three-dimensional problems, with elaboration of their implementational aspects, the interested reader is referred to [277, 276, 275]

### 5.3.2 Refinement strategy

In general, stress concentration and sharp solution features can be caused either by sudden changes in the boundary conditions, the applied body load, or sharp geometric features—such as re-entrant corners. In this work, we mainly consider stress concentrations induced

by sharp geometric features of the material interfaces. To resolve such features, an *a priori* refinement scheme is applied. Here, the design of the discretization is guided by existing knowledge of the solution features, based on engineering experience.

### $h$-refinement

Typically, *hp*-mesh design includes a geometric progression of elements towards the singularities, with small linear elements close to the singularities, and increasing element size as well as increasing polynomial orders away from the singularities. In the framework of the multi-level *hp*-FEM, the high-order overlay meshes are generated by recursive bisection of the base mesh. To geometrically grade the mesh towards a point $\boldsymbol{P_x} = (p_x, p_y, p_z)$, for each leaf element $K$, the point is mapped into the index space of the element $\Omega_\square = [-1, 1]^d$ as follows:

$$\boldsymbol{P}_{\boldsymbol{\xi}_K} = \boldsymbol{Q}_K^{-1}(\boldsymbol{P_x}), \tag{5.11}$$

where $\boldsymbol{P}_{\boldsymbol{\xi}_K} = (p_\xi, p_\eta, p_\zeta)$ are the local coordinates of $\boldsymbol{P_x}$ in the index space of the leaf-element $K$, and $\boldsymbol{Q}_K(\boldsymbol{x})$ denotes the geometric mapping between the global and local spaces. The element is sub-divided if the mapped point lies within an extended index space $\hat{\Omega}_\square$, which is larger than $\Omega_\square$

$$\boldsymbol{P}_{\boldsymbol{\xi}_K} \in \hat{\Omega}_\square. \tag{5.12}$$

Typical choices for $\hat{\Omega}_\square$ are between $[-1.25, 1.25]^d$ and $[-2, 2]^d$. Thereby, not only the elements containing $\boldsymbol{P_x}$ are refined, but possibly also the neighboring elements. By carrying out several recursive refinement steps, this approach produces a geometrically graded mesh—with decreasing element size towards the point of interest, as demonstrated in Figure 5.3. For Cartesian grid meshes, which are used in the FCM, this inverse mapping carries a trivial computational cost.

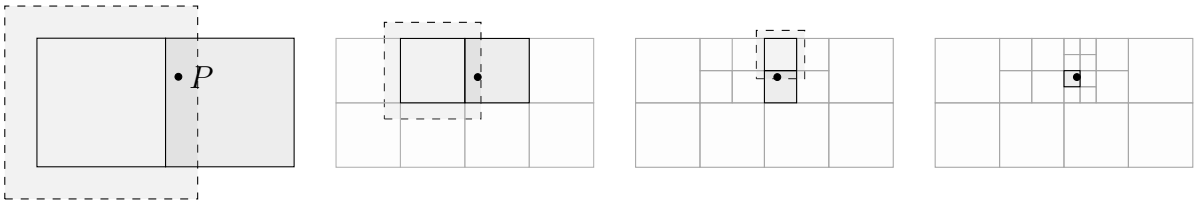


(a) $k = 0$ (b) $k = 1$ (c) $k = 2$ (d) $k = 3$

Figure 5.3: Mesh grading towards $\boldsymbol{P}$ using an extended index space $\hat{\Omega}_\square = [-1.25, 1.25]^2$. An element is refined if $\boldsymbol{P}$ lies within its extended space (drawn with dashed lines).

### $p$-distribution

The distribution of the polynomial degree $p$ across the layers determines the convergence properties of the *hp*-discretization. The optimum $p$-distribution is not known *a priori*.

In one case, the high-order basis functions can be kept on the base mesh, and only linear basis functions are used on the overlay meshes (Figure 5.4a). This case corresponds to the hierarchical *hp-d* scheme [215], as a special case of the multi-level *hp*-scheme. The linear overlay meshes introduce a moderate number of additional unknowns. However, the large support of the high-order basis functions causes the global error to propagate through the domain, yielding a minimal improvement in the convergence rates [277].
On the other end of the spectrum, the high-order basis functions are all shifted to the highest (finest) overlay mesh (Figure 5.4b). Obviously, this uniform multi-level *hp*-approach introduces significantly more unknowns. However, with the limited support of the high-order functions, the discretization error is confined to the smallest elements, which yields superior convergence properties.

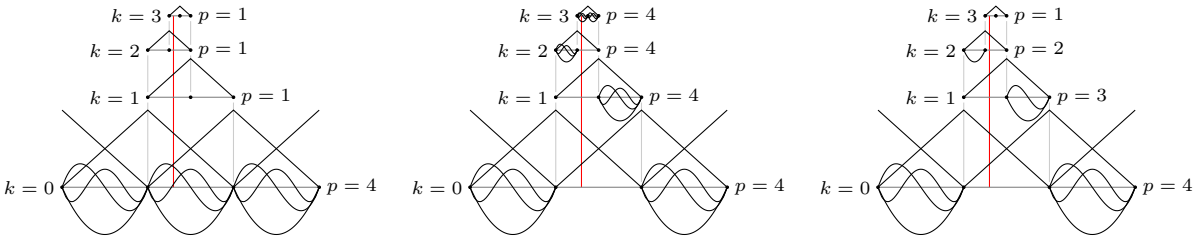


(a) Linear overlay, *hp-d*-approach

(b) Uniform multi-level *hp*-approach

(c) Non-uniform multi-level *hp*-approach

Figure 5.4: Comparison of different approaches for hierarchical, high-order refinement [276].

In this work, we adopt the uniform multi-level *hp*-refinement approach, which is equivalent to uniform *p*-elevation on a geometrically graded mesh. This scheme has been shown to be robust and efficient, although it might not be optimal regarding the approximation error for a number of degrees of freedom. For singular problems, the uniform multi-level *hp*-refinement shows exponential convergence in the pre-asymptotic range, which can be extended by increasing the refinement depth [277, 276]. For boundary conforming problems, an *a posteriori* error estimator for multi-level *hp*-FEM coupled with a smoothness indicator was developed [53], where automatically generated multi-level *hp*-FEM discretizations with non-uniform *p*-distributions further improved the efficiency.

## 5.4 Numerical experiments

In this section, we examine a series of benchmarks involving material interfaces where the geometry induces high solution gradients and singularities. This includes the two-dimensional benchmark of a plate with an elliptical inclusion, where we perform a systematic study of the influence of the numerical integration accuracy on the quality of the approximation. The second benchmark considers a circular plate with a sharp inclusion, where the kink in the material interface introduces a vertex singularity. In three dimensions, we examine the problem of an embedded ellipsoidal inclusion, as well as a singular

benchmark of a cylinder with an embedded cubical inclusion, which causes a vertex-edge singularity. In all examples, we examine the $p$-convergence and the numerical approximation of the first derivatives of the solution. For more details on the benchmarks and the reference solutions, the interested reader is referred to [220].

### 5.4.1 Plate with an elliptical inclusion

#### Problem setup

The first material interface benchmark we study is a plane stress problem of a plate $\Omega^{(1)}$ with an embedded elliptical inclusion $\Omega^{(2)}$, which has a large aspect ratio, $r_y/r_x = 0.15$, and a moderate stiffness ratio to the plate, $E^{(2)}/E^{(1)} = 10$ (see Figure 5.5a). The displacement field within the plate is distorted by the curved inclusion, leading to high stress concentration in the plate. The stress concentration is amplified by the high curvature of the interface at the major axis of the ellipse (points A and C) as shown in Figures 5.5c and 5.5b. The displacement field within the elliptic inclusion remains smooth. The exact solution for the displacements is piecewise-analytic, i.e. it can be *exactly* represented by a Taylor expansion in each sub-domain. An overkill solution was obtained for reference using a conforming $p$-FEM mesh which has 26 elements with a uniform polynomial degree $p = 30$ and 47 102 degrees of freedom. In the conforming mesh, the elements at the interface are blended on the ellipse's exact geometry using a quasi-regional mapping [135]. For the setup shown here, the strain energy obtained using the overkill discretization is

$$\mathcal{U}_{\text{ex}} = 9.10131116644 \times 10^{-2}. \tag{5.13}$$

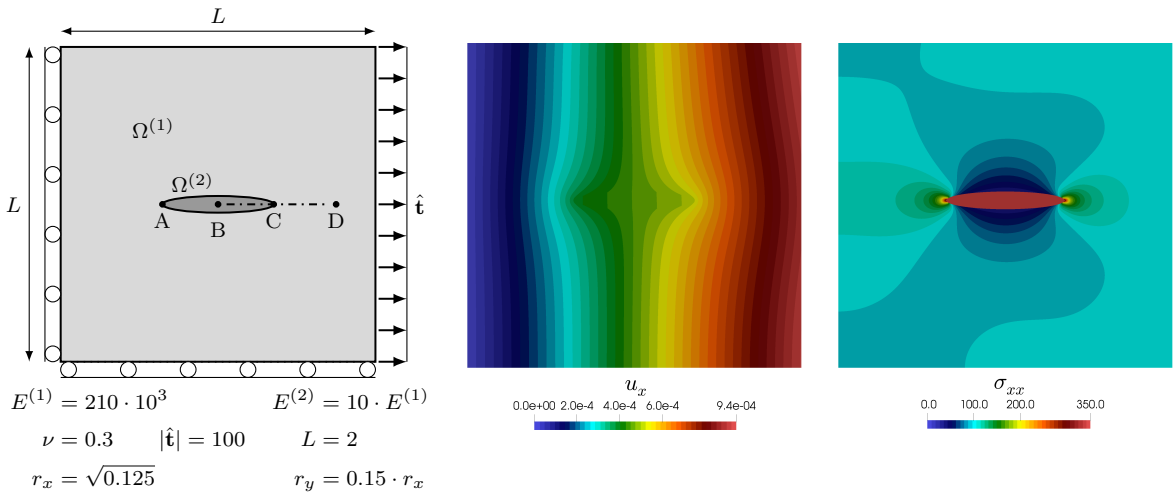


(a) Benchmark setup (b) Reference $u_x$ displacement (c) Reference $\sigma_{xx}$ stress

Figure 5.5: Plate with elliptical inclusion

### Discretization

The problem was solved numerically based on the FCM and a weak enforcement of the interface conditions. Two separate FCM meshes were used to discretize the plate and the inclusion. A base discretization matching the outer boundary of the plate with $4 \times 4$ finite cells was used. The same parametrization was used for the inclusion's mesh, excluding cells that do not intersect the ellipse's domain, leaving $2 \times 2$ finite cells—as shown in Figure 5.6. The ellipse's dimensions and the mesh parameters are setup such that the mesh does not exactly match points A or C for any number of recursive bisection steps. To adequately describe the local solution in the plate, the mesh was locally refined using the uniform multi-level *hp*-refinement scheme. The mesh was refined *a priori*, with a geometrically driven grading towards points A and C, as described in Section 5.3.2. The FCM mesh of the inclusion was left without local refinement, as the solution within the inclusion $\Omega^{(2)}$ is smooth. The use of different mesh resolutions for the two sub-domains is possible thanks to the weak coupling approach, and leads to an improved numerical efficiency, as the refinement stays local to the region of interest. To avoid ill-conditioning of the stiffness matrices, the fictitious domain in both meshes was assigned a low stiffness of $E_{\text{fict}} = E^{(1)} \cdot 10^{-11}, \nu_{\text{fict}} = 0.3$. Since the exterior boundary of the plate's mesh conforms to the true geometry, the Dirichlet and Neumann boundary conditions were enforced in a conventional manner.

For the numerical integration of the finite cells, two possibilities were considered. The first approach employs a recursive sub-division algorithm for integration sub-cells that are intersected by the geometric boundary, resulting in a spacetree—as shown in [219], for example. The second approach considered is the blended partitioning following [143], where the cut cells are automatically partitioned into boundary-conforming quadrilaterals and triangles, which are blended on the exact geometry. It needs to be pointed out that this approach produces geometry-conforming sub-cells to be used for numerical integration. Yet, it cannot be used in general to generate an analysis-suitable FEM mesh, as it does not need to satisfy requirements on shape and regularity at cell edges and faces, e.g. at the transition to the neighboring cells. This approach shares some similarities with the method presented by Fries *et al.* [83, 84, 184]. The integration meshes for both considered approaches are displayed in Figure 5.6.

The penalty method was used to weakly couple the two meshes at the material interface as described in Section 5.2.2. The penalty parameter $\beta_{12} = 10^7$ was chosen empirically. For the numerical integration of the interface coupling terms, a linear discretization of the embedded interface was generated using a marching squares algorithm [160]. The marching squares implementation uses the implicit geometric description of the ellipse and a grid of $n_g \times n_g$ points per sub-cell (leaf element) of the plate's mesh, yielding a total of $n_{\text{seg}}$ linear segments, as can be seen in Figure 5.7a. An advantage of this approach is that the resulting segments do not cross the finite-cell boundaries, resulting in a more accurate evaluation of the interface integral, which the terms of which are only $C^0$-continuous. Additionally, the segments have the same size relative to the leaf element in which they lie. Consequently, the non-uniform resolution of the FCM mesh carries over to the discretization of the interface.

An extension to this approach generates high-order segments using Lagrange interpolation polynomials with degree $p_{\text{seg}}$, by adding $(p_{\text{seg}} - 1)$ interpolation nodes within the linear

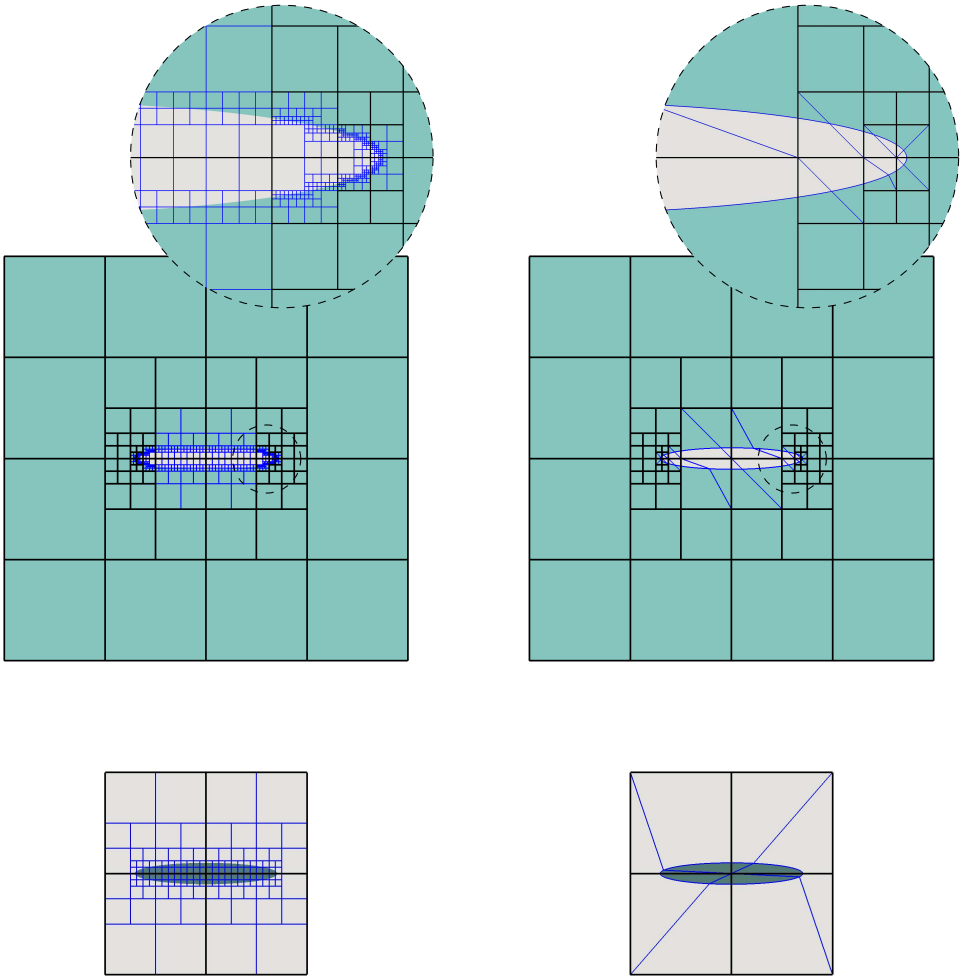

(a) Spacetree partitioning, $m = 4$, following [215]

(b) Blended partitioning, following [143]

Figure 5.6: Domain discretization for the plate and the inclusion, refinement depth $k = 4$. The finite cells' edges are drawn with thick black lines, whereas the integration meshes are drawn with thin blue lines.

segments. The implicit geometry description was used in conjunction with a line-search method to correctly place the additional interpolation points on the interface. This approach finally yields a high-order boundary discretization, as shown in Figure 5.7b (note that the figure shows only the extreme nodes). For a more detailed description of this high-order interface recovery algorithm, the reader is referred to [24]. This convenient approach for embedded boundary parametrization highlights another advantage of using Cartesian grids for the finite cell meshes and the same mesh parameters for both domains - in contrast to using unstructured FCM meshes, where the generation of cell-conforming boundary segments would be more challenging.

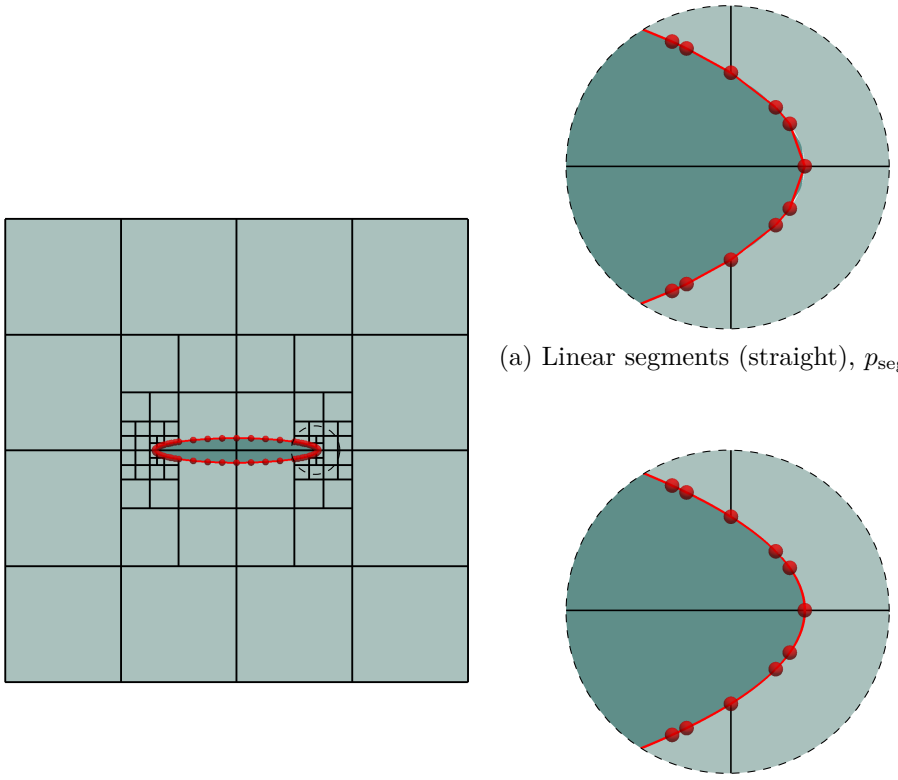

(a) Linear segments (straight), $p_{\text{seg}} = 1$

(b) Quadratic segments (curved), $p_{\text{seg}} = 2$

Figure 5.7: Discretization of the elliptical interface, $n_g = 4$, $n_{\text{seg}} = 72$

### Numerical solution

Figure 5.8 shows the numerical approximation of the axial stresses $\sigma_{xx}$ obtained using the FCM with weak coupling and multi-level *hp*-refinement. The plots shown here are the superposition of the solutions from the physical part of each domain, whereas the solution in the fictitious domain is omitted. Without applying any local refinement (Figure 5.8a), the FCM with weak coupling is able to reproduce the overall solution characteristics. However, the approximation for the stresses exhibits severe oscillations. In particular, the four finite cells in the plate's mesh that are intersected by the interface are affected by the high curvature of the concave geometry at points A and C, leading to stress concentration. This local solution characteristic cannot be represented well by the smooth basis functions of the coarse mesh, which leads to an oscillatory approximation of the stresses. Figure 5.8b depicts the numerical approximation obtained with the multi-level *hp*-scheme, using two levels of overlay meshes with uniform $p$-distribution. Applying local refinement to the FCM mesh of the plate improves the numerical approximation significantly. The solution benefits from the local support of the high-order basis functions with $C^0$-continuity, and the oscillations in the stresses are confined to the cells on the finest overlay mesh. Increasing the refinement depth with $k = 4$, the quality of the approximation improves further.

Figure 5.9 examines the stresses along the cutting line B-D (see Figure 5.5a) in closer detail. Since the cutting line is orthogonal to the ellipse's boundary, the exact solution

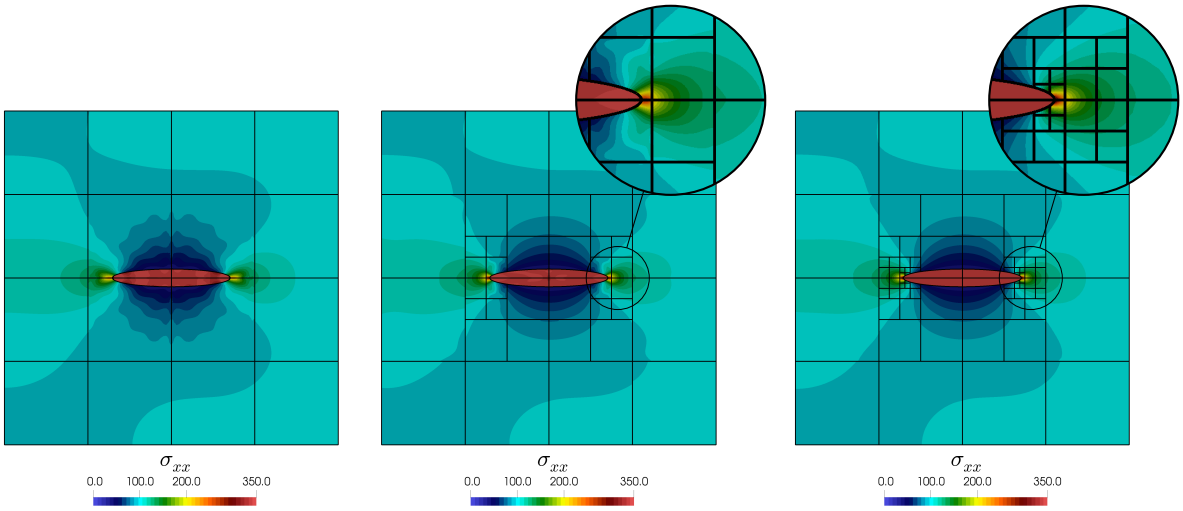


(a) $p = 8$, no refinement (b) $p = 4, k = 2$ (c) $p = 4, k = 4$

Figure 5.8: Plate with elliptical inclusion: numerical approximation of the axial stresses $\sigma_{xx}$

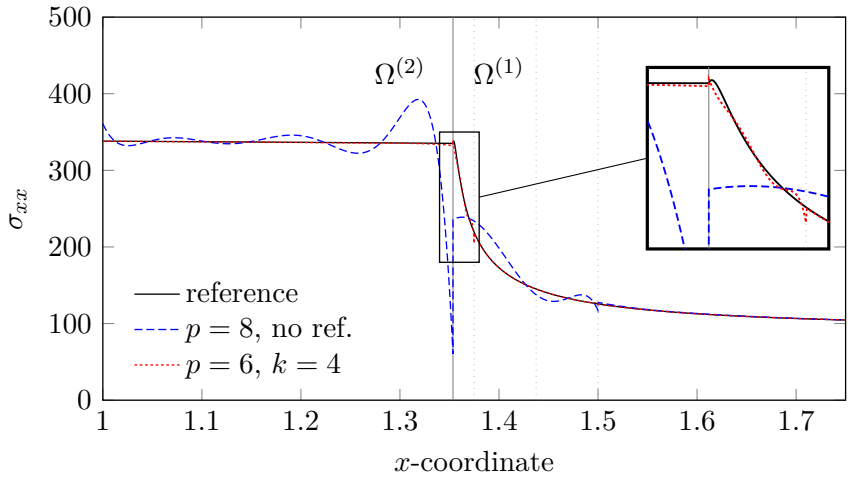


Figure 5.9: Plate with elliptical inclusion: numerical approximation of the axial stresses $\sigma_{xx}$ along cutting line B-D

for $\sigma_{xx}$ is continuous along the cutting line. Hence, jumps in the numerical approximation of the stresses, either at the interface or at element boundaries, correspond to the approximation error directly. The numerical approximation obtained without local refinement exhibits severe oscillations and a large jump at the interface. Due to the coupling condition, the oscillations extend into both domains. Due to the oscillations, the maximum stresses are overestimated and the local stress distribution is misrepresented. Applying multi-level *hp*-refinement to the plate's FCM mesh enhances the quality of the approximation appreciably, as the oscillations are mainly restricted to the finite cells on

the finest overlay mesh. The zoomed plot at the interface reveals the fine-scale features of the solution in the plate. The local solution characteristics are not fully resolved by the refined mesh with $k = 4$, which suggests that this problem would benefit from further local refinement.

### Influence of domain integral accuracy

To assess the accuracy of the numerical integration for the domain integral, Figure 5.10 compares the error in $\sigma_{xx}$ along cutting line B-D, based on multi-level $hp$-refinement of the plate's mesh with $k = 4$, polynomial degree $p = 6$, and different domain partitioning schemes. The error here is calculated with respect to the reference solution generated using the overkill $p$-FEM discretization. The blended partitioning approach gives a highly accurate evaluation of the domain integrals, as it uses the exact geometric description of the interface. Using the spacetree partitioning scheme with a depth $m = 2$ leads to high approximation errors. The error is highest in the finite cell from inclusion's mesh, which is attributed to the coarser spatial resolution of the integration, as demonstrated by Figure 5.6a. The high error propagates through the mesh, carrying over to finite cells which are not cut by the material interface, and to the other mesh through the coupling condition. Increasing the depth $m$ of the spacetree reduces the approximation error appreciably. Using depth $m = 7$, the achieved accuracy is comparable to that of the blended partitioning approach.

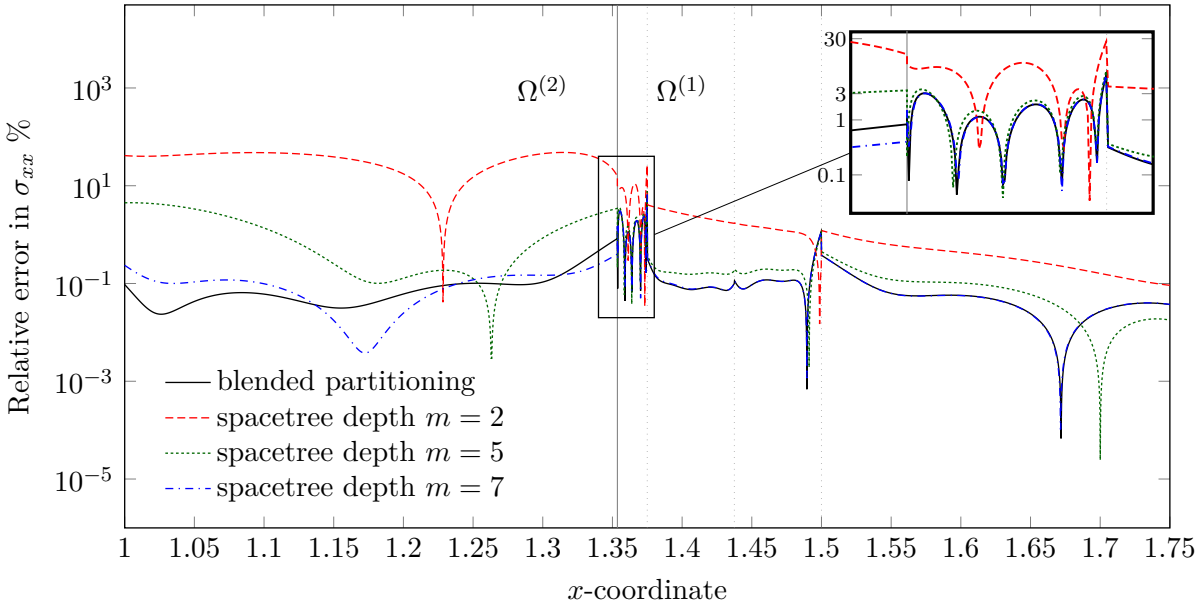


Figure 5.10: Error in $\sigma_{xx}$ along cutting line B-D with different domain integration schemes, $p = 6$, $k = 4$

### Influence of interface integral accuracy

To evaluate the effect of the integration accuracy of the interface integral, Figure 5.11 plots the local distribution of the approximation error for the von-Mises stresses $\sigma_{\text{eq}}$ along the interface in the plate. Using a grid dimension of $n_g = 4$ for the marching squares implementation, $n_{\text{seg}} = 72$ linear segments are generated (see Figure 5.7a). However, this linear discretization of the curved interface introduces artificial stress singularities at the interpolation nodes between the segments, as the segments touch at the extreme nodes but have discontinuous normals, which introduces artificial kinks at the interpolation nodes. At ellipse parameter $t = 0$ (point C), the artificial singularity takes over the approximation error, causing the entire solution to diverge. To reduce the error at the interface, $h$-refinement of the interface's discretization is carried out by refining the grid for the marching squares. Figure 5.11a shows the resulting error distribution with $n_g = \{4, 8, 16, 32, 64\}$, which yields $n_{\text{seg}} = \{72, 136, 280, 564, 1120\}$. The $h$-refinement of the segments delivers a uniform decrease in the approximation error, with a maximum error in $\sigma_{\text{eq}}$ of approximately 3% using 1120 segments.
Alternatively, $p$-refinement of the interface segments using Lagrange polynomials, as described earlier, leads to a faster convergence as demonstrated by Figure 5.11b. Using 72 quadratic segments already decreases the error significantly, as the high-order discretization approximates the tangents at the interpolation nodes with better accuracy, as shown in Figure 5.7b. Increasing $p_{\text{seg}}$ further from 3 to 4 in this example, gives a marginal improvement in accuracy, indicating that the numerical integral at the interface converges. The remaining approximation error is attributed to the FCM discretization with $p = 8$, and $k = 6$. The two refinement schemes for the interface discretization converge to the same local error distribution.

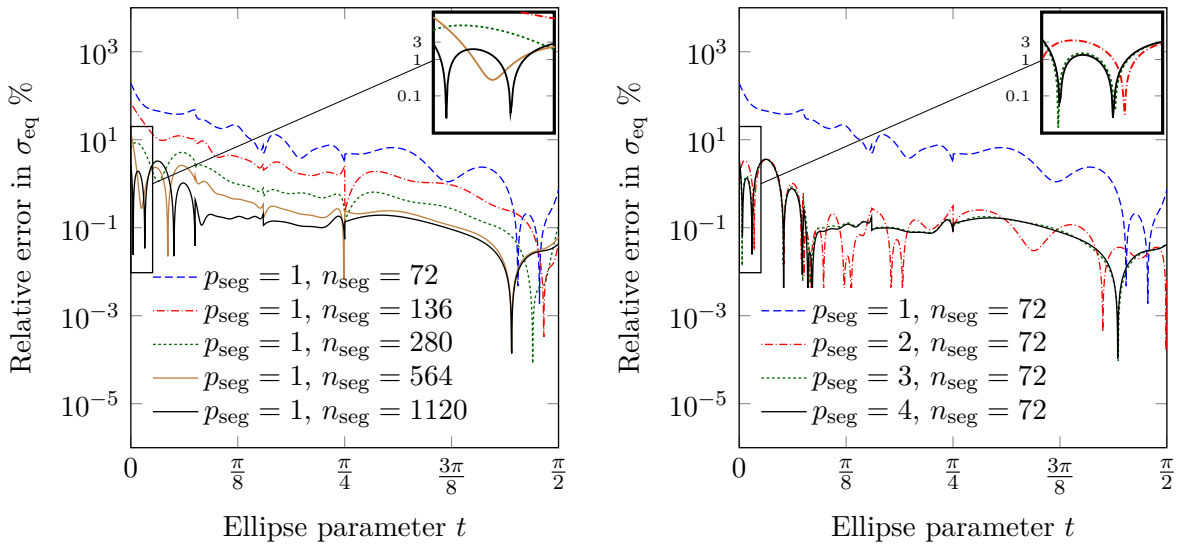


(a) $h$-refinement (b) $p$-refinement

Figure 5.11: Error in $\sigma_{eq}$ along the interface using different interface discretizations, $p = 8$, $k = 4$

### Convergence study

A uniform $p$-refinement study was carried out to assess the overall convergence behavior of multi-level $hp$-refinement in conjunction with weak coupling. Figure 5.12a shows the relative error in the energy norm for different refinement depths

$$||e||_E = \sqrt{\frac{|\mathcal{U}_{\text{num}} - \mathcal{U}_{\text{ex}}|}{\mathcal{U}_{\text{ex}}}} \cdot 100\%, \tag{5.14}$$

where $\mathcal{U}_{\text{num}}$ denotes the numerically approximated strain energy, and $\mathcal{U}_{\text{ex}}$ denotes the reference strain energy. For this study, the blended approach is used for the domain integration, in conjunction with a high-order parametrization of the interface. As the exact solution is piecewise-analytic, FCM with a weak enforcement of the interface conditions converges exponentially under uniform $p$-elevation, even without applying any local refinement. For a more detailed analysis of the convergence rates, Figure 5.12b shows the convergence plot in a log-$\sqrt{\ }$ scaling. Here, the linear plots characterize exponential convergence in the form [238]:

$$||e||_E \leq C \exp\left(\gamma N^{\theta}\right) \quad \text{with } \theta = \frac{1}{2}, \tag{5.15}$$

where $C$ is a positive constant, and $\gamma$ is a negative constant describing the convergence rate. Increasing the refinement depth with the multi-level $hp$-scheme for this example leads to a steeper convergence rate $\gamma$, allowing for a higher gain in accuracy. To achieve an engineering accuracy of 1% error, the discretization with $k = 4$ needs approximately five times less the degrees of freedom than the non-refined case.

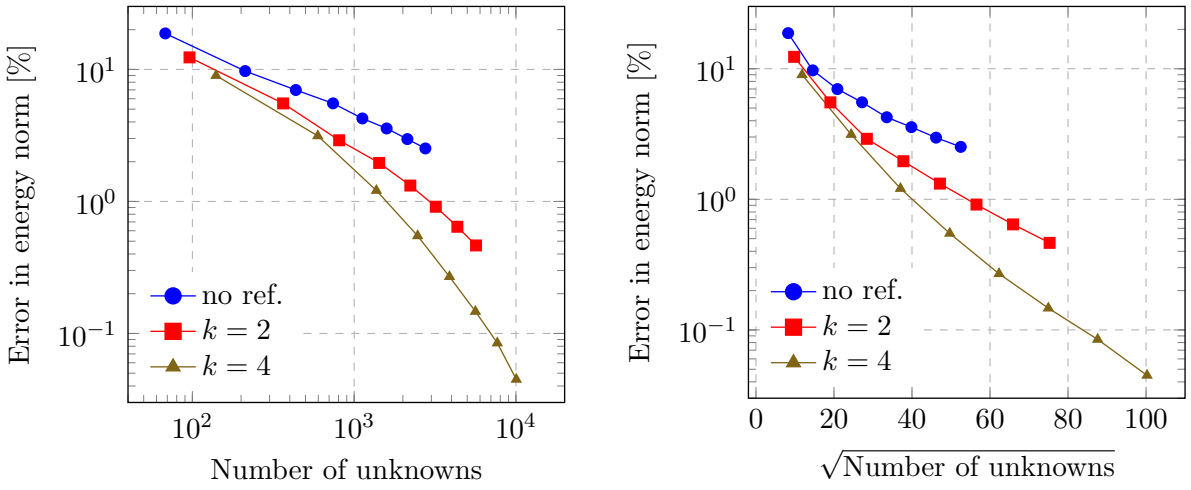


(a) Convergence in log-log scale

(b) Convergence in semi-log scale

Figure 5.12: Plate with elliptical inclusion: $p$-convergence for multi-level $hp$-refinement

### 5.4.2 Bi-material inclusion corner

In the next study, we consider a singular material-interface benchmark problem adapted from [269]. The two-dimensional temperature problem is governed by the Poisson equation:

$$\kappa^{(i)} \nabla^2 \phi^{(i)} = -1 \qquad \forall \boldsymbol{x} \in \Omega^{(i)} \tag{5.16}$$

$$\phi = 0 \qquad \forall \boldsymbol{x} \in \Gamma_D, \tag{5.17}$$

where $\phi^{(i)}$ denotes the temperature, $\kappa^{(i)}$ the thermal diffusivity, $\Omega^{(i)}$ and $\Gamma_D$ are defined as shown in Figure 5.13a. Here, the material interface $\Gamma_{12}$ has a sharp corner, inducing a vertex singularity. Moreover, the intersection of the material interface with the Dirichlet boundary $\Gamma_D$ for the applied boundary condition introduces two additional weak singularities, where the solution exhibits reduced continuity.

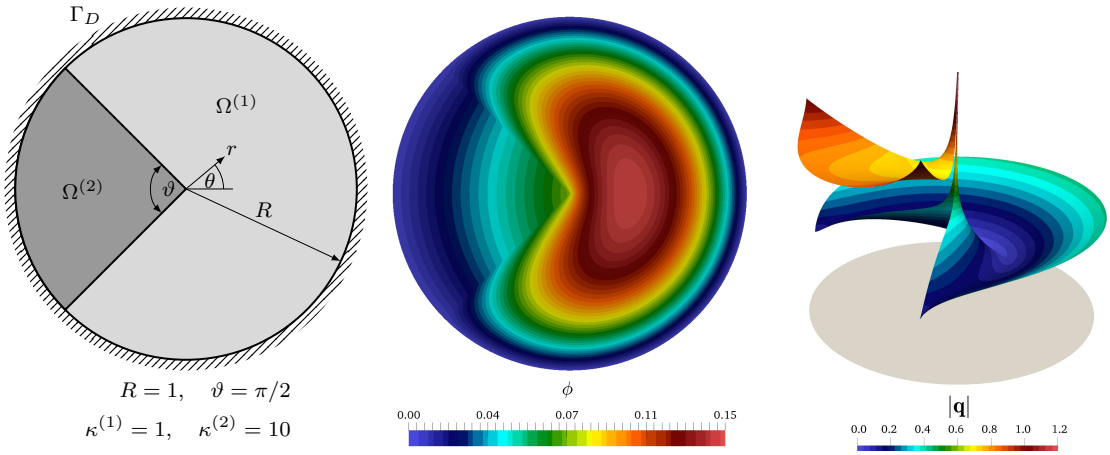


(a) Benchmark setup (b) Reference temperature $\phi$ (c) Reference heat flux $|\boldsymbol{q}|$

Figure 5.13: Bi-material inclusion corner

The exact solution to this problem is given in radial coordinates $(r, \theta)$ by [133] :

$$\phi(r, \theta) = A_1 r^{\lambda_1} h_1(\theta) + A_2 r^{\lambda_2} h_2(\theta) + \mathcal{O}(r^2), \tag{5.18}$$

where $A_1$ and $A_2$ are scalar constants, $h_1(\theta)$ and $h_2(\theta)$ are smooth sinusoidal functions and

$$\lambda_1 = 0.731691779, \quad \lambda_2 = 1.268308221. \tag{5.19}$$

For reference, an overkill solution was generated using a conforming $p$-FEM with exact blending, where the mesh was geometrically graded towards the vertex singularity. The reference mesh has 21 elements with polynomial degree $p = 30$ and 18 991 degrees of freedom. The strain energy for the setup shown here is

$$\mathcal{U}_{\text{ex}} = 1.0168443145 \times 10^{-1}. \tag{5.20}$$

Using the FCM with weak coupling, separate meshes were used for the disc and the inclusion, as shown in Figure 5.14. Unlike the previous example, where the stress concentration in the plate was caused by the concave geometry, the singularities affect the solution in both sub-domains. Consequently, *both meshes* need local refinement to resolve the singularities. The meshes were graded towards the vertex singularity, and the two weak singularities on the boundary. The same refinement depth was applied to all three refinement points. Here, the discretizations match the singularities with nodes of the FCM mesh.

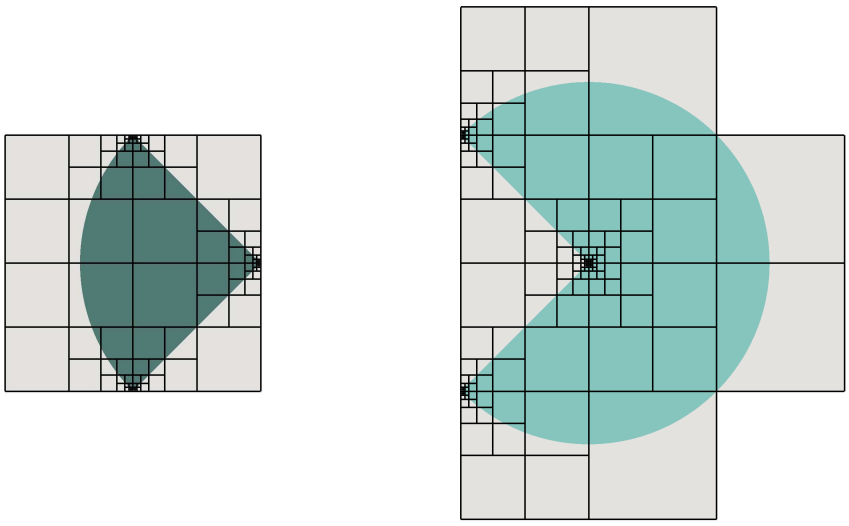

(a) Inclusion (b) Disc

Figure 5.14: Bi-material inclusion corner: discretization with refinement depth $k = 6$

The penalty method was used to couple the FCM meshes along the straight material interface. Additionally, the embedded Dirichlet boundary condition was weakly enforced on $\Gamma_D^{(i)}$ in each mesh using the penalty method with $\beta_D = 10^7$. The weak enforcement of the boundary conditions does not influence the convergence behaviour, provided that the penalty parameter is chosen large enough [254]. The fictitious domain was penalized with $\kappa_{\text{fict}} = \kappa^{(1)} \cdot 10^{-9}$. Note that this value is higher than in the previous example, and was chosen to have a lower condition number to allow the use of high polynomial degrees, up to $p = 10$, in the convergence studies. The blended partitioning approach was used to numerically evaluate the domain integral. The coupling integral was evaluated on linear segments, whereas the weak Dirichlet boundary conditions were integrated over curved segments, automatically generated with the same approach described for the previous example.

The magnitude of numerical solution for the heat flux, $\boldsymbol{q}^{(i)} = \kappa^{(i)} \nabla \phi^{(i)}$, is depicted in Figure 5.15. For the first case, without any local refinement of the meshes, the numerical approximations of the heat fluxes exhibit oscillations within the domain and jumps at element boundaries. The oscillatory behavior is attributed to the inability of the smooth polynomials to represent the high gradients in the vicinity of the singularities. For the

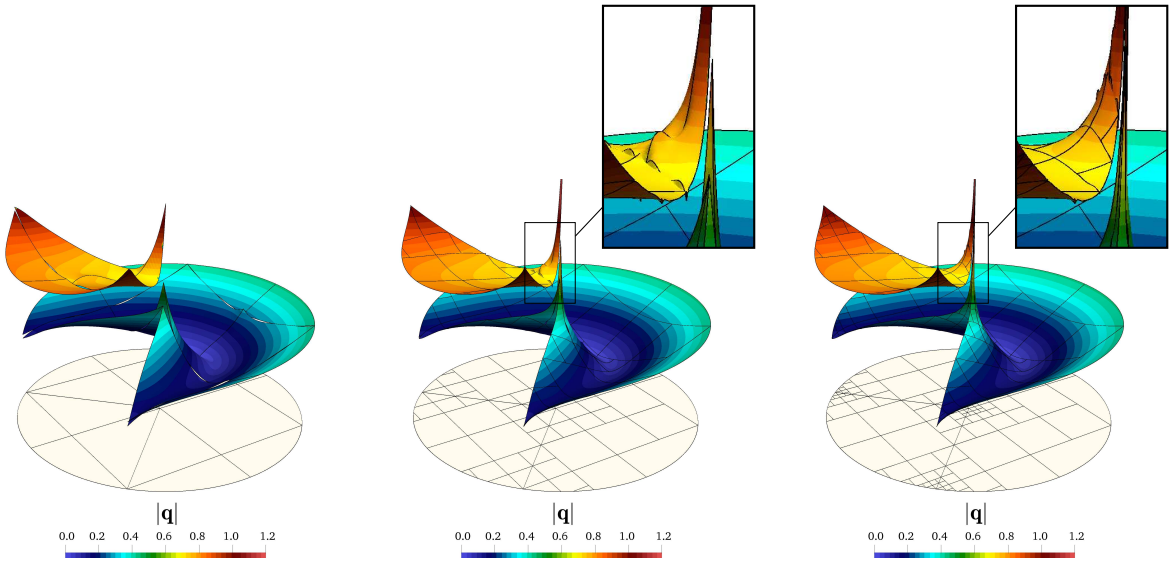


(a) $p = 4$, no refinement (b) $p = 4, k = 2$ (c) $p = 4, k = 4$

Figure 5.15: Bi-material inclusion corner: numerical approximation of the flux $|\boldsymbol{q}|$

second discretization, two levels of uniform high-order overlay meshes are used to grade the meshes towards the three singularities.The $C^0$-continuity of the high-order basis functions limits the pollution error from the singularities at the finest refinement level, as revealed in the zoomed plot. Using four refinement levels improves the solution further, as the geometric progression of element size arrests the propagation of the error, while having larger elements to describe the smooth solution away from the singularities.

Figure 5.16a shows the results of a $p$-elevation study carried out to assess the convergence properties. Without applying local refinement, the convergence under $p$-elevation is identified as being algebraic in the form

$$||e||_E \leq aN^{\eta}, \tag{5.21}$$

where $a$ is a positive constant, and $\eta$ is a negative constant indicating the convergence rate. The estimate for $\eta \approx -\lambda_1$ matches the theoretical expectation for a discretization where the vertex singularities are matched by nodes of the mesh [13]. With multi-level $hp$-refinement the convergence behavior shows a pre-asymptotic range with a higher convergence rate, and an asymptotic range, where the behavior returns to being algebraic with the same rate $\eta$. Increasing the refinement depth $k$ extends the pre-asymptotic range, allowing for a significant decrease in the total approximation error. Changing the scaling to a log-$\sqrt[3]{\ }$ in Figure 5.16b, the extended pre-asymptotic range appears linear, indicating exponential convergence in the pre-asymptotic range.

Note the apparent leveling-off of the error in the energy norm around $10^{-2}\%$, which is attributed to the use of $\kappa_{\text{fict}} \neq 0$, adding a modeling error to the numerical approximation. The introduced error in the energy norm is in the order of $\sqrt{\kappa_{\text{fict}}}$ [54]. Using a smaller value for $\kappa_{\text{fict}}$ lowers the leveling-off threshold, at the cost of the conditioning of the system.

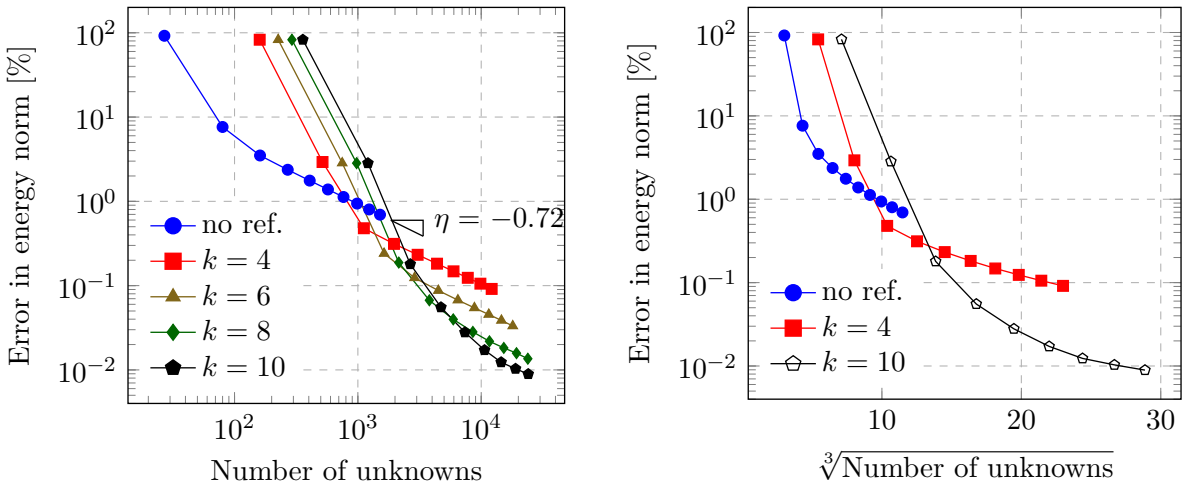


(a) Convergence in log-log scale

(b) Convergence in semi-log scale

Figure 5.16: Bi-material inclusion corner: $p$-convergence for multi-level $hp$-refinement

### 5.4.3 Cube with ellipsoidal inclusion

Next, we consider a three-dimensional example, which is a generalization of the benchmark presented in Section 5.4.1. A linear elastic analysis is considered for a cube with an embedded ellipsoidal (prolate spheroid) inclusion - depicted in Figure 5.17. The spheroidal inclusion induces stress concentration in the cube around the two points on its major axis. The solution within the spheroidal inclusion remains smooth.

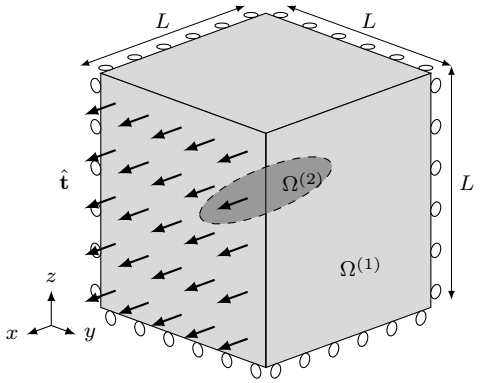


Figure 5.17: Cube with ellipsoidal inclusion

Two FCM meshes were used to discretize the sub-domains, using a base discretization of $4 \times 4 \times 4$ finite cells which match the outer boundaries of the cube. To resolve the stress concentration, the cube's mesh was refined towards the two points on the major axis of

the spheroid, as shown in Figure 5.18. For the inclusion's mesh, $2 \times 2 \times 2$ elements remain after excluding all cells that are completely in the fictitious domain. Finite cells that are cut by the interface were further partitioned for integration using the spacetree approach described earlier.
The penalty coupling terms were integrated over a surface triangulation, automatically generated using marching cubes [154, 27, 160]. The implementation is a three-dimensional extension of the high-order parametrization algorithm used in Section 5.4.1, where a grid of $n_g \times n_g \times n_g$ points per sub-cell was used for the surface recovery. An example of the resulting triangulation is shown in Figure 5.18. Note that the surface mesh is irregular and that the triangles have severe aspect ratios. The high-order penalty terms are then integrated over the triangles by collapsing one side of the integration domain (bi-unit square) and mapping it to each triangle. As demonstrated by the two-dimensional ellipse benchmark the linear parametrization needs a fine resolution to achieve accurate results.

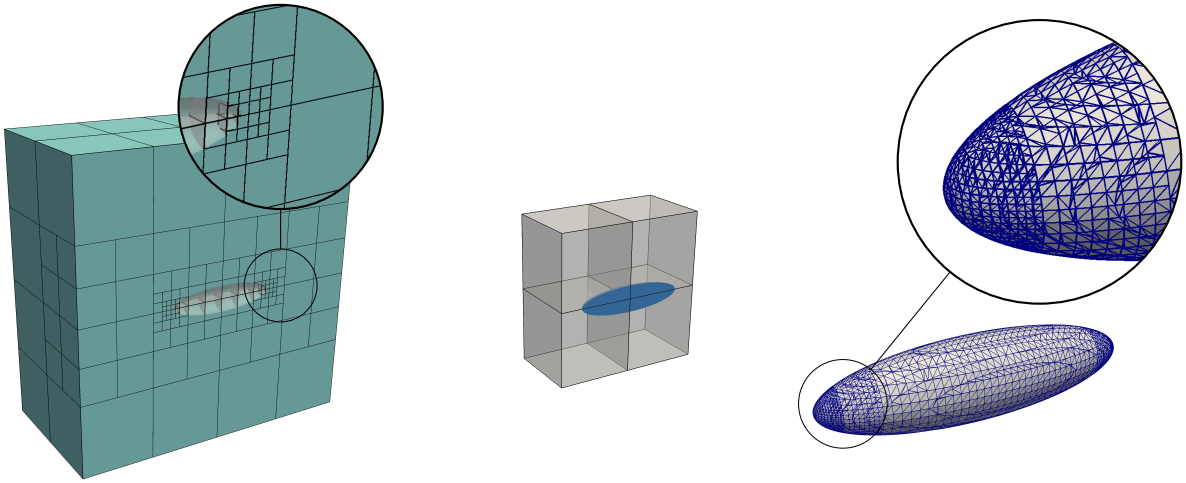

(a) Cube (b) Ellipsoidal inclusion (c) Coupling surface

Figure 5.18: Discretization of cube and ellipsoid using $k = 4$ - Section view

The numerical approximation for the axial stresses $\sigma_{xx}$ is depicted in Figure 5.19. Note that half of the domain is removed to visualize the internal solution. For the unrefined meshes, the approximated stresses exhibit oscillations and non-physical jumps at the element boundaries. If the cube's mesh, which is affected by the concave geometry, is refined towards the two points, the stress concentration can be localized quickly. Similar to the two-dimensional case, the solution within the ellipsoid remains smooth, and does not require local mesh refinement.
The results show that the improvement in accuracy brought on by the multi-level *hp*-refinement scheme also carries over to three-dimensional problems. The example also demonstrates that a surface mesh for the interface discretization is easily obtained for smooth implicit geometries. The surface mesh is only used to integrate the penalty terms, and hence can be irregular or have severe aspect ratios, unlike what is required of an analysis-suitable finite element mesh.

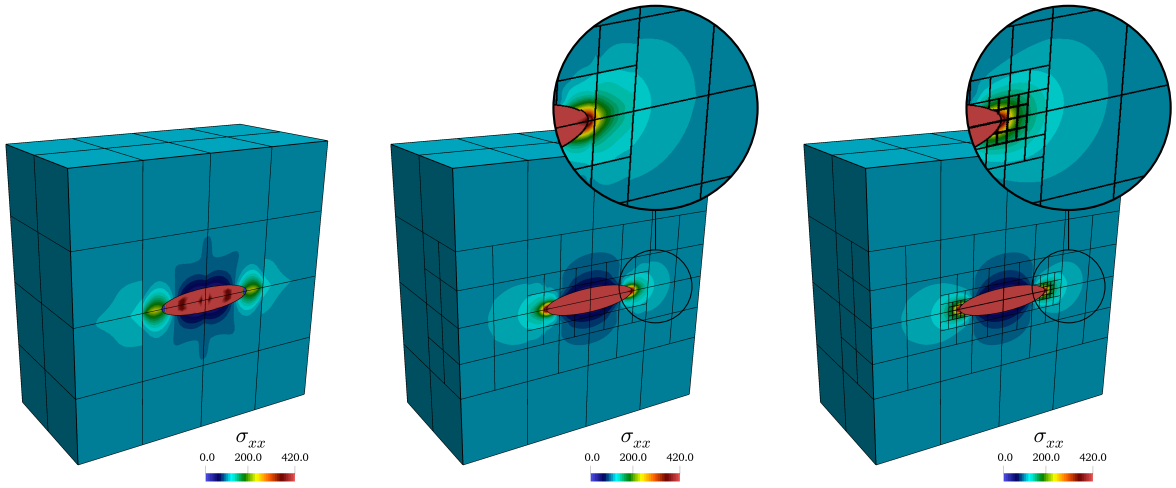


(a) $p = 8$, no refinement (b) $p = 6, k = 2$ (c) $p = 6, k = 4$

Figure 5.19: Cube with ellipsoidal inclusion: numerical approximation of axial stresses

### 5.4.4 Cylinder with cubical inclusion

The last numerical benchmark for us to consider is a three-dimensional problem with a vertex-edge singularity. We study a cylinder under axial tension, which has an embedded cubical inclusion. Due to the symmetry of the problem, we consider only one-eighth of the system. An overkill solution was generated for reference, using seven conforming hexahedral $p$-FEM elements with exact blending, and a local refinement using the multi-level $hp$-scheme. Using 5 levels of refinement and a polynomial degree $p = 9$, the overkill discretization has $506,199$ degrees of freedom. The reference strain energy for the setup shown in Figure 5.20a is

$$\mathcal{U}_{\text{ex}} = 1.037455 \times 10^3. \tag{5.22}$$

Two non-geometry-conforming FCM meshes were used for the cylinder and the cubical inclusion. A coarse base discretization of $2 \times 2 \times 2$ finite cells was used. The dimensions of the mesh were setup in such a way that the edges of the FCM meshes do *not* exactly coincide with the cube's edges. Similar to the two-dimensional benchmark presented in Section 5.4.2, the vertex-edge singularity affects the solution in both domains. Accordingly, both meshes were refined towards the singular edges, as shown in Figure 5.21. The symmetry boundary conditions were enforced in a classical manner on the corresponding faces of the FCM meshes.

The numerical approximation for the von-Mises stresses, $\sigma_{\text{eq}}$, is shown in Figure 5.22 for the cylinder and in Figure 5.23 for the cubical inclusion. The complete domain is clipped diagonally to reveal the solution at the vertex-edge singularity. Note that the geometry of the cylinder is rotated to show the solution along the singular edges. Whereas the solution obtained without refinement is highly oscillatory, the local refinement with the multi-level $hp$-scheme is able to confine the error to the finest level of sub-cells.

To assess the convergence behavior, a $p$-elevation study was carried out. The results,

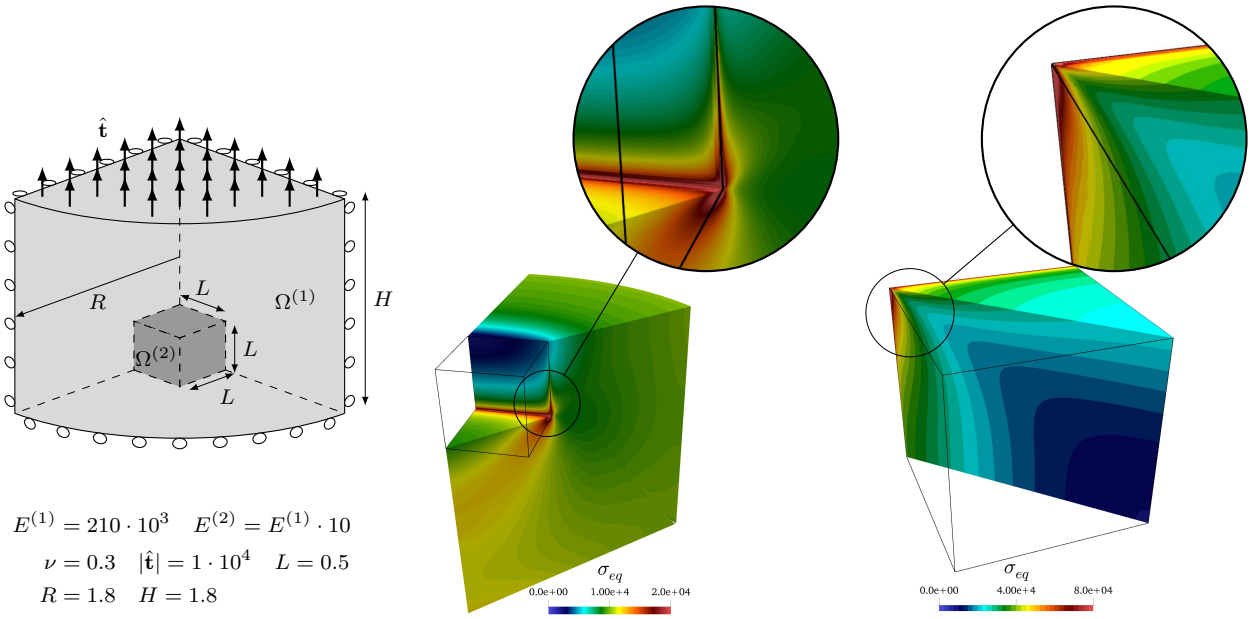


$E^{(1)} = 210 \cdot 10^3 \quad E^{(2)} = E^{(1)} \cdot 10$
$\nu = 0.3 \quad |\hat{\mathbf{t}}| = 1 \cdot 10^4 \quad L = 0.5$
$R = 1.8 \quad H = 1.8$

(a) Benchmark setup (b) Reference $\sigma_{\text{eq}}$ in cylinder (c) Reference $\sigma_{\text{eq}}$ in inclusion

Figure 5.20: Cylinder with cubical inclusion

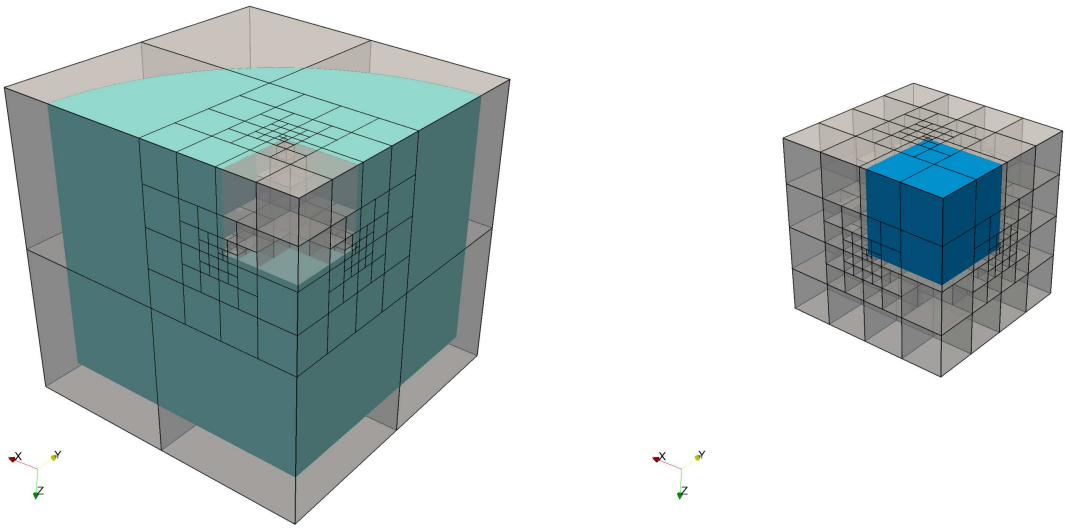

(a) Cylinder (b) Cubical inclusion

Figure 5.21: Discretization of cylinder and cubical inclusion, $k = 5$

shown in Figure 5.24, indicate a slow algebraic rate for coupled FCM without refinement. Applying a local refinement starting with $k > 2$, a pre-asymptotic range can be identified as having a steeper convergence rate. This allows the discretization with $k = 5$ to achieve an engineering accuracy of 1% error using a moderate polynomial order. This would

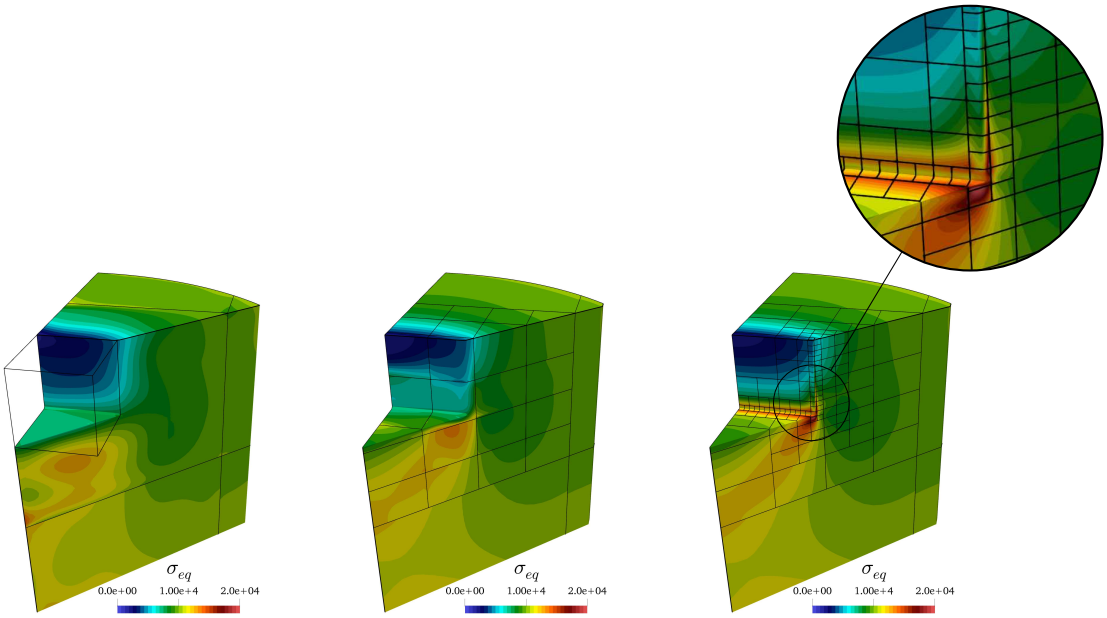


(a) $p = 8$, no refinement (b) $p = 4, k = 2$ (c) $p = 4, k = 5$

Figure 5.22: Cylinder: numerical approximation of $\sigma_{\text{eq}}$

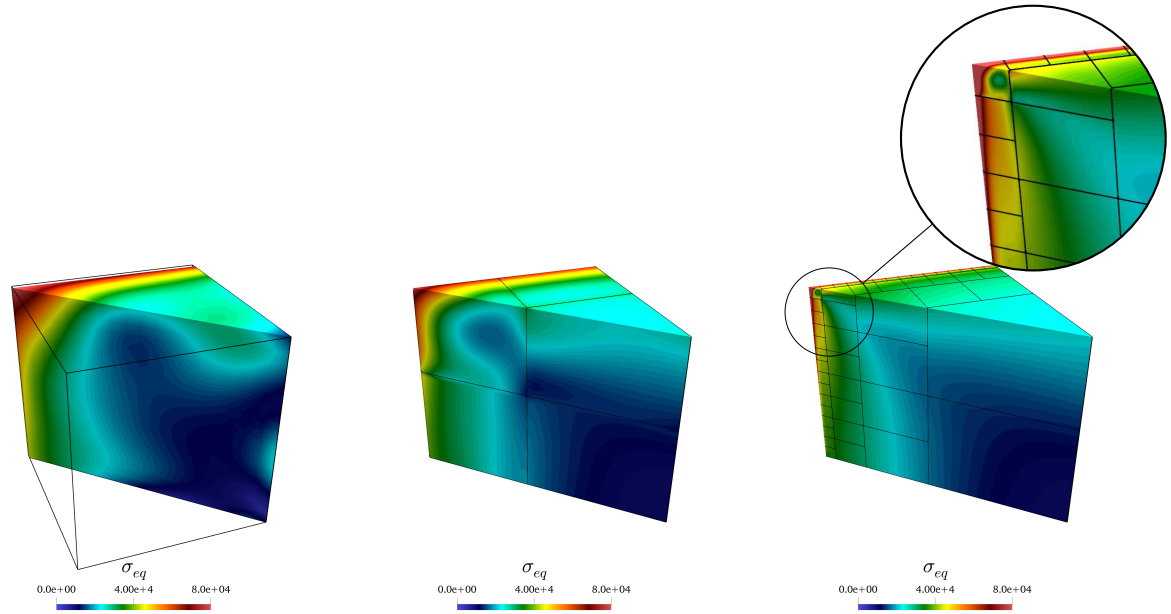


(a) $p = 8$, no refinement (b) $p = 4, k = 2$ (c) $p = 4, k = 5$

Figure 5.23: Cubical inclusion: numerical approximation of $\sigma_{\text{eq}}$

require at least an order of magnitude more degrees of freedom with uniform $h$- or $p$-refinement. The pre-asymptotic convergence is also characterized as algebraic, albeit with

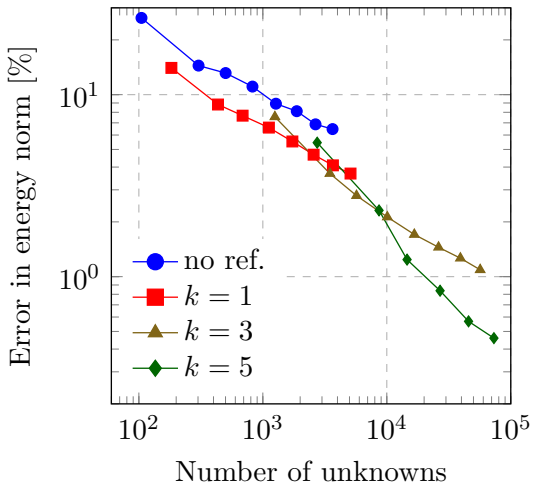


Figure 5.24: Cylinder with cubical inclusion: $p$-convergence for multi-level $hp$-refinement

a higher rate. For vertex-edge singularities, an anisotropic refinement scheme is necessary to attain exponential convergence [13], which was not applied in this work. However, this is not always feasible for the general case of embedded vertex-edge singularities, where the (possibly curved) singular edges might not be parallel to edges of the mesh. Nevertheless, the improved algebraic convergence brought on by the multi-level $hp$-refinement allows for a significant reduction of the approximation error.

## 5.5 Discussion

In this chapter, we demonstrated that the application of the multi-level $hp$-scheme for local refinement in the finite cell method in conjunction with weak enforcement of the interface conditions constitutes an efficient and robust approach for the solution of material interface problems involving complex geometries. Several numerical benchmarks of two- and three-dimensional material interface problems show that the convergence behavior is significantly improved by the multi-level $hp$-refinement scheme for problems with stress concentration and singularities. The results also show that the proposed approach can provide an accurate approximation of the stresses at the material interface, and highlight the importance of a high-order accurate geometric description of the interface and the boundaries.

This combination of numerical methods can be used for mechanical simulations involving material interface problems and very complex geometry while circumventing volumetric mesh generation. Another advantage of using a separate discretization for each subdomain is the flexibility in refining each mesh separately, i.e. the local refinement of one mesh doesn't necessarily propagate across the interface—as demonstrated in Section 5.4.1—which can lead to more efficient discretizations.

In this work, we have used the penalty method for the weak imposition of the Dirichlet boundary conditions and interface constraints. With a suitable choice for the penalty parameter and an accurate surface representation, we have demonstrated that the interface

conditions can be enforced with sufficient accuracy. However, the approximation error depends on the penalty parameter. For a more robust methodology, more sophisticated weak enforcement methods can be implemented, e.g. Nitsche's method [208, 217].
These methods modify the weak form with additional surface integrals over the interface. For the numerical integration of these terms, a surface mesh of the material interface needs to be generated. Fortunately, this is a task of lower difficulty than generating an interface-conforming volumetric mesh. However, for geometries where a surface representations might not be available, e.g. geometries represented by point clouds, alternative methods for the weak imposition of boundary and interface conditions need to be considered.
Another limitation of the current implementation is the inability to perform anisotropic mesh refinement—i.e. the mesh can only be locally refined concurrently in all spatial directions. For three-dimensional problems with vertex-edge singularities, anisotropic refinement is necessary to achieve exponential convergence. Future research should investigate the applicability of anisotropic refinement in the context of the multi-level *hp*-scheme together with the embedded domain approach.
In this work, we have used a priori refined meshes, where we applied geometric grading towards locations where singularities and high solution gradients were expected, and we have used uniform polynomial degrees within the meshes. More efficient discretizations can be achieved through adaptation of the polynomial degree in addition to automatic local mesh refinement. To that end, the development of a posteriori error estimators is necessary, which is the subject of current research [62].

# Chapter 6

# Applications of the FCM for material interfaces in bone mechanics

In this chapter, we present two applications of the FCM for the numerical solution of problems with material interfaces in bone mechanics. In the first application, we present a numerical technique to incorporate loads stemming from musculoskeletal models of the spine into patient-specific finite cell analysis. The second application demonstrates the applicability of the FCM in combination with the multi-level *hp*-refinement scheme for the simulation of vertebrae with pedicle screws.

## 6.1 Combination with musculoskeletal models

Musculoskeletal models can be used to provide more realistic boundary conditions to patient-specific numerical models of bone. In the context of the FCM, the consideration of concentrated loads stemming from musculoskeletal models presents a challenge. In this work, we present a numerical approach to include such loads in FCM models. This is achieved by applying the loads on a separate load-transfer mesh which is weakly coupled to the original discretization. We present a numerical example which illustrates the applicability of the proposed approach to patient-specific FCM models.
This section is based on work that was done in the master's thesis [185] of Oguz Oztoprak[1], which was supervised by the author of this work. This was carried out as part of a collaboration project. The contributions and efforts of Alexander Valentinitsch[2], Amirhossein Bayat[2], Tanja Lerchl[3] and Jan S. Kirschke[2] are gratefully acknowledged.

### 6.1.1 Introduction

Osteoporosis compromises bone strength, increasing the risk of vertebral fractures with severe health consequences. The development of an accurate and reliable patient-specific numerical model for the biomechanical analysis of the vertebra would be beneficial for

[1]Chair for Computational Modeling and Simulation, TUM
[2]Department of Neuroradiology, TUM
[3]Associate Professorship of Sport Equipment and Sport Materials, TUM

the prediction of fractures and supporting medical professionals in choosing a suitable treatment. The mechanical stresses in the vertebra are determined by its geometry and—locally— the bone density. Moreover, accurate modeling of the boundary conditions has a great influence on the predictive ability of the numerical models [119].

Musculoskeletal models are a valuable tool used to study the relationship between body motion and internal biomechanical forces. In a musculoskeletal model, the human body is modeled as a multibody dynamic system, in which bones are characterized as rigid segments connected by joints, muscles as tensile actuator elements connecting the bony segments and ligaments as passive elastic structures that connect the articulating bones and keep the joints assembled [15]. The dynamic simulation of the musculoskeletal models determines the motion of the body segments and calculates the forces in the muscles and the joints. Patient-specific musculoskeletal models can also be created based on the patient's individual geometry reconstructed from medical images, e.g. quantitative CT scans [151].

There have been several efforts in the combination of musculoskeletal models and patient-specific finite element analysis for biomechanical analysis, which allows for more realistic loading scenarios, especially taking into account muscle forces. Commonly, the two simulations are considered separately, assuming the bones to be rigid in the multibody simulation. The loads calculated using the musculoskeletal model are then used as external loads in the subsequent FE analysis. In [152], this decoupled approach was followed for the simulation of the lumbar spine to estimate the loads on the intervertebral discs, and FE analysis of the discs was carried out to calculate their deformation. Kamal et al. [126] also followed this approach for patient-specific analysis of the spine to estimate the forces and the resulting stresses on the growth plates of vertebrae in patients with scoliosis. In [125], musculoskeletal simulations are used to estimate muscle and joint contact forces, which are combined with adaptive mechanobiological finite element analysis to predict femoral growth in children.

Alternatively, concurrent musculoskeletal dynamic simulations and finite element analysis can be used to model more complex scenarios, where the deformation of the bones or the joints need to be considered in the musculoskeletal model [94]. In [225], a coupling of musculoskeletal models with the finite element analysis of deformable joints was used for the mechanical analysis of knee replacement. As the FE models typically have significantly more degrees of freedom than the musculoskeletal models, concurrent simulations are much more computationally expensive.

The incorporation of loads estimated using musculoskeletal models into FCM models presents some challenges. As the joints typically used in the models are idealized as points [264], the loads resulting from the solution of the multibody dynamics are represented as concentrated forces and moments. In three-dimensional solid models, point loads induce singularities [77], which require special attention in the numerical discretization. It is considered a better practice to model the surface loads as distributed tractions [77, 87]. Point forces can be modeled as uniformly distributed tractions. However, for surfaces of complex geometry, special attention is needed if the point where the load is applied does not coincide with the centroid of the load surface. Furthermore, modeling concentrated moments on surfaces of arbitrary geometry is not straightforward, especially if an exact surface description is not available. It is also not possible to directly incorporate moments

in three-dimensional solid elements which are formulated in terms of the displacements as the primary variables (degrees of freedom), with the respective external forces—in contrast to beam and shell elements which have rotational degrees of freedom [77, 111].
For conventional finite elements, there are several approaches to incorporate concentrated moments in models that use three-dimensional solid elements. A common approach involves the use of rigid beam elements which are coupled to the nodes of the solid FE mesh at the load surface [87]. The moment load is applied to the beam elements (which is possible due to their rotational degrees of freedom), and is transferred to the nodes of the solid mesh through the coupling constraints. A similar approach is to use an additional mesh of shell elements to discretize the load surface, and couple the shells to the solid elements [228, 87]. In the context of fictitious domain methods, embedded shell finite elements have been investigated by Schillinger et al. [216]. However, only examples including distributed pressure loads were presented. A downside of this approach is the need to generate an analysis-suitable finite element mesh with shell elements for the load surface.
In this work, we propose a numerical approach for the consideration of concentrated loads in patient-specific FCM vertebra models. Here, the load surfaces at the endplates are extended using load-transfer blocks which have very high stiffness. The load-transfer blocks are discretized using separate meshes that are weakly coupled to the FCM mesh of the vertebra to account for the material interface. The concentrated loads are modeled as distributed tractions on the surfaces of the blocks which have a simple geometry. The idea is similar to the approaches described above, but uses a solid model for coupling instead of beams or shells. It is also related to the "stiff strip" method, which was suggested as a simple approach to impose embedded boundary conditions for FCM models [190, 70], but includes an adequate treatment of the weak discontinuity at the material interface.

### 6.1.2 Musculoskeletal models

Musculoskeletal models of the spine are an example of multibody dynamic systems. Multibody systems are defined as a system of interconnected bodies, where the joints constrain the relative motion of the bodies, and springs and dampers act as compliant elements [226]. The bodies have mass and moment of inertia, whereas the interconnections are assumed to be massless.
In musculoskeletal models of the spine, the vertebrae are modeled as rigid bodies. The intervertebral discs are often modeled as three degrees-of-freedom spherical joints located in the center of the joints between the vertebrae, that allow relative rotation of the vertebrae [59]. More sophisticated models consider the discs as nonlinear spring-damper systems with six degrees-of-freedom, resulting in reaction forces and moments, and the viscoelastic parameters are determined from the disc's geometry [151]. Muscles are defined as unilateral force elements that can only exert force in tension, and their mechanical properties are modeled using a Hill-type muscle model (a spring in series with a spring-damper in parallel). Ligaments are modeled as nonlinear spring-dampers, similar to muscles but as passive elements [15]. To that end, the geometry of the muscles and ligaments are modeled by line elements, and the points of origin and insertion (attachment to the bone) are defined in the model. Moreover, contact between the vertebral segments

can be calculated using a polygon contact model [104]. An example of a musculoskeletal model of the lumbar spine is shown in Figure 6.1.

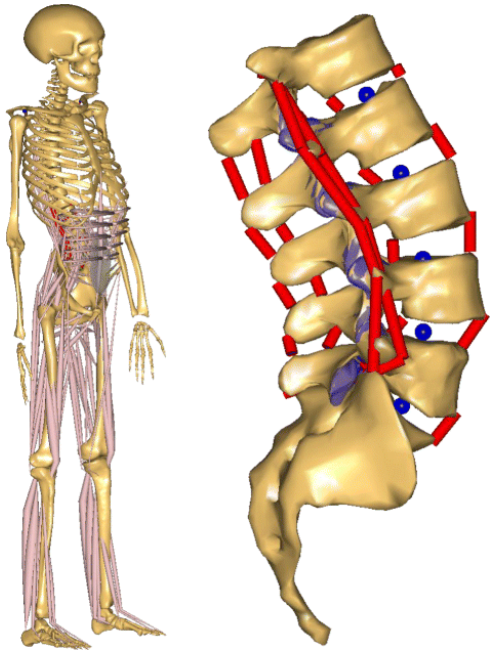

Figure 6.1: Musculoskeletal model of the lumbar spine, reproduced from [195]

The combined translational and rotational motion of a rigid body can be characterized by the Newton–Euler equations, or Lagrange's equations [264]. These relate the motion of the center of gravity of the rigid body to the forces and moments acting on it. Considering a system of $n$ interconnected rigid bodies which have $n_q$ degrees of freedom, the equation of motion can be expressed as:

$$\boldsymbol{M}\ddot{\boldsymbol{q}}(t) + \boldsymbol{G}(\boldsymbol{q})^\top \boldsymbol{\lambda} = \boldsymbol{F}(\boldsymbol{q}, \dot{\boldsymbol{q}}, t) \tag{6.1a}$$

$$\boldsymbol{g}(\boldsymbol{q}) = \boldsymbol{0}. \tag{6.1b}$$

Here, $\boldsymbol{q}(t) \in \mathbb{R}^{n_q}$ is a vector that comprises the coordinates for position and orientation of all rigid bodies in the system at time $t$. The system is subject to $n_\lambda$ constraints represented by the vector $\boldsymbol{g}$. The rectangular matrix

$$\boldsymbol{G}(\boldsymbol{q}) = \frac{\partial \boldsymbol{g}(\boldsymbol{q})}{\partial \boldsymbol{q}} \in \mathbb{R}^{n_\lambda \times n_q}$$

is called the constraint *Jacobian*, and $\boldsymbol{\lambda}$ are the additional Lagrange multipliers. The mass matrix, $\boldsymbol{M} \in \mathbb{R}^{n_q \times n_q}$, describes the mass and moment of inertia properties of the rigid bodies, whereas the vector $\boldsymbol{F}(\boldsymbol{q}, \dot{\boldsymbol{q}}, t) \in \mathbb{R}^{n_q}$ describes the applied (external) and internal forces due to motion at the joints with elastic or damping elements.
The solution to the constrained equation of motion (6.1) defines the motion and generalized forces of the multibody system. The equation system can be solved numerically by using time-integration methods, e.g. Newmark's method or Runge-Kutta schemes [55, 226].

In this work, the musculoskeletal models of the spine treat the vertebrae as rigid bodies. An independent biomechanical analysis using the FCM is carried out, using the forces estimated from the musculoskeletal model, to calculate the elastic deformation in the bone, which is not considered in the multibody dynamic system. As the stiffness of bone is considerably higher than that of the joints modeling the intervertebral discs, the modeling error introduced by this assumption should not be significant.

### 6.1.3 Weak enforcement of concentrated loads

Here, we propose a numerical approach for the inclusion of point loads resulting from musculoskeletal models into FCM models. The modeling of point loads on surfaces having arbitrary geometry presents some challenges for the FCM. Representing concentrated forces as surface tractions that are uniformly distributed over the whole load surface (inhomogeneous Neumann boundary conditions) is a possibility for simple geometries. However, if the concentrated force does not coincide with the centroid of the load surface, then this approach would be inconsistent, as it introduces additional moments due to the eccentricity. Moreover, modeling concentrated moments as spatially varying tractions becomes challenging for surfaces with complex geometry, especially if an exact surface description is not available.

Furthermore, modeling techniques which are commonly used in conventional FEM to model concentrated moments in three-dimensional solid models often rely on adding constraints to the nodes of the FE mesh on the load surface. However, in embedded domain methods, such as the FCM, the geometric boundary of the object is not resolved by the edges and nodes of the mesh, which hinders the applicability of such techniques.

In the proposed approach, we extend the problem at the load surface, $\Gamma_N$, by adding a surrogate load-transfer block, which is coupled to the original domain $\Omega_{\text{phy}}$ at the original load surface. The load-transfer block, $\Omega_{\text{LT}}$, is defined such that it matches the load surface and extends beyond the original domain to a simple geometry with flat surfaces. The block is assigned a linear elastic material that has a very high stiffness compared to bone. The material interface is treated by using separate FCM discretizations for $\Omega_{\text{phy}}$ and $\Omega_{\text{LT}}$, and weakly enforcing the interface condition as explained in the previous chapter. A load equivalent to the concentrated load is then defined on the flat surface of the surrogate load-transfer block and integrated as an inhomogeneous Neumann boundary condition. The concept is illustrated in Figure 6.2.

This numerical approach has been investigated in the master's thesis of Oztoprak [185]. Therein, the method was verified using numerical examples of solid models of beams subjected to concentrated loads. The verification study shows that moments can be applied on embedded surfaces of FCM models using the coupling approach with similar accuracy to a more direct approach, where the moment is modeled as a distributed traction. Furthermore, it was shown that the approach is applicable to minimally restrained problems, where balanced loads are applied to the body, and Dirichlet constraints are only necessary to restrict the rigid body modes. A numerical example of a combined musculoskeletal of a mobile spinal segment with an FCM model was also presented, which we discuss in the following.

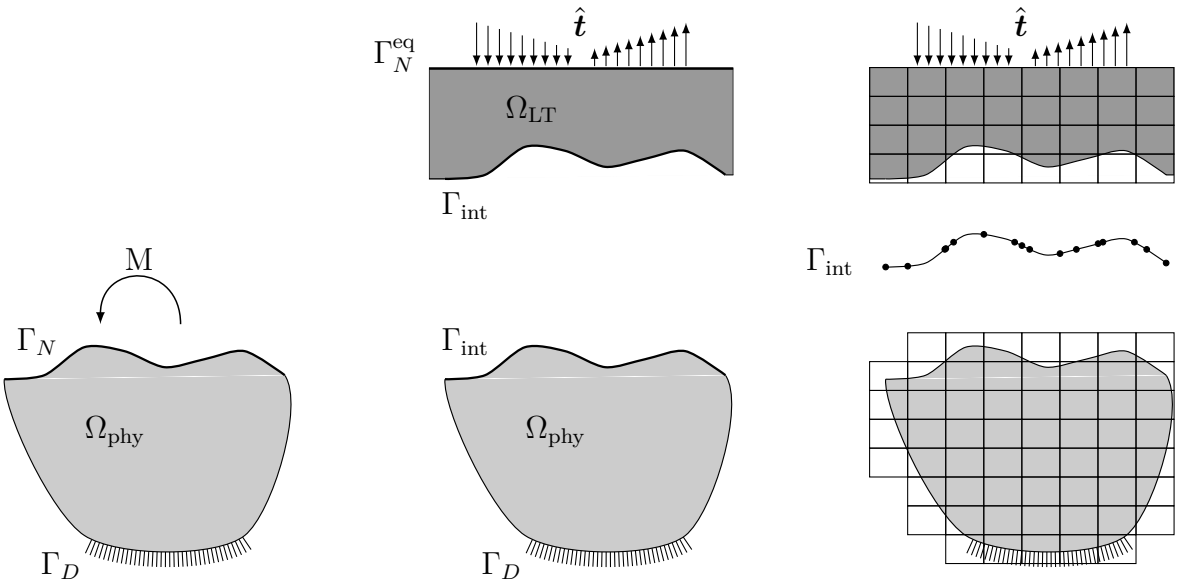


Figure 6.2: Load interface mesh, adapted from [185]

### 6.1.4 Numerical example

As a proof of concept, we present a simple example of the combination of a musculoskeletal model with the FCM. The analysis considers a single spinal segment, where a multibody dynamic simulation is used to determine the reactions at the joint and the support. The reaction forces and moments are then applied as loads in the FCM models of the vertebrae to predict the mechanical stresses.

#### Geometry

A clinical QCT-scan of the spine of a healthy patient who does not suffer from spinal deformities was used in this example.* The QCT scan provides the data to define the geometry and the local bone density for the patient's spine. For an accurate estimation of the bone density distribution, the scan was calibrated through use of the phantoms provided by the manufacturer of the scanner. The complete scan consists of $1533 \times 512 \times 81$ voxels with a voxel size of $0.318 \times 0.318 \times 2$ mm$^3$. Here, the $x$-, $y$- and $z$-axes correspond to the longitudinal, sagittal and frontal axes, respectively.
As a first step, the QCT scans were segmented to identify the geometry of each vertebra separately. Additionally, the location of the centroid of each intervertebral disc and the tangent vectors to the spinal axis were estimated from the scans and recorded. A surface description of the vertebrae was reconstructed from the segmentation using the marching cubes algorithm [154]. The segmented surfaces were further processed (trimming and smoothing) to generate a surface description for the endplates (shown here in Figure 6.3), which is necessary for the imposition of boundary conditions and coupling constraints.

*Image acquisition and processing were carried out at the Department of Neuroradiology, TUM. The efforts of Amirhossein Bayat and Alexander Valentinitsch are gratefully acknowledged.

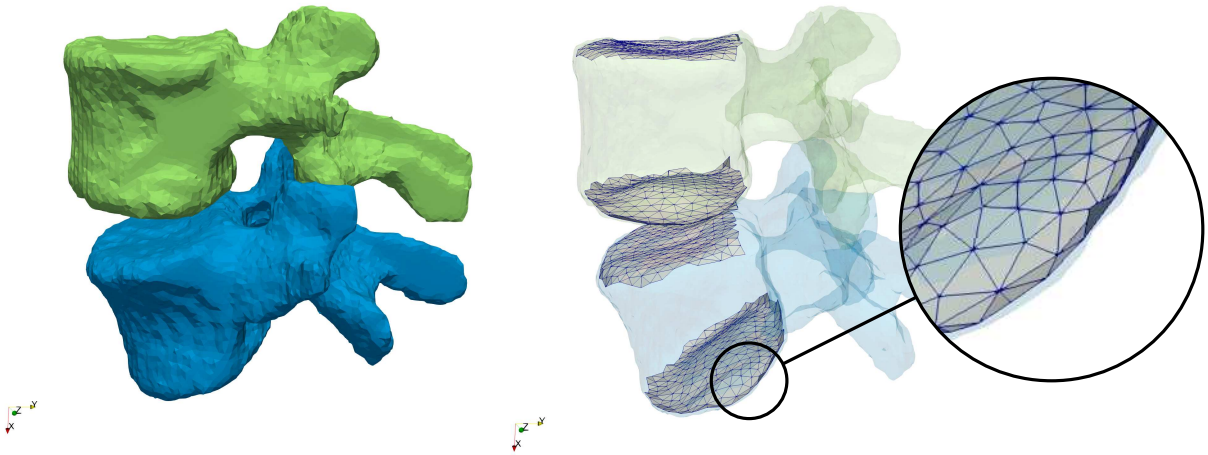

(a) Surface model

(b) Surface meshes for the endplates

Figure 6.3: Segmented L4 and L5 vertebrae

### Musculoskeletal model[†]

The musculoskeletal model considers a single mobile spinal segment (L4–L5), comprised of the two vertebrae and the intervertebral disc. Here, we do not consider the L5–S1 joint in the musculoskeletal model, i.e., the L5 vertebra is fixed relative to the sacrum. The multibody system was modeled using the software `Simpack` (Dassault Systèmes). The geometry models of the segmented vertebrae were imported as surface triangulations. The mass properties and moment of inertia tensors of the vertebrae were estimated based on the reconstructed geometry.

Two points were defined as special "markers" corresponding to the centroids of the L3–L4 and L4–L5 intervertebral discs. The top marker (L3–L4) is used to define the point where external load is applied. The intermediate marker (L4–L5) is used to define a mechanical joint, which models the intervertebral disc as a nonlinear spring damper system. The stiffness and damping coefficients of the joint were calculated depending on the disc's individual geometry [151]. The model of the multibody system is shown in Figure 6.4.

### Constraints and boundary conditions

For this model, we only study the movement in the sagittal plane ($x$-$y$). The spinal segment is fixed at the bottom, i.e. at the inferior endplate of the L5 vertebra, whereas the L4 vertebra has three degrees of freedom (translation in $x$- and $y$-directions, and rotation around the $z$-axis). Similarly, the spring-damper element connecting L4 and L5 has three degrees of freedom. At the top marker (L3–L4), the segment is subjected to a constant vertical load of 500 N and a harmonic moment around the sagittal axis with an amplitude of $10\,\mathrm{N}\cdot\mathrm{m}$ and a period $T = 2\pi$ s. The model does not consider muscle or ligament forces in the analysis.

[†]Musculoskeletal modeling was carried out at the Associate Professorship of Sport Equipment and Sport Materials, TUM, by Tanja Lerchl. Her efforts are gratefully acknowledged.

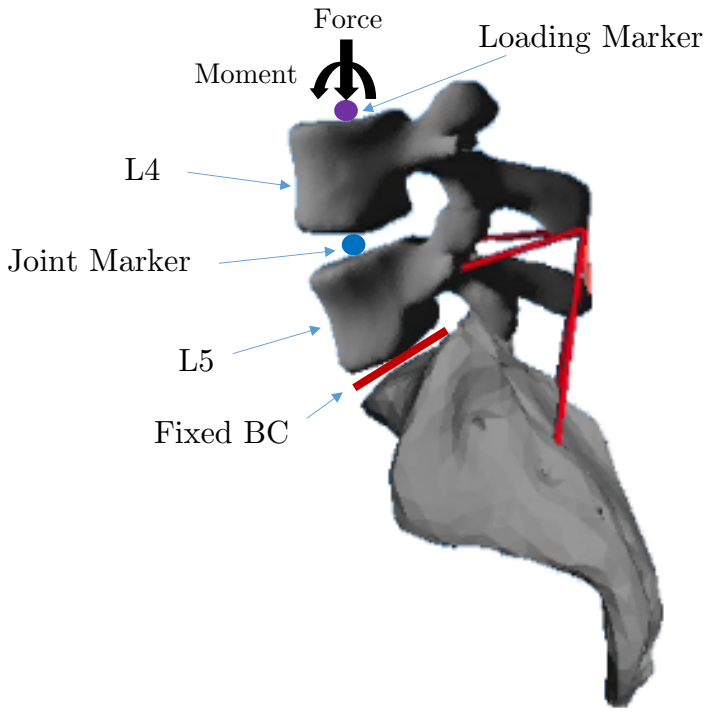


Figure 6.4: Illustration of the musculoskeletal model in the multibody simulation software `Simpack` (Dassault Systèmes), adapted from [185]

### Numerical solution of the multibody system

The multibody dynamic system for the musculoskeletal model was solved for a total simulation timespan of 10 seconds using an implicit time integration scheme and a time-step size $\Delta t = 0.01$ s (1000 time-steps). The computed reactions at the joint and at the support (forces and moments) were recorded, as well as the position and the orientation of the L4 vertebra. The results were exported in a delimited text file using the `.csv` format.

The results were verified by evaluating the equilibrium equation (6.1) for each body at each time step. It was also observed that the dynamic (D'Alembert) forces due to the acceleration of the L4 vertebra were negligible, as they were several orders of magnitude smaller than the applied loads and the resulting reactions at the joint and at the support. This affirms the modeling assumptions for the quasistatic analysis of the elastic FCM model of the bone in a non-inertial reference frame, where each time step is analyzed independently and the D'Alembert forces are neglected, only taking into account the external load and the reactions at the joint and the support.

### FCM model[‡]

The FCM model of the elastic bone considers each vertebra separately. The bounding box for each vertebra was discretized by a uniform grid of finite cells with $4 \times 4 \times 4$ voxels per finite cell. Using the segmentation, cells within the bounding box that lie completely outside the physical domain of the vertebra were identified and excluded from the FCM model. This filtering left 10,970 and 13,414 finite cells for the L4 and L5 vertebrae models, respectively. Sagittal sections through the FCM meshes are shown in Figure 6.5.

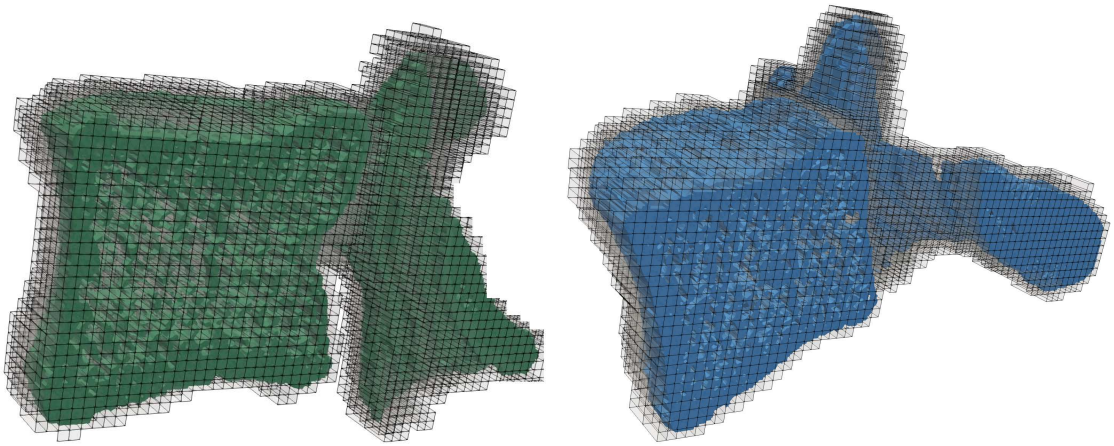

(a) The discretization of L4 (b) The discretization of L5

Figure 6.5: The FCM discretization of the vertebrae, reproduced from [185].

The material properties of the bone's model were assigned voxel-wise. As the material description of the vertebrae is based on a clinical QCT scan, where the resolution of the images does not resolve the trabecular microstructure, a continuum-level material model was used for the bone. Here, we used the heterogeneous material model described by the linear $E$–$\rho$ relationship introduced by Kopperdahl [141]:

$$E = -34.7 + 3230\rho, \tag{6.2}$$

where $E$ is the local Young's modulus in MPa, and $\rho$ is the equivalent mineral density in g/cm$^3$. The equivalent density was obtained from the QCT numbers (Hounsfield units) using the scan's calibration parameters. As the Kopperdahl model can give a negative elastic modulus for voxels with very low density, a cutoff threshold for $\rho = 0.01$ g/cm$^3$ was set. Voxels that are outside the segmentation of the vertebrae (in finite cells that are cut by the boundary), or within the cancellous region of the bone with an equivalent density that is lower than the cutoff threshold were assigned a "void material" with $E_{\text{fict}} = 10^{-4}$ MPa and Poisson ratio $\nu = 0.3$.

For the L4 vertebra, the loads considered are the external loads (constant vertical load, and the harmonic sagittal moment), and the reaction force and moment from the intervertebral disc. The loads acting on L5 are the reaction force and moment from the disc at the superior endplate, and the reactions at the fixed support at the inferior endplate. The

[‡]The model was implemented by Oguz Oztoprak in [185]. His efforts are gratefully acknowledged.

non-inertial reference frame for each vertebra is set in its initial configuration. As the L4 vertebra changes its orientation during the course of the analysis (rigid rotation), the vertical load applied on the top is accordingly transformed.
To apply the concentrated loads in the FCM model, the proposed method of coupling additional load-transfer blocks to the load surfaces was employed. To that end, for the L4 two additional domains were defined, which extend above and below the endplates. For L5, only one load-transfer block was defined to apply the loads from the joint, as the inferior endplate was fixed (Dirichlet boundary condition). The geometry of the blocks were implicitly defined as cuboids that were rotated to align with the tangent vectors of the spinal axis at the centroids of the intervertebral discs. A Boolean difference operation was used to remove the overlap between the blocks and the embedded vertebrae. The load-transfer blocks were assigned a linear elastic material with Young's modulus $E = 10^7$ MPa, and Poisson ratio $\nu = 0.3$—approximately 3 orders of magnitude stiffer than cortical bone. The bounding boxes of the blocks were discretized by Cartesian grids of finite cells of the same size and orientation as the FCM meshes of the bones. This added a total of 5,521 and 3,165 finite cells to the FCM models of L4 and L5, respectively. Using a polynomial degree $p = 4$, the complete models have approximately 900 thousand and 600 thousand degrees of freedom. The FCM discretization of the blocks are shown in Figure 6.6.

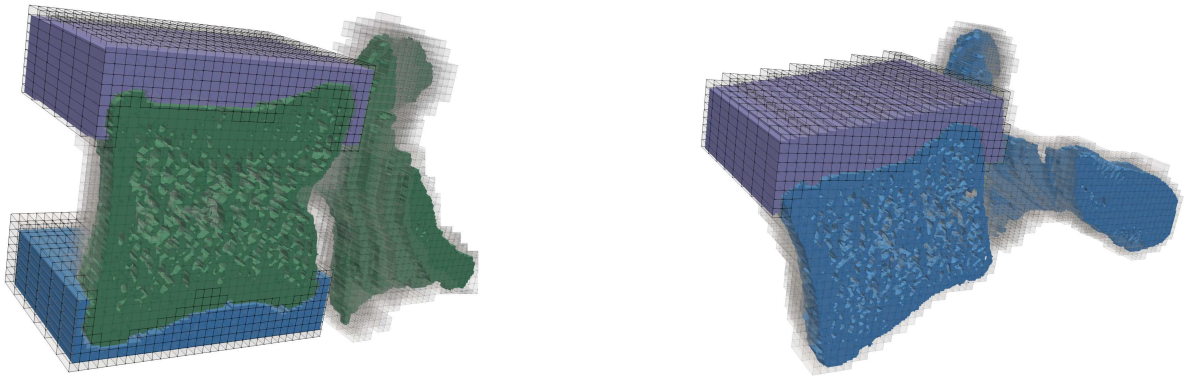

(a) The discretization of L4 with two load interfaces

(b) The discretization of L5 with one loading interface

Figure 6.6: The FCM discretization of the loading interfaces, reproduced from [185].

To apply the distributed loads, rectangular load surfaces were defined on the flat load-transfer blocks. The load surfaces are centered at the previously defined markers which represent the centroids of the intervertebral discs. The forces are applied to the load surfaces as uniformly distributed surface tractions, whereas the moments are applied as varying tractions. Thereby, the application of the loads is consistent with the musculoskeletal model.
The load-transfer blocks were coupled to the FCM meshes of the vertebrae at the interfaces defined by the endplates. To that end, the penalty method was applied, as described in the previous chapter. The penalty terms were numerically integrated using the surface meshes of the endplates, shown in Figure 6.3. Additionally, the clamped boundary condition at the inferior endplate of L5 was weakly enforced, also employing the penalty method. The penalty parameter was chosen empirically as $\beta = 10^{15}$.

As only external loads were applied on L4 without defining a support, it was necessary to constrain its rigid body modes. Here, the external loads are in equilibrium, so the constraints were only applied to remove the six rigid body modes (3 translations and 3 rotations) to result in a stiffness matrix with full rank. This is accomplished by constraining six displacement components at four points as described e.g. in [77] (see Figure 6.7). To that end, Dirichlet constraints were applied on four points of the L4 vertebra using a penalty approach. The constraint points were selected such that they lie within the physical domain of the FCM model, i.e. within the bone with full stiffness. As the external loads are in static equilibrium, there are no reaction forces exhibited at the point constraints.

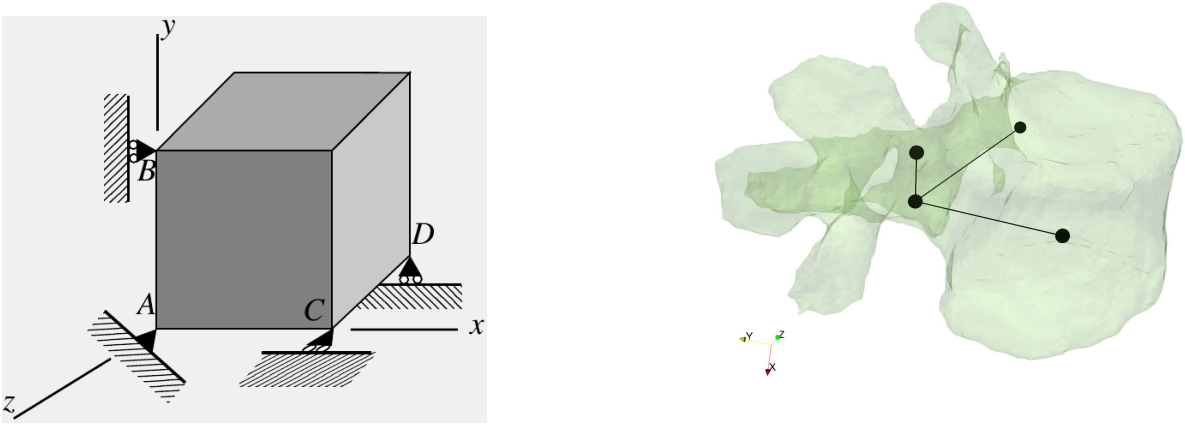


(a) Constraining a three-dimensional body, reproduced from [77].

(b) Four points used to constrain L4

Figure 6.7: Suppressing rigid body modes for the vertebra

### Numerical solution of the FCM model

The FCM analysis was carried out using our in-house high-order framework `AdhoC++`. The quasistatic analysis considers each time-step independently. Therefore, the system of linear equations for the coupled meshes was set up and the Dirichlet constraints were applied, then the system was solved with a new right-hand side for each time-step representing a new load-case.

The penalization of the stiffness in the fictitious domain leads to ill-conditioning of the resulting stiffness matrices. Additionally, the high stiffness contrast between the bone and the load-transfer blocks, and the use of the penalty method for the weak imposition of Dirichlet boundary conditions and constraints exacerbate the ill-conditioning. Hence, the use of a direct solver for this application is necessary. We used the parallel direct solver `Pardiso` provided as part of the Intel Math Kernel Library [114].

Fortunately, the use of a direct solver provides an advantage for the purpose of this application. As we need to solve the same linear system with multiple right-hand sides, the main cost of using a direct solver, namely the factorization of the constrained system matrix, is incurred just once for the whole analysis. Hence, we can cache the factorized

matrix and only carry out the forward and backward solution steps for each right-hand side.
Running on a six-core Intel® Core™ i5 9600K @4.6 GHz CPU, the quasistatic analysis of the L4 vertebra required a run-time of approximately 3 minutes to integrate the stiffness matrix and 3 minutes for the Cholesky factorization of the matrix. For each load-case (corresponding to a time-step of the multibody dynamic simulation), the forward/ backward solution requires approximately 3 seconds. Solving the FCM analysis for 50 time-steps for the whole timespan ($\Delta t = 0.2$ s), the whole computation, including post-processing (numerical computation of the stresses and writing the result files disk), takes under 20 minutes for each vertebra.

### Results

A surface mesh for a sagittal section through the vertebrae was generated using `ParaView` [10]. This mesh was used for the visualization of the numerically calculated von-Mises stresses, which are shown for the L4 vertebra at three different time-steps in Figure 6.8, alongside the respective animations of the multibody dynamic simulation. Here, the vertebra is shown in the initial configuration, which is used for the quasistatic analysis as a non-inertial reference frame. The elastic deformations of the vertebra are scaled by a factor of 30 for better visibility.
In the first time-step (Figure 6.8a), the L4 vertebra is subjected to the vertical load, and the corresponding reaction force and moment at the joint. Note that a moment is necessary at the joint to balance the couple of the applied force and the reaction force, which are not vertically aligned, as the loading marker is slightly in front of the joint marker (see Figure 6.4). Hence, in the first time-step the vertebra is subjected to both axial compression and bending in the sagittal plane. The computed stresses show high stresses (compression) at the anterior (front) portion of the cortical shell, whereas at the posterior part of the shell the tensile stresses caused by the bending are partially compensated by the axial compression load. Here, we point out that the model neglects the actions of muscle and ligaments which stabilize the spinal segment. Including these forces in the analysis could significantly influence the results, as demonstrated in [259].
The second time-step shown (Figure 6.8b) corresponds to the state where the applied harmonic sagittal moment has the maximum magnitude (10 N.m.), and the joint is in flexion. Here, the stresses state is more dominated by the bending, compared to the first-time step. The computed stresses at the anterior part of the cortical shell are significantly higher, whereas the posterior part of the shell exhibits higher stresses in tension. Whereas the annulus fibrosus is able to transmit tensile forces [25], this result was possibly exaggerated due to the missing ligament forces.
In contrast, in the last time-step (Figure 6.8c), the applied moment has the maximum magnitude in the opposite direction with the joint in extension. Here, the bending is in the opposite direction, meaning that the anterior part of the shell is under tension, whereas the posterior part is under compression.
Overall, the numerical prediction of the stresses agree well with the loading states. The results do not exhibit large oscillations, and there are no discernible discontinuities at the element boundaries, which indicates a low approximation error. The model includes

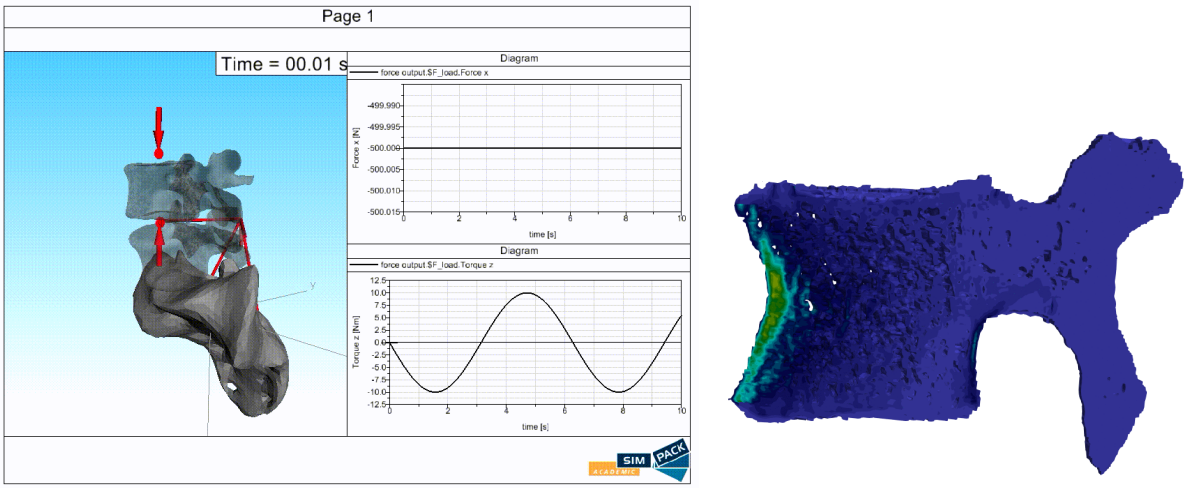


(a) $t = 0.01$ s, vertical load

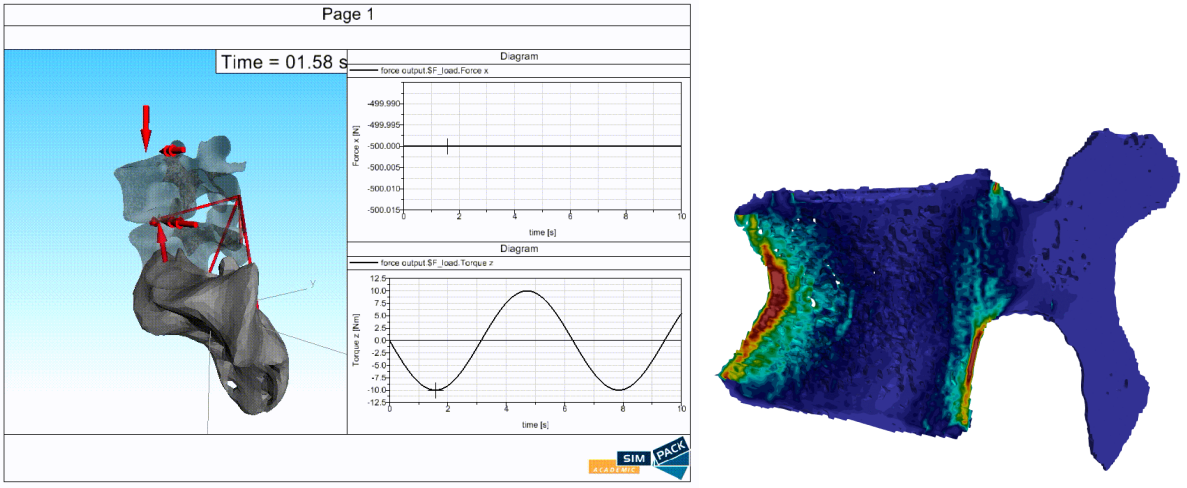


(b) $t = 1.58$ s, vertical load and maximum flexion

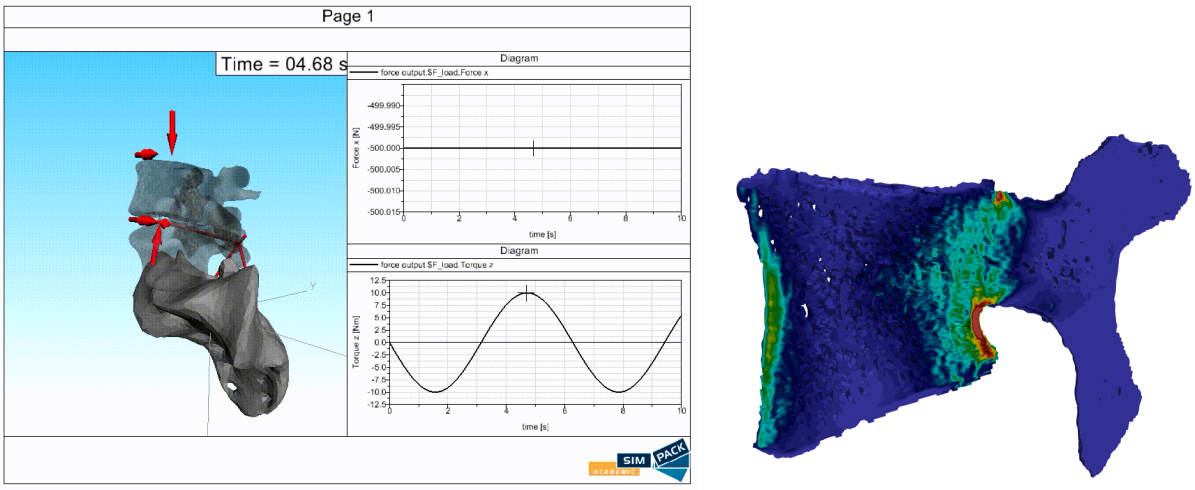


(c) $t = 4.68$ s, vertical load and maximum extension

Figure 6.8: Results of the combined musculoskeletal model and FCM analysis of L4, equivalent stresses

singularities, e.g. at the outer edges of the boundaries of the endplates, and at the re-entrant corner of the pedicle. Local refinement of the meshes to treat these singularities would further reduce the approximation error. For a more extensive discussion of the results and the setup of this example, the interested reader is referred to [185].

### 6.1.5 Discussion

In this application, we have presented a numerical approach for the inclusion of concentrated loads in patient-specific FCM models of the vertebra. The results demonstrate the applicability of the FCM as part of a pipeline for patient-specific biomechanical modeling, where the forces are calculated using musculoskeletal models.

The proposed approach provides a convenient way of including the concentrated loads in a way that is consistent with the musculoskeletal simulation. No additional assumptions are introduced by this approach, and it requires no additional modeling effort. Hence, it is well suited as part of an automated workflow, where the estimated forces from the musculoskeletal simulation are directly input to the FCM simulation kernel without the need for additional manual post-processing.

There are, however, some limitations to the proposed approach. As the load-transfer blocks are modeled by three-dimensional solid elements, the additional coupling leads to a significant increase in the size of the linear system. In comparison, coupling approaches which utilize beam or shell elements to apply constraints on the load surfaces result in a marginal increase of the total number of degrees of freedom. Further work should investigate the applicability of coupled FCM–shell elements for the imposition of moment loads in FCM models. Additionally, the very stiff material assigned to the load-transfer block adds a constraint to the deformation of the load surface which prevents warping deformation, that is out of plane deformation caused by torsional loads on non-circular cross sections. Fortunately, such deformations are not a dominant mode in the intended use-case of this approach—namely the simulation of the biomechanics of the spine.

Future work should address the use of local refinement, e.g. through the use of the multi-level *hp*-scheme as described in the previous chapter, which would lead to more efficient computations. Especially the load-transfer meshes can benefit from local refinement at the coupling interface. Further optimization of the computational performance could be achieved by using axis aligned FCM meshes for the load-transfer blocks. In this work, all FCM meshes were aligned to the scan. Rotating the FCM meshes for the blocks to match their orientation (aligned with the tangent vectors of the spinal axis at the respective markers) would significantly reduce the number of cut cells, thereby reducing the computational cost.

More complex musculoskeletal models consider several vertebral segments, which also makes it necessary to include muscles and ligaments to stabilize the model. These are modeled as nonlinear force elements and passive elastic elements that are attached to the bone at single points. The resulting point forces are more challenging to include in the model, in contrast to the forces resulting from the intervertebral discs, which are distributed over the endplates. A possible approach to include such forces in FCM models is to distribute the muscle forces over small patches on the surface, and applying local mesh refinement at the points of attachment.

## 6.2 Vertebra–screw simulation

The numerical simulation of vertebra–screw systems is of high importance. An adequate resolution of the trabecular microstructure at the bone–implant interface is necessary, which makes accurate simulations very computationally intensive and necessitates the use of high-performance computing resources. In the work presented in the following section, we apply the FCM in conjunction with the multi-level *hp*-refinement scheme—as outlined in the previous chapter—to resolve the bone–implant interfaces in finite-cell analysis of vertebrae with pedicle screws. Local refinement allows us to resolve the microstructure at the interface at a moderate computational cost. A numerical example is presented to illustrate the applicability of the numerical scheme for the solution of a high-resolution vertebra–screw model.

### 6.2.1 Introduction

Pedicle screw rod instrumentation is a widespread surgical procedure used to treat a diverse range of spinal disorders [252]. Through spinal fusion, two or more vertebrae are permanently joined to treat instabilities or correct spinal deformities, e.g. scoliosis (abnormal lateral curvature of the spine) [164]. To this end, two screws are inserted posteriorly through the pedicles into each vertebral body. The pedicle screws are joined together with metal rods that restrict relative motion of the vertebrae, thereby stabilizing the spine. In interbody fusion, the intervertebral disc is additionally removed and replaced by a bone graft contained within a metallic cage, which bonds the two vertebrae together. For corrective surgeries, forces are applied to the screws and rods in order to correct the abnormal curvature. An X-ray image of a fused vertebral segment is shown in Figure 6.9.

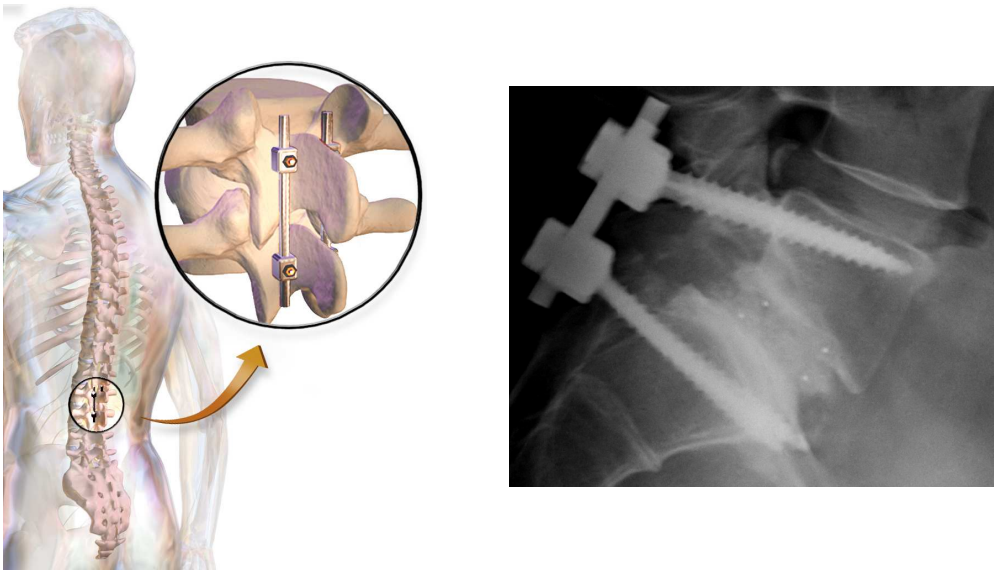

(a) Schematic showing fusion rods [21] (b) X-ray image of fused L5 and S1 [205]

Figure 6.9: Spinal fusion of a vertebral segment

The decision of how and when to perform surgery is a highly subjective one based on the surgeon's experience. It has been demonstrated in clinical trials that surgery is not beneficial for patients with unspecific back pain [158]. However, for many other patients spinal fusion is still indicated due to conditions like spondylolisthesis, spinal canal stenosis, fractures or tumors [177]. Despite the extensive use of pedicle screw fixation, issues such as screw loosening and breakage are recurring complications [194]. Particularly in elderly patients with poor bone quality due to osteoporosis, anchorage of the pedicle screws remains challenging [182].

The anchorage of pedicle screws depends mainly on the local quality of the trabecular bone at the screw's interface. To improve anchorage, the mechanical strength of this interface can be enhanced, e.g. through the use of bone cement [124], or screws with hydroxyapatite coating [100]. Furthermore, surgery-related parameters (screw size, orientation and insertion points) should be optimized to achieve better anchorage.

Finite element analysis of bone–implant interaction is a valuable tool in studying the fixation of implants. Numerical models can predict pull-out strength [262, 61], also for different loading conditions [35]. Furthermore, FE models can be used to assess the stability of the interfaces resulting from different configurations (e.g. variable screw sizes [196, 165, 222] and angles [172]), which can be used to assist surgeons in achieving better outcomes.

However, accurate finite element simulations of fused vertebrae with pedicle screws can be very challenging. As the anchorage depends mainly on the interaction between the screws and the trabecular bone in the peri-implant region, the stability of the implants depends on the local trabecular microstructure [261]. Hence, spatially resolving the trabecular microstructure is necessary for an accurate simulation of the bone–screw interface [263]. It has also been shown that finite element models with simplified screw geometry underestimate the resulting mechanical stresses [222]. The geometry of the trabecular microstructure can be resolved from micro-CT or HR-pQCT scans. Currently, such scans cannot be performed in vivo for the human vertebra, which limits the possibility of patient-specific FE analysis. Nevertheless, simulations that are based on in vitro models are useful in gaining a better understanding of bone–implant interaction.

The very complex geometry of the bone–screw interface presents a challenge for finite element modeling, as generating an analysis suitable mesh at a microstructural level is a difficult task [162]. To that end, a surface triangulation of the trabeculae is generated, and used together with the CAD model of the implant to generate a boundary conforming tetrahedral mesh. In studies dealing with the numerical modeling of dental implants, generating quadratic tetrahedral meshes for small volumes of interest surrounding the screws already generates around 10 million elements with 30 million degrees of freedom [265, 161, 163]. Including bone-cement in the model, or assigning different material properties for the peri-implant zone would make this even more challenging.

Alternatively, high-resolution micro-voxel FEM ($\mu$-FEM) models based on micro-CT images which resolve the trabecular microstructure can be used for numerical studies of bone–implant interfaces [262, 242, 211, 35]. $\mu$-FEM models are considered the current gold standard for the simulation of vertebra–screw interaction. As described in Section 2.3.2, the $\mu$-FEM directly converts voxels of the micro-CT scan to hexahedral finite elements. Thereby, it can resolve the geometry of the trabecular microstructure without complex

mesh generation procedures. As the $\mu$-FEM is voxel-based by definition, the model of the screws, typically implicit geometrical CAD models have to be voxelized. Since $\mu$-FEM models have meshes with very small element sizes, local solution features such as stress concentration and singularities in the peri-implant region are also adequately represented. However, due to the very high resolution of the models origination from micro-CT scans and the uniform element-size in $\mu$-FEM models, the resulting finite element systems for models of regions of interest are very large (typical in the range of hundreds of millions of degrees of freedom), making the use of supercomputing power often necessary [80]. Hence, in many published studies, e.g. [262, 263, 35], only part of the vertebra around the screw can be modeled, applying simplified boundary conditions at the surfaces bounding the volume of interest, which limits the applicability of $\mu$-FEM modeling of more complex configurations involving multiple vertebrae.
To address these shortcomings, in this work we use the finite cell method (FCM) for the simulation of vertebra–screw mechanics. This approach provides several benefits making it very suitable for the task. Similar to the $\mu$-FEM, the FCM requires a low human modeling effort in setting up the simulations, as the FCM does not require the generation of boundary-conforming meshes. As demonstrated in Chapter 4, FCM models based on high-resolution CT images can accurately simulate the biomechanical behavior of vertebral bodies. Furthermore, with an adequate approach to deal with the weak discontinuity at the material interface, and employing local refinement as necessary, the FCM can accurately model the bone–screw interface using a moderate number of degrees of freedom. Additionally, thanks to the inherent flexibility of the FCM in utilizing various types of geometric descriptions, no additional effort is required for the re-parametrization of the geometries of either the bone or the screws. In the following, we outline the proposed simulation approach, and present a numerical simulation of a vertebra with two pedicle screws.

### 6.2.2 Vertebra–screw FCM model

Here, we assume that the screw is in full contact with the bone at the interface, and treat the contact as a material interface problem. We use linear elastic material models for both the bone and the screw. The material interface problem is treated numerically in the framework of the FCM as described in Chapter 5. The workflow of our simulation approach is illustrated in Figure 6.10.
We use two separate geometric descriptions for the vertebra and the screws. For the vertebra, the geometry and the local material properties are described by a CT scan with sufficiently fine resolution to distinguish the trabecular microstructure, e.g. a micro-CT or high-resolution peripheral quantitative CT (HR-pQCT) scan. Segmentation of the high resolution scan is necessary in order to identify the structure of the vertebra within the scan without the surrounding soft tissue. The binary image resulting from the segmentation is used in conjunction with a threshold filter of the original scan to create an image-based FCM model, as presented in Chapters 3 and 4.
The FCM model for the screws is based on a B-Rep model created using CAD software. In the context of FCM, the geometric models only needs to provide a reliable point membership test. To that end, the B-Rep model, which describes the bounding surfaces of the

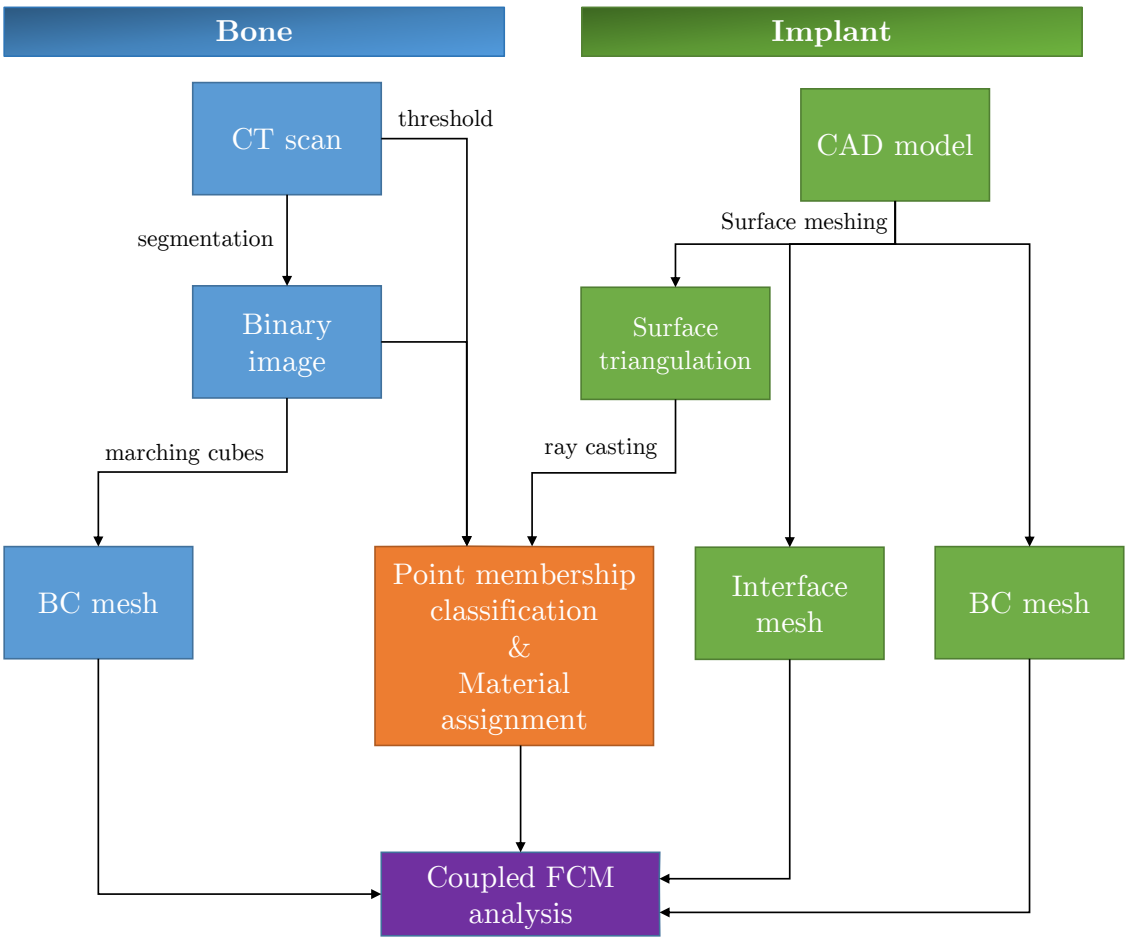


Figure 6.10: Workflow of coupled FCM analysis of the vertebra–screw model

screw as trimmed NURBS patches can be directly used with a ray-casting algorithm. This is possible if the B-Rep model is free of modeling flaws. However, using the exact surface description provided by the NURBS surfaces can be computationally expensive. Instead, a water-tight surface triangulation of the CAD model can be used for the ray-casting-based point membership test. An alternative approach was presented by Wassermann et al. [257], where flawed CAD models can be directly used for the point membership test.

Here, we highlight the fact that the FCM for interface material problems can be used to easily combine different types of material descriptions in a single model. There is no need to generate a boundary-conforming mesh, and the geometrical model is used for the numerical integration of the element matrices. Hence, the FCM bone–implant requires no additional effort for geometry re-parametrization, in contrast to conventional approaches employing $p$-FEM, where a B-Rep model of the CT-based bone geometry needs to be first generated [129], or voxel based $\mu$-FEM analysis where the implant's geometry is voxelized [262].

The FCM models of the vertebra and the screws are then combined in a single analysis. We use separate discretizations for the bounding box of each object, which is embedded in a regular grid of finite cells. The screws are then positioned within the vertebral body using a CAD software. In the FCM grid describing the vertebra, the bone tissue displaced by the screws is accounted for through a Boolean difference operation. Here, cannulated screws require additional attention to remove the bone tissue within their hollow shafts.

To resolve singularities and stress concentration caused by the geometry, material interface and boundary conditions, we use the multi-level $hp$-refinement to locally refine the FCM meshes as described in the previous section. Here, the coupled FCM approach allows us to refine each mesh independently. We refine the meshes a priori guided by the geometry. Within the mesh for the vertebra, we expect singularities at the bone–screw interface, at the re-entrant corner of the pedicle, and at the intersections with the shafts of the screws at the points of insertion. For the meshes of the screws, we expect singularities around the threads—especially at the concave geometry at the roots of the threads—and at the shafts where the contact zone ends. Additionally, clamped boundary conditions induce singularities. Accordingly, we apply a local refinement on each mesh towards its expected singularities as described in Section 5.3.2.

The overlapping multi-level $hp$-FCM meshes are then weakly coupled at the bone–screw interfaces. To that end, we use the penalty method as described in Section 5.2. Other coupling methods, such as e.g. Nitsche's method, are also applicable here. For the numerical integration of the penalty terms along the material interface, surface meshes can be easily generated from the CAD model of the screw.

The boundary conditions are applied to each mesh separately. Depending on the load-case being studied, forces and/or moments are applied to the screws, whereas the vertebra is fixed. Since the CAD models of the screws have well-defined surfaces for load-application, defining the forces and moments as distributed tractions is easily achieved. The tractions are included in the respective meshes of the screws as inhomogeneous Neumann boundary conditions. For the numerical integration, surface meshes for load-bearing surfaces can be easily generated utilizing the CAD models. Dirichlet boundary conditions are weakly enforced, also using the penalty method. For the numerical integration, a surface mesh

of the endplates can be generated using the marching cubes algorithm and the segmented binary image.

### 6.2.3 Numerical example[§]

In the following, we present an example of a vertebra–implant simulation using the multi-level *hp*-FCM. It is noteworthy that the numerical model considers the whole vertebra with the local refinement resolving the microstructure at the interface.

#### Setup

We consider a lower thoracic vertebra into which two cannulated pedicle screws are inserted. We use the FCM with the weak coupling approach to solve the interface problem, and employ multi-level *hp*-refinement to resolve the high gradients around the threads of the screws.

The geometry of the vertebra originates from a CT scan with high spatial resolution, carried out for a formalin-fixated specimen of the eleventh thoracic vertebra of an 84-year-old donor. She had dedicated her body for educational and research purposes to the local Institute of Anatomy prior to death, in compliance with the local institutional and legislative requirements. Images were acquired by using a whole-body 256-row CT scanner (iCT, Philips Medical Care, Best, The Netherlands) after 24 hours of degassing. Scan parameters were a tube voltage of 120 kVp, a tube load of 585 mAs, an image matrix of $1024 \times 1024$ pixels, and a field of view of 150 mm. Transverse sections were reconstructed with an interpolated voxel size of $146 \times 146 \times 146$ $\mu$m$^3$, and the intensity values of the CT images were calibrated with a reference phantom (Mindways Osteoporosis Phantom, San Francisco, CA, USA) to derive calcium hydroxyapatite values in (mg/cm$^3$).

The geometric model of the screws is a B-Rep CAD model of a Viper2-Screw (DePuy Synthes, Umkirch, Germany), kindly provided to us by the manufacturer.

The material properties for the vertebra were resolved on the voxel level, as a threshold was set to the intensity values to distinguish the trabecular structure. The voxels that are identified as inside the bone were assigned a Young's modulus $E^{(1)} = 10$ GPa, and Poisson ratio $\nu = 0.3$, which are commonly used parameters in HR-pQCT based voxel FEM [186]. The material of the screws is titanium with $E^{(2)} = 100$ GPa and $\nu = 0.3$.

The considered load case simulates a pull-out test, where the vertebral body is clamped and the screws are pulled axially outwards—as depicted in Figure 6.11. The Dirichlet boundary conditions are defined as clamping of superior and inferior end-plates, whereas the Neumann boundary condition is defined on the screws head, as a uniformly distributed axial force.

[§]This section is based on work that was published in [75]. The main scientific research as well as the textual elaboration of the publication was performed by the author of this work.

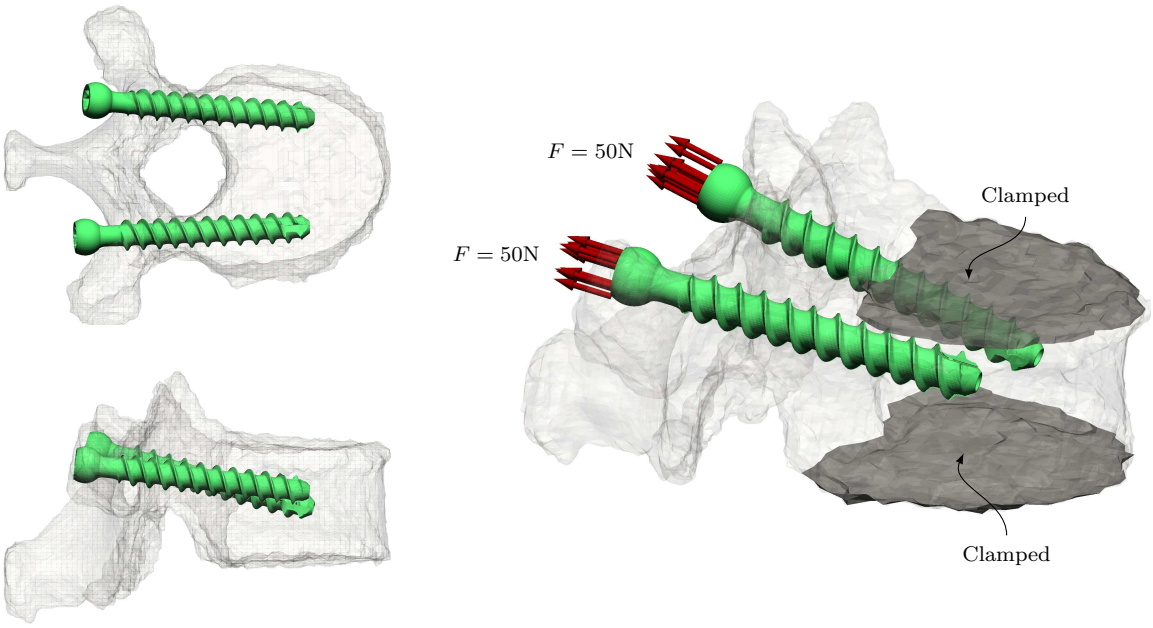


(a) Geometry (b) Boundary conditions

Figure 6.11: Pull-out test

### Discretization

#### *hp*-FCM

The complete model of the vertebra–screw system was setup virtually by combining both geometric models as described in the following. First, the CT-scan was segmented using `ITK-SNAP` [274] to obtain a separate model of the vertebral body without the surrounding tissue. This segmentation only considers the outer boundary of the vertebra, and does not distinguish between cortical and trabecular bone.

The CAD model of the screws was suitably positioned in the same coordinate space. To carry out the point membership test on the CAD model, a watertight surface triangulation of the screws was created using `Rhinoceros` [203]. The surface triangulation was then utilized by a ray tracing algorithm [19], to determine whether a given integration point lies within the screws' geometry.

The first FCM mesh is used to discretize the embedding domain of the vertebral body. The mesh is axis-aligned with the CT-scan. The FCM model uses the geometric description based on the voxel data, as presented in [209, 268]. The geometry is defined by applying a threshold to the CT-scan to define the bone-structure and subtracting the screws through a Boolean operation. To account for the hollow shafts of the screws, an additional cylinder at the central axis of each screw was subtracted. The numerical evaluation of the domain integrals performs an intersection of the voxel grid with the refined FCM mesh to give the integration sub-cells. This is necessary as the number of voxels per spatial direction for one finite cell is not a power of two.

To resolve the stress concentration, the mesh is refined using the multi-level *hp*-scheme

towards the cusps of the screws' threads (concave geometry) and towards the re-entrant corner at the pedicle. The second FCM mesh is used to discretize the embedding domain of the screws. This mesh is refined towards the roots of the screws' threads, where stress concentration within the screws is expected. The spacetree scheme is used for the numerical integration on the second mesh.
The complete discretization results in a total of $1,322$ finite cells for first mesh and 155 finite cells for the second mesh. Using polynomial degree $p = 3$ and $k = 3$ refinement levels, the discretization has approximately 1.13 million degrees of freedom. The final refined meshes are depicted in Figure 6.12.
To control the ill-conditioning of the stiffness matrices, the fictitious domain in both meshes is given a stiffness of $E_{\text{fict}} = 10^{-4}$ GPa and $\nu_{\text{fict}} = 0.3$. The FCM model contains badly cut cells, which are expected in cases involving complex geometry, resulting in an ill-conditioned matrix even with relatively low polynomial degrees [58]. Hence, the chosen fictitious stiffness is relatively high. Nevertheless, as discussed at the end of Section 5.4.2, the introduced modeling error is expected to be much lower than the approximation error for this complex model.

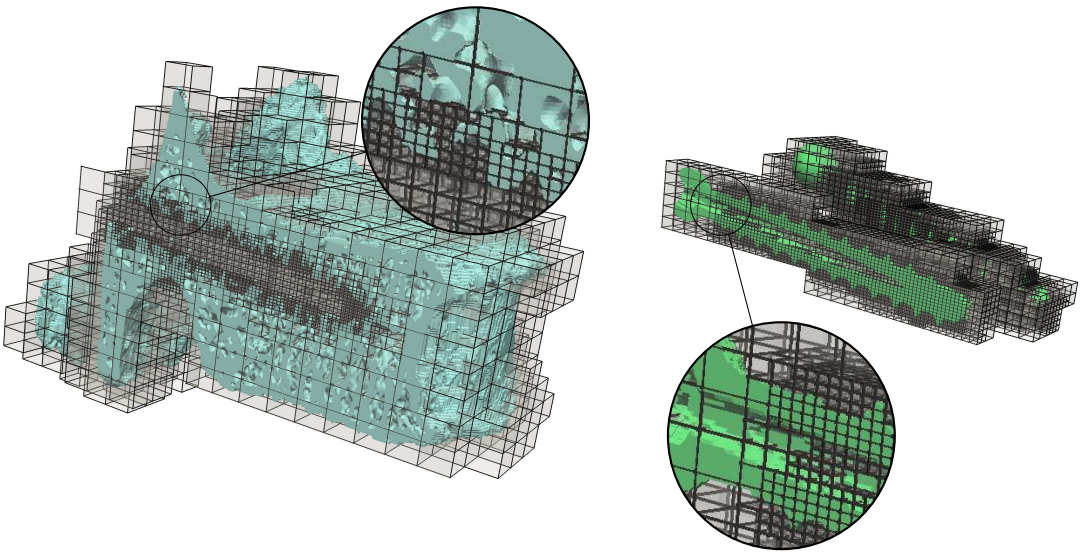

(a) Vertebra (b) Screws

Figure 6.12: Discretization using FCM

### Material interface

The penalty approach (see (5.8a)) was used to couple the meshes with $\beta_{12} = 10^9$. To integrate the coupling terms, a fine surface triangulation for the bone-screw interfaces was created using `Rhinoceros`, by meshing the outer surfaces of the screws. For an accurate and efficient evaluation of the surface integral, the triangulation was intersected with the refined finite cell grid, as shown in Figure 6.13. The triangles were then associated to the finite cell pairs from the two meshes, such that the coupling terms were added to the assembled stiffness matrices only once per finite-cell pair.

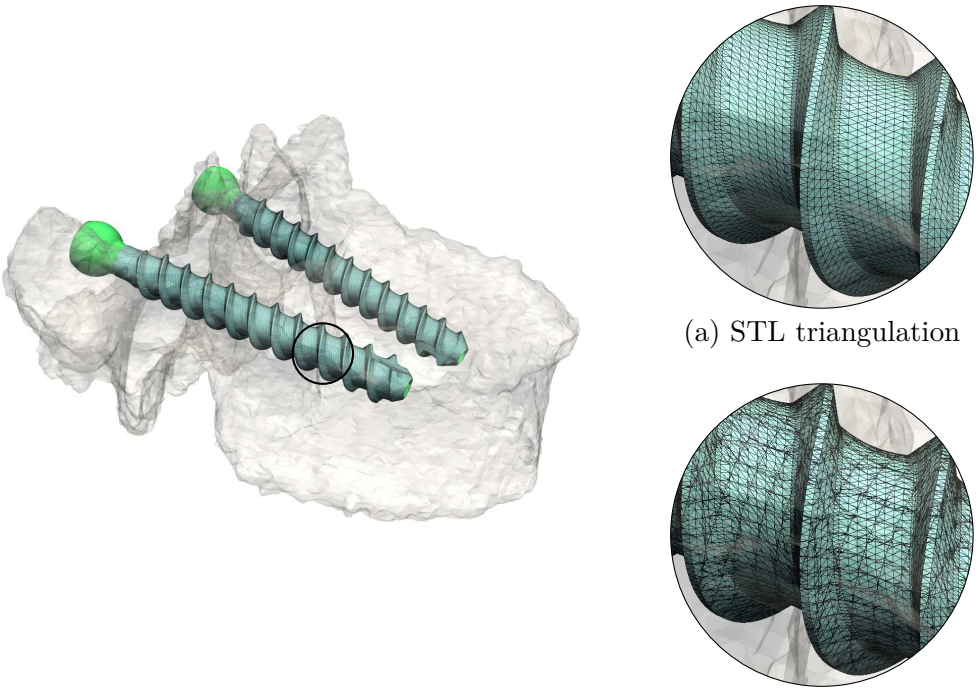

(a) STL triangulation

(b) Intersected triangulation

Figure 6.13: Discretization of coupling surface

### Boundary conditions

Dirichlet boundary conditions were applied at the superior and inferior end-plates of the vertebra. These were weakly enforced using the penalty method, with the penalty terms integrated over a surface triangulation. The surface description was generated using the marching cubes algorithm and the segmentation. The penalty value was selected empirically, $\beta_D = 10^7$. The Neumann boundary conditions modeling the axial load on the screws were applied on a surface mesh created from the CAD model. The surface mesh was also intersected with the faces of the refined FCM mesh, to allow for a more accurate evaluation of the Neumann integral.

### Solution and numerical results

The resulting system of linear equations was solved using the parallel direct solver `Intel® Pardiso` which is provided as part of the Intel Math Kernel Library [114]. The simulation was run on two eight-core Intel® Xeon® E5-2690 @ 2.9 GHz CPUs. The model takes approximately 40 minutes for the integration, solution and post-processing. Visualization was carried out using `ParaView` [10] on the same hardware.
The surface of the trabecular bone was recovered using `ParaView`, for an axial and a sagittal section. The recovered surface was used for the plots shown here. The computed displacements are depicted in Figure 6.14. It can be observed that the applied boundary conditions are fulfilled, and that the displacement field appears continuous across the interface.
The von-Mises stresses calculated for the screws and the bones are depicted in Figure 6.15

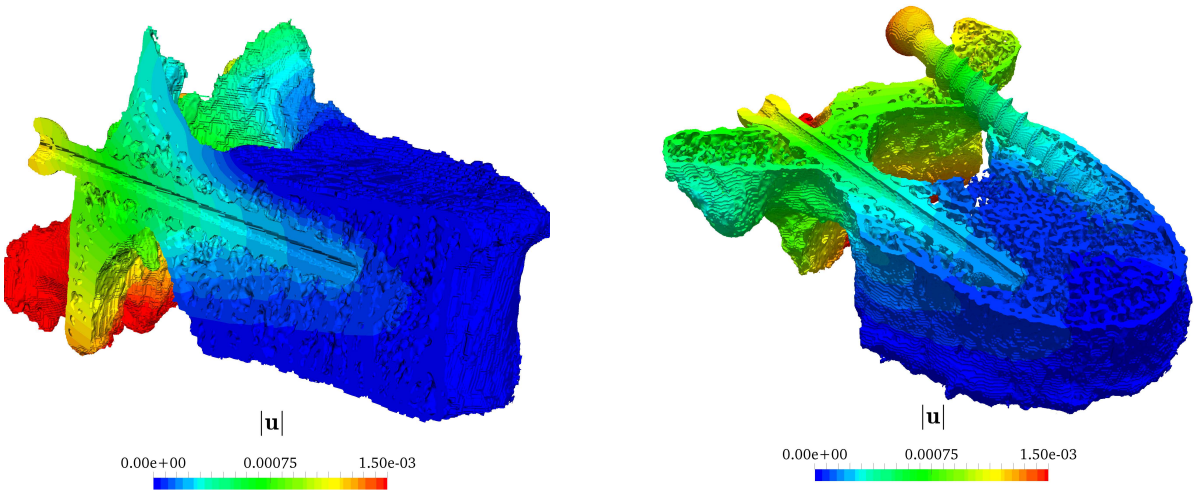


(a) Sagittal section (b) Axial section

Figure 6.14: Vertebra with pedicle screws: numerical approximation of displacements

for a sagittal and an axial section. The numerically approximated stresses are continuous within the screw's geometry, with no discernible jumps at element boundaries or large scale oscillations. This indicates a low discretization error.
High stresses are visible in the neck region between the applied load and the vertebra. Additionally, a bending stress distribution is observed for the helical thread, with the maximum stress occurring at the roots of the thread. In the vertebra, the stress concentration is localized around the screws, and at the pedicle's re-entrant corner, which is a common site of fracture initiation. Similar stress distribution patterns were also reported for simulations using $\mu$-FEM models [261, 263, 211, 35]. Altogether, it can be concluded that the numerical results are mechanically plausible, and correspond well to the applied load case.

### 6.2.4 Discussion

In this application, we demonstrated that the FCM for material interface problems in conjunction with the multi-level *hp*-refinement scheme is directly applicable for the simulation of geometrically complex vertebra–screw models. Furthermore, we demonstrated that the flexible nature of the FCM in dealing with different types of geometric description allows for an easy combination of the image-based model of the vertebra and the CAD-based model of the screws. Together with the first application presented in this chapter, the results showcase the potential of the FCM as an efficient tool for the accurate simulation of material interface problems in bone mechanics.
As an embedded domain method, the FCM is able to resolve the complex geometries of the trabecular microstructure, and that of the detailed CAD-model, without the need for time-consuming mesh generation procedures. Using the weak coupling approach, the FCM can also represent the weak discontinuity at the material interface, thereby

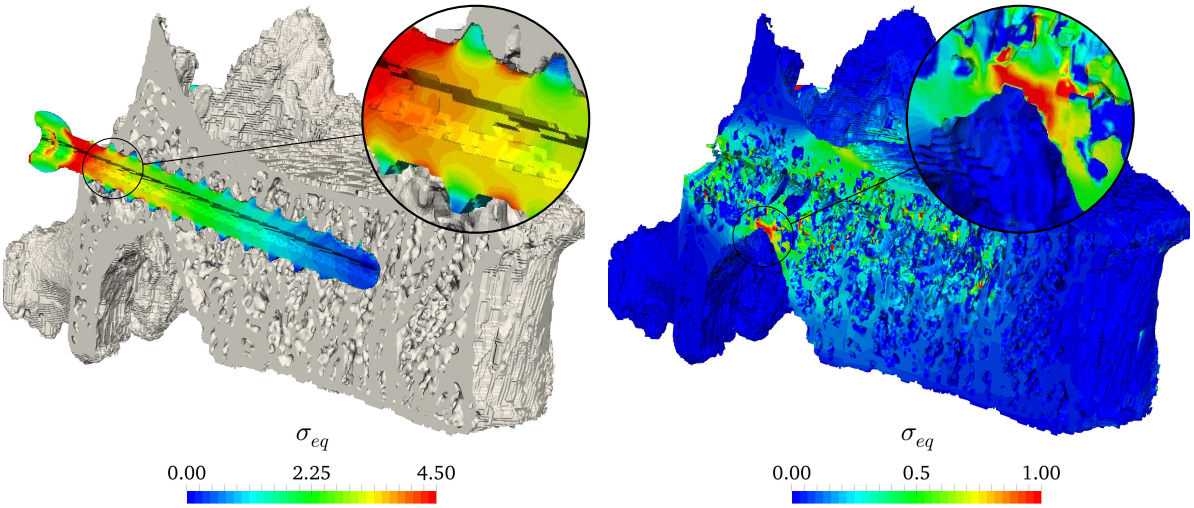


(a) Sagittal section

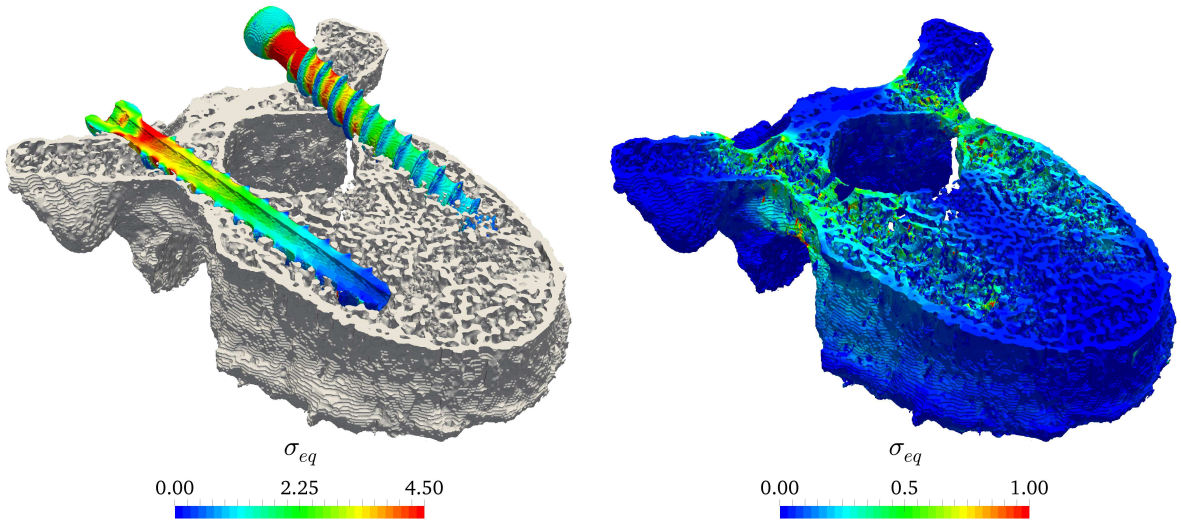


(b) Axial section

Figure 6.15: Vertebra with pedicle screws: numerical approximation of von-Mises stresses

recovering its favorable convergence properties. Employing the multi-level *hp*-scheme for local refinement allows us to accurately represent the complex stress state at the bone–screw interface using a moderate number of degrees of freedom (approx. 1 million degrees of freedom), while considering the whole vertebra with two pedicle screws. Furthermore, using separate meshes for each object allows for an effortless combination of different types of geometrical description without need for any re-parametrization (voxelization of the screw, surface meshing of the vertebral body).

There are, however, some limitations to our proposed approach for the simulation of vertebra–screw models. We used a linear elastic material model for both the bone and screws, which is used in the current gold standard of $\mu$-FEM simulations. However, this oversimplifies some aspects of the problem. For instance, it has been recently shown that pre-stresses in the bone induced by the insertion process are significant and need to be included in the models for an accurate simulation [72]. More sophisticated contact models also allow for interface de-bonding for a more realistic scenario [61].

Moreover, due to the ill-conditioning of the stiffness matrices resulting from the FCM discretization, we are restricted to the use of direct linear system solvers, which limits the size of the largest system we can solve. The simulation of larger and more complex configurations—involving several vertebrae and fusion rods—would estimate the loads on the screws more realistically. To be able to solve larger models, or models with higher resolution, the use of an iterative solver is necessary. Recent work shows that using a multi-grid approach as a pre-conditioner is an effective approach for multi-level *hp*-refined FCM grids [118].

The results presented in this application suggest that the FCM can be directly applied for the numerical simulation of similar bone–implant problems. For example, the simulation of femurs with implanted stems should be easily applicable with the proposed scheme, presenting even fewer challenges. Another application with a very similar setup is the simulation of dental implants, which can make use of the FCM to easily model problems involving several layers of materials.

In this work, we have used a priori refined meshes, with a geometrically-driven local refinement towards points where singularities are expected. The use of automatic refinement based on an error estimator would help to further improve the numerical efficiency of the proposed method. The development of error estimators for the FCM is a topic of active current research [62].

# Chapter 7

# Conclusion

## 7.1 Summary and conclusion

In this thesis, we have investigated the suitability of the finite cell method (FCM) as a simulation tool for the biomechanical analysis of the human vertebra, and proposed effective solutions to overcome its limitations.

We presented a new validation study for the FCM, which considered micro-CT-based models of human vertebral bodies. The validation experiments used digital volume correlation to estimate the displacement fields within the vertebral bodies under axial compression. The boundary conditions for the FCM models were interpolated from the DVC data and weakly enforced using the penalty method. The numerical predictions of the displacements were compared to the DVC measurements of the internal fields for validation. The results show a very good agreement between the FCM simulations and the experiments, underlining the potential of the micro-CT-based FCM as an attractive alternative simulation approach to the well-established $\mu$-FEM.

We also presented a numerical discretization technique using the FCM for solving three-dimensional material interface problems involving complex geometry. We proposed the combination of the FCM with a weak coupling approach to treat the issues caused by the weak discontinuity. Additionally, we applied the multi-level *hp*-refinement scheme to locally refine the FCM meshes in order to resolve singularities and local solution features at the interfaces. A series of numerical experiments with two- and three-dimensional benchmark problems was presented, showing that the proposed refinement scheme in conjunction with the weak enforcement of the interface conditions leads to a significant improvement of the convergence rates. To showcase the potential of the proposed combination of methods, we presented an application considering the high-resolution simulation of a vertebra with pedicle screws.

Additionally, we proposed a numerical approach for the weak enforcement of concentrated (point) loads in the FCM. This allows to consider boundary conditions stemming from patient-specific musculoskeletal models, which we demonstrated in a proof-of-concept numerical example which considered a single spinal segment.

In conclusion, we have demonstrated that the FCM is a powerful discretization technique with great potential a simulation tool for biomechanical analysis. When combined with an

adequate method for the treatment of weak discontinuities and a suitable scheme for local mesh refinement, the FCM can be used to carry out accurate high-resolution simulations for a moderate computational cost. A particularly attractive feature is its flexibility in handling different types of geometric representation, allowing for an effortless combination of image-based bone models with CAD-models of implants.

## 7.2 Outlook

The results presented in this thesis open the door for exploring further applications of the proposed numerical approach, but also highlight some limitations which should be addressed by future research.
Whereas our validation study for the $\mu$-FCM considered microstructural models, further validation studies should also consider continuum-level patient-specific FCM models of vertebra which are based on clinical QCT images. This would bring the method closer to clinical applications.
The definition of realistic boundary conditions is important to ensure the reliability of patient-specific clinical models. To that end, more detailed multibody simulations are necessary. Moreover, accounting for the degeneration of the intervertebral discs should make the FCM models more realistic, as the discs' degeneration causes a redistribution of the load profile over the vertebral bodies.
In our study, we examined the numerical predictions of the displacements within the trabecular structure. Validation of the strains has more significance to the estimation of fracture risk, but is also considerably more challenging. From the experimental side, the registration algorithms require coarser grids to have enough physical features to identify the displacements, which in turn limits their applicability for the pointwise validation of strain fields. Moreover, the FCM models would need to be further refined to provide numerically accurate predictions of the strains.
In our opinion, the main limitation of the FCM stems from the ill-conditioning of the stiffness matrices, caused by the penalization of the material parameters in the fictitious domain. This prevents the use of iterative methods to solve the linear systems of equation. In this work, we resorted to using a direct solver, which imposes a hard limit on the maximum solvable problem size due to its high memory requirements. The development of effective preconditioners for the FCM is necessary to unlock its potential to solve more complex problems in higher resolution. Recent research suggests that Additive-Schwarz [117] and multigrid approaches [118] can be effectively used as preconditioners for the multi-level *hp*-refined FCM to enable the use of iterative solvers.
In this work, we have used isotropic linear elastic constitutive equations to model the bone tissue, both in continuum and microstructural scales. We apply an inhomogeneous material distribution, which allows us to capture the anisotropic behavior of bone on a larger scale. Clearly, employing anisotropic material models should increase the scope of validity and reliability of the numerical models, while being straightforward to include in the framework of the FCM.

# Bibliography

[1] Abedian, A., Parvizian, J., Düster, A., Khademyzadeh, H., and Rank, E. (2013). Performance of Different Integration Schemes in Facing Discontinuities in the Finite Cell Method. International Journal of Computational Methods, 10(03):1350002.

[2] Adams, M. F., Bayraktar, H. H., Keaveny, T. M., and Papadopoulos, P. (2004). Ultrascalable Implicit Finite Element Analyses in Solid Mechanics with over a Half a Billion Degrees of Freedom. In SC '04: Proceedings of the 2004 ACM/IEEE Conference on Supercomputing, pages 34–34.

[3] Adams, M. F., Bayraktar, H. H., Keaveny, T. M., and Papdopoulos, P. (2003). Applications of Algebraic Multigrid to Large-Scale Finite Element Analysis of Whole Bone Micro-Mechanics on the IBM SP. In SC '03: Proceedings of the 2003 ACM/IEEE Conference on Supercomputing, pages 26–26.

[4] Allaire, B. T., Lu, D., Johannesdottir, F., Kopperdahl, D., Keaveny, T. M., Jarraya, M., Guermazi, A., Bredella, M. A., Samelson, E. J., Kiel, D. P., Anderson, D. E., Demissie, S., and Bouxsein, M. L. (2018). Prediction of incident vertebral fracture using CT-based finite element analysis. Osteoporosis International.

[5] Anderson, A. E., Ellis, B. J., and Weiss, J. A. (2007). Verification, validation and sensitivity studies in computational biomechanics. Computer Methods in Biomechanics and Biomedical Engineering, 10(3):171–184.

[6] Annavarapu, C., Hautefeuille, M., and Dolbow, J. E. (2012a). A robust Nitsche's formulation for interface problems. Computer Methods in Applied Mechanics and Engineering, 225–228:44–54.

[7] Annavarapu, C., Hautefeuille, M., and Dolbow, J. E. (2012b). Stable imposition of stiff constraints in explicit dynamics for embedded finite element methods. International Journal for Numerical Methods in Engineering, 92(2):206–228.

[8] Apostolatos, A., Schmidt, R., Wüchner, R., and Bletzinger, K.-U. (2014). A Nitsche-type formulation and comparison of the most common domain decomposition methods in isogeometric analysis. International Journal for Numerical Methods in Engineering, 97(7):473–504.

[9] Arbenz, P., van Lenthe, G. H., Mennel, U., Müller, R., and Sala, M. (2008). A scalable multi-level preconditioner for matrix-free $\mu$-finite element analysis of human bone structures. International Journal for Numerical Methods in Engineering, 73(7):927–947.

[10] Ayachit, U. (2015). The ParaView Guide: A Parallel Visualization Application. Kitware, Inc., USA.

[11] Babuška, I. (1973a). The finite element method with Lagrangian multipliers. Numerische Mathematik, 20(3):179–192.

[12] Babuška, I. (1973b). The Finite Element Method with Penalty. Mathematics of Computation, 27(122):221–228.

[13] Babuška, I. and Guo, B. (1996). Approximation properties of the h-p version of the finite element method. Computer Methods in Applied Mechanics and Engineering, 133(3-4):319–346.

[14] Basler, S. E., Mueller, T. L., Christen, D., Wirth, A. J., Müller, R., and van Lenthe, G. H. (2011). Towards validation of computational analyses of peri-implant displacements by means of experimentally obtained displacement maps. Computer Methods in Biomechanics and Biomedical Engineering, 14(2):165–174.

[15] Bassani, T. and Galbusera, F. (2018). Chapter 15 - Musculoskeletal Modeling. In Galbusera, F. and Wilke, H.-J., editors, Biomechanics of the Spine, pages 257–277. Academic Press.

[16] Bathe, K. J. (2007). Finite Element Procedures. Prentice Hall, New Jersey.

[17] Bayraktar, H. H., Buckley, J. M., Adams, M. F., Gupta, A., Hoffmann, P. F., Lee, D., Papadopoulos, P., and Keaveny, T. M. (2003). Cortical shell thickness and its contribution to vertebral body stiffness. In ASME Bioengineering Conference, Key Biscayne, Florida.

[18] Bazilevs, Y. and Hughes, T. J. R. (2007). Weak imposition of Dirichlet boundary conditions in fluid mechanics. Computers & Fluids, 36(1):12–26.

[19] Bindick, S., Stiebler, M., and Krafczyk, M. (2011). Fast kd-tree-based hierarchical radiosity for radiative heat transport problems. International Journal for Numerical Methods in Engineering, 86(9):1082–1100.

[20] Blanchard, R., Morin, C., Malandrino, A., Vella, A., Sant, Z., and Hellmich, C. (2016). Patient-specific fracture risk assessment of vertebrae: A multiscale approach coupling X-ray physics and continuum micromechanics: Patient-specific fracture risk assessment of vertebrae: A multiscale approach coupling X-ray physics and continuum micromechanics. International Journal for Numerical Methods in Biomedical Engineering, 32(9).

[21] Blausen Medical Communications, Inc. (2014). Medical gallery of Blausen Medical 2014.

[22] Bog, T. (2017). Frictionless Contact Simulation Using the Finite Cell Method. PhD Thesis, Technische Universität München, Munich.

[23] Bog, T., Zander, N., Kollmannsberger, S., and Rank, E. (2015). Normal contact with high order finite elements and a fictitious contact material. Computers & Mathematics with Applications, 70(7):1370–1390.

[24] Bog, T., Zander, N., Kollmannsberger, S., and Rank, E. (2017). Weak imposition of frictionless contact constraints on automatically recovered high-order, embedded interfaces using the finite cell method. Computational Mechanics.

[25] Bogduk, N. (2005). Clinical Anatomy of the Lumbar Spine and Sacrum. Elsevier Health Sciences.

[26] Bonet, J. and Wood, R. D. (1997). Nonlinear Continuum Mechanics for Finite Element Analysis. Cambridge University Press, Cambridge ; New York, NY, USA.

[27] Bourke, P. (1994). Polygonising a scalar field (Marching Cubes). `http://paulbourke.net/geometry/polygonise/`.

[28] Brebbia, C. A. (1978). The Boundary Element Method for Engineers. Pentech Press, London.

[29] Brenner, S. C. and Scott, L. R. (2008). The Mathematical Theory of Finite Element Methods. Number 15 in Texts in applied mathematics. Springer, New York, USA, 3rd edition.

[30] Cai, Q., Kollmannsberger, S., Mundani, R.-P., and Rank, E. (2011). The finite cell method for solute transport problems in porous media. In Proceedings of the International Conference on Finite Elements in Flow Problems.

[31] Chen, Y. (2016). Verification and Validation of MicroCT-Based Finite Element Models of Bone Tissue Biomechanics. PhD Thesis, University of Sheffield, United Kingdom.

[32] Chen, Y., DallAra, E., Sales, E., Manda, K., Wallace, R., Pankaj, P., and Viceconti, M. (2017). Micro-CT based finite element models of cancellous bone predict accurately displacement once the boundary condition is well replicated: A validation study. Journal of the Mechanical Behavior of Biomedical Materials, 65:644–651.

[33] Chen, Y., Pani, M., Taddei, F., Mazzà, C., Li, X., and Viceconti, M. (2014). Large-Scale Finite Element Analysis of Human Cancellous Bone Tissue Micro Computer Tomography Data: A Convergence Study. Journal of Biomechanical Engineering, 136(10):101013–101013–7.

[34] Chevalier, Y., Charlebois, M., Pahr, D., Varga, P., Heini, P., Schneider, E., and Zysset, P. (2008). A patient-specific finite element methodology to predict damage accumulation in vertebral bodies under axial compression, sagittal flexion and combined loads. Computer Methods in Biomechanics and Biomedical Engineering, 11(5):477–487.

[35] Chevalier, Y., Matsuura, M., Krüger, S., Fleege, C., Rickert, M., Rauschmann, M., and Schilling, C. (2018). Micro-CT and micro-FE analysis of pedicle screw fixation under different loading conditions. Journal of Biomechanics, 70:204–211.

[36] Chevalier, Y., Pahr, D., Allmer, H., Charlebois, M., and Zysset, P. (2007). Validation of a voxel-based FE method for prediction of the uniaxial apparent modulus of human trabecular bone using macroscopic mechanical tests and nanoindentation. Journal of Biomechanics, 40(15):3333–3340.

[37] Chevalier, Y., Pahr, D., and Zysset, P. K. (2009). The role of cortical shell and trabecular fabric in finite element analysis of the human vertebral body. Journal of Biomechanical Engineering, 131(11):111003.

[38] Chevalier, Y., Quek, E., Borah, B., Gross, G., Stewart, J., Lang, T., and Zysset, P. (2010). Biomechanical effects of teriparatide in women with osteoporosis treated previously with alendronate and risedronate: Results from quantitative computed tomography-based finite element analysis of the vertebral body. Bone, 46(1):41–48.

[39] Chevalier, Y. and Zysset, P. K. (2012). A Patient-Specific Computer Tomography-Based Finite Element Methodology to Calculate the Six Dimensional Stiffness Matrix of Human Vertebral Bodies. Journal of Biomechanical Engineering, 134(5):051006–051006–6.

[40] Christiansen, B. A., Kopperdahl, D. L., Kiel, D. P., Keaveny, T. M., and Bouxsein, M. L. (2011). Mechanical contributions of the cortical and trabecular compartments contribute to differences in age-related changes in vertebral body strength in men and women assessed by QCT-based finite element analysis. Journal of Bone and Mineral Research, 26(5):974–983.

[41] Ciarlet, P. G. (2002). The Finite Element Method for Elliptic Problems. Number 40 in Classics in applied mathematics. Society for Industrial and Applied Mathematics, Philadelphia, PA.

[42] Clouthier, A. L., Hosseini, H. S., Maquer, G., and Zysset, P. K. (2015). Finite element analysis predicts experimental failure patterns in vertebral bodies loaded via intervertebral discs up to large deformation. Medical Engineering & Physics, 37(6):599–604.

[43] Cook, R. D. (1977). Detection of Influential Observation in Linear Regression. Technometrics, 19(1):15–18.

[44] Coradello, L., D'Angella, D., Carraturo, M., Kiendl, J., Kollmannsberger, S., Rank, E., and Reali, A. (2020). Hierarchically refined isogeometric analysis of trimmed shells. Computational Mechanics.

[45] Costa, M. C., Tozzi, G., Cristofolini, L., Danesi, V., Viceconti, M., and Dall'Ara, E. (2017). Micro Finite Element models of the vertebral body: Validation of local displacement predictions. PLOS ONE, 12(7):e0180151.

[46] Cottrell, J. A., Hughes, T. J. R., and Bazilevs, Y. (2009). Isogeometric Analysis: Toward Integration of CAD and FEA. John Wiley & Sons.

[47] Crawford, R. P., Cann, C. E., and Keaveny, T. M. (2003). Finite element models predict in vitro vertebral body compressive strength better than quantitative computed tomography. Bone, 33(4):744–750.

[48] Currey, J. D. (2002). Bones: Structure and Mechanics. Princeton University Press.

[49] Dahan, G., Trabelsi, N., Safran, O., and Yosibash, Z. (2016). Verified and validated finite element analyses of humeri. Journal of Biomechanics, 49(7):1094–1102.

[50] Dall'Ara, E., Barber, D., and Viceconti, M. (2014). About the inevitable compromise between spatial resolution and accuracy of strain measurement for bone tissue: A 3D zero-strain study. Journal of Biomechanics, 47(12):2956–2963.

[51] Dall'Ara, E., Pahr, D., Varga, P., Kainberger, F., and Zysset, P. (2012). QCT-based finite element models predict human vertebral strength in vitro significantly better than simulated DEXA. Osteoporosis International, 23(2):563–572.

[52] Dall'Ara, E., Schmidt, R., Pahr, D., Varga, P., Chevalier, Y., Patsch, J., Kainberger, F., and Zysset, P. (2010). A nonlinear finite element model validation study based on a novel experimental technique for inducing anterior wedge-shape fractures in human vertebral bodies in vitro. Journal of Biomechanics, 43(12):2374–2380.

[53] D'Angella, D., Zander, N., Kollmannsberger, S., Frischmann, F., Rank, E., Schröder, A., and Reali, A. (2016). Multi-level hp-adaptivity and explicit error estimation. Advanced Modeling and Simulation in Engineering Sciences, 3(1):33.

[54] Dauge, M., Düster, A., and Rank, E. (2015). Theoretical and Numerical Investigation of the Finite Cell Method. Journal of Scientific Computing, 65(3):1039–1064.

[55] de Jalon, J. G. and Bayo, E. (1994). Kinematic and Dynamic Simulation of Multibody Systems: The Real-Time Challenge. Mechanical Engineering Series. Springer-Verlag, New York.

[56] de Prenter, F., Lehrenfeld, C., and Massing, A. (2018). A note on the stability parameter in Nitsche's method for unfitted boundary value problems. Computers & Mathematics with Applications, 75(12):4322–4336.

[57] de Prenter, F., Verhoosel, C. V., van Brummelen, E. H., Evans, J. A., Messe, C., Benzaken, J., and Maute, K. (2020). Multigrid solvers for immersed finite element methods and immersed isogeometric analysis. Computational Mechanics, 65(3):807–838.

[58] de Prenter, F., Verhoosel, C. V., van Zwieten, G. J., and van Brummelen, E. H. (2017). Condition number analysis and preconditioning of the finite cell method. Computer Methods in Applied Mechanics and Engineering, 316(Supplement C):297–327.

[59] de Zee, M., Hansen, L., Wong, C., Rasmussen, J., and Simonsen, E. B. (2007). A generic detailed rigid-body lumbar spine model. Journal of Biomechanics, 40(6):1219–1227.

[60] Demkowicz, L., Rachowicz, W., and Devloo, P. (2002). A Fully Automatic hp-Adaptivity. Journal of Scientific Computing, 17(1-4):117–142.

[61] den Abbeele, M. V., Valiadis, J.-M., Lima, L. V. P. C., Khalifé, P., Rouch, P., and Skalli, W. (2018). Contribution to FE modeling for intraoperative pedicle screw strength prediction. Computer Methods in Biomechanics and Biomedical Engineering, 21(1):13–21.

[62] Di Stolfo, P. and Schröder, A. (2021). Reliable Residual-Based Error Estimation for the Finite Cell Method. Journal of Scientific Computing, 87(1):12.

[63] Dolbow, J. and Harari, I. (2009). An efficient finite element method for embedded interface problems. International Journal for Numerical Methods in Engineering, 78(2):229–252.

[64] Duczek, S., Duvigneau, F., and Gabbert, U. (2016). The finite cell method for tetrahedral meshes. Finite Elements in Analysis and Design, 121:18–32.

[65] Duczek, S. and Gabbert, U. (2015). Efficient integration method for fictitious domain approaches. Computational Mechanics.

[66] Duczek, S. and Gabbert, U. (2016). The finite cell method for polygonal meshes: Poly-FCM. Computational Mechanics, pages 1–32.

[67] Duczek, S., Joulaian, M., Düster, A., and Gabbert, U. (2014). Numerical analysis of Lamb waves using the finite and spectral cell methods. International Journal for Numerical Methods in Engineering, 99(1):26–53.

[68] Düster, A. (2010). High Order FEM - Lecture Notes. Technical report, TU München, Chair for Computation in Engineering.

[69] Düster, A., Parvizian, J., and Rank, E. (2010). Topology optimization based on the finite cell method. PAMM, 10(1):151–152.

[70] Düster, A., Parvizian, J., Yang, Z., and Rank, E. (2008). The finite cell method for three-dimensional problems of solid mechanics. Computer Methods in Applied Mechanics and Engineering, 197(45–48):3768–3782.

[71] Düster, A., Rank, E., and Szabó, B. A. (2017). The p-version of the finite element method and finite cell methods. In Stein, E., Borst, R., and Hughes, T. J. R., editors, Encyclopedia of Computational Mechanics, volume 2, pages 1–35. John Wiley & Sons, Chichester, West Sussex.

[72] Einafshar, M., Hashemi, A., and van Lenthe, G. H. (2021). Homogenized finite element models can accurately predict screw pull-out in continuum materials, but not in porous materials. Computer Methods and Programs in Biomedicine, 202:105966.

[73] Eisenträger, S., Atroshchenko, E., and Makvandi, R. (2020). On the condition number of high order finite element methods: Influence of p-refinement and mesh distortion. Computers & Mathematics with Applications, 80(11):2289–2339.

[74] Elhaddad, M., Kollmannsberger, S., Valentinitsch, A., Kirschke, J., Ruess, M., and Rank, E. (2017). Micro-CT based finite cell analysis of vertebral bodies. In Engineering Mechanics Institute Conference 2017.

[75] Elhaddad, M., Zander, N., Bog, T., Kudela, L., Kollmannsberger, S., Kirschke, J. S., Baum, T., Ruess, M., and Rank, E. (2018). Multi-level hp-finite cell method for embedded interface problems with application in biomechanics. International Journal for Numerical Methods in Biomedical Engineering, 34(4):e2951.

[76] Elhaddad, M., Zander, N., Kollmannsberger, S., Shadavakhsh, A., Nübel, V., and Rank, E. (2015). Finite Cell Method: High-Order Structural Dynamics for Complex Geometries. International Journal of Structural Stability and Dynamics, 15(7):1540018.

[77] Felippa, C. A. (2013). Introduction to Finite Element Methods. Lecture Notes, Department of Aerospace Engineering Sciences, University of Colorado at Boulder, Boulder, Colorado, USA.

[78] Fernández-Méndez, S. and Huerta, A. (2004). Imposing essential boundary conditions in mesh-free methods. Computer Methods in Applied Mechanics and Engineering, 193(12-14):1257–1275.

[79] Fields, A. J. (2010). Trabecular Microarchitecture, Endplate Failure, and the Biomechanics of Human Vertebral Fractures. PhD thesis, UC Berkeley.

[80] Flaig, C. and Arbenz, P. (2012). A Highly Scalable Matrix-Free Multigrid Solver for $\mu$FE Analysis Based on a Pointer-Less Octree. In Lirkov, I., Margenov, S., and Waśniewski, J., editors, Large-Scale Scientific Computing, Lecture Notes in Computer Science, pages 498–506, Berlin, Heidelberg. Springer.

[81] Fries, T.-P. (2008). A corrected XFEM approximation without problems in blending elements. International Journal for Numerical Methods in Engineering, 75(5):503–532.

[82] Fries, T.-P. and Belytschko, T. (2010). The extended/generalized finite element method: An overview of the method and its applications. International Journal for Numerical Methods in Engineering, 84(3):253–304.

[83] Fries, T.-P. and Omerović, S. (2015). Higher-order accurate integration of implicit geometries. International Journal for Numerical Methods in Engineering, 106(5):323–371.

[84] Fries, T. P., Omerović, S., Schöllhammer, D., and Steidl, J. (2017). Higher-order meshing of implicit geometries—Part I: Integration and interpolation in cut elements. Computer Methods in Applied Mechanics and Engineering, 313(Supplement C):759–784.

[85] Gerstenberger, A. and Wall, W. A. (2010). An embedded Dirichlet formulation for 3D continua. International Journal for Numerical Methods in Engineering, 82(5):537–563.

[86] Giraldo, D. and Restrepo, D. (2017). The spectral cell method in nonlinear earthquake modeling. Computational Mechanics, pages 1–21.

[87] Gokhale, N. (2008). Practical Finite Element Analysis. Finite To Infinite.

[88] Gordon, W. J. and Hall, C. A. (1973). Transfinite element methods: Blending-function interpolation over arbitrary curved element domains. Numerische Mathematik, 21(2):109–129.

[89] Grassi, L. and Isaksson, H. (2015). Extracting accurate strain measurements in bone mechanics: A critical review of current methods. Journal of the Mechanical Behavior of Biomedical Materials, 50:43–54.

[90] Groen, J. P., Langelaar, M., Sigmund, O., and Ruess, M. (2017). Higher-order multi-resolution topology optimization using the finite cell method. International Journal for Numerical Methods in Engineering, 110(10):903–920.

[91] Gui, W. and Babuška, I. (1986a). The h, p and h-p versions of the finite element method in 1 dimension Part I: The error analysis of the p-version. Numerische Mathematik, 49(6):577–612.

[92] Gui, W. and Babuška, I. (1986b). The h, p and h-p versions of the finite element method in 1 dimension Part II: The error analysis of the h-and h-p versions. Numerische Mathematik, 49(6):613–657.

[93] Gui, W. and Babuška, I. (1986c). The h, p and h-p versions of the finite element method in 1 dimension Part III: The Adaptive h-p Version. Numerische Mathematik, 49(6):659–683.

[94] Halloran, J., Ackermann, M., Erdemir, A., and van den Bogert, A. (2010). Concurrent musculoskeletal dynamics and finite element analysis predicts altered gait patterns to reduce foot tissue loading. Journal of biomechanics, 43:2810–5.

[95] Hambli, R. (2013). Micro-CT finite element model and experimental validation of trabecular bone damage and fracture. Bone, 56(2):363–374.

[96] Hansbo, A. and Hansbo, P. (2002). An unfitted finite element method, based on Nitsche's method, for elliptic interface problems. Computer Methods in Applied Mechanics and Engineering, 191(47-48):5537–5552.

[97] Hansbo, P. (2005). Nitsche's method for interface problems in computational mechanics. GAMM-Mitteilungen, 28(2):183–206.

[98] Hansbo, P., Larson, M. G., and Larsson, K. (2017). Cut Finite Element Methods for Linear Elasticity Problems. arXiv:1703.04377 [math].

[99] Hansbo, P., Lovadina, C., Perugia, I., and Sangalli, G. (2005). A Lagrange multiplier method for the finite element solution of elliptic interface problems using non-matching meshes. Numerische Mathematik, 100(1):91–115.

[100] Hasegawa, T., Inufusa, A., Imai, Y., Mikawa, Y., Lim, T.-H., and An, H. S. (2005). Hydroxyapatite-coating of pedicle screws improves resistance against pull-out force in the osteoporotic canine lumbar spine model: A pilot study. The Spine Journal: Official Journal of the North American Spine Society, 5(3):239–243.

[101] Heisserer, U. (2008). High Order Finite Elements for Material and Geometric Nonlinear Finite Strain Problems. PhD thesis, Shaker, Aachen.

[102] Helgason, B., Perilli, E., Schileo, E., Taddei, F., Brynjólfsson, S., and Viceconti, M. (2008). Mathematical relationships between bone density and mechanical properties: A literature review. Clinical Biomechanics, 23(2):135–146.

[103] Herman, G. T. (2009). Fundamentals of Computerized Tomography: Image Reconstruction from Projections. Springer, Dordrecht ; New York, 2nd ed. 2010 edition edition.

[104] Hippmann, G. (2004). Modellierung von Kontakten komplex geformter Körper in der Mehrkörperdynamik. Thesis, Technische Univeristät Wien.

[105] Höllig, K., Reif, U., and Wipper, J. (2001). Weighted extended B-spline approximation of Dirichlet problems. SIAM Journal on Numerical Analysis, 39(2):442–462.

[106] Hollister, S. J., Brennan, J. M., and Kikuchi, N. (1994). A homogenization sampling procedure for calculating trabecular bone effective stiffness and tissue level stress. Journal of Biomechanics, 27(4):433–444.

[107] Holzapfel, G. A. (2000). Nonlinear Solid Mechanics: A Continuum Approach for Engineering. Wiley, Chichester, New York.

[108] Hongo, M., Abe, E., Shimada, Y., Murai, H., Ishikawa, N., and Sato, K. (1999). Surface strain distribution on thoracic and lumbar vertebrae under axial compression. The role in burst fractures. Spine, 24(12):1197–1202.

[109] Hosseini, H. S. (2013). Constitutive Modeling of Trabecular Bone in Large Strain Compression. PhD thesis, University of Bern.

[110] Hosseini, H. S., Pahr, D. H., and Zysset, P. K. (2012). Modeling and experimental validation of trabecular bone damage, softening and densification under large compressive strains. Journal of the Mechanical Behavior of Biomedical Materials, 15:93–102.

[111] Hughes, T. J. R. (2000). The Finite Element Method: Linear Static and Dynamic Finite Element Analysis. Dover Publications, Mineola, NY.

[112] Huiskes, R. and Chao, E. Y. S. (1983). A survey of finite element analysis in orthopedic biomechanics: The first decade. Journal of Biomechanics, 16(6):385–409.

[113] Hussein, A. I., Barbone, P. E., and Morgan, E. F. (2012). Digital Volume Correlation for Study of the Mechanics of Whole Bones. Procedia IUTAM, 4:116–125.

[114] Intel (2017). Intel Math Kernel Library. http://software.intel.com/en-us/intel-mkl.

[115] Janssen, D., Mann, K. A., and Verdonschot, N. (2008). Micromechanical modeling of the cement-bone interface: The effect of friction, morphology and material properties on the micromechanical response. Journal of biomechanics, 41(15):3158–3163.

[116] Jiang, W. and Dolbow, J. E. (2015). Adaptive refinement of hierarchical B-spline finite elements with an efficient data transfer algorithm. International Journal for Numerical Methods in Engineering, 102(3-4):233–256.

[117] Jomo, J., de Prenter, F., Elhaddad, M., D'Angella, D., Verhoosel, C., Kollmannsberger, S., Kirschke, J., Nübel, V., van Brummelen, E., and Rank, E. (2019). Robust and parallel scalable iterative solutions for large-scale finite cell analyses. Finite Elements in Analysis and Design, 163:14–30.

[118] Jomo, J., Oztoprak, O., de Prenter, F., Zander, N., Kollmannsberger, S., and Rank, E. (2020). Hierarchical multigrid approaches for the finite cell method on uniform and multi-level hp-refined grids. arXiv:2010.00881 [cs, math].

[119] Jones, A. C. and Wilcox, R. K. (2007). Assessment of factors influencing finite element vertebral model predictions. Journal of Biomechanical Engineering, 129(6):898–903.

[120] Jones, A. C. and Wilcox, R. K. (2008). Finite element analysis of the spine: Towards a framework of verification, validation and sensitivity analysis. Medical Engineering & Physics, 30(10):1287–1304.

[121] Joulaian, M., Duczek, S., Gabbert, U., and Düster, A. (2014). Finite and spectral cell method for wave propagation in heterogeneous materials. Computational Mechanics, 54(3):661–675.

[122] Joulaian, M. and Düster, A. (2013). Local enrichment of the finite cell method for problems with material interfaces. Computational Mechanics, 52(4):741–762.

[123] Joulaian, M., Hubrich, S., and Düster, A. (2016). Numerical integration of discontinuities on arbitrary domains based on moment fitting. Computational Mechanics, 57(6):979–999.

[124] Kafchitsas, K., Geiger, F., Rauschmann, M., and Schmidt, S. (2010). Cement distribution in vertebroplasty pedicle screws with different designs. Der Orthopäde, 39(7):679–686.

[125] Kainz, H., Killen, B. A., Wesseling, M., Perez-Boerema, F., Pitto, L., Aznar, J. M. G., Shefelbine, S., and Jonkers, I. (2020). A multi-scale modelling framework combining musculoskeletal rigid-body simulations with adaptive finite element analyses, to evaluate the impact of femoral geometry on hip joint contact forces and femoral bone growth. PLOS ONE, 15(7):e0235966.

[126] Kamal, Z., Rouhi, G., Arjmand, N., and Adeeb, S. (2019). A stability-based model of a growing spine with adolescent idiopathic scoliosis: A combination of musculoskeletal and finite element approaches. Medical Engineering & Physics, 64:46 – 55.

[127] Kanis, J. A., Burlet, N., Cooper, C., Delmas, P. D., Reginster, J.-Y., Borgstrom, F., Rizzoli, R., and on behalf of the European Society for Clinical and Economic Aspects of Osteoporosis and Osteoarthritis (ESCEO) (2008). European guidance for the diagnosis

and management of osteoporosis in postmenopausal women. Osteoporosis International, 19(4):399–428.

[128] Katsikadelis, J. (2016). The Boundary Element Method for Engineers and Scientists. Theory and Application. Elsevier.

[129] Katz, Y., Lubovsky, O., and Yosibash, Z. (2018). Patient-specific finite element analysis of femurs with cemented hip implants. Clinical Biomechanics, 58:74–89.

[130] Keaveny, T. M. and Buckley, J. M. (2006). Chapter 4 - Biomechanics of Vertebral Bone. In Kurtz, S. M. and Edidin, A. A., editors, Spine Technology Handbook, pages 63–98. Academic Press, Burlington.

[131] Keaveny, T. M., Donley, D. W., Hoffmann, P. F., Mitlak, B. H., Glass, E. V., and San Martin, J. A. (2007). Effects of teriparatide and alendronate on vertebral strength as assessed by finite element modeling of QCT scans in women with osteoporosis. Journal of Bone and Mineral Research: The Official Journal of the American Society for Bone and Mineral Research, 22(1):149–157.

[132] Keaveny, T. M., Guo, X. E., Wachtel, E. F., McMahon, T. A., and Hayes, W. C. (1994). Trabecular bone exhibits fully linear elastic behavior and yields at low strains. Journal of Biomechanics, 27(9):1127–1136.

[133] Kellogg, R. B. (1974). On the poisson equation with intersecting interfaces. Applicable Analysis, 4(2):101–129.

[134] Keyak, J. H., Meagher, J. M., Skinner, H. B., and Mote, C. D. (1990). Automated three-dimensional finite element modelling of bone: A new method. Journal of Biomedical Engineering, 12(5):389–397.

[135] Királyfalvi, G. and Szabó, B. A. (1997). Quasi-regional mapping for the p-version of the finite element method. Finite elements in analysis and design, 27(1):85–97.

[136] Klein, S., Staring, M., Murphy, K., Viergever, M. A., and Pluim, J. P. W. (2010). Elastix: A Toolbox for Intensity-Based Medical Image Registration. IEEE Transactions on Medical Imaging, 29(1):196–205.

[137] Klein, S., Staring, M., and Pluim, J. P. W. (2007). Evaluation of optimization methods for nonrigid medical image registration using mutual information and B-splines. IEEE transactions on image processing: a publication of the IEEE Signal Processing Society, 16(12):2879–2890.

[138] Kollmannsberger, S., Özcan, A., Baiges, J., Ruess, M., Rank, E., and Reali, A. (2015). Parameter-free, weak imposition of Dirichlet boundary conditions and coupling of trimmed and non-conforming patches. International Journal for Numerical Methods in Engineering, 101(9):670–699.

[139] Kopperdahl, D. L., Aspelund, T., Hoffmann, P. F., Sigurdsson, S., Siggeirsdottir, K., Harris, T. B., Gudnason, V., and Keaveny, T. M. (2014). Assessment of incident spine and hip fractures in women and men using finite element analysis of CT scans. Journal of Bone and Mineral Research, 29(3):570–580.

[140] Kopperdahl, D. L. and Keaveny, T. M. (1998). Yield strain behavior of trabecular bone. Journal of Biomechanics, 31(7):601–608.

[141] Kopperdahl, D. L., Morgan, E. F., and Keaveny, T. M. (2002). Quantitative computed tomography estimates of the mechanical properties of human vertebral trabecular bone. Journal of Orthopaedic Research: Official Publication of the Orthopaedic Research Society, 20(4):801–805.

[142] Kudela, L., Kollmannsberger, S., Almac, U., and Rank, E. (2020). Direct structural analysis of domains defined by point clouds. Computer Methods in Applied Mechanics and Engineering, 358:112581.

[143] Kudela, L., Zander, N., Bog, T., Kollmannsberger, S., and Rank, E. (2015). Efficient and accurate numerical quadrature for immersed boundary methods. Advanced Modeling and Simulation in Engineering Sciences, 2(1):1–22.

[144] Kudela, L., Zander, N., Kollmannsberger, S., and Rank, E. (2016). Smart octrees: Accurately integrating discontinuous functions in 3D. Computer Methods in Applied Mechanics and Engineering, 306:406–426.

[145] Kusins, J., Knowles, N., Columbus, M., Oliviero, S., Dall'Ara, E., Athwal, G. S., and Ferreira, L. M. (2020a). The Application of Digital Volume Correlation (DVC) to Evaluate Strain Predictions Generated by Finite Element Models of the Osteoarthritic Humeral Head. Annals of Biomedical Engineering, 48(12):2859–2869.

[146] Kusins, J., Knowles, N., Ryan, M., Dall'Ara, E., and Ferreira, L. (2019). Performance of QCT-Derived scapula finite element models in predicting local displacements using digital volume correlation. Journal of the Mechanical Behavior of Biomedical Materials, 97:339–345.

[147] Kusins, J., Knowles, N., Ryan, M., Dall'Ara, E., and Ferreira, L. (2020b). Full-field comparisons between strains predicted by QCT-derived finite element models of the scapula and experimental strains measured by digital volume correlation. Journal of Biomechanics, 113:110101.

[148] Ladd, A. J. C., Kinney, J. H., Haupt, D. L., and Goldstein, S. A. (1998). Finite-element modeling of trabecular bone: Comparison with mechanical testing and determination of tissue modulus. Journal of Orthopaedic Research, 16(5):622–628.

[149] Legrain, G., Allais, R., and Cartraud, P. (2011). On the use of the extended finite element method with quadtree/octree meshes. International Journal for Numerical Methods in Engineering, 86(6):717–743.

[150] Legrain, G., Chevaugeon, N., and Dréau, K. (2012). High order X-FEM and levelsets for complex microstructures: Uncoupling geometry and approximation. Computer Methods in Applied Mechanics and Engineering, 241-244:172–189.

[151] Lehner, S., Wallrapp, O., and Senner, V. (2010). Use of headgear in football A computer simulation of the human head and neck. Procedia Engineering, 2(2):3263–3268.

[152] Liu, T., Khalaf, K., Adeeb, S., and El-Rich, M. (2018). Effects of lumbo-pelvic rhythm on trunk muscle forces and disc loads during forward flexion: A combined musculoskeletal and finite element simulation study. Journal of Biomechanics.

[153] Liu, X. S., Zhang, X. H., Rajapakse, C. S., Wald, M. J., Magland, J., Sekhon, K. K., Adam, M. F., Sajda, P., Wehrli, F. W., and Guo, X. E. (2010). Accuracy of high-resolution in vivo micro magnetic resonance imaging for measurements of microstructural and mechanical properties of human distal tibial bone. Journal of Bone and Mineral Research, 25(9):2039–2050.

[154] Lorensen, W. E. and Cline, H. E. (1987). Marching cubes: A high resolution 3D surface construction algorithm. In Proceedings of the 14th Annual Conference on Computer Graphics and Interactive Techniques, pages 163–169, New York, NY. ACM Press.

[155] Lu, Y., Maquer, G., Museyko, O., Püschel, K., Engelke, K., Zysset, P., Morlock, M., and Huber, G. (2014). Finite element analyses of human vertebral bodies embedded in polymethylmethalcrylate or loaded via the hyperelastic intervertebral disc models provide equivalent predictions of experimental strength. Journal of Biomechanics, 47(10):2512–2516.

[156] Majumdar, S., Genant, H. K., Grampp, S., Newitt, D. C., Truong, V.-H., Lin, J. C., and Mathur, A. (1997). Correlation of Trabecular Bone Structure with Age, Bone Mineral Density, and Osteoporotic Status: In Vivo Studies in the Distal Radius Using High Resolution Magnetic Resonance Imaging. Journal of Bone and Mineral Research, 12(1):111–118.

[157] Malvern, L. E. (1977). Introduction to the Mechanics of a Continuous Medium. Prentice Hall, Englewood Cliffs.

[158] Mannion, A. F., Brox, J. I., and Fairbank, J. C. T. (2013). Comparison of spinal fusion and nonoperative treatment in patients with chronic low back pain: Long-term follow-up of three randomized controlled trials. The Spine Journal: Official Journal of the North American Spine Society, 13(11):1438–1448.

[159] Manske, S. L., Zhu, Y., Sandino, C., and Boyd, S. K. (2015). Human trabecular bone microarchitecture can be assessed independently of density with second generation HR-pQCT. Bone, 79:213–221.

[160] Maple, C. (2003). Geometric design and space planning using the marching squares and marching cube algorithms. In 2003 International Conference on Geometric Modeling and Graphics, 2003. Proceedings, pages 90–95. IEEE.

[161] Marcián, P., Borák, L., Valášek, J., Kaiser, J., Florian, Z., and Wolff, J. (2014). Finite element analysis of dental implant loading on atrophic and non-atrophic cancellous and cortical mandibular bone – a feasibility study. Journal of Biomechanics, 47(16):3830–3836.

[162] Marcián, P., Konečný, O., Borak, L., Valášek, J., Řehák, K., Krpalek, D., and Florian, Z. (2011). On the level of computational models in biomechanics depending on gained data from CT/MRI and micro-CT. Mendel, pages 455–462.

[163] Marcián, P., Wolff, J., Horáčková, L., Kaiser, J., Zikmund, T., and Borák, L. (2018). Micro finite element analysis of dental implants under different loading conditions. Computers in Biology and Medicine, 96:157–165.

[164] Maruyama, T. and Takeshita, K. (2009). Surgery for Idiopathic Scoliosis: Currently Applied Techniques. Clinical Medicine. Pediatrics, 3:39–44.

[165] Matsukawa, K., Yato, Y., and Imabayashi, H. (2020). Impact of Screw Diameter and Length on Pedicle Screw Fixation Strength in Osteoporotic Vertebrae: A Finite Element Analysis. Asian Spine Journal.

[166] McBroom, R. J., Hayes, W. C., Edwards, W. T., Goldberg, R. P., and White, A. A. (1985). Prediction of vertebral body compressive fracture using quantitative computed tomography. The Journal of Bone and Joint Surgery. American Volume, 67(8):1206–1214.

[167] McKay, M., Jackman, T. M., Hussein, A. I., Guermazi, A., Liu, J., and Morgan, E. F. (2020). Association of vertebral endplate microstructure with bone strength in men and women. Bone, 131:115147.

[168] McNally, D. S., Shackleford, I. M., Goodship, A. E., and Mulholland, R. C. (1996). In vivo stress measurement can predict pain on discography. Spine, 21(22):2580–2587.

[169] Melenk, J. M. and Babuška, I. (1996). The partition of unity finite element method: Basic theory and applications. Computer Methods in Applied Mechanics and Engineering, 139(1):289–314.

[170] Middleditch, A. and Oliver, J. (2002). Functional Anatomy of the Spine. Butterworth-Heinemann, Edinburgh etc., second edition.

[171] Moës, N., Cloirec, M., Cartraud, P., and Remacle, J. F. (2003). A computational approach to handle complex microstructure geometries. Computer Methods in Applied Mechanics and Engineering, 192(28–30):3163–3177.

[172] Molinari, L., Falcinelli, C., Gizzi, A., and Di Martino, A. (2021). Effect of pedicle screw angles on the fracture risk of the human vertebra: A patient-specific computational model. Journal of the Mechanical Behavior of Biomedical Materials, 116:104359.

[173] Morgan, E. F., Bayraktar, H. H., and Keaveny, T. M. (2003). Trabecular bone modulus–density relationships depend on anatomic site. Journal of Biomechanics, 36(7):897–904.

[174] Mote, C. D. (1971). Global-local finite element. International Journal for Numerical Methods in Engineering, 3(4):565–574.

[175] Müller-Karger, C. M., Rank, E., and Cerrolaza, M. (2004). $p$-version of the finite-element method for highly heterogeneous simulation of human bone. Finite Elements in Analysis and Design, 40(7):757–770.

[176] Nagaraja, S., Elhaddad, M., Ambati, M., Kollmannsberger, S., De Lorenzis, L., and Rank, E. (2018). Phase-field modeling of brittle fracture with multi-level hp-FEM and the finite cell method. Computational Mechanics.

[177] National Guideline Centre (UK) (2016). Low Back Pain and Sciatica in Over 16s: Assessment and Management. National Institute for Health and Care Excellence: Clinical Guidelines. National Institute for Health and Care Excellence (UK), London.

[178] Niebur, G. L., Feldstein, M. J., Yuen, J. C., Chen, T. J., and Keaveny, T. M. (2000). High-resolution finite element models with tissue strength asymmetry accurately predict failure of trabecular bone. Journal of Biomechanics, 33(12):1575–1583.

[179] Nitsche, J. (1971). Über ein Variationsprinzip zur Lösung von Dirichlet-Problemen bei Verwendung von Teilräumen, die keinen Randbedingungen unterworfen sind. Abhandlungen aus dem Mathematischen Seminar der Universität Hamburg, 36(1):9–15.

[180] Nordin, M. and Ph. D. Frankel, V. H., editors (2001). Basic Biomechanics of the Musculoskeletal System. Lippincott Williams & Wilkins, Philadelphia, subsequent edition edition.

[181] Nübel, V., Düster, A., and Rank, E. (2007). An rp-adaptive finite element method for the deformation theory of plasticity. Computational Mechanics, 39(5):557–574.

[182] Okuyama, K., Sato, K., Abe, E., Inaba, H., Shimada, Y., and Murai, H. (1993). Stability of transpedicle screwing for the osteoporotic spine. An in vitro study of the mechanical stability. Spine, 18(15):2240–2245.

[183] Oliviero, S., Giorgi, M., and Dall'Ara, E. (2018). Validation of finite element models of the mouse tibia using digital volume correlation. Journal of the Mechanical Behavior of Biomedical Materials, 86:172–184.

[184] Omerović, S. and Fries, T.-P. (2017). Conformal higher-order remeshing schemes for implicitly defined interface problems. International Journal for Numerical Methods in Engineering, 109(6):763–789.

[185] Oztoprak, O. (2020). Enforcement of Boundary Conditions in FCM with Applications to Biomechanics. Master's Thesis, Technische Universität München, München.

[186] Pahr, D. H., Dall'Ara, E., Varga, P., and Zysset, P. K. (2012). HR-pQCT-based homogenised finite element models provide quantitative predictions of experimental vertebral body stiffness and strength with the same accuracy as $\mu$FE models. Computer Methods in Biomechanics and Biomedical Engineering, 15(7):711–720.

[187] Pahr, D. H. and Zysset, P. K. (2009). A comparison of enhanced continuum FE with micro FE models of human vertebral bodies. Journal of Biomechanics, 42(4):455–462.

[188] Palanca, M., Tozzi, G., and Cristofolini, L. (2016). The use of digital image correlation in the biomechanical area: A review. International Biomechanics, 3(1):1–21.

[189] Palanca, M., Tozzi, G., Cristofolini, L., Viceconti, M., and Dall'Ara, E. (2015). Three-dimensional local measurements of bone strain and displacement: Comparison of three digital volume correlation approaches. Journal of Biomechanical Engineering, 137(7).

[190] Parvizian, J., Düster, A., and Rank, E. (2007). Finite cell method. Computational Mechanics, 41(1):121–133.

[191] Pistoia, W., van Rietbergen, B., Lochmüller, E. M., Lill, C. A., Eckstein, F., and Rüegsegger, P. (2002). Estimation of distal radius failure load with micro-finite element analysis models based on three-dimensional peripheral quantitative computed tomography images. Bone, 30(6):842–848.

[192] Plitman, R., Trabelsi, N., and Yosibash, Z. (2011). Investigating the mechanical response of a single vertebra using high order finite element analysis. In 17th International Symposium on Computational Biomechanics, Ulm, Germany.

[193] Polgar, K., Viceconti, M., and O'Connor, J. J. (2001). A comparison between automatically generated linear and parabolic tetrahedra when used to mesh a human femur. Proceedings of the Institution of Mechanical Engineers. Part H, Journal of Engineering in Medicine, 215(1):85–94.

[194] Prud'homme, M., Barrios, C., Rouch, P., Charles, Y. P., Steib, J.-P., and Skalli, W. (2015). Clinical Outcomes and Complications After Pedicle-anchored Dynamic or Hybrid Lumbar Spine Stabilization: A Systematic Literature Review. Clinical Spine Surgery, 28(8):E439.

[195] Putzer, M., Auer, S., Malpica, W., Suess, F., and Dendorfer, S. (2016). A numerical study to determine the effect of ligament stiffness on kinematics of the lumbar spine during flexion. BMC Musculoskeletal Disorders, 17(1):95.

[196] Qi, W., Yan, Y.-b., Zhang, Y., Lei, W., Wang, P.-j., and Hou, J. (2011). Study of stress distribution in pedicle screws along a continuum of diameters: A three-dimensional finite element analysis. Orthopaedic Surgery, 3(1):57–63.

[197] Raj, P. P. (2008). Intervertebral Disc: Anatomy-Physiology-Pathophysiology-Treatment. Pain Practice, 8(1):18–44.

[198] Rank, E. (1992). Adaptive remeshing and h-p domain decomposition. Computer Methods in Applied Mechanics and Engineering, 101(1–3):299–313.

[199] Rank, E., Kollmannsberger, S., Sorger, C., and Düster, A. (2011). Shell Finite Cell Method: A high order fictitious domain approach for thin-walled structures. Computer Methods in Applied Mechanics and Engineering, 200(45-46):3200–3209.

[200] Rank, E., Ruess, M., Kollmannsberger, S., Schillinger, D., and Düster, A. (2012). Geometric modeling, isogeometric analysis and the finite cell method. Computer Methods in Applied Mechanics and Engineering, 249-252:104–115.

[201] Reddy, B. D. (1997). Introductory Functional Analysis: With Applications to Boundary Value Problems and Finite Elements. Number 27 in Texts in applied mathematics. Springer, New York, 1998 edition.

[202] Rho, J. Y., Tsui, T. Y., and Pharr, G. M. (1997). Elastic properties of human cortical and trabecular lamellar bone measured by nanoindentation. Biomaterials, 18(20):1325–1330.

[203] Robert McNeel (2017). Rhinoceros 3D. http://www.rhino3d.com/.

[204] Roy, M. E., Rho, J. Y., Tsui, T. Y., Evans, N. D., and Pharr, G. M. (1999). Mechanical and morphological variation of the human lumbar vertebral cortical and trabecular bone. Journal of Biomedical Materials Research, 44(2):191–197.

[205] Rudi, P. (2009). Röntgenaufnahme meiner durch Spondylodese versorgten Spondylolisthesis. Wikimedia Commons. `https://commons.wikimedia.org/wiki/File:Roe_LWS_Spondylodese_L5-S1_seitlich.jpg` – License: Creative Commons CC BY-SA 3.0.

[206] Rueckert, D., Sonoda, L. I., Hayes, C., Hill, D. L., Leach, M. O., and Hawkes, D. J. (1999). Nonrigid registration using free-form deformations: Application to breast MR images. IEEE transactions on medical imaging, 18(8):712–721.

[207] Ruess, M., Schillinger, D., Bazilevs, Y., Varduhn, V., and Rank, E. (2013). Weakly enforced essential boundary conditions for NURBS-embedded and trimmed NURBS geometries on the basis of the finite cell method. International Journal for Numerical Methods in Engineering, 95(10):811–846.

[208] Ruess, M., Schillinger, D., Özcan, A. I., and Rank, E. (2014). Weak coupling for isogeometric analysis of non-matching and trimmed multi-patch geometries. Computer Methods in Applied Mechanics and Engineering, 269:46–71.

[209] Ruess, M., Tal, D., Trabelsi, N., Yosibash, Z., and Rank, E. (2012). The finite cell method for bone simulations: Verification and validation. Biomechanics and modeling in mechanobiology, 11(3-4):425–37.

[210] Ruffoni, D. and van Lenthe, G. H. (2017). Finite Element Analysis in Bone Research: A Computational Method Relating Structure to Mechanical Function. In Ducheyne, P., editor, Comprehensive Biomaterials II, pages 169–196. Elsevier, Oxford.

[211] Ruffoni, D., Wirth, A. J., Steiner, J. A., Parkinson, I. H., Müller, R., and van Lenthe, G. H. (2012). The different contributions of cortical and trabecular bone to implant anchorage in a human vertebra. Bone, 50(3):733–738.

[212] Safdari, M., Najafi, A. R., Sottos, N. R., and Geubelle, P. H. (2015). A NURBS-based interface-enriched generalized finite element method for problems with complex discontinuous gradient fields. International Journal for Numerical Methods in Engineering, 101(12):950–964.

[213] Safdari, M., Najafi, A. R., Sottos, N. R., and Geubelle, P. H. (2016). A NURBS-based generalized finite element scheme for 3D simulation of heterogeneous materials. Journal of Computational Physics, 318:373–390.

[214] Schillinger, D. (2012). The P- and B-Spline Versions of the Geometrically Nonlinear Finite Cell Method and Hierarchical Refinement Strategies for Adaptive Isogeometric and Embedded Domain Analysis. PhD thesis, Technische Universität München, Munich.

[215] Schillinger, D., Düster, A., and Rank, E. (2012a). The hp-d-adaptive finite cell method for geometrically nonlinear problems of solid mechanics. International Journal for Numerical Methods in Engineering, 89(9):1171–1202.

[216] Schillinger, D., Gangwar, T., Gilmanov, A., Heuschele, J. D., and Stolarski, H. K. (2018). Embedded shell finite elements: Solid–shell interaction, surface locking, and application to image-based bio-structures. Computer Methods in Applied Mechanics and Engineering, 335:298–326.

[217] Schillinger, D., Harari, I., Hsu, M.-C., Kamensky, D., Stoter, S. K. F., Yu, Y., and Zhao, Y. (2016). The non-symmetric Nitsche method for the parameter-free imposition of weak boundary and coupling conditions in immersed finite elements. Computer Methods in Applied Mechanics and Engineering, 309:625–652.

[218] Schillinger, D. and Rank, E. (2011). An unfitted hp-adaptive finite element method based on hierarchical B-splines for interface problems of complex geometry. Computer Methods in Applied Mechanics and Engineering, 200(47-48):3358–3380.

[219] Schillinger, D., Ruess, M., Zander, N., Bazilevs, Y., Düster, A., and Rank, E. (2012b). Small and large deformation analysis with the p- and B-spline versions of the Finite Cell Method. Computational Mechanics, 50(4):445–478.

[220] Schröder, J., Wick, T., Reese, S., Wriggers, P., Müller, R., Kollmannsberger, S., Kästner, M., Schwarz, A., Igelbüscher, M., Viebahn, N., Bayat, H. R., Wulfinghoff, S., Mang, K., Rank, E., Bog, T., D'Angella, D., Elhaddad, M., Hennig, P., Düster, A., Garhuom, W., Hubrich, S., Walloth, M., Wollner, W., Kuhn, C., and Heister, T. (2021). A Selection of Benchmark Problems in Solid Mechanics and Applied Mathematics. Archives of Computational Methods in Engineering, 28(2):713–751.

[221] Sekuboyina, A., Husseini, M. E., Bayat, A., Löffler, M., Liebl, H., Li, H., Tetteh, G., Kukačka, J., Payer, C., Štern, D., Urschler, M., Chen, M., Cheng, D., Lessmann, N., Hu, Y., Wang, T., Yang, D., Xu, D., Ambellan, F., Amiranashvili, T., Ehlke, M., Lamecker, H., Lehnert, S., Lirio, M., de Olaguer, N. P., Ramm, H., Sahu, M., Tack, A., Zachow, S., Jiang, T., Ma, X., Angerman, C., Wang, X., Brown, K., Kirszenberg, A.,

Puybareau, É., Chen, D., Bai, Y., Rapazzo, B. H., Yeah, T., Zhang, A., Xu, S., Hou, F., He, Z., Zeng, C., Xiangshang, Z., Liming, X., Netherton, T. J., Mumme, R. P., Court, L. E., Huang, Z., He, C., Wang, L.-W., Ling, S. H., Huynh, L. D., Boutry, N., Jakubicek, R., Chmelik, J., Mulay, S., Sivaprakasam, M., Paetzold, J. C., Shit, S., Ezhov, I., Wiestler, B., Glocker, B., Valentinitsch, A., Rempfler, M., Menze, B. H., and Kirschke, J. S. (2021). VerSe: A Vertebrae Labelling and Segmentation Benchmark for Multi-detector CT Images. Medical Image Analysis, 73:102166.

[222] Sensale, M., Vendeuvre, T., Schilling, C., Grupp, T., Rochette, M., and Dall'Ara, E. (2021). Patient-Specific Finite Element Models of Posterior Pedicle Screw Fixation: Effect of Screw's Size and Geometry. Frontiers in Bioengineering and Biotechnology, 9.

[223] Shamonin, D. P., Bron, E. E., Lelieveldt, B. P. F., Smits, M., Klein, S., and Staring, M. (2014). Fast Parallel Image Registration on CPU and GPU for Diagnostic Classification of Alzheimer's Disease. Frontiers in Neuroinformatics, 7.

[224] Sharabi, M., Wilke, H.-J., and Haj-Ali, R. (2018). Chapter 5 - The Vertebral Bone. In Galbusera, F. and Wilke, H.-J., editors, Biomechanics of the Spine, pages 71–87. Academic Press.

[225] Shu, L., Yamamoto, K., Yao, J., Saraswat, P., Liu, Y., Mitsuishi, M., and Sugita, N. (2018). A subject-specific finite element musculoskeletal framework for mechanics analysis of a total knee replacement. Journal of Biomechanics, 77:146 – 154.

[226] Simeon, B. (2013). Computational Flexible Multibody Dynamics. Springer Berlin Heidelberg, Berlin, Heidelberg.

[227] Slaughter, W. S. (2002). The Linearized Theory of Elasticity. Birkhäuser Basel.

[228] Smith, M. (2009). ABAQUS/Standard User's Manual, Version 6.9. Dassault Systèmes Simulia Corp, United States.

[229] Soghrati, S. and Ahmadian, H. (2015). 3D hierarchical interface-enriched finite element method: Implementation and applications. Journal of Computational Physics, 299:45–55.

[230] Soghrati, S., Aragón, A. M., Armando Duarte, C., and Geubelle, P. H. (2012). An interface-enriched generalized FEM for problems with discontinuous gradient fields. International Journal for Numerical Methods in Engineering, 89(8):991–1008.

[231] Soghrati, S. and Geubelle, P. H. (2012). A 3D interface-enriched generalized finite element method for weakly discontinuous problems with complex internal geometries. Computer Methods in Applied Mechanics and Engineering, 217–220:46–57.

[232] Šolín, P. and Červený, J. (2006). Automatic hp-Adaptivity with Arbitrary-Level Hanging Nodes. Technical Report Research Report No. 2006-07, The University of Texas at El Paso, Department of Mathematical Sciences.

[233] Sorger, C., Frischmann, F., Kollmannsberger, S., and Rank, E. (2014). TUM.GeoFrame: Automated high-order hexahedral mesh generation for shell-like structures. Engineering with Computers, 30(1):41–56.

[234] Sorger, C. G. (2012). Generierung von Netzen für Finite Elemente hoher Ordnung in zwei und drei Raumdimensionen. PhD thesis, Technische Universität München, Chair for Computation in Engineering.

[235] Stavrev, A., Nguyen, L. H., Shen, R., Varduhn, V., Behr, M., Elgeti, S., and Schillinger, D. (2016). Geometrically accurate, efficient, and flexible quadrature techniques for the tetrahedral finite cell method. Computer Methods in Applied Mechanics and Engineering, 310:646–673.

[236] Strouboulis, T., Copps, K., and Babuška, I. (2001). The generalized finite element method. Computer methods in applied mechanics and engineering, 190(32):4081–4193.

[237] Szabó, B. A. and Babuška, I. (1991). Finite Element Analysis. John Wiley & Sons, New York.

[238] Szabó, B. A., Düster, A., and Rank, E. (2004). The p-version of the finite element method. In Stein, E., editor, Encyclopedia of Computational Mechanics. John Wiley & Sons, Chichester, West Sussex.

[239] Taddei, F., Schileo, E., Helgason, B., Cristofolini, L., and Viceconti, M. (2007). The material mapping strategy influences the accuracy of CT-based finite element models of bones: An evaluation against experimental measurements. Medical Engineering & Physics, 29(9):973–979.

[240] Thiagarajan, V. and Shapiro, V. (2014). Adaptively weighted numerical integration over arbitrary domains. Computers & Mathematics with Applications, 67(9):1682–1702.

[241] Thomas, J. W. (1995). Numerical Partial Differential Equations: Finite Difference Methods. Springer, New York, 1st ed. 1995. corr. 2nd printing 1998 edition edition.

[242] Torcasio, A., Zhang, X., Oosterwyck, H. V., Duyck, J., and van Lenthe, G. H. (2012). Use of micro-CT-based finite element analysis to accurately quantify periimplant bone strains: A validation in rat tibiae. Biomechanics and Modeling in Mechanobiology, 11(5):743–750.

[243] Tozzi, G., Danesi, V., Palanca, M., and Cristofolini, L. (2016). Elastic Full-Field Strain Analysis and Microdamage Progression in the Vertebral Body from Digital Volume Correlation. Strain, 52(5):446–455.

[244] Trabelsi, N., Yosibash, Z., Wutte, C., Augat, P., and Eberle, S. (2011). Patient-specific finite element analysis of the human femur–a double-blinded biomechanical validation. Journal of Biomechanics, 44(9):1666–72.

[245] Turner, C. H., Rho, J., Takano, Y., Tsui, T. Y., and Pharr, G. M. (1999). The elastic properties of trabecular and cortical bone tissues are similar: Results from two microscopic measurement techniques. Journal of Biomechanics, 32(4):437–441.

[246] van Rietbergen, B. (2001). Micro-FE Analyses of Bone: State of the Art. In Majumdar, S. and Bay, B. K., editors, Noninvasive Assessment of Trabecular Bone Architecture and the Competence of Bone, Advances in Experimental Medicine and Biology, pages 21–30. Springer US, Boston, MA.

[247] van Rietbergen, B., Weinans, H., Huiskes, R., and Odgaard, A. (1995). A new method to determine trabecular bone elastic properties and loading using micromechanical finite-element models. Journal of Biomechanics, 28(1):69–81.

[248] Varduhn, V., Hsu, M.-C., Ruess, M., and Schillinger, D. (2016). The tetrahedral finite cell method: Higher-order immersogeometric analysis on adaptive non-boundary-fitted meshes. International Journal for Numerical Methods in Engineering, 107(12):1054–1079.

[249] Verhoosel, C., van Zwieten, G., van Rietbergen, B., and de Borst, R. (2015). Image-based goal-oriented adaptive isogeometric analysis with application to the micro-mechanical modeling of trabecular bone. Computer Methods in Applied Mechanics and Engineering, 284:138–164.

[250] Verhulp, E., Rietbergen, B. V., Müller, R., and Huiskes, R. (2008a). Micro-finite element simulation of trabecular-bone post-yield behaviour – effects of material model, element size and type. Computer Methods in Biomechanics and Biomedical Engineering, 11(4):389–395.

[251] Verhulp, E., van Rietbergen, B., Müller, R., and Huiskes, R. (2008b). Indirect determination of trabecular bone effective tissue failure properties using micro-finite element simulations. Journal of Biomechanics, 41(7):1479–1485.

[252] Verma, K., Boniello, A., and Rihn, J. (2016). Emerging Techniques for Posterior Fixation of the Lumbar Spine. The Journal of the American Academy of Orthopaedic Surgeons, 24(6):357–364.

[253] Viceconti, M., Bellingeri, L., Cristofolini, L., and Toni, A. (1998). A comparative study on different methods of automatic mesh generation of human femurs. Medical Engineering & Physics, 20(1):1–10.

[254] Vinci, C. (2009). Application of Dirichlet Boundary Conditions in the Finite Cell Method. Master's Thesis, Lehrstuhl für Computation in Engineering, Technische Universität München.

[255] Wagnac, E., Arnoux, P.-J., Garo, A., and Aubin, C.-E. (2012). Finite element analysis of the influence of loading rate on a model of the full lumbar spine under dynamic loading conditions. Medical & Biological Engineering & Computing, 50(9):903–915.

[256] Wassermann, B., Kollmannsberger, S., Bog, T., and Rank, E. (2017). From geometric design to numerical analysis: A direct approach using the Finite Cell Method on Constructive Solid Geometry. Computers & Mathematics with Applications.

[257] Wassermann, B., Kollmannsberger, S., Yin, S., Kudela, L., and Rank, E. (2019). Integrating CAD and numerical analysis: 'Dirty geometry' handling using the Finite Cell Method. Computer Methods in Applied Mechanics and Engineering, 351:808–835.

[258] White, A. A. (1990). Clinical Biomechanics of the Spine. Lippincott Williams & Wilkins, Philadelphia, 2nd edition.

[259] Wilke, H. J., Wolf, S., Claes, L. E., Arand, M., and Wiesend, A. (1995). Stability increase of the lumbar spine with different muscle groups. A biomechanical in vitro study. Spine, 20(2):192–198.

[260] Wille, H., Ruess, M., Rank, E., and Yosibash, Z. (2016). Uncertainty quantification for personalized analyses of human proximal femurs. Journal of Biomechanics, 49(4):520–527.

[261] Wirth, A. J., Goldhahn, J., Flaig, C., Arbenz, P., Müller, R., and van Lenthe, G. H. (2011). Implant stability is affected by local bone microstructural quality. Bone, 49(3):473–478.

[262] Wirth, A. J., Mueller, T. L., Vereecken, W., Flaig, C., Arbenz, P., Müller, R., and van Lenthe, G. H. (2009). Mechanical competence of bone-implant systems can accurately be determined by image-based micro-finite element analyses. Archive of Applied Mechanics, 80(5):513–525.

[263] Wirth, A. J., Müller, R., and van Lenthe, G. H. (2012). The discrete nature of trabecular bone microarchitecture affects implant stability. Journal of Biomechanics, 45(6):1060–1067.

[264] Wittenburg, J. (2008). Dynamics of Multibody Systems. Berlin-Springer.

[265] Wolff, J., Narra, N., Antalainen, A.-K., Valášek, J., Kaiser, J., Sándor, G. K., and Marcián, P. (2014). Finite element analysis of bone loss around failing implants. Materials & Design, 61:177–184.

[266] Wolfram, U., Wilke, H.-J., and Zysset, P. K. (2010). Valid $\mu$ finite element models of vertebral trabecular bone can be obtained using tissue properties measured with nanoindentation under wet conditions. Journal of Biomechanics, 43(9):1731–1737.

[267] Yang, Z., Kollmannsberger, S., Düster, A., Ruess, M., Garcia, E. G., Burgkart, R., and Rank, E. (2012a). Non-standard bone simulation: Interactive numerical analysis by computational steering. Computing and Visualization in Science, 14(5):207–216.

[268] Yang, Z., Ruess, M., Kollmannsberger, S., Düster, A., and Rank, E. (2012b). An efficient integration technique for the voxel-based finite cell method. International Journal for Numerical Methods in Engineering, 91(5):457–471.

[269] Yosibash, Z. (1997). Numerical analysis on singular solutions of the Poisson equation in two-dimensions. Computational Mechanics, 20(4):320–330.

[270] Yosibash, Z. (2012). P-FEMs in biomechanics: Bones and arteries. Computer Methods in Applied Mechanics and Engineering, 249-252:169–184.

[271] Yosibash, Z., Katz, A., and Milgrom, C. (2013). Toward verified and validated FE simulations of a femur with a cemented hip prosthesis. Medical Engineering & Physics, 35(7):978–987.

[272] Yosibash, Z., Trabelsi, N., and Hellmich, C. (2008). Subject-Specific p-FE Analysis of the Proximal Femur Utilizing Micromechanics-Based Material Properties. International Journal for Multiscale Computational Engineering, 6(5):483–498.

[273] Yosibash, Z., Trabelsi, N., and Milgrom, C. (2007). Reliable simulations of the human proximal femur by high-order finite element analysis validated by experimental observations. Journal of Biomechanics, 40(16):3688–3699.

[274] Yushkevich, P. A., Piven, J., Hazlett, H. C., Smith, R. G., Ho, S., Gee, J. C., and Gerig, G. (2006). User-guided 3D active contour segmentation of anatomical structures: Significantly improved efficiency and reliability. NeuroImage, 31(3):1116–1128.

[275] Zander, N. (2017). Multi-Level Hp-FEM: Dynamically Changing High-Order Mesh Refinement with Arbitrary Hanging Nodes. PhD Thesis, Technische Universität München, München.

[276] Zander, N., Bog, T., Elhaddad, M., Frischmann, F., Kollmannsberger, S., and Rank, E. (2016). The multi-level hp-method for three-dimensional problems: Dynamically changing high-order mesh refinement with arbitrary hanging nodes. Computer Methods in Applied Mechanics and Engineering, 310:252–277.

[277] Zander, N., Bog, T., Kollmannsberger, S., Schillinger, D., and Rank, E. (2015). Multi-level hp-adaptivity: High-order mesh adaptivity without the difficulties of constraining hanging nodes. Computational Mechanics, 55(3):499–517.

[278] Zander, N., Kollmannsberger, S., Ruess, M., Yosibash, Z., and Rank, E. (2012). The Finite Cell Method for linear thermoelasticity. Computers & Mathematics with Applications, 64(11):3527–3541.

[279] Zander, N., Ruess, M., Bog, T., Kollmannsberger, S., and Rank, E. (2017). Multi-level hp-adaptivity for cohesive fracture modeling. International Journal for Numerical Methods in Engineering, 109(13):1723–1755.

[280] Zannoni, C., Mantovani, R., and Viceconti, M. (1999). Material properties assignment to finite element models of bone structures: A new method. Medical Engineering & Physics, 20(10):735–740.

[281] Zauel, R., Yeni, Y. N., Bay, B. K., Dong, X. N., and Fyhrie, D. P. (2006). Comparison of the linear finite element prediction of deformation and strain of human cancellous bone to 3D digital volume correlation measurements. Journal of Biomechanical Engineering, 128(1):1–6.

[282] Zhang, Q.-H., Tozzi, G., and Tong, J. (2014). Micro-mechanical damage of trabecular bone–cement interface under selected loading conditions: A finite element study. Computer Methods in Biomechanics and Biomedical Engineering, 17(3):230–238.

[283] Zhu, M.-L., Zhang, Q.-H., Lupton, C., and Tong, J. (2016). Spatial resolution and measurement uncertainty of strains in bone and bone–cement interface using digital volume correlation. Journal of the Mechanical Behavior of Biomedical Materials, 57:269–279.

[284] Zhu, T. and Atluri, S. N. (1998). A modified collocation method and a penalty formulation for enforcing the essential boundary conditions in the element free Galerkin method. Computational Mechanics, 21(3):211–222.

[285] Zienkiewicz, O., Taylor, R., and Zhu, J. (2005). The Finite Element Method: Its Basis and Fundamentals. Butterworth-Heinemann, 6th edition.

[286] Zysset, P. K. (2003). A review of morphology–elasticity relationships in human trabecular bone: Theories and experiments. Journal of Biomechanics, 36(10):1469–1485.